ABSORPTION BASED PROCESSES APPLYING PHASE TRANSITION FOR ENERGY EFFICIENT POSTCOMBUSTION CO_2 CAPTURE

BY

QING YE

DISSERTATION

Submitted in partial fulfillment of the requirements
for the degree of Doctor of Philosophy in Agricultural and Biological Engineering
in the Graduate College of the
University of Illinois at Urbana-Champaign, 2018

Urbana, Illinois

Doctoral Committee:

Professor Xinlei Wang, Chair
Dr. Yongqi Lu
Professor Paul Kenis
Professor Emeritus Mike Tumbleson
Professor Vijay Singh

ABSTRACT

The conventional CO_2 absorption process, using an aqueous 30 wt% monoethanolamine (MEA) solvent for postcombustion CO_2 capture, is energy intensive and thus costly. The novel phase transitional CO_2 absorption process has been regarded as a promising alternative to the benchmark MEA process. The solvent in a phase transitional process turns into two phases after CO_2 absorption; one phase contains the majority of the absorbed CO_2 while the other is CO_2 lean. This key feature of a phase transitional process enables the use of only the CO_2 rich phase for CO_2 stripping and solvent regeneration, which can reduce the energy requirement compared with the MEA process. We investigated two scenarios of phase transitional processes (i.e., liquid-solid and liquid-liquid) to overcome the energy disadvantages associated with the MEA process.

For the liquid-solid CO_2 absorption process, an aqueous solution of potassium carbonate was applied and the CO_2 absorption product, i.e., potassium bicarbonate ($KHCO_3$), was subjected to a crystallization process due to its limited aqueous solubility at low temperatures (<40°C). The $KHCO_3$ rich slurry separated from the mother solution was sent to the stripper for CO_2 desorption at elevated temperatures (>140°C). The kinetics of $KHCO_3$ crystallization and the solubility of $KHCO_3$ both were investigated under typical operating conditions. The resultant data were fit to a size dependent crystal growth model, and applied to perform the crystallizer design analysis for the proposed carbonate based CO_2 absorption process.

The liquid-solid process had drawbacks related to issues incurred by the slurry operation. Therefore, additional research efforts were focused on studying the liquid-liquid phase transition which constitutes the major part of this dissertation.

The first step was to select the proper liquid-liquid phase transitional (i.e., biphasic) solvents. A feasible biphasic solvent that is subject to a liquid-liquid phase separation during CO_2 absorption can be a blend of compounds “A” and “B”. Compound “A”, containing primary or secondary amino groups, acts as an absorption accelerator. Compound “B”, containing tertiary amino groups, serves as a promoter for solvent regeneration. A screening study was conducted using a large pool of candidate compounds “A” and “B”. The aqueous blends of “A” and “B” were

investigated with respect to their performance of CO_2 absorption (i.e., rate and capacity), CO_2 desorption (i.e., CO_2 desorption pressure) and phase separation behavior. The qualitative relationship between the solvent structure and performance was evaluated. A polyamine based compound "A" was indispensable for liquid-liquid phase separation. The compound "A" with 4 to 6 carbon atoms and up to 3 nitrogen atoms favored the performance of its solvent blend.

A further screening study was conducted using two aqueous biphasic solvents, with diethylenetriamine (DETA) as the common absorption accelerator. The first solvent blended *N*,*N*,*N′*,*N″*,*N″*-pentamethyldiethylenetriamine (PMDETA) as the regeneration promoter, and the second blended bis[2-(*N*,*N*-dimethylamino)ethyl]ether. Similar screening criteria as for the prior study were adopted. The formula of a solvent blend affected its CO_2 loading capacity and phase separation behavior. The blend of DETA and PMDETA was superior to MEA with respect to its larger capacity and higher desorption pressure of CO_2; thus, it was selected for further study.

Two formulae of the blend of DETA and PMDETA, i.e., 2 m DETA + 3 m PMDETA, and 1.5 m DETA + 3.5 m PMDETA, were adopted to study the mechanisms of liquid-liquid phase separation associated with reactions of CO_2 absorption and desorption. Quantitative speciation analyses in the dual phases were conducted with ^{1}H, ^{13}C and two dimensional (2D) nuclear magnetic resonance (NMR) spectroscopic techniques, focusing on the evolvement of species upon different CO_2 loadings. CO_2 absorption into the biphasic solvent blend of DETA and PMDETA underwent a two stage process. In the early stage, CO_2 reacted with DETA, and monocarbamate and dicarbamate species (including their protonated species) were formed. In the latter stage, further CO_2 absorption resulted in the protonation of PMDETA via proton exchange reactions and production of HCO_3^-/CO_3^{2-} (i.e., PMDETA catalyzed CO_2 hydration). The volumetric fraction of the CO_2 rich phase increased gradually in the early stage and abruptly in the latter stage. CO_2 desorption from the CO_2 rich phase, separated from the CO_2 laden biphasic solvent, was a reverse process of CO_2 absorption and coupled with a dual phase transition.

The biphasic solvent blend of DETA and PMDETA was characterized further with respect to its thermodynamic and kinetic behaviors. A comprehensive thermodynamic model was developed to predict the liquid-liquid phase separation and vapor-liquid-liquid equilibrium in the aqueous

biphasic solvents comprised of DETA and PMDETA for CO_2 capture. The unknown reaction equilibrium constants and binary interaction parameters were retrieved by data regression. The predicted partial pressures of CO_2 over the biphasic solvent or the separated CO_2 rich phase agreed with the experimental data. Detailed speciation in either liquid phase evolving with changing CO_2 loadings and temperatures was predicted based on the model, and the results were consistent with the prior NMR data. Moreover, the phase separation behavior with respect to the volumetric fraction of each liquid phase and the partitioning of DETA or PMDETA between the dual phases was predicted with accuracy. The heat of absorption reactions for the mother biphasic solvent was predicted to be smaller than the heat of desorption reactions for the separated CO_2 rich phase. The thermodynamic modeling approach developed in this study could be applied to other biphasic solvent systems.

The kinetics of CO_2 absorption into neat DETA solutions, neat PMDETA solutions and their blends were studied. The intrinsic rate constants of reactions between CO_2 and DETA, and between CO_2 and PMDETA (PMDETA catalyzed CO_2 hydration), were retrieved from the data measured for the monophasic solutions of neat DETA and neat PMDETA, respectively, based on an established mass transfer and kinetic model. Reactions of forming dicarbamate species from monocarbamate of DETA were as fast as the reactions of forming monocarbamate from molecular DETA. The obtained rate constants and the concentrations of species estimated by the prior thermodynamic model were used together to predict the kinetics of CO_2 absorption into the solvent blend of DETA and PMDETA with and without the presence of dual liquid phases. A modified two film mass transfer model was applied to account for the scenario when dual phases were present. The prediction results were consistent with the experimental data, indicating that the absorption of CO_2 into two liquid phases could be represented as the simultaneous absorption of CO_2 into each of the two monophasic liquid solvents.

ACKNOWLEDGEMENTS

First and the foremost, I would like to express gratitude to my advisors, Dr. Xinlei Wang and Dr. Yongqi Lu, for their patient guidance, persistent support and great encouragement throughout the years of my Ph.D. studies. Not only have they taught me to be an independent researcher, but also have they helped me grow to be a man taking responsibility. Special thanks are given to Dr. Lu who introduced me to the interesting research topic in this dissertation, and mentored me with inspiration in every stage of my research. My gratitude is extended to Mrs. Wang and Mrs. Lu for the cordial hospitality at their homes upon each of my visits. I also would like to thank my Ph.D. committee members, Dr. Paul Kenis, Dr. Mike Tumbleson and Dr. Vijay Singh for their constructive criticism and suggestions on my research, as well as detailed assistance in structuring and revising this dissertation.

With sincerity, I thank US Department of Energy/National Energy Technology Laboratory and Prairie Research Institute of University of Illinois at Urbana-Champaign for providing me with funding support during the course of my Ph.D. program. I also appreciate Illinois State Geological Survey for providing me with every opportunity to conduct activities related to my research. Particularly, I would thank my current and previous colleagues in Geological Survey Laboratory where I have performed all my research, such as David Ruhter, Dr. Hong Lu, Dr. Shihan Zhang and Dr. Yang Du, for their huge support and numerous advices in lab matters and in daily life. I am thankful to Ms. Susan Krusemark, the scientific editor of Illinois State Geological Survey, who has reviewed every manuscript I submitted for publication with meticulous care. Besides, I would like to thank Derek Sompong, Jiaxing Li, Priscilia Sinata, Renlong Zhu, Rohan Kalyani and Ruth Kaplan, whom I worked with closely, for their assistance in various aspects during the time I spent in Illinois State Geological Survey.

I also appreciate all the opportunities that my home department, Department of Agricultural and Biological Engineering provided me with during the period of my Ph.D. studies, such as the courses I took, seminars I attended and hosted, conference traveling I got financial support for, etc. I am grateful truly to all the kind suggestions from and helpful discussions with Dr.

Liangcheng Yang, Shang-Jen Yang and Jiangong Li, the current and former members of Dr. Xinlei Wang's group.

I have been privileged to learn nuclear magnetic resonance spectroscopy in School of Chemical Sciences, and various material characterization techniques in Material Research Laboratory and Illinois Sustainable Technology Center. Special thanks are given to Dr. Lingyang Zhu for the patient, one on one instructions on operating the nuclear magnetic resonance spectrometers and decoding the spectra, Dr. Mauro Sardela for his excellent training on powder X-ray diffraction, and Viktoriya Yurkiv for the sample analysis by using gas chromatography-mass spectrometry.

I would like to thank all my friends I met during these years, especially Albert Wang, Bing O'Dowd, Greg Chu, Huihuo Zheng, Ian Hsiao, John Meng, Josh Huang, Matt Edwin, Nehemiah Tan, Pei-Wen Tsai, Yizhe Zhang, and the couple of Zijun Chang and Manying Mu Chang. Without them, I could not have accomplished this study.

Last but not the least, my deepest gratitude goes to my most beloved parents and my wife, Wenyan Li, for their long lasting love, endless support and faithful accompaniment through this whole period. My thanks to them are unspeakable.

TABLE OF CONTENTS

LIST OF TABLES

LIST OF FIGURES

LIST OF ABBREVIATIONS

AAS	amino acid salt
AEEA	2-(2-aminoethylamino)ethanol
AMP	2-amino-2-methyl-1-propanol
BDA	1,4-butanediamine
BDMAEE	bis[2-(*N*,*N*-dimethylamino)ethyl]ether
BiCAP	biphasic solvent based CO_2 absorption process
BIP	binary interaction parameter
BP	boiling point
CAP	chilled ammonia process
CCS	CO_2 capture and storage
CCU	carbon capture and utilization
COE	cost of electricity
CSD	crystal size distribution
CTB	carbonate to bicarbonate (conversion ratio)
DAC	direct air capture
DEA	diethanolamine
DEEA	2-(diethylamino)ethanol
DETA	diethylenetriamine
DEGDEE	diethylene glycol diethyl ether
DOE	Department of Energy
DMAEE	2-[2-(dimethylamino)ethoxy]ethanol
DMBA	*N*,*N*-dimethylbutylamine
DMCA	*N*,*N*-dimethylcyclohexylamine
DPA	dipropylamine
e-NRTL	electrolyte nonrandom two liquid
EIA	Energy Information Administration
EPA	Environmental Protection Agency
gCOSY	gradient correlation spectroscopy
gHMBC	gradient heteronuclear multiple bond correlation spectroscopy
gHSQC	gradient heteronuclear single quantum correlation spectroscopy
GC-MS	gas chromatography-mass spectrometry
GDP	gross domestic product
Hot CAP	hot carbonate absorption process
HSS	heat stable salts
ID	inner diameter
IEA	International Energy Agency
IFPEN	French Institute of Petroleum Energies Nouvelles
IGCC	integrated gasification combined cycle
IPCC	Intergovernmental Panel on Climate Change
LLE	liquid-liquid equilibrium
LLPS	liquid-liquid phase separation
LVC	lean vapor compression
MAPA	3-(methylamino)propylamine
CHxMA	*N*-methylcyclohexylamine

MDEA	*N*-methyldiethanolamine
MEA	monoethanolamine
MSMPR	mixed suspension, mixed product removal
NETL	National Energy Technology Laboratory
NMP	*N*-methyl-2-pyrrolidone
NMR	nuclear magnetic resonance
OD	outer diameter
PC	pulverized coal
PCB	potassium carbonate/bicarbonate
PCC	postcombustion CO_2 capture
PFO	pseudo first order
PMDETA	*N*,*N*,*N′*,*N″*,*N″*-pentamethyldiethylenetriamine
PtA	pentylamine
PZ	piperazine
RKS	Redlich-Kwong-Soave
SCR	stirred cell reactor
SDG	size dependent growth
SEM	scanning electron microscopy
TETA	triethylenetetramine
TMS	tetramethylsilane
Triglyme	triethylene glycol dimethyl ether
UNFCCC	United Nations Framework Convention on Climate Change
UNIFAC	UNIQUAC functional group activity coefficient
UNIQUAC	universal quasichemical
VLE	vapor-liquid equilibrium
VLLE	vapor-liquid-liquid equilibrium
VLSE	vapor-liquid-solid equilibrium
VP	vapor pressure
WWC	wetted wall column
XRD	X-ray diffraction

CHAPTER 1: INTRODUCTION

1.1 Global climate change

The current trend of global climate change, especially the persistent warming effect in the climate system, is unequivocal (IPCC, 2014). The change of global surface (land and ocean combined) temperature relative to the average between 1951 and 1980 is illustrated in Fig. 1-1. The current global temperature is 1.2°C higher than the level in 1880, and sustained warming at the Earth's surface has been observed over the past half century. The global temperature shall not exceed 2°C above the preindustrial level by the end of the 21st century to avoid dangerous climate change effects according to the United Nations Framework Convention on Climate Change (UNFCCC), and aggressive efforts shall be pursued to limit the temperature rise below 1.5°C because even a 2°C increase will be outside the range of temperatures experienced by human beings (IPCC, 2014).

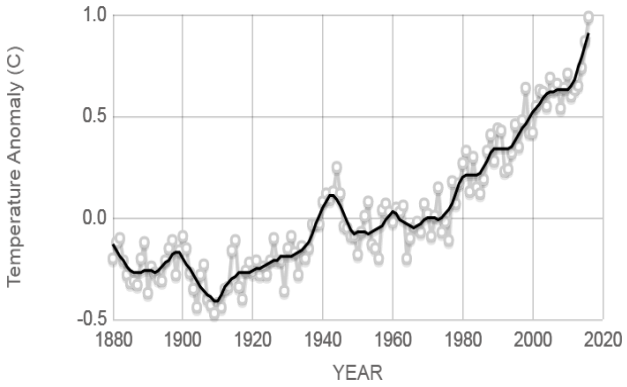

Fig. 1-1. Change of global surface temperature between 1880 and 2016 relative to the average temperature between 1951 and 1980. A grey dot is an annual mean and the black line is smoothed by the lowness of five year average. Data source and image credit: Goddard Institute for Space Studies, National Aeronautics and Space Administration (NASA/GISS, 2017).

Discernable consequences of global climate change are multifarious on physical, biological and human systems (IPCC, 2007). One major consequence is the changing weather such as the undesirable rainfall patterns (i.e., amount, intensity, frequency and type of precipitation). As a result, regions which are dry will become even drier, while regions that are wet will become even wetter. Moreover, the length and severity of some extreme weather events (e.g., heat wave,

drought and hurricane) are increasing. The second consequence affects the Earth's cryosphere, such as the decline of Arctic sea ice, retreat and disappearance of alpine glaciers, melting of ice sheets in Greenland and Antarctic, and reduction of snow cover and loss of ice caps in the land of the Northern Hemisphere. The third is related to the ocean, such as the sea level rise and increase in ocean heat content. Thermal expansion of sea water under warmer temperatures will exacerbate the sea level rise. Moreover, ocean acidification and ocean deoxygenation are observed. Ocean acidification results from excessive absorption of CO_2, primarily from anthropogenic emission sources, which lowers the availability of CO_3^{2-} for calcifying organisms to form shells thus threatening marine life, coral reefs and fisheries together with other physiological and ecological processes. Oxygen depletion is due to the declining O_2 dissolved in warmer oceans, which poses adverse consequences for ocean life. Fourth, the ecosystems suffer the negative impacts of the global warming, such as extinction of species and loss of biodiversity in vulnerable ecosystems (e.g., conifer forest, Arctic tundra, savanna and Mediterranean climate systems). Moreover, the earlier timing of spring events (e.g., the leafing or flowering of plants) is observed. Last, harmful global warming effects threaten the human society. For example, the coastal flooding and abandonment of human settlements in lowland areas are inevitable due to the sea level rise. Because of the extended areas of salinization in groundwater and estuaries, the availability of freshwater resources for human beings and ecosystems are decreased in coastal zones. Moreover, agricultural production and food security will be affected adversely by the threat from soil erosion, land degradation and desertification, which results in decreasing crop yields, especially in low latitude areas.

The climate change and global warming and their associated environmental and socioeconomic changes will jeopardize the sustainable development for humans. In 2014, the intergovernmental panel on climate change (IPCC) concluded in its assessment report that human influence "is extremely likely to have been the dominant cause of the observed warming since the mid 20th century" (IPCC, 2014). The human activities interfering with the climate system include burning fossil fuels (i.e., coal, petroleum and natural gas), nonfuel industrial processes (e.g., cement production), land use change (e.g., deforestation and forest degradation) and agricultural production (e.g., farming ruminants for meat consumption). These activities have become the main drivers of gross domestic product (GDP) increase and population growth, especially since

the beginning of Industrial Revolution (circa 1750). In the meanwhile, these activities result in excess emissions of greenhouse gases to the atmosphere and contribute to the global warming and climate change. Before the industrial era, the atmospheric concentrations of greenhouse gases were stable from a rough balance between their natural emission sources and the Earth's natural removal sinks (e.g., photosynthesis by plants and marine plankton). However, this balance has been broken since the industrial era, because excess release of anthropogenic greenhouse gases exceeds the adaptive capacity of natural sinks.

1.2 Greenhouse gases and greenhouse effect

The major greenhouse gases present in the air are polyatomic molecules, such as carbon dioxide (CO_2), methane (CH_4), nitrous oxide (N_2O), tropospheric ozone (O_3, 90% of atmospheric O_3 is in the stratosphere) and fluorinated gases in the order of decreasing abundance (IPCC, 2007). Fluorinated gases include chlorofluorocarbons (CFCs), hydrofluorocarbons (HFCs), perfluorocarbons (PFCs), tetrafluoromethane (CF_4), nitrogen trifluoride (NF_3) and sulfur hexafluoride (SF_6). Except the fluorinated gases synthesized by humans (e.g., used for refrigeration and fire suppression), most greenhouse gases have both natural and anthropogenic sources. The most important source of anthropogenic CO_2 emissions is combustion of fossil fuels. Land use change contributes to an additional portion of CO_2 emissions by altering the Earth's carbon cycle (i.e., less CO_2 entering the carbon sinks such as forests). A higher atmospheric CH_4 concentration results from enteric fermentation of livestock, manure management, rice cultivation, manmade lakes and vented landfill emissions. Agricultural activities, including the tillage and use of fertilizers, lead to a higher atmospheric N_2O concentration.

The trends of atmospheric concentrations of several major greenhouse gases since 1975 are shown in Fig. 1-2. The current level of CO_2 concentration has exceeded 400 ppm. Exactly, the level reached 405 ppm in November, 2017, as measured at the world's principal benchmark site in Mauna Loa Observatory, compared with the preindustrial level of 280 ppm. Based on the reliable measurements from the extracted Antarctic ice cores, the atmospheric concentration of CO_2 was in the range of 180 to 280 ppm (temperature dependent) throughout the past 800,000 years and in the range of 260 to 280 ppm throughout the preceding 10,000 years (starting from

the end of the latest glacial maximum), until the rise since 1750. Similar evidences were found with regard to the other greenhouse gases. Therefore, IPCC concluded the "atmospheric concentrations of carbon dioxide, methane and nitrous oxide are unprecedented in at least the last 800,000 years. Their effects have been detected throughout the climate system and are extremely likely to have been the dominant cause of the observed warming since the mid 20th century" (IPCC, 2014).

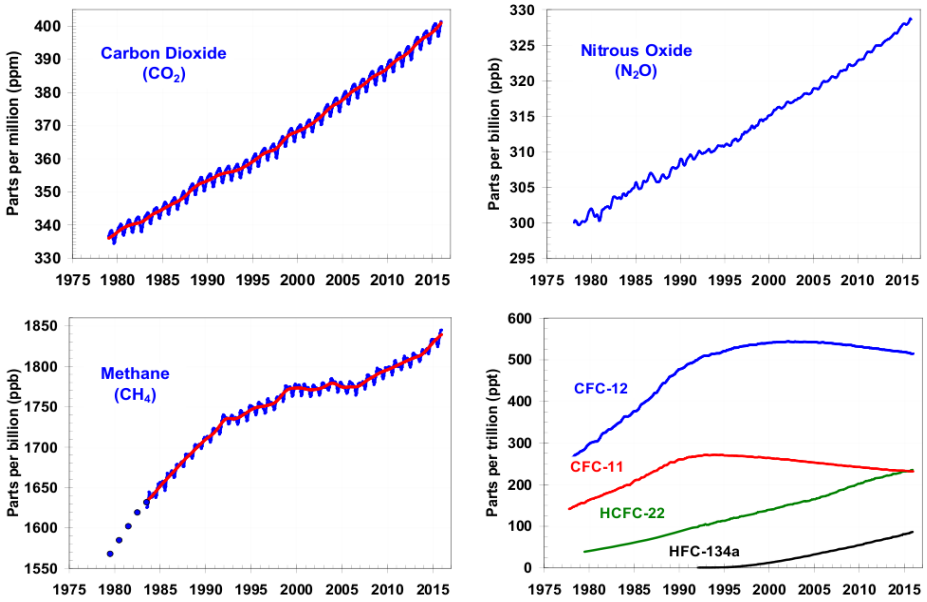

Fig. 1-2. Atmospheric concentrations (mole fractions in dry air) of major greenhouse gases. Data source and image credit: Earth System Research Laboratory of National Oceanic and Atmospheric Administration (NOAA/ESRL, 2017).

The greenhouse gases in the atmosphere can absorb and emit the longwave (infrared) thermal radiation emitted by the Earth. The greenhouse effect is the process by which radiation from the greenhouse gases warms the Earth's lower atmosphere and surface, which works by preventing the absorbed heat from leaving the atmosphere through radiative transfer. The Earth's natural greenhouse effect is critical to supporting life, which results in the present average of the Earth's surface temperature of 16 rather than -18°C without greenhouse gases. However, human activities increasing the concentrations of atmospheric greenhouse gases have intensified the natural greenhouse effect and caused the rise in global temperatures.

The greenhouse effect of a gas is determined by its abundance in the atmosphere and its global warming potential (GWP), which is a relative measure of the amount of heat trapped by a kg of a greenhouse gas compared with that trapped by a kg of CO_2. The GWP for a specific gas depends on its radiative efficiency (i.e., ability of absorbing infrared radiation), its atmospheric lifetime and the spectral location of the absorbing wavelengths. Efficient infrared absorption and a long lifetime (i.e., slow decay of concentration) both indicate a high GWP value. However, large absorption of radiation at a certain wavelength may not increase the GWP if the atmosphere has absorbed much radiation at that wavelength. The greenhouse effect is the most pronounced if a gas absorbs radiation in a "window" of wavelengths where the atmosphere is transparent. GWP is evaluated over a specific time horizon (20, 100 or 500 yrs), because a gas quickly removed from the air may have a large greenhouse effect but becomes less important after an extended time period. The GWP value of CO_2 is normalized to 1 over any time horizon adopted. If a molecule has a longer lifetime than CO_2, its GWP will increase with the timescale considered. Conversely, if a gas has a short lifetime, it will have a larger GWP on a 20 yr scale than that on a 100 yr scale. GWP values (CO_2 equivalent) for some typical greenhouse gases are shown in Table 1-1. For example, CH_4 is 86 times more effective at trapping heat than CO_2 in a time horizon of 20 yrs, but only 34 times in a time horizon of 100 yrs.

Table 1-1. Atmospheric lifetime and GWP relative to CO_2 at different time horizons for typical greenhouse gases.

Greenhouse gases	Lifetime (years)	GWP values		
		20 years*	100 years*	500 years**
CO_2	30 to 95	1	1	1
CH_4	12.4	86	34	7.6
N_2O	121.0	268	298	153
CF_4	50,000	4,950	7,350	11,200
CH_2FCF_3 (HFC134a)	13.4	3,790	1,550	435
CCl_3F (CFC11)	45.0	7,020	5,350	1,620

* Data source: IPCC, 2013 (values with climate carbon feedbacks). ** Data source: IPCC, 2007.

Water vapor (H_2O), primarily as vapor or condensed microscopic droplets suspended in clouds, is the most abundant greenhouse gas in the atmosphere (10 to 50,000 ppm that fluctuates regionally). Water vapor accounts for the largest direct contribution to the overall greenhouse effect, i.e., 36 to 66% under clear sky conditions and 66 to 85% when cloudy, compared with 9 to 26% for CO_2 and 4 to 9% for CH_4 (it is not possible to assign a specific percentage to a gas because the absorption and emission bands overlap between gases). However, human activities,

such as irrigation and deforestation, have a small influence on the atmospheric concentration of water vapor. A water molecule has a short atmospheric lifetime (nine days); therefore, the presence of water vapor does not strengthen directly the natural greenhouse effect.

1.3 Mitigation of anthropogenic CO_2 emissions

In light of the relationship between the increasing global temperature and the increasing atmospheric concentrations of greenhouse gases, there is a need for substantial and sustained reduction of greenhouse gas emissions, such that their concentrations can be stabilized at a level where ecosystems can adapt naturally to climate change, food production is not threatened and economic development can proceed in a sustainable fashion. To achieve the goal of 2℃ rise in global temperature, the greenhouse gas concentration (CO_2 equivalent) should be controlled below 450 ppm by the end of the 21st century (IPCC, 2014).

The total amount of global anthropogenic greenhouse gas emissions in 2010 was 49 (±4.5) gigatonne (CO_2 equivalent); the contribution of each gas is shown in Fig. 1-3 (IPCC, 2014). CO_2 emissions from fossil fuel combustion, industrial processes and forestry and other land use contributed to 76% of global greenhouse gas emissions in 2010, much higher than the contributions from CH_4 (16%) and N_2O (6%). In the US, the total amount of emissions of greenhouse gases in 2015 was 6,587 megatonne (CO_2 equivalent), with the contribution of each gas shown in Fig. 1-3, based on the data from the US Environmental Protection Agency (EPA). CO_2 had the largest contribution (82%) in domestic greenhouse gas emissions in 2015, followed by CH_4 (10%) and N_2O (5%). With this in view, it is crucial to mitigate the CO_2 emissions and lower the atmospheric CO_2 concentration. Various strategies have been proposed.

One type of solution is to enhance the capacity of natural carbon sinks, such as preventing deforestation, reforestation and afforestation. Similar approaches include enhanced weathering, ocean fertilization and biochar sequestration. Enhanced weathering refers to geoengineering approaches which strengthen the natural carbon cycle by dissolving minerals in the Earth's crust with CO_2 (mineral sequestration). Ocean fertilization is to introduce nutrients to the upper ocean to increase food production and thus to remove CO_2 from the atmosphere. Biochar is charcoal

made from biomass via pyrolysis under low O_2 levels, which is used as a soil amendment and potential a carbon sequestration material. The direct air capture (DAC) is a solution which removes CO_2 from the air (in combination with the long term storage of CO_2) and thus lowers the atmospheric concentration of CO_2 directly. For instance, an aqueous hydroxide absorbent (e.g., NaOH) can be employed to scrub the ambient CO_2 and the product Na_2CO_3 reacts with $Ca(OH)_2$ to regenerate the absorbent and obtain $CaCO_3$, which is subject to heat recovery of pure CO_2. DAC is energy intensive, especially in the calcination step. Moreover, CO_2 in the air is diluted. Both factors make DAC not cost effective to be deployed massively.

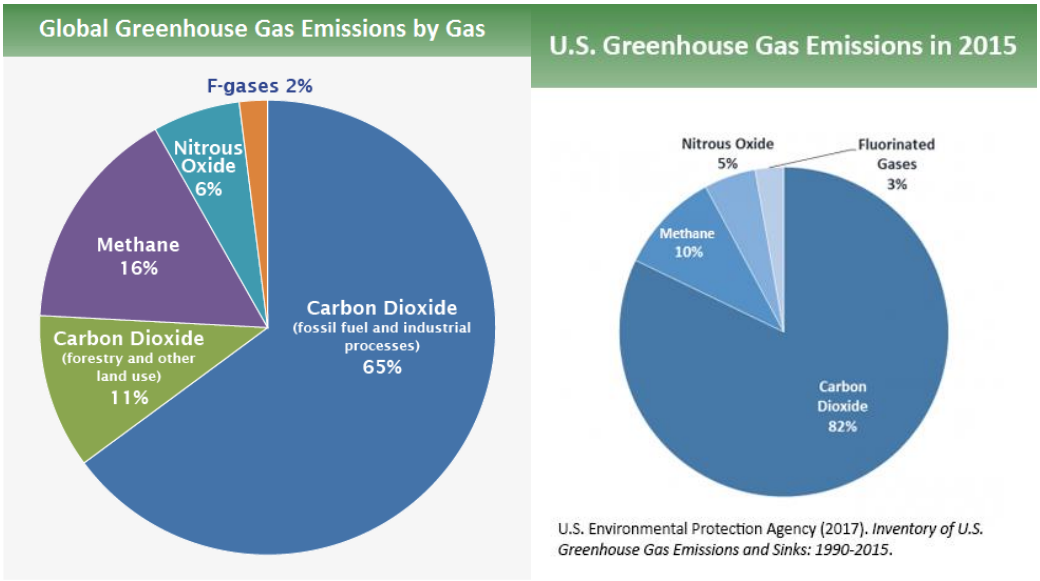

Fig. 1-3. Contribution to greenhouse gas emissions by gas. Left panel: global emission data in 2010. Right panel: US emission data in 2015 (Image credit: US EPA).

Besides the solutions pointing to the carbon sinks, another type of solutions is focused on reducing the CO_2 emissions from its sources. Although it does not lower the atmospheric concentration of CO_2 directly, the price paid to reduce the emissions of CO_2 is less than the loss suffered by the world to allow CO_2 to be released to the air (Stern, 2007). The major CO_2 emission sources in the US in 2015 are shown in Fig. 1-4. The electricity generation contributed to 35% of the total domestic CO_2 emissions, followed by transportation (32%), and the industrial, commercial, residential and other economic sectors (33%). The energy related CO_2 emissions in the US in 2016 was 5,170 megatonne, in which the largest contributor was the electric power

sector (2,055, 40%), followed by the transportation sector (1,883, 36%), and the industrial, commercial and residential sectors (1,232, 24%) (EIA, 2016).

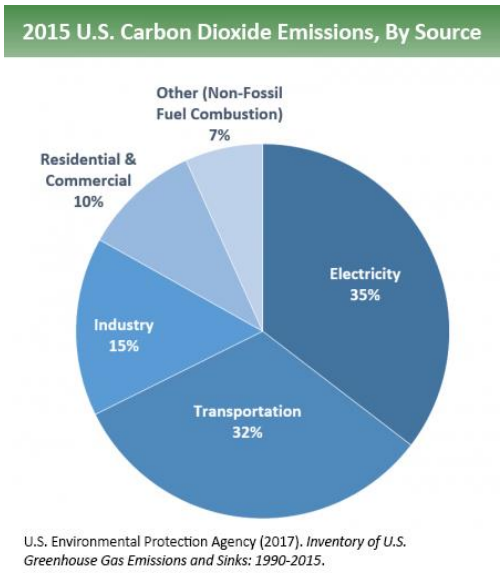

Fig. 1-4. Economic sectors contributing to US CO_2 emissions in 2015 (Image credit: US EPA).

Considering the fact that the energy sector is the major source of CO_2 emissions, it is urgent to improve the energy efficiency thus reducing the amount of energy use required. Examples include improvement of the insulation of buildings, installation of compact fluorescent lights and increase of fuel economy in automobiles. Moreover, it is urgent to develop cleaner production processes and apply the replacement power sources to phase out the usage of the conventional fossil fuels with high carbon emissions. This entails the switching to low carbon energy sources, such as nuclear power and renewable energies (solar power, wind power, hydropower, marine energy, geothermal power and bioenergy), in power generation (producing electricity and heat), transportation fuels, hot water and space heating. An alternative solution is to capture CO_2 from its emission sources. Stationary combustion of fossil fuels in electric utility power plants and industrial sectors has been identified as the primary source of CO_2 emissions (Ciferno et al., 2009). The amount of CO_2 emissions attributable to the electric power sector is projected to increase until 2040 in the US, despite the increase of electric power generation from low and noncarbon sources (USDOE/NETL, 2012). Capturing CO_2 from the power generation and industrial sectors (large point sources) is more cost effective than from sectors such as transportation, due to the concentrated CO_2 in flue gases (10 to 15% for coal combustion and 5 to

10% for natural gas combustion). Therefore, it is crucial to develop CO_2 capture and storage (CCS) technologies for the large point sources.

1.4 Carbon capture and storage

Deployment of CCS is deemed an important approach to reduce CO_2 emissions, considering the consumption of fossil fuels will continue in the future (Steeneveldt et al., 2006; IEA, 2013). CCS is effective in capturing exhaust CO_2 from the flue gas of large stationary point sources such as fossil fuel power plants and refineries. The captured CO_2 is purified, compressed, transported to a storage site (normally a deep underground geological formation) and deposited to prevent its release into the air. Although it requires additional energy to run a CCS based power plant, i.e., more fuel has to be consumed to produce the same amount of power, CCS can remove more than 90% of the CO_2 emitted by the power plant. The additional energy requirement is high for pulverized coal (PC) fired plants, compared with the coal based integrated gasification combined cycle (IGCC) plants and the natural gas combined cycle (NGCC) plants. When CCS is combined with biofuel refineries (bioenergy with CCS), net negative emissions of CO_2 are resulted in.

CCS is in a different technological category from carbon capture and utilization (CCU). In CCU, the captured CO_2 is not transported to storage sites but utilized for other purposes. A typical example of CCU is to use CO_2 in the flue gas (e.g., from coal fired power plants) as feedstock to synthesize oil rich algae in solar membranes. The algae are used to produce oil for plastics and transportation fuels, and provide nutritious feedstock for farm animal production (Global CCS Institute, 2011).

In an integrated CCS process, the first and most expensive step is the separation and capture of CO_2 from the combustion sources (75% of the total cost) (Yang et al., 2008). The transport and storage steps of CCS are more mature technologies than that of the capture step. Therefore, it is crucial to optimize the capture process and increase the feasibility of CCS. There are four technological configurations for CO_2 capture: postcombustion, precombustion, oxy-fuel combustion and chemical looping combustion. In postcombustion CO_2 capture (PCC), CO_2 is removed from the flue gas after fuel is combusted with air in a boiler. This configuration is

applied to conventional PC power plants because existing fossil fuel plants can be retrofitted to include CCS in this configuration. In a precombustion CO_2 capture system, applicable to IGCC power plants, the fossil fuel (i.e., coal) is oxidized partially in a gasifier in the presence of steam, producing syngas (CO and H_2) that is converted to CO_2 and H_2 through a water gas shift process. CO_2 can be captured from the gas stream before H_2 is combusted as fuel. This configuration can be applied to new utility power plants. In oxy-fuel combustion, the fuel is burned in oxygen (diluted with the recycled flue gas) instead of air. The resulting flue gas consists mainly of CO_2 and water vapor, the latter of which can be condensed out by cooling, and the purified CO_2 stream can be transported to the storage site after compression. This configuration is energy intensive due to the initial air separation step. Chemical looping combustion employs a metal oxide (e.g., CaO, NiO) as a solid oxygen carrier. Metal oxide particles react with fuel in a fluidized bed combustor, producing metal particles and a mixture of CO_2 and water vapor. The water vapor is condensed, leaving pure CO_2 for sequestration. Metal particles are circulated to another fluidized bed reactor where they are reoxidized in air to regenerate metal oxide particles.

After capture, the compressed CO_2 stream is transported by pipelines to suitable storage sites. One example is to transport CO_2 to oil production fields where it is injected into oil wells to extract additional oil (enhanced oil recovery). This option is desirable because the geology of oil reservoirs is understood and the storage cost can be offset partially by the additional oil recovered. However, subsequent burning of the recovered oil will offset partially the reduced CO_2 emissions. Moreover, long term storage of CO_2 in nonoil producing geologic formations (e.g., saline aquifers and exhausted gas fields) has been demonstrated. One important factor to be considered is the risk of CO_2 leakage into the atmosphere. Various physical and geochemical trapping mechanisms can prevent CO_2 from escaping to the surface. One example of physical trapping is with impermeable cap rock (Global CCS Institute, 2010). For geochemical trapping, CO_2 can form thermodynamically stable carbonates (e.g., calcite or magnesite) with abundant mineral metal oxides. CO_2 trapping by reacting with minerals is regarded as a permanent and secure way of geological storage. Ocean sequestration is not considered feasible due to the exacerbation of ocean acidification, and concerns about its stability and negative impacts on marine life (Benson and Surles, 2006).

1.5 PCC technologies and the benchmark absorption process

Coal burning has been responsible for the largest portion of CO_2 emissions from fossil fuel combustion, and coal fired power plants will remain the largest electricity generator amongst the carbon combustion sources until 2040 (USDOE/NETL, 2012). Therefore, development of PCC technologies, especially for existing coal fired power plants, is preferable because it requires minimal retrofitting of existing infrastructure (Zhao et al., 2013). Current PCC technologies include membrane separation, adsorption and absorption (chemical scrubbing). Membrane separation works by selectively permeating CO_2 and retaining the remaining components (primarily N_2 in PCC) in the flue gas stream. The selectivity results from differences in molecular size, molecular weight and affinity to the membrane material. The dominant mechanism of membrane separation is size sieving separation. Adsorption based PCC technologies employ solid sorbents (e.g., activated carbon, zeolite and silica supported amines) in an adsorption and desorption cycle, with the desorption process induced by a temperature swing approach. Compared with membrane separation and adsorption, chemical absorption of CO_2 is more advantageous due to its superior operability and scalability (Svendsen et al., 2011). The most technologically mature and commercially available CO_2 absorption process is amine scrubbing. Aqueous monoethanolamine (MEA) has been the benchmark solvent used for amine scrubbing in the chemical and gas industry (Freguia and Rochelle, 2003; Rochelle, 2009). Various alternative amine solvents have been investigated, such as piperazine (PZ), 2-(2-aminoethylamino)ethanol (AEEA), the mixture of MEA and *N*-methyldiethanolamine (MDEA) and aqueous potassium carbonate (K_2CO_3) promoted by PZ (Freeman et al., 2010b; Idem et al., 2006; Ma'mun et al., 2007; Oyenekan and Rochelle, 2006).

The benchmark process using MEA for PCC adopted by the US Department of Energy (DOE) is based on the Econamine FG Plus^{SM} carbon capture technology designed by Fluor Corporation. This technology is applied to a supercritical PC fired Rankine cycle power plant with a nominal net output of 550 MWe in DOE Case 12 (USDOE/NETL, 2013) (Fig. 1-5). This process is comprised primarily of flue gas cooling, SO_2 polishing, CO_2 absorption, solvent stripping and reclaiming, and CO_2 compression and drying. The incoming flue gas from a flue gas desulfurization (FGD) unit contains 1% more CO_2 than the original flue gas, due to CO_2

liberated from the limestone used in the FGD process. The sulfur removal efficiency is 98% in the FGD unit, but the SO_2 content in the treated gas entering the CO_2 capture facility is about 44 ppm, which needs to be reduced further to a level below 10 ppm as required by the Econamine FG Plus^{SM} Process. A SO_2 polishing scrubber serves this purpose by using a 20 wt% NaOH solution with a removal efficiency of more than 75%, which minimizes the accumulation of heat stable salts (HSS) formed from the reaction between SO_2 and the amine during CO_2 absorption. The treated flue gas enters the bottom of the CO_2 absorber and flows up through the absorption tower countercurrent to a stream of lean MEA solvent. 90% of the CO_2 in the feed gas is absorbed into the solvent; the remaining gas leaves the top of the absorber and is subject to a water wash section to remove the entrained amine and water before it is released to the atmosphere. The lean MEA solvent entering the top of the absorber leaves the bottom with the absorbed CO_2. The CO_2 rich solvent from the bottom of the absorber is heated by the lean solvent from the solvent stripper in a cross heat exchanger. The heated rich solvent enters the stripper from the top for removal of the absorbed CO_2 by the countercurrent steam vapor produced by the reboiler. The stripped solvent from the bottom of the stripper is pumped to the cross heat exchanger and sent to the absorber, thus completing the loop. In the stripper, the steam used to heat the CO_2 rich solvent is 5 bar and 152°C. The hot vapor leaving the top of the stripper contains CO_2, steam and solvent vapor, the latter two of which are condensed in a reflux condenser by cooling water. The dried CO_2 rich gas product is delivered to a CO_2 compressor. In the compression section, CO_2 is compressed to 153 bar by a six stage centrifugal compressor.

Another commercial PCC process, based on the Shell Cansolv solvent (amine based), is comprised of a prescrubber, a CO_2 absorber, a CO_2 stripper, and an amine purification unit (USDOE/NETL, 2015) (Fig. 1-6). The prescrubber serves a similar function to a SO_2 polisher, and it reduces the SO_2 concentration in the flue gas entering the CO_2 absorber column to 1 ppm. In the absorber, 90% of the inlet CO_2 is absorbed into the Cansolv solvent, and the remaining flue gas is subject to a water wash section at the top of the absorber. The CO_2 rich solvent exiting the absorber is heated in a cross heat exchanger by the CO_2 lean solvent from the regeneration step. The rich solvent enters the stripper from the top and CO_2 is desorbed. The regenerated lean solvent is pumped through the cross heat exchanger and sent to the absorber. The product gas leaving the top of the stripper is condensed to remove water vapor, and the separated CO_2 is sent

to the CO_2 compressor (8 stages). A batch amine purification section is added to the Cansolv process to remove the HSS and amine degradation products.

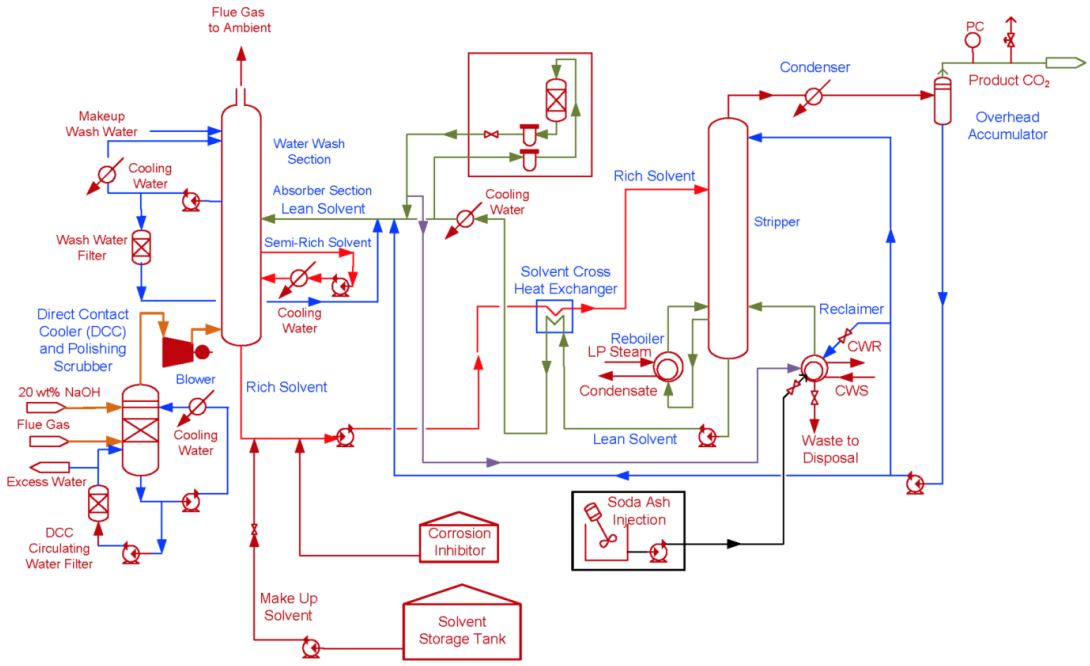

Fig. 1-5. Flow diagram of Fluro Econamine FG Plus^{SM} Process (USDOE/NETL, 2013).

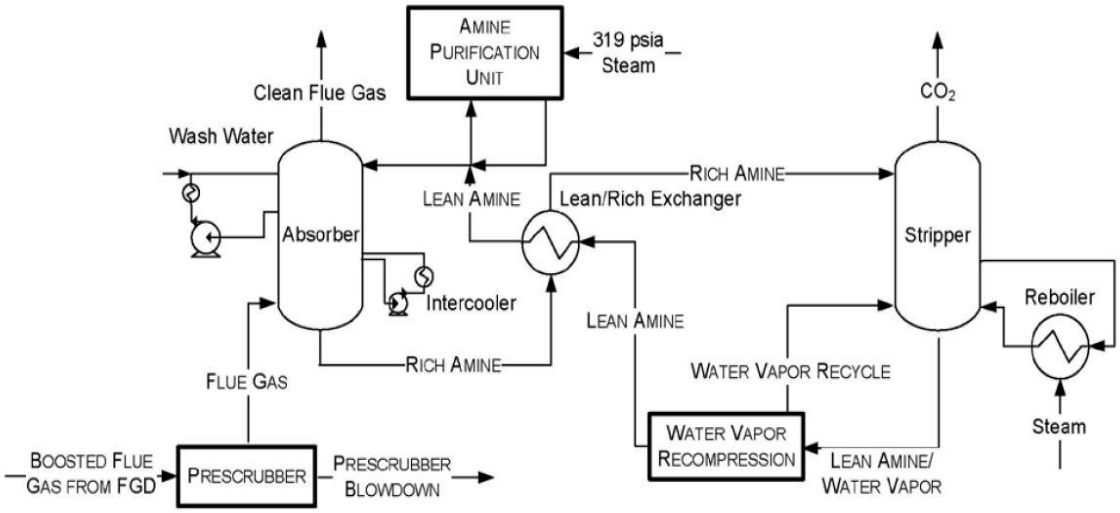

Fig. 1-6. Flow diagram of the Shell Cansolv Process (USDOE/NETL, 2015).

Amine based solvents possess the merits of fast absorption rate and high CO_2 loading capacity. However, absorption processes using conventional amine based solvents are expensive, undermining their applicability. For example, the cost of electricity (COE) is estimated at 107

mills kWh^{-1} for a PC fired supercritical power plant (nominal 550 MWe) equipped with a benchmark MEA process (DOE Case 12), which results in an 81% increase over the COE of the plant without CO_2 capture and is equivalent to a cost of \$69/tonne CO_2 (USDOE/NETL, 2013). 60% of the COE increase due to CO_2 capture with the MEA process is attributable to the parasitic power loss resulting from steam extraction, CO_2 compression work and auxiliary power use, with the remaining attributable to capital, operating and maintenance costs (Ciferno, 2007). Steam is required to supply the heat demanded in the stripper, which is responsible for 60% of the total energy use (Meldon, 2011). Compression work is necessary to pressurize CO_2 from the stripper pressure (1.6 bar for the MEA process) to the pipeline pressure (153 bar) to prepare for sequestration. Compression work is responsible for 30% of the total energy use, and the remaining 10% is attributable to the auxiliary power use which supplies electricity for pumps, fans, etc. required in the capture process. Therefore, the key to lowering the PCC cost is to reduce the energy consumption, especially the steam used for the stripping process.

A simplified schematic diagram of the conventional amine based process is shown in Fig. 1-7. The steam is supplied to provide the heat required for CO_2 stripping. The total heat usage (i.e., reboiler heat duty) includes three components: reaction heat required to desorb CO_2 from the CO_2 rich solution, sensible heat required to heat the rich solution entering the stripper to the stripping temperature and stripping heat required to compensate the latent heat carried by water vapor leaving the top of the stripper. The total energy requirement in the stripper for the MEA process is 3,556 kJ/kg CO_2 (2,559 kJ/kg CO_2 for the Cansolv Process). The steam is withdrawn from the turbine of a power plant, which reduces the plant's electricity output. Overall, the total parasitic power loss attributable to the MEA process (DOE Case 12) is 0.37 kWh/kg CO_2 captured, equivalent to 31% of the gross power output (USDOE/NETL, 2013).

Besides the intensive energy penalty and high cost associated with the conventional amine process, environmental issues from the deployment of CCS arise, such as the emissions of air pollutants derived from the vapor of the solvent used. For amine based processes, volatile nitrosamines can be formed by side reactions between amines and NO_2 present in the flue gas.

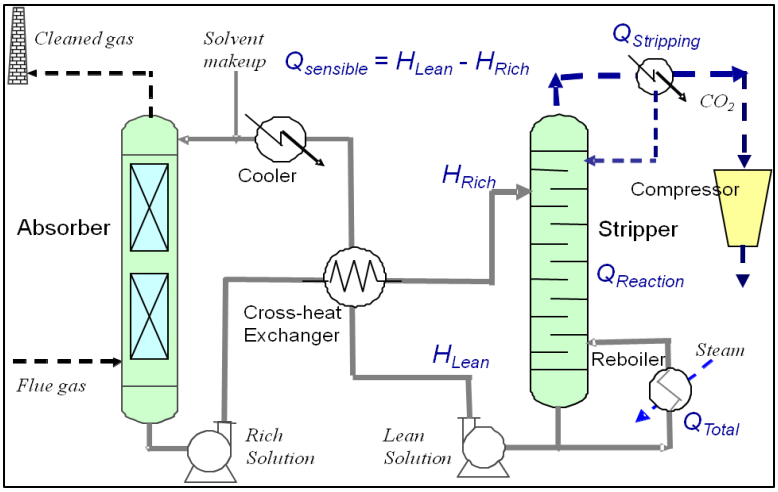

Fig. 1-7. The MEA process with three components of steam heat usage for CO_2 stripping (Lu et al., 2014).

In light of the energy use disadvantages of the conventional amine processes, emerging research efforts are devoted to developing advanced solvents and innovative absorption processes. Among those, the application of phase transitional solvents for PCC has received growing interest (Aleixo et al., 2011; Monteiro et al., 2015b; Zhang et al., 2013). Phase transitional solvents enabled processes have the potential to overcome the cost and performance drawbacks of the conventional processes. A phase refers to a medium with uniform physical and chemical properties. Phase transition is a thermodynamic transformation of one phase to another driven by heat or mass transfer, during which some properties of the original phase change due to variations in certain internal or external conditions, e.g., temperature, pressure and chemical composition. For instance, when the temperature of a homogeneous solvent is increased, a thermally induced phase separation can occur to form two phases that possess distinct physicochemical characteristics. The location and shape of phase boundaries are determined primarily by the thermodynamic interaction between the solutes and diluent (Kim and Lloyd, 1992). In the context of PCC, phase transitional solvents can undergo phase separation upon the loading of CO_2. As a result, the absorbed CO_2 is concentrated in one phase with the other phase being CO_2 lean. This enables the use of only the CO_2 rich phase for CO_2 desorption, thus reducing the mass of solvent to be regenerated and facilitating the attainment of a high stripping pressure. As a result, the heat use for CO_2 desorption (especially the sensible heat and stripping heat) and the CO_2 compression work required to deliver CO_2 to a storage site can be reduced.

1.6 Objectives and scope of research

The aim of this work was to develop novel phase transitional solvents and the enabled absorption processes to improve the energy performance and cost effectiveness of the conventional CO_2 absorption processes. Two fundamental scenarios of phase transition, i.e., liquid-solid and liquid-liquid phase transitions, were both investigated. For the first scenario (liquid-solid), the objective was:

a. To understand the critical kinetics and solubility with respect to the crystallization of $KHCO_3$.

For the second scenario (liquid-liquid), the objectives were:

b. To develop novel biphasic solvents with desired CO_2 absorption and desorption performance and phase separation behavior.

c. To understand the underlying mechanisms of liquid-liquid phase transition under CO_2 absorption and desorption conditions.

d. To characterize the thermodynamic and kinetic properties of the selected solvents.

This thesis was written in the following order, with each chapter addressing a particular objective. Chapter 2 is a thorough review of the relevant literature with respect to the phase transitional solvents and processes for PCC. In Chapter 3, objective (a) was addressed, in which a hot carbonate absorption process featuring a liquid-solid phase transition (crystallization) of the CO_2 loaded solution was investigated. The kinetics of bicarbonate crystallization, characterization of bicarbonate crystals and solubility of bicarbonate under typical operating conditions were examined. The resultant data were used to conduct a preliminary crystallizer design analysis.

In Chapters 4 through 8, liquid-liquid phase transitions were the focus. In Chapters 4 and 5, we addressed objective (b) and detailed the comprehensive efforts on solvent screening that were made in an attempt to identify appropriate solvents for the proposed biphasic solvent based CO_2 absorption process. In Chapter 4, the relationship between the solvent structure and CO_2 absorption and desorption performance was explored. In Chapter 5, the effects of solvent compositions and formulae on the phase separation and CO_2 capture performance were detailed.

As a result, the aqueous blend of *N*,*N*,*N′*,*N″*,*N″*-pentamethyldiethylenetriamine (PMDETA) and diethylenetriamine (DETA) was selected for further studies.

In Chapter 6, objective (c) was addressed and the fundamental mechanisms of liquid-liquid phase separation (LLPS) induced by CO_2 absorption into or desorption from the blend of DETA and PMDETA were elucidated with NMR spectroscopy.

In Chapters 7 and 8, objective (d) was addressed. In Chapter 7, a thermodynamic model was established for the biphasic solvent blend of DETA and PMDETA to predict the equilibrium partial pressures of CO_2, speciation in the two liquid phases, phase separation evolvement and the heat of absorption and desorption reactions. The generic approach developed in this model could be applied to other biphasic solvent systems. In Chapter 8, the kinetic measurements and modeling of CO_2 absorption into the neat DETA solutions, neat PMDETA solutions and solvent blends of DETA and PMDETA were conducted.

In Chapter 9, conclusions from the current study were described and insights toward future research on phase transitional solvents were provided.

CHAPTER 2: LITERATURE REVIEW

We reviewed the state of the art research and development of phase transitional solvents and the enabled processes for PCC.

2.1 Liquid-solid phase transition

In a liquid-solid phase change process, the absorbed CO_2 is transformed to a solid product, which is separated from the mother liquid to make a slurry that can be desorbed and regenerated. Depending on the solvents used, these studies are categorized into two groups: amine based solvents, and salt solutions with specific cations (K^+, Na^+, NH_4^+ or quaternary ammonium cation).

2.1.1 Amine based solvents

In studies utilizing amine based solvents, amines are reagents for the chemical absorption of CO_2, with inert organic chemicals adopted as diluents instead of water. Relative to water, these organic cosolvents can reduce the energy required for regeneration by enhancing the solubility of CO_2 in solution and lowering the specific heat capacity of the solution. An application of aminosilicones for PCC from coal fired power plants was proposed by Perry et al. (2012), and the performance of neat liquid aminosilicones was investigated. The highest performing solvent was 1,3-Bis(3-aminopropy1)-1,1,3,3-tetramethyldsiloxane, which demonstrated high cyclic CO_2 loading capacity, excellent thermal stability and low vapor pressure and heat capacity. The low viscosity and hydrophilic aminosilicones were subject to solid phase conversion upon exposure to CO_2 in a simulated flue gas. The authors suggested using solutions of glycol (e.g., triethylene glycol) as nonvolatile cosolvents for aminosilicones, as alternatives to benchmark aqueous amine systems.

A nonaqueous solvent mixture of 2-amino-2-methyl-1-propanol (AMP), diethanolamine (DEA), and 1-propanol (Barzagli et al., 2013b), and a mixture of AMP and *N*-methyl-2-pyrrolidone (NMP) or triethylene glycol dimethyl ether (Triglyme) (Svensson et al., 2014a; Svensson et al., 2014b; Svensson et al., 2014c), were both applied in CO_2 absorption; the solid reaction products

were the carbamate derivative of AMP, a sterically hindered amine. In another study, a nonaqueous solvent of 0.2 M triethylenetetramine (TETA) in ethanol was investigated (Zheng et al., 2014). After CO_2 absorption, 82% of the trapped CO_2 precipitated in the form of TETA carbamate, separated out by filtration before being regenerated thermally. The TETA/ethanol solvent was superior to aqueous TETA solution in absorption rate and capacity, since ethanol had higher CO_2 solubility relative to water and could facilitate the reaction between TETA and CO_2. In a similar study (Zhang et al., 2017c), DETA was utilized as the absorbent and various organic solvents were tested, including ethanol, diethylene glycol dimethyl ether, NMP and dimethyl carbonate. The solid phase formed upon maximum CO_2 absorption was a DETA carbamate of equimolar DETA reacted with CO_2 from the single crystal structure analyses, which was not influenced by organic solvent selection. Furthermore, an ionic liquid of DETA, produced by mixing DETA with hydrobromide in the presence of a polyethylene glycol 200 cosolvent, was used for CO_2 absorption, where a phase change occurred with solids precipitated from the solution (Chen and Hu, 2017). The presence of the glycol cosolvent enhanced the CO_2 capacity (1.2 mol CO_2/mol DETA bromide) and contributed to the biphasic separation. The role of bromide anion was to stabilize the solution system by overcoming the electrostatic attractions between organic ions and preventing the biphasic separation from occurring at an early stage of CO_2 absorption. In another study, CO_2 was loaded into water/ethanol solutions containing various amines (e.g., 1-aminobutane, 1-aminooctane, aminocyclohexane and PZ), and the amine carbamates were separated in the solid phase and thermally converted to 1,3-disubstituted ureas (Barzagli et al., 2016).

A group of researchers from India reported mixtures of alkanolamines and green (nontoxic) deep eutectic solvents (Maheswari and Palanivelu, 2015), as well as mixtures of alkylamines and green vegetable oils (Maheswari and Palanivelu, 2017). Both types of solvents had higher CO_2 absorption capacities than their respective aqueous counterparts dissolving the same amines. In the former study, AMP mixed with a choline chloride:urea (1:2) medium achieved the highest absorption capacity under the optimized conditions, among the combinations studied. In the latter study, TETA in coconut oil performed the best. The carbamate solids from the absorption process were value added products, so the authors claimed their proposed scheme should be a good alternative to CCU.

2.1.2 Salt solutions with special cations

In studies utilizing salt solutions, CO_2 was absorbed by salts with inorganic cations dissolved in organic solvents or water. The anions in these salt solutions were amino acid or carbonate based.

Precipitating amino acid salt (AAS) based solvents attracted attention, by their merits of low specific reboiler heat duty, high CO_2 loading capacity and environmental benignity (low ecotoxicity and no emissions to the air). Researchers at the Netherlands Organization for Applied Scientific Research developed the DECAB (potassium taurate based) and DECAB Plus (potassium alanate based) processes with a lean vapor compression (LVC) configuration for PCC from coal fired power plants (Fernandez et al., 2013; Sanchez-Fernandez et al., 2014a; Sanchez-Fernandez et al., 2014b; Sanchez-Fernandez et al., 2013). In these processes, an aqueous solution of 4 M potassium taurate or alanate was applied as the absorbent, with pure amino acid zwitterions as precipitates during CO_2 absorption. The absorption capacity was enhanced on the basis of the Le Chatelier's principle, as the equilibrium of absorption reaction was shifted forward by removing the precipitates from the reaction products (Fernandez and Goetheer, 2011). A fraction of the supernatant rich in CO_2 was fed to the stripper. Because the supernatant had a lower pH than the original potassium solution, CO_2 desorption was promoted. The zwitterion precipitate was redissolved in the remaining supernatant and recycled to the absorption column. The energy consumption, which included solvent regeneration, CO_2 compression (to 110 bar) and redissolution of precipitates (low grade energy was used), was claimed to be 2.4 GJ/ton CO_2, a 35 to 45% reduction compared with the baseline MEA process.

Research was performed on CO_2 absorption with 5 M potassium sarcosine. Precipitation began when CO_2 loading reached 0.52 mol/mol. The vapor-liquid-solid equilibrium (VLSE) data were measured from 40 to 120℃, and a model was established to predict the occurrence of precipitation and the heat of absorption using the Gibbs-Helmholtz equation (Aronu et al., 2014; Ma'mun and Kim, 2013). In another study, the protonation constants (pK_a) of eleven AAS were studied, with the sarcosine based AAS solution maintaining a higher pK_a value than that of the others at high temperatures (pK_a decreases with increasing temperatures), indicating its potential as a fast CO_2 absorption solvent (Yang et al., 2014). However, the protonation reaction of

sarcosine was the least exothermic, which could have led to a high regeneration energy demand in a sarcosine based CO_2 capture process. The phase change behavior of CO_2 absorption into aqueous solutions of various sodium based AAS also was studied (Wang et al., 2016). 90% of the captured CO_2 was present in the solid phase in the form of sodium bicarbonate, indicating a high loading capacity and good regenerability of these AAS based solutions. The authors also studied the speciation evolution of sodium alanine during CO_2 absorption and desorption with NMR spectroscopy. As CO_2 loading increased up to 0.6 mol/mol of alanine, the dominant products changed from carbamate to bicarbonate due to hydrolysis (Wang et al., 2015). A mixture of 2-[2-(dimethylamino)ethoxy]ethanol (DMAEE) and tetramethylammonium glycinate (an ionic liquid of amino acid) was used for CO_2 absorption, and DMAEE accelerated the CO_2 absorption and increased the CO_2 loading in the ionic liquid because it reduced the liquid's viscosity and acted as a proton acceptor. The precipitates produced from the reaction were removed and regenerated upon heating (Zhang et al., 2016a). Recently, a nonaqueous solution produced by dissolving potassium prolinate (1 and 2 M) in ethanol was employed for CO_2 absorption under PCC conditions (Shen et al., 2017). The solvent exhibited a fast absorption rate, and underwent a liquid-solid phase transition upon CO_2 loading. At the end of absorption, 55 to 60% of the absorbed CO_2 was enriched in the solid phase, while the rest stayed in the liquid. Using ^{13}C NMR and X-ray diffraction (XRD) analyses, the components in the solid phase were the carbamate salt of potassium prolinate and a minor amount of bicarbonate salt (due to the presence of a small quantity of H_2O in the CO_2 free solvent). The CO_2 in the liquid phase was detected in the form of ethyl carbonate salts, as a result of the reaction between CO_2 and ethanol in the presence of potassium prolinate.

Carbonate solutions have been applied to absorb CO_2 in industries for decades (Benson et al., 1954; Benson and Parrish, 1974; Nysing and Kramers, 1958; Williamson and Mathews, 1924). Recently, the carbonate based CO_2 absorption process was investigated as an alternative option to amine based processes for PCC from coal fired power plants because of its low solvent cost, low equipment corrosion, negligible solvent volatility and degradation, and environmental benignity (Cullinane and Rochelle, 2006; Mumford et al., 2012; Oyenekan and Rochelle, 2009; Plaza et al., 2010; Smith et al., 2012). The chilled ammonia process (CAP) was applied to absorb CO_2 into an aqueous ammonium carbonate (or ammonia) solution at low temperatures (e.g., 2 to

10°C) both in laboratory and pilot plant studies (Darde et al., 2009, 2010; Hanak et al., 2015; Kozak et al., 2009; Mathias et al., 2010). The ammonia based solvents had a heat of CO_2 absorption of 70 kJ/mol CO_2, lower than that of MEA (Qin et al., 2011), high CO_2 capacity as inorganic carbonate and no solvent degradation. Therefore, there was potential for energy savings. Formation of precipitates consisting of ammonium bicarbonate was controlled in the absorber and the separated solids were redissolved with a higher CO_2 concentration before entering the stripper, which reduced the energy requirement compared with the CAP without solid formation (Sutter et al., 2016).

Barzagli et al. (2013a) applied aqueous Na_2CO_3 or K_2CO_3 solutions for CO_2 absorption; the precipitated bicarbonate salts of sodium or potassium were decomposed at 200 to 250°C to regenerate the carbonates ($NaHCO_3$ could be decomposed at temperatures above 80°C, and between 100 to 120°C for $KHCO_3$). A group at the Illinois State Geological Survey (ISGS) developed a novel hot carbonate absorption process (Hot CAP) with crystallization enabled high pressure stripping, which had potential to improve the energy performance of carbonate based solvents (Ye et al., 2015a; Zhang et al., 2014). In Hot CAP, a concentrated carbonate solution (e.g., 40 wt% K_2CO_3) was utilized to absorb CO_2 and the produced bicarbonate (e.g., $KHCO_3$) crystallized upon cooling due to the lower solubility of the bicarbonate salt than its carbonate counterpart. As depicted in Fig. 2-1, the flue gas (40 to 60°C) from a FGD unit was introduced to a packed bed column operating continuously at atmospheric pressure and an elevated temperature (70°C), where CO_2 was absorbed in a 40 wt% (K_2CO_3 equivalent) potassium carbonate/bicarbonate (PCB) solution. The CO_2 rich solution exiting from the absorber, with a 40 to 45% conversion ratio of carbonate to bicarbonate (CTB), was cooled in a cross heat exchanger by the lean solution (15 to 20% CTB) circulating to the absorber, before entering a cooling crystallizer (30 to 35°C), where $KHCO_3$ crystallized from the liquid phase. The crystals separated from the bulk solution by filtration were used to produce a bicarbonate slurry (≥ 50 wt% PCB), which was fed to the stripping column after being heated in a cross heat exchanger by the hot regenerated solution (CTB ≤ 30%) from the stripper. The slurry with a high CO_2 loading was decomposed at 140 to 200°C to release CO_2, achieving a high stripping pressure (≥ 6 atm). The gas product leaving the top of the stripper was cooled and dehydrated for CO_2 compression.

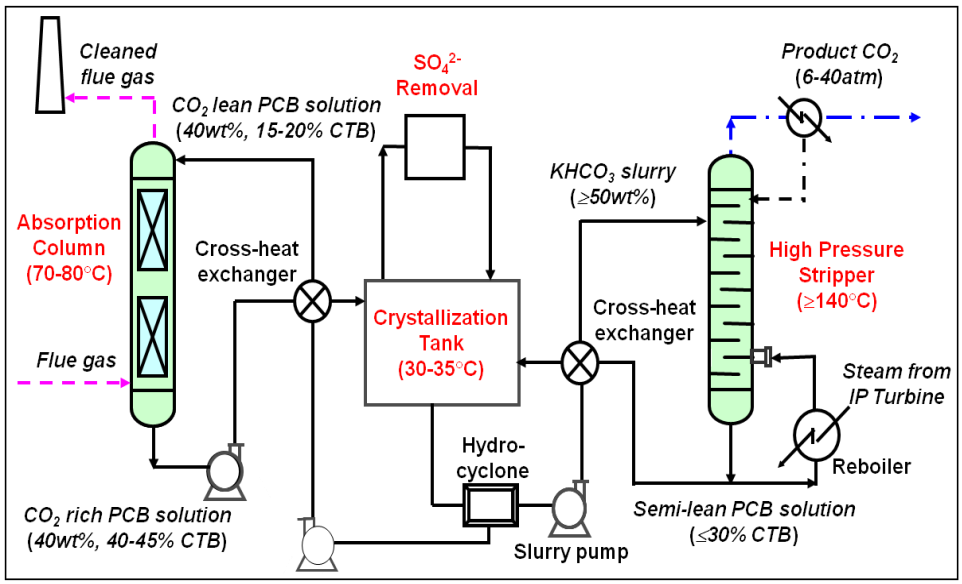

Fig. 2-1. Schematic diagram of the Hot CAP (Lu et al., 2014).

The liquid-solid phase transition (crystallization) was crucial to reducing the energy requirement in the Hot CAP. A detailed heat use analysis was performed for the Hot CAP by the ISGS group (Lu et al., 2014). First, the potassium carbonate based solution had a lower reaction heat (17 kcal/mol CO_2), which included both CO_2 absorption and bicarbonate crystallization, than the 21 kcal/mol CO_2 of the benchmark MEA solvent (Kim and Svendsen, 2007). Second, a bicarbonate slurry (e.g., 60 wt%) subject to a CTB change of 40 to 50% during the stripping process had up to 60% higher working capacity and more than 30% lower specific heat capacity (i.e., a lower sensible heat) than MEA (Aronu et al., 2009; Weiland et al., 1997). Third, CO_2 stripping with the slurry could be operated at 6 to 40 atm, predicted from the vapor-liquid equilibrium (VLE) relationship of the PCB/H_2O/CO_2 system (Tosh et al., 1959). A high stripping pressure reduced both the stripping heat and CO_2 compression work requirement.

Among those liquid-solid phase transitional solvents mentioned above, AAS containing a primary amino group (e.g., taurate), which reacted with CO_2 to form ionic carbamate species in the liquid phase and pure amino acid zwitterion species in the solid phase, were classified as L solvents. AAS containing a tertiary or sterically hindered secondary amino group (e.g., prolinate, sarcosine), ammonia or alkali carbonates, which reacted with CO_2 to form bicarbonate precipitates, were classified as S solvents (Raksajati et al., 2014). These two types of phase

changing solvents were investigated in a technoeconomic analysis (Raksajati et al., 2016), with potassium taurate as an exemplary L solvent (CO_2 incorporated in the liquid phase) and promoted potassium carbonate as an exemplary S solvent (CO_2 incorporated in the solid phase). The difference in capture costs between the two solvents was negligible, and the minimum cost was obtained for the power plant by operating the CO_2 absorption in a packed bed column and using an advanced heat integration configuration by which the heat duty associated with solid dissolution was supplied (i.e., no need of consuming the low pressure steam).

2.2 Liquid-liquid phase transition

Compared with the aforementioned liquid-solid systems, liquid-liquid phase transitional systems are more promising for PCC, because liquid phases can be handled more easily than solids during operation. In an absorption process involving a LLPS, the liquid phase rich in CO_2 is regenerated, thus avoiding the issues associated with slurry operation, such as clogging in the absorber, fouling in the cross heat exchanger, low thermal efficiency and difficulty in transporting solids to the stripper. Studies on liquid-liquid biphasic solvents and the associated processes have been summarized below.

2.2.1 Undisclosed DMX™ solvents

Investigators at the French Institute of Petroleum Energies Nouvelles (IFPEN) developed the DMX™ process and tested it at both laboratory and pilot scales. A class of undisclosed DMX™ solvents was formulated that could form two immiscible liquid phases under certain temperature and CO_2 loading conditions. The light phase was considered to be free of CO_2; whereas, the heavy phase had high CO_2 loading, which was the only phase sent to the stripper for regeneration. The DMX™ process could reduce the reboiler heat duty to as low as 2.1 GJ/ton CO_2, compared with that of 3.7 GJ/ton CO_2 for the reference MEA process (Aleixo et al., 2011; Gomez et al., 2014; Raynal et al., 2011a; Raynal et al., 2011b; Raynal et al., 2014).

2.2.2 Single amine solvents

Aqueous solutions of several singular amines (e.g., 3 M trimethylamine or 5 M diallylamine), which were homogeneous after CO_2 absorption, exhibited phase transitions into dual phases

under high temperature desorption conditions and remained dual phases even when they were cooled down (Xu et al., 2012). This phenomenon was confirmed in a study (Coulier et al., 2017), in which the phase separation behavior was tracked as a function of temperature for the CO_2 laden aqueous solutions of either *N*-methylpiperidine, a tertiary amine, or 2-methylpiperidine, a secondary amine. The phase separation incurring temperature decreased with increasing CO_2 loading for the tertiary amine while an opposite trend was observed for the secondary amine. For the secondary amine, the formed ionic carbamate species stabilized the solution, so a higher temperature was required to incur phase separation for the solvent with an increased CO_2 loading. For the tertiary amine, however, the formed carbonate/bicarbonate species upon increasing CO_2 loading competed with the molecular amine for water and enabled phase separation of the solvent at a lower temperature. Nonetheless, under the conditions typical of CO_2 absorption, a LLPS after the loading of CO_2 entailed a blend of two or more components, of which at least one was an amine based compound.

2.2.3 Thermomorphic phase transitional solvents

A German group of researchers screened a series of lipophilic amine blends that, after being loaded with CO_2 in a homogeneous state, exhibited a thermally induced LLPS upon heating. This feature led to an self extractive behavior of molecular amines and facilitated the regeneration reactions of CO_2 laden solvents (Zhang et al., 2011a; Zhang et al., 2011b; Zhang et al., 2012a, b; Zhang et al., 2013). With the aid of N_2 stripping or its alternative methods, including nucleation, ultrasonication, magnetic agitation and addition of an inert and hydrophobic (alkyl) solvent, the extraction of amines was intensified and desorption occurred under low temperatures (70 to 90°C). The amine extraction (either self extraction or by an inert compound) from the CO_2 rich aqueous phase was conducted in a multiple stage configuration. Purification of the inert compound from the mixture with the extracted amines involved a distillation process. Typical lipophilic amine solvents included a blend of tertiary amine *N*,*N*-dimethylcyclohexylamine (DMCA) and secondary amine *N*-methylcyclohexylamine (CHxMA) or dipropylamine (DPA), which had a high cyclic CO_2 loading capacity, i.e., 0.9 mol CO_2/mol absorbent (Zhang et al., 2010; Zhang et al., 2011c). This solvent blend could separate into dual phases by heating the CO_2 loaded solvent to greater than 60°C. The separated CO_2 rich phase could be regenerated at a low temperature of 80°C (Zhang et al., 2013). The above process enabled the use of low value or

even waste heat for CO_2 desorption, so the process economics were improved. However, it was not clear why there was no separation of the dual phases before CO_2 desorption.

2.2.4 Polyamine/tertiary amine blends

A solvent blending 2 M 3-(methylamino)propylamine (MAPA) and 5 M 2-(diethylamino)ethanol (DEEA) could form dual phases after CO_2 was loaded. Such a blend has been studied intensively primarily by Svendsen's group.

As a typical diamine or polyamine, MAPA had a favorable CO_2 loading capacity and absorption rate because it has two reactive amino sites for CO_2 binding (Kierzkowska-Pawlak and Kruszczak, 2017; Muchan et al., 2017; Pinto et al., 2014b). For the neat aqueous MAPA solution, kinetic data were measured and interpreted using the two film mass transfer model, assuming a pseudo first order reaction. The 1 M MAPA solution had an initial rate of CO_2 absorption twice as fast as PZ and 8 and 15 times faster than aminoethylethanolamine and MEA, respectively, at 25°C (Monteiro et al., 2014). For the neat aqueous DEEA solution, the mass transfer data and CO_2 absorption kinetics were measured using a stirred cell reactor. When the concentration of DEEA was greater than 3 M, the findings could not be explained by using the two film model (even considering the system nonideality and activities of species); therefore, a DEEA clustering hypothesis compatible with the thermodynamic properties of DEEA solution was proposed (Monteiro et al., 2015a). For the MAPA and DEEA blend, the kinetic data were described by combining the two film theory and the DEEA clustering hypothesis. MAPA acted as an effective absorption activator in the aqueous DEEA solution, such that a small amount of MAPA resulted in an enhancement of the CO_2 absorption rate of the DEEA solution (Monteiro et al., 2015b).

The VLE data of the neat DEEA solution (Luo et al., 2016b; Monteiro et al., 2013; Xu et al., 2014b) and the MAPA/DEEA blend under both CO_2 free (Hartono et al., 2013) and CO_2 loaded conditions (Arshad et al., 2014; Arshad et al., 2016) were measured experimentally. Different models including the Kent Eisenberg model, the electrolyte nonrandom two liquid (eNRTL) model and the universal quasichemical (UNIQUAC) model were used to correlate the measured VLE data. Specifically, an extended UNIQUAC framework was used to model the VLE of the systems involving dual liquid phases under a wide range of temperatures and CO_2 partial

pressures. In their aqueous solutions, MAPA was less volatile than DEEA, even though pure MAPA had a higher vapor pressure than pure DEEA. The solvent blend of 5 M DEEA and 2 M MAPA achieved a high cyclic capacity and high CO_2 stripping pressure.

The heats of CO_2 absorption were measured for the neat MAPA, neat DEEA and their blend solutions (Arshad et al., 2013a; Arshad et al., 2013b; Knuutila and Nannestad, 2017). The absorption heat increased with increasing temperature for the aqueous neat solutions of both MAPA and DEEA; the neat solution of DEEA as a tertiary amine had a lower heat of absorption compared with MAPA which is a diamine containing primary and secondary amino groups. Meanwhile, the heat of absorption decreased with increasing CO_2 loading at a given solvent composition and temperature. The species in the dual liquid phases formed during the loading of CO_2 also were analyzed quantitatively using NMR spectroscopy (Ciftja et al., 2013b). The lower phase was rich in CO_2 and MAPA and the upper phase was lean in CO_2 but rich in DEEA. Increasing the partial pressure of CO_2 (i.e., increasing CO_2 loading) increased the ratio of DEEA to MAPA in the lower phase, because more DEEA molecules became protonated and dissolved in the lower phase. The solvent blends were tested in a pilot plant with no issues regarding high viscosity and foaming, although a greater solvent loss than MEA was observed due to its higher volatility (Pinto et al., 2014a). Several scenarios of process configuration integrated to greenfield and retrofit power plants were analyzed (Liebenthal et al., 2013). For the greenfield case, the optimal operation conditions of the CO_2 capture process did not match with the conditions with the lowest energy consumption.

A few other solvents similar to the blend of MAPA and DEEA also were studied. Examples included a blend of two tertiary amines, i.e., *N*,*N*-dimethylbutylamine (DMBA) and DEEA (Wang et al., 2017), a blend of AEEA and DEEA (Kierzkowska-Pawlak, 2015) and a blend of 1,4-butanediamine (BDA) and DEEA (Xu et al., 2013a, b; Xu et al., 2014a). In the study of the BDA and DEEA blend, the performance of the solvent blend (2 M BDA + 4 M DEEA, abbreviated as 2B4D) was compared with an aqueous solution (abbreviated as 2B4DL) which had the same composition as that of the lower phase of 2B4D upon the loading of CO_2. Compared with 2B4DL, the cyclic capacity of 2B4D was similar, but its absorption rate was lower at the tested CO_2 loadings. Both BDA dicarbamate and carbonate/bicarbonate species were

present in greater amounts in the 2B4DL than those in the 2B4D solution after CO_2 loading. The opposite was true for the molecular BDA and BDA carbamate species. For the fresh solvents, the overall reaction of the BDA/DEEA blend with CO_2 could be represented by the reactions between CO_2 and DEEA and between CO_2 and BDA.

2.2.5 Inert organics/amine blended solvents

Nonaqueous biphasic solvents were proposed for CO_2 absorption in various studies. Hu et al. (2009) reported a "self concentrating" phase transitional process by using a nonaqueous solvent comprising of an amine acting as a rate activator, and an alcohol (e.g., isooctanol and decylalcohol) acting as an extractive agent. Other nonaqueous biphasic solvents were reported later, including the solvent blends of MEA or DEA with alcohols (Kim et al., 2014) and 2-(methylamino)ethanol or 2-(ethylamino)ethanol with diethylene glycol diethyl ether (DEGDEE) as the diluent (Barzagli et al., 2017). A nonaqueous blend of MEA, sulfolane, and 1-butyl-3-methylimidazolium bis(trifluoromethylsulfonyl)imide (an ionic liquid), formed biphasic layers upon CO_2 loading (Kassim et al., 2016).

Quasiaqueous solvents, such as the water-oil emulsion based solvents, also attracted attention. For example, water-oil (i.e., kerosene, *n*-heptane) emulsions containing MEA or DEA (Mortaheb et al., 2012), water-oil (i.e., silicone oil) emulsions containing MDEA (Gomez-Diaz et al., 2016) and water-oil (i.e., Tween 80) emulsions containing lipophilic amines such as CHxMA and 2,6-dimethylpiperidine (Jeon et al., 2014; Jeon et al., 2016), were studied. These solvents split into dual phases upon the loading of CO_2, with the diluent partitioned mainly in the CO_2 lean phase, and the reaction products between amine and CO_2 in the rich phase. Increasing the reactant concentration increased the rate and capacity of CO_2 absorption. Increasing the portion of the dispersed phase increased the absorption rate (due to higher CO_2 solubility in the tested organic solvents than in water) but lowered the capacity. Other quasiaqueous solvents, such as a ternary blend of an amine, a water miscible organic solvent and water, were reported for CO_2 capture. For example, a MEA/water miscible alcohol/H_2O mixture was investigated (Zhang et al., 2017a, b); the diluent alcohols used were 1-propanol, 2-propanol and tertiary butanol. After CO_2 absorption, a phase separation occurred due to the salting out effect. CO_2 loading was key to the partitioning of components in the dual phases. For the solvent containing 30 wt% MEA, 30 wt%

1-propanol and 40 wt% H_2O, the CO_2 desorption capacity (1.7 mol/kg) was 52% higher than 30 wt% aqueous MEA due to the decrease in solvent mass sent to the stripper. Another ternary solvent composed of DETA, sulfolane and water behaved similarly as the MEA/alcohol/H_2O solvent, except the sulfolane remained in the lower phase after the CO_2 loading due to its higher density than water (Luo et al., 2016a). Machida et al. (2017) investigated the phase separation characteristics of a mixture of DEGDEE, H_2O and a monoamine. Seven monoamines were studied; DEGDEE was used as a physical coabsorbent. The three types of phase separation, i.e., no phase separation, phase separation upon CO_2 loading and an initially immiscible solution (and remained to be immiscible upon CO_2 loading), depended on the hydrophobicity of an amine characterized by its partition coefficient between water and octanol (K_{ow}). The phase separation point for the second type solvent (e.g., DEGDEEA/H_2O/2-(ethylamino)ethanol) was observed experimentally. The CO_2 absorption performance of the aqueous, quasiaqueous and nonaqueous solutions of MEA were studied. Ethylene glycol was the best additive to prepare the quasi and nonaqueous MEA solutions, which reduced the energy consumption compared to the aqueous solvent (Kang et al., 2017).

2.2.6 Biphasic solvents developed in this study

The biphasic solvents investigated in this study were a class of ternary A-B-H_2O systems which could be homogenous or heterogeneous. Component A possesses at least one primary (–NH_2) or secondary (–NH) amino group, which functioned as an absorption accelerator. Component B, which has one or more tertiary (–N) amino groups, provided the CO_2 loading capacity as an absorption sink and also served as a regeneration promoter. As an electron donor, –NH_2 or –NH could bond with CO_2 through the lone pair of electrons on the nitrogen atom to form a carbamate. Meanwhile, as a proton acceptor (base), the amino group could form a protonated cation. The general reaction between CO_2 and component A is:

$$2R_1R_2NH + CO_2 \leftrightarrow R_1R_2NCOO^- + R_1R_2NH_2^+ \quad (2\text{-}1)$$

where $R_1R_2NCOO^-$ and $R_1R_2NH_2^+$ are the carbamate and protonated species, respectively. R_1 and R_2 are alkyl or alkanol groups. The mechanism of reaction Eq. (2-1) was explained in detail by the termolecular (Vaidya and Kenig, 2010) or zwitterion intermediate (Caplow, 1968) model as:

$$R_1R_2NH + CO_2 \leftrightarrow R_1R_2NH^+COO^- \quad (2\text{-}2)$$

$$R_1R_2NH^+COO^- + R_1R_2NH\ (\text{base}) \leftrightarrow R_1R_2NCOO^- + R_1R_2NH_2^+ \quad (2\text{-}3)$$

Reaction Eq. (2-2) is the rate limiting step, and reaction Eq. (2-3) is faster. The base in reaction Eq. (2-3) used to deprotonate the intermediate $R_1R_2NH^+COO^-$ is a fresh amine molecule. It also can be a water molecule. If component A has sterically hindered amino groups present at α-carbons, the resultant carbamate is hydrolyzed to produce bicarbonate:

$$R_1R_2NCOO^- + H_2O \leftrightarrow R_1R_2NH + HCO_3^- \quad (2\text{-}4)$$

Component B reacts with CO_2 via a single step:

$$R_1'R_2'R_3'N + CO_2 + H_2O \leftrightarrow R_1'R_2'R_3'NH^+ + HCO_3^- \quad (2\text{-}5)$$

Reaction Eq. (2-5) is a base catalyzed hydration of CO_2, which implies that tertiary amines do not react with CO_2 directly without water (Littel et al., 1990). Although reaction Eq. (2-5) is slow, it can be expedited by the coexisting component A due to the "shuttle mechanism", which dictates that primary or secondary amines shuttle between the gas-liquid interface and bulk liquid to transport CO_2 that is combined with tertiary amines, simultaneously regenerating the primary or secondary amines (Astarita et al., 1981; Rangwala et al., 1992). Due to this effect, the solvent blends in this study exhibited both rapid absorption rates and large CO_2 uptake.

A schematic diagram of the proposed biphasic solvent based CO_2 absorption process (BiCAP) is illustrated in Fig. 2-2. In this process, the CO_2 in the flue gas is absorbed into a solvent at 40 to 50°C (the typical temperature of a flue gas after SO_2 scrubbing treatment), during which the solvent undergoes a phase transition to form dual liquid phases. The two liquid phases are separated in a downstream phase separation unit. The resultant CO_2 rich phase (the lower phase) is preheated in a cross heat exchanger by the hot regenerated solution from the stripper and fed into the stripper operated at 80 to 130°C, where CO_2 is released by dissociation of the carbamate or bicarbonate species. The regenerated solution from the stripper, as well as the lean solution from the phase separation unit, are mixed and recycled to the absorber.

Because the proposed biphasic solvent is amine based, there could be solvent loss caused by solvent vaporization, foaming, degradation or equipment corrosion, which would increase the operation and maintenance cost (Freeman et al., 2010a; Tanthapanichakoon et al., 2006). Volatile loss is less notable for alkanolamines with low vapor pressures, and can be mitigated by water washing. Foaming can be controlled by adjusting the operating conditions or applying defoaming methods. Corrosion of stainless or carbon steel produces HSS, such as oxalates,

malonates and formates, which are nonregenerable and hazardous (Tanthapanichakoon et al., 2006). Solvent degradation occurs at high stripping temperatures (thermal degradation) or in the presence of O_2 in the flue gas during absorption (oxidative degradation), and degraded products pose environmental concerns. For example, the carbamate played a preeminent role in the thermal degradation of MEA, whose degradation products included oxazolidones and imidazolidones (Davis and Rochelle, 2009). In addition, a series of aldehyde and carboxylic acid compounds were formed from the oxidative degradation of MEA (Goff and Rochelle, 2004). Alkylation/dealkylation reactions were the major mechanisms for the thermal degradation of DMCA and CHxMA. However, their thermal degradation products underwent CO_2 desorption and were recovered as the "solvent" which was still active in CO_2 absorption. Ketone or oxime was formed by the oxidative degradation of CHxMA (Zhang et al., 2013). The issues such as degradation and corrosion of the biphasic solvents developed in this study are beyond the current scope of work.

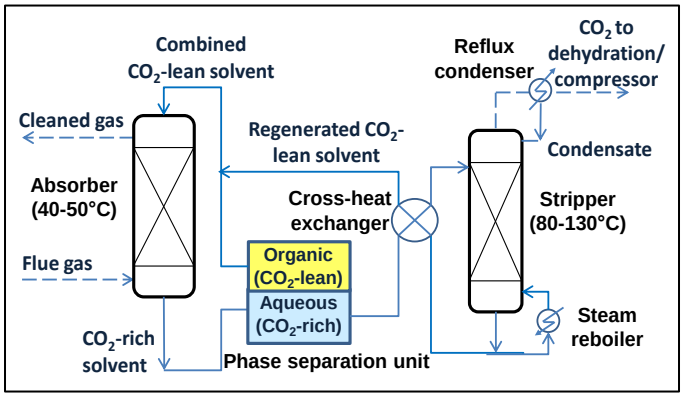

Fig. 2-2. Schematic diagram of the BiCAP.

2.3 Findings from the literature review and rationale of this research

Research efforts have been devoted to studying phase transitional solvents and the enabled processes to overcome the energy penalty associated with the benchmark MEA based CO_2 absorption process.

The reported liquid-solid phase transitional solvents included various amine or salt based solvents, such as nonaqueous mixtures of amine and alcohol as well as aqueous solutions of AAS or K_2CO_3. For these types of solvents, most of the absorbed CO_2 was concentrated in a solid

product, which was separated as a slurry before proceeding to CO_2 desorption and solvent regeneration. One major problem in a liquid-solid system is slurry handling, which can cause issues such as fouling in the cross heat exchanger. Another problem is associated with the use of volatile organic solubilizers (e.g., ethanol) for some solvents reported, which can cause solvent loss. In this research, a CO_2 absorption process based on an aqueous K_2CO_3 solution and a unique heat integration configuration was investigated (Chapter 3). The carbonate solvent was superior to MEA in terms of allowable working capacity and CO_2 desorption. Despite the risk associated with slurry handling, the carbonate solvent had the advantages of being nonvolatile, not degradable, less corrosive, inexpensive and environmentally benign compared with other solvents.

Various liquid-liquid phase transitional solvents also have been reported in the literature. Most studies involved solvent characterization, such as property measurements, speciation analyses, VLE measurements, and absorption kinetics determination. However, this area of research is emerging, and additional research is needed to understand phase transition phenomena and their implications for practical CO_2 capture application. Thus, several important research areas have been identified and the rationale of our efforts in response is described as follows.

Firstly, systematic screenings of biphasic solvents for their feasibility in CO_2 capture are scarce in the literature. This is due to the complexity of biphasic solvent compositions, which require multiple components to formulate a blend that can undergo a phase separation. In contrast, a monophasic solvent consists of a single solute and a single solubilizer. In Chapters 4 and 5, a solvent screening study was presented to address this concern. More than fifty different solvent blends were formulated and assessed with respect to their phase separation behavior and CO_2 absorption and desorption performance. Practical factors such as stability, commercial availability, price and environmental effects also were considered in selecting solvent components.

Secondly, the mechanism of LLPS, which constitutes a key feature of biphasic solvent based CO_2 absorption, has not been understood. Reported in Chapter 6, we conducted a detailed study to identify the chemical species present during CO_2 absorption into the biphasic solvent through

a quantitative NMR speciation analysis. The mechanism of phase transition induced by the loading of CO_2 in the solvent was elucidated.

Thirdly, the characterization and modeling methods commonly used for the study of monophasic solvents are not applicable to biphasic solvents. We developed thermodynamic models and kinetic methods that were dedicated specifically to biphasic solvent systems. The developed vapor-liquid-liquid equilibrium (VLLE) based thermodynamic model was used to predict the liquid-liquid phase transition and partitioning of species in two liquid phases during the CO_2 absorption and desorption processes (Chapter 7). The intrinsic kinetic rate constants of the CO_2 absorption reactions in the complex biphasic solvent system were determined by individually measuring the absorption rates into both the neat solutions of each solvent component as well as their blends (Chapter 8).

CHAPTER 3: KINETIC BEHAVIOR OF POTASSIUM BICARBONATE CRYSTALLIZATION IN A CARBONATE BASED CO_2 ABSORPTION PROCESS

3.1 Introduction

The conventional MEA absorption process for PCC is energy intensive and costly, and often incurs operational concerns associated with equipment corrosion, solvent loss and amine waste discharge (Freeman et al., 2010a; Tanthapanichakoon et al., 2006). In this chapter, a carbonate based CO_2 absorption process coupled with a liquid-solid phase transition (crystallization from a liquid solution) was investigated as a feasible solution to the energy use and operational disadvantages of the benchmark MEA process.

Carbonate based absorption processes are emerging as technical alternatives that can overcome the disadvantages encountered with amine based processes. For dozens of years, several potassium or sodium carbonate based absorption processes have been applied extensively for the absorption of CO_2 and H_2S from gas streams in various industries, such as coking, natural gas purification, refining and synthesis of liquid fuels from coal (Benson et al., 1954; Benson and Parrish, 1974; Nysing and Kramers, 1958; Williamson and Mathews, 1924). Recently, research efforts were focused on carbonate based processes for CO_2 capture from coal fired power plants. Researchers from the University of Texas at Austin investigated CO_2 absorption into potassium carbonate/bicarbonate (K_2CO_3/$KHCO_3$, or PCB) solutions promoted with PZ (Cullinane and Rochelle, 2006; Oyenekan and Rochelle, 2009; Plaza et al., 2010). The promoted PCB solutions possessed greater absorption rates and capacities than those of 7 M MEA at the typical flue gas temperatures (Oyenekan and Rochelle, 2009). A group of researchers in Australia studied the performance of CO_2 capture by using a 30 wt% PCB solution promoted with boric acid in pilot tests (Smith et al., 2012). The chilled ammonia process was proposed as another carbonate based technology (Mathias et al., 2010; Versteeg and Rubin, 2011), in which aqueous ammonia (in the form of ammonium carbonate) was used to absorb CO_2 at low temperatures (2 to 10°C) in the presence of ammonium bicarbonate precipitation (Darde et al., 2010).

Our group has developed a new variant of the carbonate based absorption process, i.e., a hot carbonate absorption process with crystallization enabled high pressure stripping (Hot CAP) for PCC from coal fired power plants (Lu et al., 2014). In this process, CO_2 is absorbed into a concentrated PCB solution (40 wt%) at an elevated temperature (70 to 80°C). Since the rate of CO_2 absorption into the PCB solution is slow even at an elevated temperature, a promoter or catalyst is required to accelerate the rate (Plaza et al., 2010; Zhang et al., 2011d). The CO_2 loadings of the lean and rich solutions in the absorber are equivalent to 15 to 20% and 40 to 45% CTB conversion, respectively, which allows us to achieve a 90% CO_2 removal from coal combustion flue gas based on the VLE data (Tosh et al., 1959). The potassium bicarbonate is crystalized from the CO_2 rich solution via cooling to 30 to 35°C. The resultant bicarbonate slurry is used to strip CO_2 at high temperatures ($\geq$ 140°C). The process is unique compared with other carbonate based processes because it involves a crystallization step to form bicarbonate slurry with an increased CO_2 loading. This enables the CO_2 stripping to be operated at a high pressure. As a result, the CO_2 stripping heat associated with water evaporation and the work required for CO_2 compression can be reduced.

Crystallization of the bicarbonate salt is a critical step in Hot CAP. Reliable data on the crystallization kinetics (nucleation and growth rates) are indispensable for optimizing the design and operation of the crystallizer. The performance of steady state crystallization has been studied for a variety of inorganic and organic chemicals, such as potassium sulfate (Jones et al., 1986; Sha et al., 1996), calcium oxalate (Bretherton and Rodgers, 1998) and adipic acid (David et al., 1991), by the adopted crystal population balance technique (Garside and Shah, 1980; Jones et al., 1986; Kougoulos et al., 2005). Previous researchers have indicated the degree of supersaturation, residence time, magma density and hydrodynamic conditions are the predominant factors affecting the crystal size and population density distribution (Garside and Shah, 1980; Jones et al., 1986). For example, at a high magma density, crystal-crystal collisions become more important to nucleation than crystal-agitator or crystal-wall collisions, because the former collisions result in a second order dependence on the secondary nucleation rate that is “removal limited” on magma density (Evans et al., 1974; Garside and Shah, 1980). In addition, secondary nucleation is expected to show a first order dependence on magma density if crystal-agitator or crystal-wall collisions are important (Ottens and Jong, 1973). Hydrodynamics can exert an effect

on both the primary and secondary nucleation rates, and thus play an role in the crystallization process (Garside and Shah, 1980). For a crystallizer operating in the "removal limited" regime, the nucleation rate is proportional to the cubed speed of agitation (Garside and Davey, 1980; Ottens and Jong, 1973). However, even for similar systems, poor specification of hydrodynamic conditions and the lack of their standardization have been the most probable causes for the observed deviations in kinetics measured among different studies.

In this chapter, the crystallization kinetics of potassium bicarbonate from PCB solutions under conditions typical of Hot CAP were investigated using a laboratory mixed suspension, mixed product removal (MSMPR) reactor. A series of experiments were carried out to evaluate the effects of variables such as agitation speed, mean residence time, feed and crystallization temperatures, feed solution composition and the presence of additives. Experimental results were used to obtain the rate constants of the crystallization process based on a size dependent growth (SDG) model. Solubility of $KHCO_3$ in PCB solutions at low temperatures ($\leq 30°C$) was measured as a complement to the literature. Based on the experimental results, preliminary analyses of the crystallization process and design of Hot CAP crystallizers were conducted.

3.2 Material and methods

3.2.1 Experimental setup

A schematic diagram of the experimental setup is shown in Fig. 3-1. The feed solution was prepared in a glass flask placed in a thermostat water bath at a predetermined temperature. A 1 L continuous stirred tank reactor (Atlas Potassium, Syrris Inc.) was used as an MSMPR crystallizer. The reactor, a round bottomed glass vessel, was double jacketed with the inner oil jacket for temperature control and the outer vacuum jacket for thermal insulation from the environment. A peristaltic pump (Masterflex) continuously withdrew the feed solution into the reactor at a constant flow rate. The tube (Masterflex Norprene) connecting the feed pump to the reactor was heated with heating tape controlled by a Variac power transformer to maintain the temperature at a preset value. Another peristaltic pump (Masterflex L/S) was used to extract continuously the product suspension (slurry) from the reactor through an overflow tube to maintain a constant liquid level inside the reactor. A thermocouple probe and a turbidity sensor were attached within

the reactor to monitor the real time temperature and in situ turbidity of the suspension, respectively. The turbidity probe was calibrated prior to each use by a standard protocol specified by the manufacturer. A 0% turbidity was for deionized water in the reactor without agitation, and a 100% turbidity was detected in a sealed box where the light beam path through a mirror cell in front of the probe was obstructed by a small piece of black matte rubber. Operation of the system, including control of the reactor temperature and agitation speed as well as data logging, was performed by a computer with Atlas software.

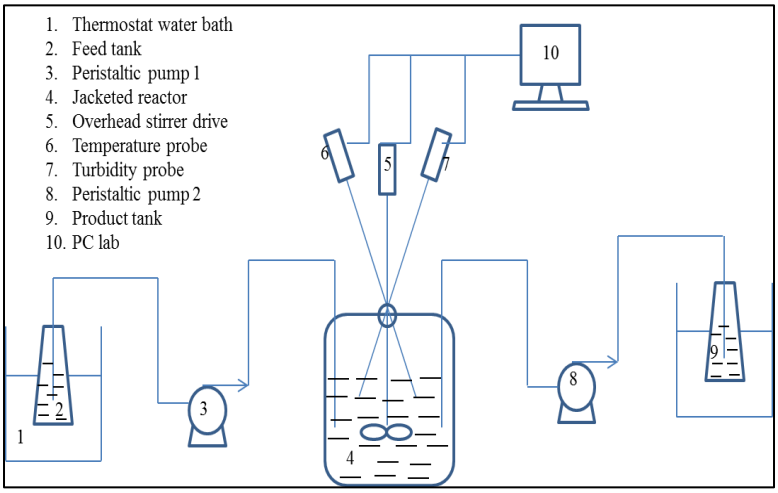

Fig. 3-1. Schematic diagram of the continuous MSMPR reactor setup.

3.2.2 Conditions and procedure for crystallization

The crystallization experiments were carried out at various agitation speeds (350, 525 and 700 rpm) and mean residence times (15, 30 and 45 min). The crystallization temperature in the reactor was 55, 45 and 35°C, and the corresponding temperature of the feed solution was at least 10°C higher. All the feed solutions used in the experiments were prepared freshly and free of seed crystals. The K_2CO_3/$KHCO_3$ solution is denoted as PCB X-Y, where X indicates the K_2CO_3 equivalent, weight percentage based total K_2CO_3/$KHCO_3$ concentration and Y indicates the percentage of CTB conversion. A PCB 40-40 solution fed at 70°C was used to simulate the CO_2 rich solution exiting from the Hot CAP absorber. PCB 38-35 and PCB 37-31 solutions were used to approximate the saturated mother solutions generated by cooling the PCB 40-40 solution from 70 to 55°C and from 70 to 45°C, respectively, based on the solubility data of $KHCO_3$ (Kohl and Nielson, 1997). In addition, PCB 37.5-36.5 and PCB 35-32.5 solutions, both of which contained the same weight percentage of K_2CO_3 as in the PCB 40-40 solution, were used as feed solutions

to investigate the effect of the supersaturation level of $KHCO_3$ on the crystallization kinetics. Moreover, the effect of PZ (0.05, 0.1 and 0.2 M) as an absorption rate activator on crystallization kinetics in PCB 40-40 solution was explored. The tests were at a feed temperature of 70°C, crystallization temperature of 55°C, agitation speed of 350 rpm and mean residence time of 15 min. Alternative tests were conducted with feed solutions prepared by bubbling CO_2 into a mixture of PCB 40-20 and PZ (0.2 or 0.5 M) until the CTB reached 40%.

In a typical experiment, 390 mL of deionized water was fed initially to the stirred reactor, heated to the preset crystallization temperature and maintained at that temperature. The feed solution at the desired temperature was pumped continuously into the reactor, where it was cooled immediately to the crystallization temperature by instantaneous heat exchange with a cooling oil medium (polydimethylsiloxane, Julabo Inc.) circulating in the oil jacket. The solution or suspension was withdrawn to maintain a constant liquid level within the reactor. When the $KHCO_3$ concentration reached and exceeded its solubility, massive crystallization began to occur. $KHCO_3$ crystals began to accumulate (a net effect of crystal generation and withdrawal), and the suspension in the reactor became denser over time before a steady state was approached. The steady state in a typical experiment was achieved after a period of 6 times the mean residence time of the suspension in the reactor (Kougoulos et al., 2005).

3.2.3 Crystal characterization

After the crystallization system reached a steady state, 20 mL of suspension was collected from the reactor with a syringe. The sample was vacuum filtered immediately through a 200 nm membrane (Whatman). Crystal solids collected on the membrane were oven dried (Precision) at 40°C, and a standard gravimetric analysis was performed on the dried sample to estimate the solid concentration of the suspension in the reactor. The size and morphology of crystal particles were analyzed using a scanning electron microscope (JEOL 6060LV). The crystal size distribution (CSD) was analyzed with a laser diffraction particle size analyzer (Horiba LA950). To verify reproducibility, the CSD measurements were performed at least twice for each sample. The compositions of crystal samples were analyzed by X-ray diffraction (Siemens-Bruker D5000 XRD) using Cu Kα (wavelength $\lambda = 0.15418$ nm) radiation (40 kV, 30 mA). Diffraction peaks were measured by step scanning from 5 to 60° at a speed of 0.5° min^{-1} and a step width of 0.05°.

3.2.4 Procedure of solubility measurement

The solubility was measured by a turbidity method without studying phase diagrams. In each test, 500 g of slurry with a desired composition was fed to the reactor agitated at 200 rpm. A high initial turbidity (>99%) was detected at a low temperature. The reactor was heated at programmed rates toward the complete dissolution of the slurry. As the full dissolution of slurry approached, the rate of temperature increase slowed (0.5 to 1°C hr^{-1}). Finally, the turbidity decreased abruptly to a minimum level (0%) and started to level off thereafter; thus, the dissolution temperature was located. The method was verified by comparing the measured solubility with the reported data. The formulae tested were PCB 20-65, 70, 75, 80, 90, 100, PCB 25-40, 45, 50, PCB 30-25, 30, PCB 35-15, 20 and PCB 40-10, corresponding to the dissolution temperatures between 10 and 30°C.

3.3 Theory of crystallization kinetics

For a steady state MSMPR crystallizer, the general population balance equation is as follows (Kougoulos et al., 2005):

$$\frac{d[G(L)n(L)]}{dL} + \frac{n(L)}{\tau} = 0 \qquad (3\text{-}1)$$

where $G(L)$ is the crystal growth rate (m s^{-1}), L is the characteristic dimension of crystal particles (diameter for spherical particles, m), $n(L)$ is the population density (m^{-4}) and τ is the mean residence time (s). Nonlinearity of the logarithmic $n(L)$ is evident for many systems due to the feature of size dependent growth or growth rate dispersion (Garside et al., 1976). Growth rate dispersion has been modeled by two mechanisms: the random fluctuation model (Randolph and White, 1977) according to which crystal growth fluctuates during the course of crystallization as a result of both flow and velocity fluctuations, and the constant crystal growth model (Myerson, 2002) according to which crystals have an inherent growth rate but the rate varies from crystal to crystal. Size dependent crystal growth can be described by an empirical correlation based on the three parameter, exponential model as follows (Mydlarz and Jones, 1993):

$$G(L) = G_m\{1 - \exp[-a(L + c)]\} \qquad (3\text{-}2)$$

where G_m is the limiting or effective size independent growth rate for large crystal particles

(m s^{-1}), and both a and c are empirical constants. Because $G(L)$ approximates the constant G_m at a large L, it also is called the linear growth rate because it remains the same after reaching some critical size. By integrating Eq. (3-2) over the entire range of particle size, the average crystal growth rate (G_{av}, m s^{-1}) can be obtained as follows:

$$G_{av} = G_m \left\{ 1 + \frac{1}{aL_m} \left[e^{-a(L_m + c)} - e^{-ac} \right] \right\} \tag{3-3}$$

where L_m is the maximum crystal size obtained (m). The minimum crystal size is assumed to be 0. Because, on average, the crystals in an MSMPR reactor are replaced within a mean residence time, G_{av} can be estimated from the measured slurry density and CSD according to the following equation:

$$G_{av} = \frac{M_T}{3\rho_s \tau k_v \int_0^\infty n(L) L^2 dL} \tag{3-4}$$

where M_T is the solid concentration of the suspension(kg m^{-3}), ρ_s is the density of $KHCO_3$ solids (2,170 kg m^{-3}) and k_v is the volumetric shape factor ($\pi/6$ for spherical particles).

By solving Eqs. (3-1) and (3-2) simultaneously, the following logarithmic population density equation can be obtained:

$$\log n(L) = \log n_0 + aL - \left(1 + \frac{1}{a\tau G_m} \right) \log \left(\frac{e^{aL} - e^{-ac}}{1 - e^{-ac}} \right) \tag{3-5}$$

where n_0 is the "zero size" (nuclei) population density (m^{-4}). The population density $n(L)$ can be determined from the measured CSD and slurry density by the following equation:

$$n(L) = \frac{M_T q_i}{k_v \rho_s L^3 \Delta L} \tag{3-6}$$

where q_i is the mass or volumetric fraction of the ith size fraction from the measured CSD, and ΔL is the crystal size range between two neighboring size fractions. The resultant $n(L)$ can be least square fitted to Eq. (3-5) to retrieve the parameters G_m, a and c using a Python program (Python version 2.7, see Appendix A for the Python codes).

The fitted G_m can be correlated to the supersaturation level, i.e., the driving force of crystallization, by the following power law relationship:

$$G_m = k_g \sigma^g \tag{3-7}$$

where σ is the relative supersaturation level (dimensionless), k_g is the overall growth rate coefficient (m s^{-1}) and g is an empirical constant. For simplicity, as shown in Eq. (3-8), σ is estimated based on the mass concentration as a reasonable approximation to the activity:

$$\sigma = \frac{w - w_{eq}}{w_{eq}} \tag{3-8}$$

where w is the concentration of $KHCO_3$ (kg m^{-3}) and w_{eq} is the solubility of $KHCO_3$ (kg m^{-3}). In a PCB solution, the coexistence of K_2CO_3, though soluble itself, reduces the solubility of $KHCO_3$ by the common ion effect. Therefore, the actual w_{eq} of $KHCO_3$ can be estimated from the solubility product of $KHCO_3$ at the crystallization temperature and the initial concentration of K^+. The variable k_g represents the two stages of the crystal growth process following the formation of stable nuclei: bulk diffusion to the crystal surface and surface reaction or integration (Karpinski, 1985). The value of k_g is a function of temperature following an Arrhenius relationship (Garside et al., 1982):

$$k_g = \alpha e^{\frac{-E_g}{RT}} \tag{3-9}$$

where α is a constant (m s^{-1}), E_g is the activation energy for crystal growth including both the diffusion and reaction (kJ mol^{-1}), R is the universal gas constant (8.314 J mol^{-1} K^{-1}) and T is the absolute temperature (K).

The total nucleation rate (B_{TOT}, s^{-1} m^{-3}), the sum of primary and secondary nucleation, is the number of new crystal particles formed per unit of suspension volume per unit of time. The formation of nuclei relies on the relative supersaturation level, the solid concentration of the suspension and hydrodynamic factors. B_{TOT} can be expressed by a semiempirical power law form:

$$B_{TOT} = k_n G_{av}{}^h N^i M_T{}^j \tag{3-10}$$

where h, i and j are the empirical exponents determined by data fitting; N is the agitation speed (rpm); k_n is the nucleation rate coefficient, a function of temperature, hydrodynamics and impurity concentration (Jones et al., 1986), the expression of which is shown as:

$$k_n = \beta e^{\frac{-E_n}{RT}} \tag{3-11}$$

where β is a fitting constant; E_n is the apparent activation energy of nucleation which could be negative (Jones et al., 1986; Wey and Terwilliger, 1980). The values of B_{TOT} can be determined

from the experimental data based on Eq. (3-12), and the results are used to obtain the exponents and constants in Eqs. (3-10) and (3-11) by data fitting.

$$B_{TOT} = \frac{\int_0^\infty n(L)dL}{\tau} \tag{3-12}$$

To predict the crystal size under various crystallization conditions, the correlation between the mass median crystal size (L_M, m) and crystallization kinetics was taken as a formula by Mullin (2001), and L_M was correlated with the mass mean crystal size ($\overline{L}$, m) assuming a log normal CSD:

$$L_M = 3.67 G_{av} \tau = \overline{L} \exp[-0.5(\ln \sigma_g)^2] \tag{3-13}$$

where σ_g is the geometric standard deviation of the CSD. The values of $\bar{L}$ can be determined by the measured CSD data according to Eq. (3-14):

$$\overline{L} = \frac{\int_0^\infty n(L)L^4 dL}{\int_0^\infty n(L)L^3 dL} \tag{3-14}$$

Rather than considering an infinite range of crystal particle size, Eqs. (3-4), (3-12) and (3-14) can be integrated practically over a size range from the minimum to maximum sizes detected by the particle size analyzer.

3.4 Results and discussion

3.4.1 Composition and morphology of crystal particles

Using XRD analysis, kalicinite ($KHCO_3$) was the only crystal phase formed in all the conducted tests, regardless of whether PZ was present. As an example, typical XRD patterns of crystal particles formed at 55°C, an agitation speed of 350 rpm and a mean residence time of 1,732 s with a PCB 40-40 solution fed at 70°C are displayed in Fig. 3-2. Kalicinite crystals produced under various test conditions showed similar morphology. A typical scanning electron microscopy (SEM) image of crystal particles obtained under the same conditions as those used in Fig. 3-2 is displayed in Fig. 3-3. Most crystals have an octagonal prism shape.

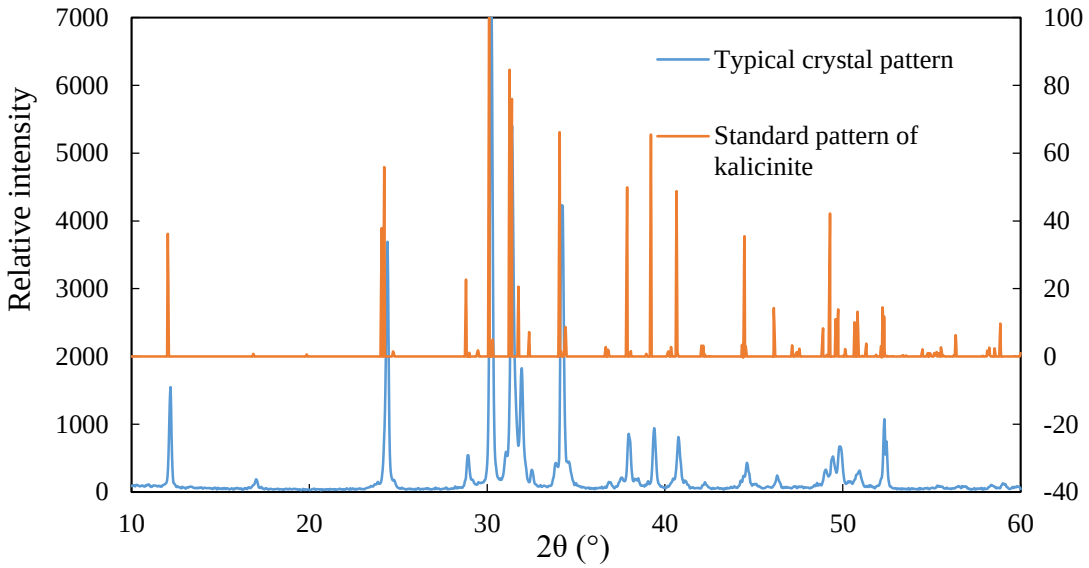

Fig. 3-2. Typical XRD patterns of crystal particles obtained from crystallization at 55°C, an agitation speed of 350 rpm and a mean residence time of 1,732 s with a PCB 40-40 solution fed at 70°C.

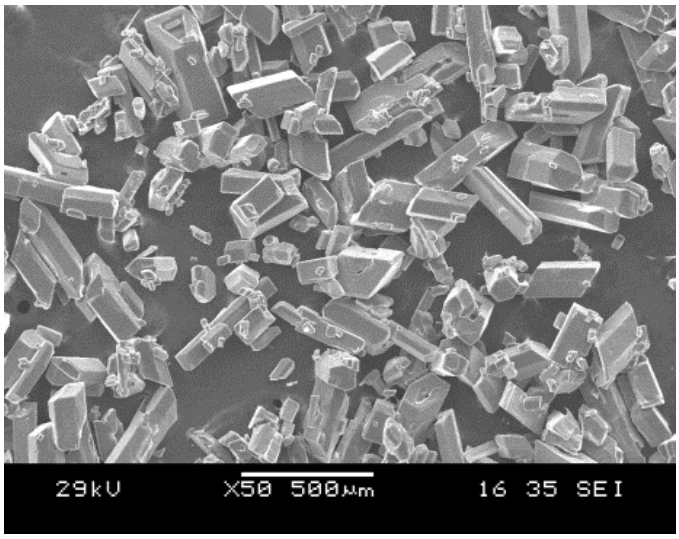

Fig. 3-3. A typical SEM image of kalicinite particles obtained from crystallization at 55°C, an agitation speed of 350 rpm and a mean residence time of 1,732 s with a PCB 40-40 solution fed at 70°C.

3.4.2 Parametric effects on crystallization kinetics

Several operating variables, including the mean residence time, agitation speed and relative supersaturation level, are critical to the crystallization. Parametric experiments were conducted

to investigate their effects on the crystallization kinetics. The experimental conditions and corresponding results are summarized in Table 3-1.

3.4.2.1 Mean residence time

Increasing the mean residence time increased the mean crystal size but decreased the total nucleation rate and crystal growth rate (Fig. 3-4). At a longer mean residence time, more crystal fragments were formed because of attrition among crystal particles by mechanical agitation. The resultant fragments acted as secondary nuclei which inhibited the crystal growth. In addition, a longer mean residence time led to a lower level of local supersaturation, as reported by Kougoulos et al. (2005) and Zauner and Jones (2000), which could slow the crystal growth. We observed the measured solid concentration of the suspension was independent of the mean residence time for a feed solution with given feed and crystallization temperatures. Therefore, crystallization of $KHCO_3$ was fast and equilibrium could be approached within the shortest mean residence time examined.

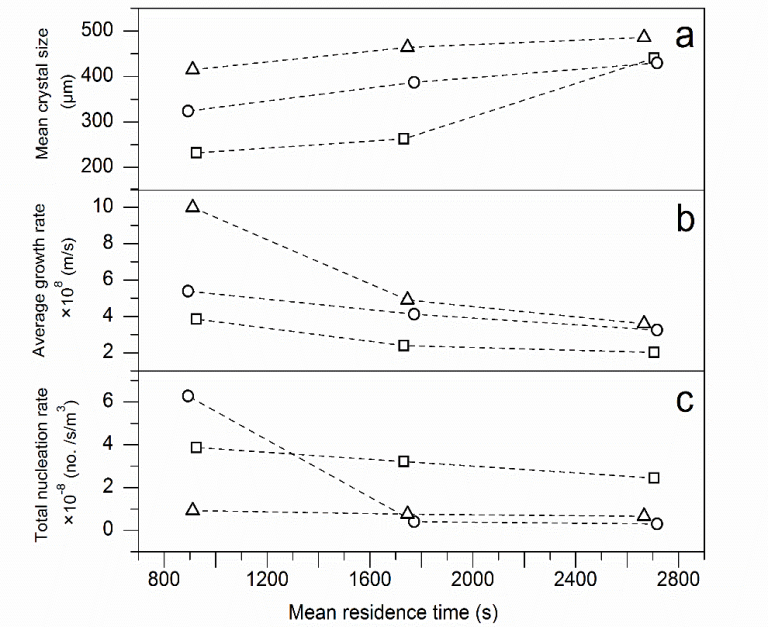

Fig. 3-4. Effect of mean residence time on (a) mean crystal size, (b) average crystal growth rate and (c) total nucleation rate.

Table 3-1. Experimental conditions and results of crystallization kinetics.

Test	Feed solution	Feed temperature (°C)	Density of feed solution (g L^{-1})	Agitation speed (rpm)	Crystallization temperature (°C)	Relative super saturation	Mean residence time (s)	Solid concentration (g L^{-1})	Mean crystal size (μm)	Mean growth rate ($\times 10^{8}$) (m s^{-1})	Total nucleation rate ($\times 10^{-8}$) (s^{-1} m^{-3})
1	PCB 40-40	70	1,340	350	55	0.271	926	63.0	232	3.84	3.87
2	PCB 40-40	70	1,330	350	55	0.288	1,732	65.7	263	2.39	3.21
3	PCB 40-40	70	1,370	350	55	0.245	2,706	59.4	440	2.02	2.44
4	PCB 40-40	70	1,340	525	55	0.266	1,804	62.1	202	2.32	3.68
5	PCB 40-40	70	1,330	700	55	0.259	1,775	60.3	141	1.76	4.31
6	PCB 38-35	55	1,330	350	45	0.238	893	47.0	324	5.39	6.28
7	PCB 38-35	55	1,310	350	45	0.220	1,772	43.5	387	4.12	0.40
8	PCB 38-35	55	1,330	350	45	0.235	2,716	46.5	430	3.25	0.30
9	PCB 38-35	55	1,330	525	45	0.178	1,765	37.0	366	3.60	1.14
10	PCB 38-35	55	1,330	700	45	0.184	1,786	38.0	129	1.59	6.30
11	PCB 37-31	45	1,330	350	35	0.372	911	57.5	415	9.98	0.92
12	PCB 37-31	45	1,330	350	35	0.350	1,746	55.0	464	4.90	0.75
13	PCB 37-31	45	1,340	350	35	0.321	2,666	52.0	486	3.60	0.66
14	PCB 37-31	45	1,320	525	35	0.320	1,797	51.0	431	4.06	2.51
15	PCB 37-31	45	1,320	700	35	0.307	1,768	49.5	381	3.40	2.64
16	PCB 40-40	70	1,320	700	35	1.084	1,799	151.5	478	6.21	1.23
17	PCB 40-40	70	1,350	700	45	0.498	1,823	99.0	393	3.93	2.10
18	PCB 38-35	55	1,330	700	35	0.577	1,788	89.5	407	4.74	1.79
19	PCB 37.5-36.5	70	1,310	700	35	0.804	1,787	111.0	381	4.34	1.52
20	PCB 35-32.5	70	1,300	700	35	0.204	1,824	35.0	343	3.47	1.93
21	PCB 40-40+ 0.05M PZ	70	1,330	350	55	0.290	937	66.0	298	6.12	2.07
22	PCB 40-40+ 0.1M PZ	70	1,330	350	55	0.307	874	69.0	358	7.75	1.74
23	PCB 40-40+ 0.2M PZ	70	1,330	350	55	0.331	889	73.0	426	9.34	0.49
24	PCB 40-40+ 0.2M PZ-CO_2	70	1,330	350	55	0.313	865	70.0	391	10.07	0.39
25	PCB 40-40+ 0.5M PZ-CO_2	70	1,330	350	55	0.319	924	71.0	397	7.46	1.81

3.4.2.2 Agitation speed

The agitation speeds were selected to ensure a mixed suspension while avoiding the formation of vortexes or air entrainment. As shown in Fig. 3-5, increasing the agitation speed reduced the mean crystal size and crystal growth rate while enhancing the nucleation rate. This observation was similar to that provided by Camblor et al. (1991), Herrera and Hartel (2000) and Sha et al. (1996). Nucleation could be improved in an agitated system because stronger agitation favored the formation of smaller crystal fragments resulting from larger shear forces and the exertion of an attrition effect (Kougoulos et al., 2005). Moreover, the air bubbles generated with strong agitation could facilitate the onset of nucleation because they acted as dark spots and provided surfaces for crystallization. Crystal growth rate was not enhanced by increasing the agitation speed, indicating the growth process was not bulk diffusion controlled.

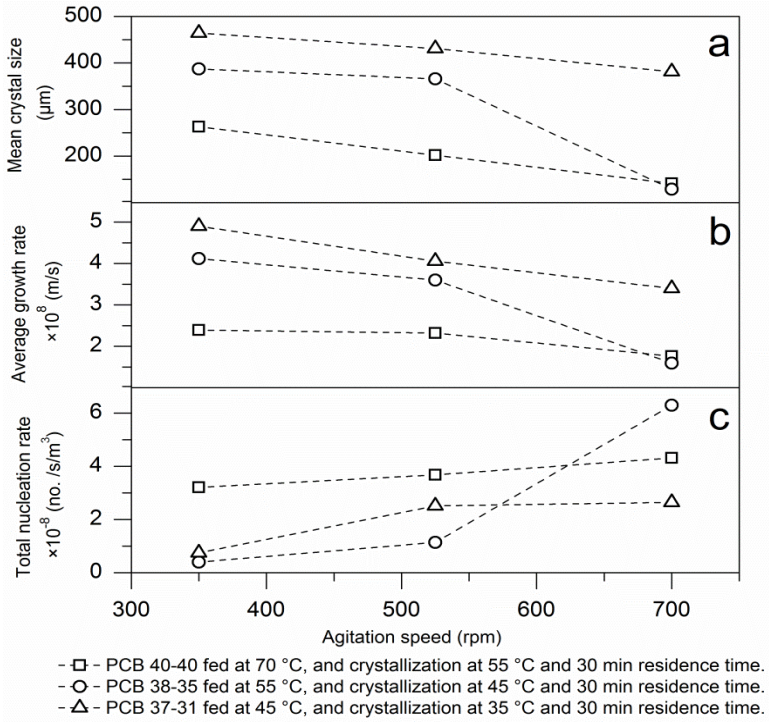

Fig. 3-5. Effect of agitation speed on (a) mean crystal size, (b) average crystal growth rate and (c) total nucleation rate.

3.4.2.3 Relative supersaturation level

The relative supersaturation level was adjusted by varying either the crystallization temperature (a lower temperature indicating a higher supersaturation level for the same feed solution) or the feed solution composition. The experimental results of three solutions (PCB 40-40, PCB

37.5-36.5 and PCB 35-32.5) fed at 70°C and crystallized at 35°C under the same mean residence time (30 min) and agitation speed (700 rpm) are presented in Fig. 3-6. These feed solutions contained the same content of K_2CO_3 but different contents of $KHCO_3$, so their respective supersaturation levels were different from each other (1.084, 0.804 and 0.204). As shown in Fig. 3-6, both the crystal growth rate and mean crystal size increased with increasing supersaturation levels, which was consistent with the report of Tanrikulu et al. (2000). However, the nucleation rate decreased with increasing relative supersaturation levels. Since the primary nucleation rates were enhanced with increasing supersaturation, the observed trend should have reflected the dominant effect of the secondary nucleation, which was incurred by the catalytic effect of the parent crystals in a supersaturated solution. When the supersaturation level was high, the primary (spontaneous) nucleation prevailed and the secondary nucleation was inhibited. However, in a solution with low supersaturation, the catalytic effect of the parent crystals was no longer inhibited and the secondary nucleation became dominating. As a result, the total nucleation rate was higher at a lower relative supersaturation level.

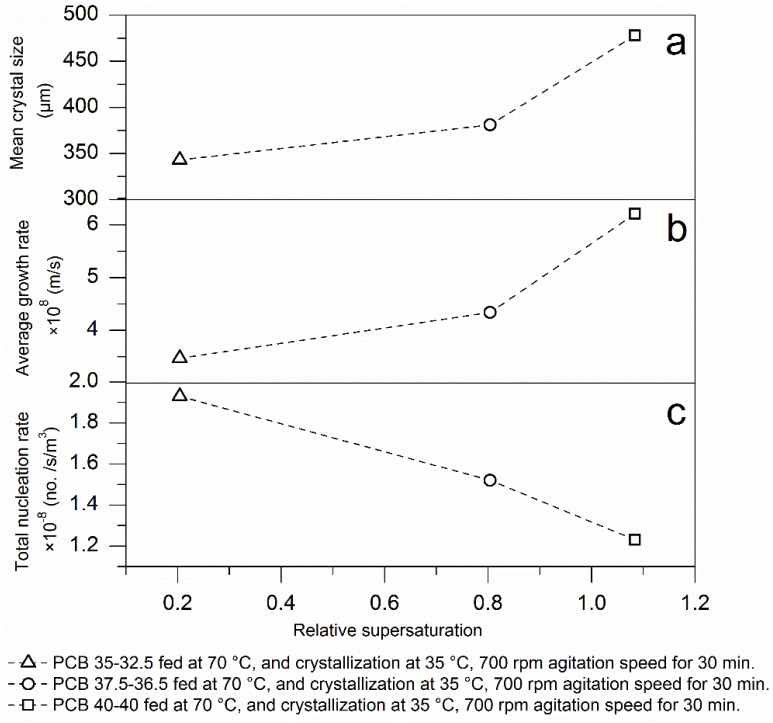

Fig. 3-6. Effect of relative supersaturation level on (a) mean crystal size, (b) average crystal growth rate and (c) total nucleation rate. All the experiments were performed at the same crystallization temperature (35°C).

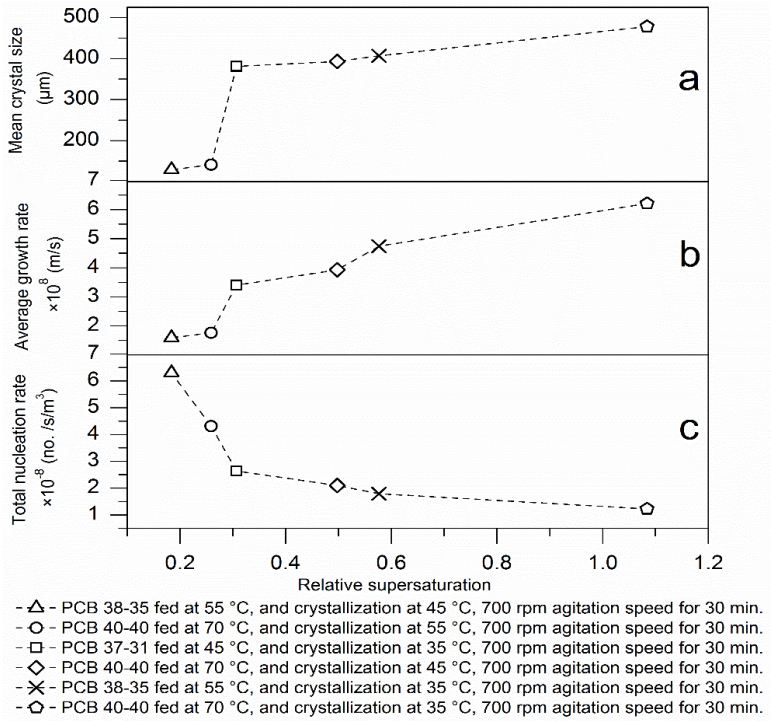

Fig. 3-7. Combined effect of relative supersaturation level and crystallization temperature on the crystallization kinetics, i.e., (a) mean crystal size, (b) average crystal growth rate and (c) total nucleation rate. The crystallization experiments were performed at different temperatures (35, 45 or 55°C).

The crystallization kinetics obtained at different relative supersaturation levels are presented in Fig. 3-7. Six feed solutions were used: PCB 40-40, fed at 70°C and tested for crystallization at 55°C (σ = 0.259), 45°C (σ = 0.498) and 35°C (σ = 1.084); PCB 38-35, fed at 55°C and tested at 45°C (σ = 0.184) and 35°C (σ = 0.577); PCB 37-31, fed at 45°C and tested at 35°C (σ = 0.307). All the tests were carried out at an agitation speed of 700 rpm and a mean residence time of 30 min. In these tests, the relative supersaturation level depended not only on the composition of the feed solution, but also on the cooling temperature. The kinetic performance of the bicarbonate crystallization shown in Fig. 3-7 was similar to that in Fig. 3-6, except that the nucleation rate shown in Fig. 3-7 was more sensitive to the relative supersaturation level than that shown in Fig. 3-6. Besides the effect of the secondary nucleation, the effect of crystallization temperature on the nucleation rate could not be separated from the effect of the supersaturation. For a given feed solution, a high crystallization temperature corresponded to a low supersaturation level. Nucleation proceeded faster at a higher crystallization temperature according to the Arrhenius

relationship. Several investigators indicated that at a low temperature (high supersaturation level), nucleation was inhibited by the retarded molecular diffusion (McClements, 2012; Ooshima et al., 2013). The combined effect of crystallization temperature and supersaturation on the nucleation rate resulted in a low nucleation rate at a high supersaturation level.

3.4.2.4 Presence of PZ

As shown in Table 3-1, the solid concentration of $KHCO_3$ slurry in the presence of PZ was higher compared with neat PCB 40-40, probably because the solubility of $KHCO_3$ was affected by PZ. When 0.2 M PZ was added to PCB 40-40, the solid concentration increased by 20%. The crystallization kinetics were accelerated by the addition of PZ. As shown in Fig. 3-8, the size of $KHCO_3$ crystal particles doubled and the average crystal growth rate was more than two fold higher with 0.2 M PZ in PCB 40-40. However, nucleation was inhibited in the presence of PZ. Such results were favorable for the Hot CAP, because PZ was used as the absorption rate activator and was present in the CO_2 rich solution entering the crystallizer.

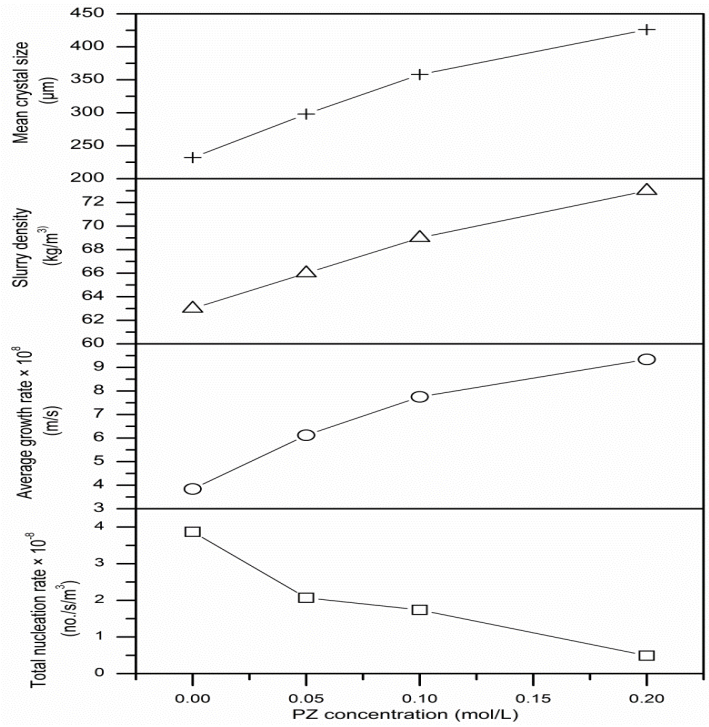

Fig. 3-8. Effects of PZ present in PCB 40-40 (70°C) on (a) mean crystal size, (b) slurry concentration, (c) average crystal growth rate and (d) total nucleation rate. The crystallization was tested at 55°C, an agitation speed of 350 rpm and a mean residence time of 15 min.

CO_2 rich solutions, obtained by bubbling CO_2 into the mixture of PCB and PZ until the required total CO_2 loading was reached to simulate CO_2 absorption, were used in the alternative experiments (No. 24 to 25 in Table 3-1). In these experiments, PZ existed as molecular PZ and its carbamate species. Similar to the prior experiments, the presence of PZ accelerated the crystallization of $KHCO_3$. The feed solution of PCB 40-40 with 0.2 M PZ added showed a higher average crystal growth rate yet a lower total nucleation rate than did with 0.5 M PZ added. As a result, a similar crystal size was observed (390 to 400 μm). The measured solid concentrations at the two PZ doses were similar (70 kg m^{-3}), because the total concentration of HCO_3^- was not changed given the small dose of PZ compared with the concentration of HCO_3^-. However, the above trends deviated from those shown in Fig. 3-6, indicating the distinctive solubilization effects of molecular PZ and its ionic derivatives (e.g., PZ carbamate and PZ dicarbamate) on HCO_3^-.

3.4.3 Modeling of crystallization kinetics

On the basis of the measured CSD and solid concentration of the suspension under various experimental conditions, the logarithmic population density distribution curves were plotted according to Eq. (3-5) to retrieve the model parameters *a*, *c* and G_m. As an example, the logarithmic population density distribution curve for PCB 38-35 solution fed at 55°C and tested for crystallization at 45°C, a mean residence time of 30 min and an agitation speed of 350 rpm is illustrated in Fig. 3-9. The logarithmic population density was not linear with the crystal size until the size was larger than 600 μm. G_m was estimated from the linear part of the curve ($-\tau^{-1}$ slope^{-1}). As indicated by the coefficients of determination (R^2) listed in Table 3-2, the models determined by nonlinear data fitting agreed with the experimental data.

When PZ was not present, the effective crystal growth rate (G_m) determined (Table 3-2) could be correlated with the relative supersaturation level according to Eqs. (3-7) and (3-9) (R^2 = 0.96):

$$G_m = 0.46e^{-\frac{39906}{RT}}\sigma_0^{0.56} \quad (3\text{-}15)$$

The constants *a* and *c* varied with the experimental conditions (Table 3-2), and the average values of *a* and *c* were 7,673 and 2.88×10^{-10} with the relative standard deviations of 84.7% and

3.9%, respectively. According to the parameters determined above, the SDG model is expressed as follows:

$$G(L) = 0.46e^{-\frac{39906}{RT}}\sigma_0^{0.56}\left[1 - e^{-7673(L+2.88\times10^{-10})}\right] \quad (3\text{-}16)$$

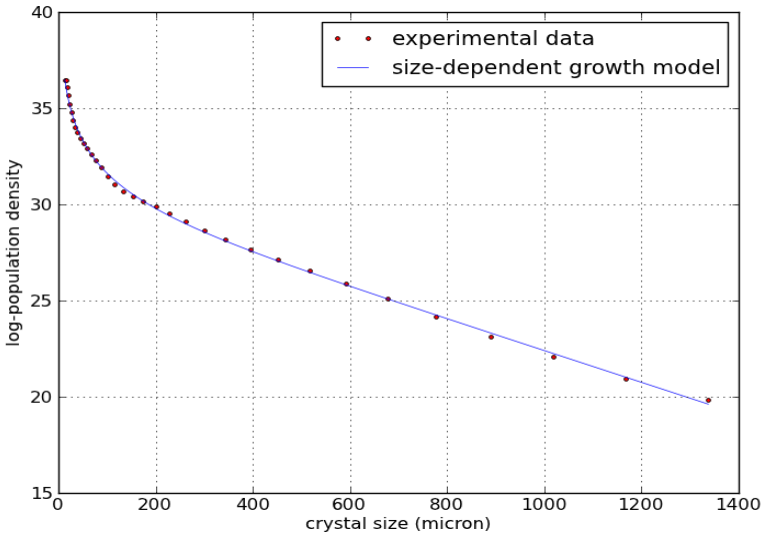

Fig. 3-9. Logarithmic population density distribution of kalicinite crystal particles obtained from PCB 38-35 solution fed at 55°C and tested at 45°C, a mean residence time of 30 min and an agitation speed of 350 rpm.

The rate and differential rate of crystal growth as a function of crystal size predicted by Eq. (3-16) for PCB 38-35 solution fed at 55°C and tested for crystallization at 45°C, a mean residence time of 30 min and an agitation speed of 350 rpm is shown in Fig. 3-10. The predicted trends were in agreement with those reported (Kougoulos et al., 2005; Sha et al., 1996). The rate of crystal growth initially increased with increasing particle size and became size independent when the size of crystal particles reached 600 µm. This critical size was consistent with that observed in Fig. 3-9. Accordingly, the differential rate of crystal growth decreased with increasing particle size and leveled off ($dG/dL = 0$, $G(L) = G_m$) at a crystal size of 600 µm.

A least square regression of experimental data was performed based on Eqs. (3-10) and (3-11) to determine the nucleation model parameters. The resultant power law equation was applied to predict the total nucleation rate:

$$B_{TOT} = 9.40\times10^{14}\exp\left(-\frac{52{,}463}{RT}\right)G_{av}^{0.20}N^{1.46}M_T^{-0.26} \quad (3\text{-}17)$$

The R^2 value of the above regression equation was estimated to be 0.39. The exponents of both G_{av} and M_T (in the absence of PZ) approached 0, indicating a weak correlation of the total nucleation rate with either the average crystal growth rate or the solid concentration of the suspension. In comparison, the total nucleation rate was affected by the agitation speed (N), as indicated by its exponent greater than 1. Unlike the agitation speed, the parameters G_{av}, M_T and T were coupled with each other; therefore, it was not surprising to see that M_T was applied with a negative exponent.

Table 3-2. Parameters of the SDG model determined from experimental data fitting.

No.	Test conditions	$\ln(n_0)$	G_m	a	c	R^2 (%)
1	PCB 40-40, 70-55°C, 350 rpm, 15 min[a]	39.13	1.21e-07	3,305.6	2.56e-05	99.5
2	PCB 40-40, 70-55°C, 350 rpm, 30 min	59.18	4.85e-08	7,312.1	4.59e-09	99.2
3	PCB 40-40, 70-55°C, 350 rpm, 45 min	69.15	6.50e-08	2,984.2	2.91e-10	99.2
4	PCB 40-40, 70-55°C, 525 rpm, 30 min	63.49	3.69e-08	11,469.2	1.86e-10	99.3
5	PCB 40-40, 70-55°C, 700 rpm, 30 min	57.38	2.08e-08	28,624.1	5.57e-10	98.6
6	PCB 38-35, 55-45°C, 350 rpm, 15 min	66.61	1.27e-07	5,234.1	2.83e-10	99.7
7	PCB 38-35, 55-45°C, 350 rpm, 30 min	60.27	6.85e-08	6,158.6	5.03e-10	99.9
8	PCB 38-35, 55-45°C, 350 rpm, 45 min	61.32	4.78e-08	5,981.3	2.14e-10	99.1
9	PCB 38-35, 55-45°C, 525 rpm, 30 min	62.19	5.84e-08	6,810.3	3.66e-10	99.1
10	PCB 38-35, 55-45°C, 700 rpm, 30 min	63.41	2.09e-08	22,829.1	1.01e-10	99.2
11	PCB 37-31, 45-35°C, 350 rpm, 15 min	61.49	1.41e-07	6,107.6	1.96e-10	98.4
12	PCB 37-31, 45-35°C, 350 rpm, 30 min	64.67	8.92e-08	4,153.6	2.31e-10	98.3
13	PCB 37-31, 45-35°C, 350 rpm, 45 min	64.26	6.09e-08	4,212.7	1.53e-10	98.3
14	PCB 37-31, 45-35°C, 525 rpm, 30 min	67.05	8.72e-08	3,788.3	1.88e-10	98.5
15	PCB 37-31, 45-35°C, 700 rpm, 30 min	65.38	7.37e-08	4,693.5	3.16e-10	99.1
16	PCB 40-40, 70-35°C, 700 rpm, 30 min	61.45	7.98e-08	5,929.3	1.40e-10	98.4
17	PCB 40-40, 70-45°C, 700 rpm, 30 min	60.99	6.58e-08	6,232.2	5.21e-10	99.5
18	PCB 38-35, 55-35°C, 700 rpm, 30 min	64.08	7.39e-08	5,486.0	1.45e-10	98.2
19	PCB 37.5-36.5, 70-35°C, 700 rpm, 30 min	60.86	7.19e-08	5,699.7	6.09e-10	99.0
20	PCB 35-32.5, 70-35°C 700 rpm 30 min	65.62	5.67e-08	6,441.1	1.30e-10	98.9
21	PCB 40-40, 70-55°C, 350 rpm, 15 min, 0.05M PZ	41.49	1.07e-07	7,440.9	2.16e-06	99.6
22	PCB 40-40, 70-55°C, 350 rpm, 15 min, 0.1M PZ	39.96	1.68e-07	4,275.8	5.17e-06	99.3
23	PCB 40-40, 70-55°C, 350 rpm, 15 min, 0.2M PZ	36.54	1.52e-07	4,417.9	2.57e-05	99.8
24	PCB 40-40, 70-55°C, 350 rpm, 15 min, 0.2M PZ-CO_2	49.06	1.24e-07	10,389.2	1.14e-08	99.7
25	PCB 40-40, 70-55°C, 350 rpm, 15 min, 0.5M PZ-CO_2	40.29	1.48e-07	4,792.2	4.39e-06	99.8

[a] Feed solution of PCB 40-40 fed at 70°C and tested for crystallization at 55°C, an agitation speed of 350 rpm and a mean residence time of 15 min. Likewise for the other feed solutions in the table.

When PZ was present, G_m was determined by regression with the PZ related data (R^2 = 0.996):

$$G_m = 3\times10^{-4} e^{-\frac{20142}{RT}} \sigma_1^{0.54} \quad (3\text{-}18)$$

The average values of a and c were 7,391 and 1.16×10^{-9} with the relative standard deviations of 80% and 16%, respectively. Thus, the modified SDG model is shown in Eq. (3-19):

$$G(L) = 3\times10^{-4} e^{-\frac{20142}{RT}} \sigma_1^{0.54} [1 - e^{-7391(L+1.16\times10^{-9})}] \quad (3\text{-}19)$$

Similarly, a power law model for B_{TOT} was obtained as follows ($R^2 = 0.37$):

$$B_{TOT} = 5.68\times10^{5} e^{-\frac{25736}{RT}} G_{av}^{-0.53} N^{1.05} M_T^{-0.03} \quad (3\text{-}20)$$

Likewise, the correlation of B_{TOT} with either G_{av} or M_T (in the presence of PZ) was weaker than that with N, and negative exponents were mathematically acceptable because G_{av}, M_T and T were coupled with each other. The empirical model obtained was specific to the investigated conditions representative of the Hot CAP.

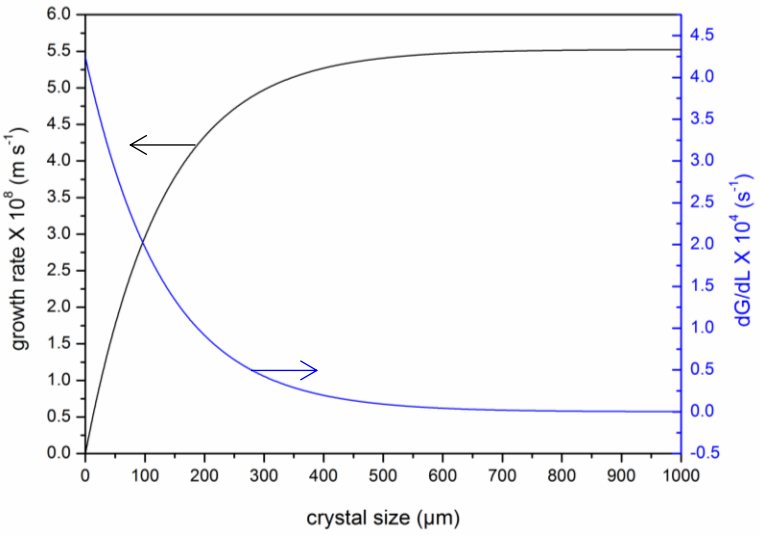

Fig. 3-10. The rate and differential rate of crystal growth as a function of crystal size for PCB 38-35 solution fed at 55°C and tested at 45°C, a mean residence time of 30 min and an agitation speed of 350 rpm.

3.4.4 Solubility of PCB solutions

The turbidity method for solubility determination was validated by the data obtained for the solutions of PCB 40-20 and PCB 30-80. In a typical measurement, the turbidity decreased sharply with increasing temperature and leveled off as the temperature approached the dissolution point. The dissolution temperatures for the solutions of PCB 40-20 and PCB 30-80 were measured at 37.5 and 59.0°C, with the reported data being 37.8 and 60°C, respectively (Kohl and Nielson, 1997). The small difference (≤ 1°C) indicated the agreement between the measured and literature values.

A summary of the measured and literature dissolution temperatures for the 20, 30 and 40 wt% PCB solutions is shown in Table 3-3. The solubility data for each PCB solution depicted as a relationship between the dissolution temperature and the CTB conversion ratio is shown in Fig. 3-11. An empirical formula was developed to describe the relationship between the composition and dissolution temperature of a PCB solution ($R^2 = 0.991$):

$$\frac{1}{T_s} = 0.0083 - 0.0011 \ln X - 0.00038 \ln Y \tag{3-21}$$

where T_s is the absolute dissolution temperature (K), X represents the total PCB concentration (K_2CO_3 equivalent, wt%) and Y is the CTB conversion ratio (%). The solubility lines based on Eq. (3-21) are overlaid in Fig. 3-11, and the predicted trends were in agreement with the measured and literature data.

Table 3-3. The measured (M) and literature (L) dissolution temperatures of PCB solutions.

	X = 20			X = 25			X = 30			X = 35			X = 40	
	T (°C)	Y		T (°C)	Y		T (°C)	Y		T (°C)	Y		T (°C)	Y
	26.2	100		48.2	100		68.3	100		89.9	100		116.9	100
	25.1	90		44.0	90		64.2	90		85	90		108.6	90
M	20.3	80	L	39.9	80		60	80		79.4	80		101	80
	18.6	75		35	70	L	53.8	70		72.5	70		91.9	70
	16.5	70		28.1	60		46.1	60	L	64.2	60	L	83.6	60
	14.6	65		22.4	50		38.9	50		54.4	50		73.2	50
			M	19	45		28.8	40		44.7	40		62.8	40
				13.9	40	M	20.4	30		35	30		51.7	30
							16.9	25	M	24.3	20		37.8	20
										15.2	15	M	19.4	10

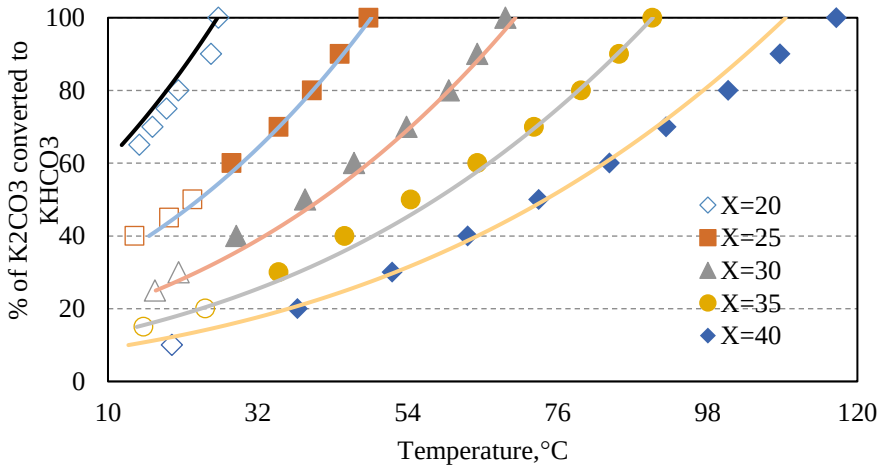

Fig. 3-11. Measured (open symbols), literature (filled symbols) and predicted (lines) solubility data of PCB solutions at various temperatures and CTB conversion ratios.

3.4.5 Design considerations for Hot CAP crystallizers

A configuration of multiple MSMPR crystallizers was proposed for the Hot CAP with the schematic diagram displayed in Fig. 3-12. Five consecutive MSMPR tanks were used instead of a single crystallizer. Such a configuration would facilitate the heat recovery required in the process and could reduce the temperature difference between the inlet and outlet streams of each crystallizer (5 to 10°C). In comparison, a single crystallizer design would require heat exchange with a large temperature difference between the inlet solution and mother liquid, thus jeopardizing heat recovery and incurring fouling problems.

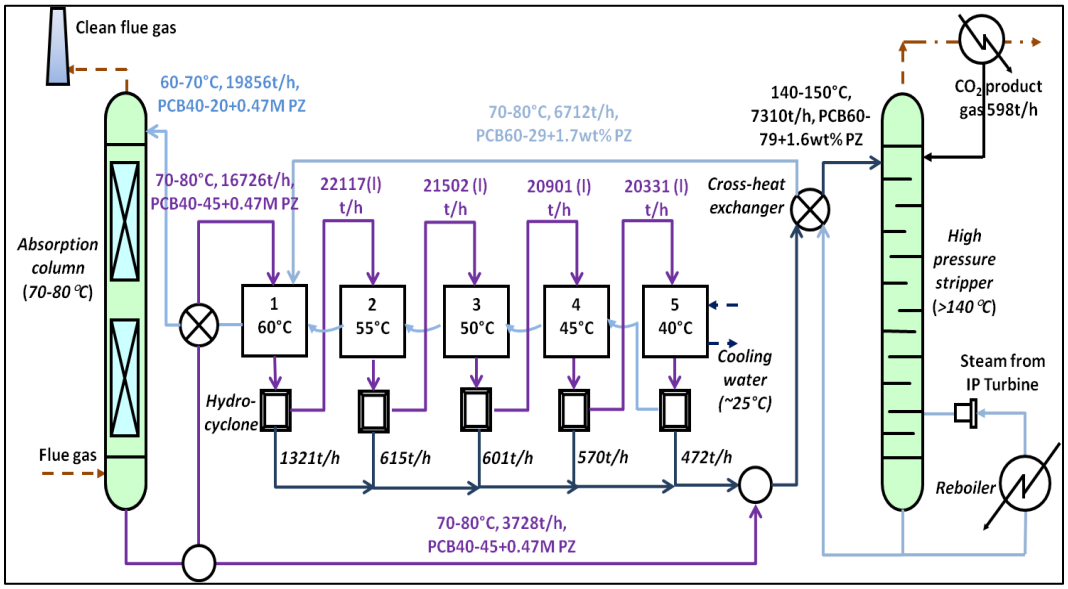

Fig. 3-12. Flowchart of the Hot CAP with five MSMPR crystallizers.

Mass and heat balance calculations were conducted based on the flue gas composition and flow rate typical of a 550 MWe (net output after CO_2 capture) power plant (USDOE/NETL, 2013). The CO_2 lean solvent entering the CO_2 absorber was PCB 40-20 with 0.47 M PZ at a total flow rate of 19,856 ton hr^{-1}. The CO_2 rich solution exiting the absorber, which had a CO_2 loading equivalent to a CTB conversion ratio of 45%, was separated into two streams: one (81.8%) went through the cross heat exchanger and entered the crystallizers after mixing with the regenerated solvent from the stripper, and the other (18.2%) was mixed with $KHCO_3$ crystal particles collected from each of the crystallization tanks (a total of 3,581 ton hr^{-1}) to produce a slurry (PCB 60-79) used for CO_2 stripping. Cooling water was required to cool down the temperature

of the last crystallizer. The mother liquor (PCB 40-20 with 0.47 M PZ) from the crystallization process returned to the absorber after its temperature was increased to 60 to 70°C via heat exchange with each of the crystallization tanks.

The residence time in the crystallizers (i.e., equipment size) and the size of crystal particles are the critical parameters in the design of crystallizers and crystal separators. The size of crystal particles depends on the nucleation and crystal growth performance. Based on Eq. (3-13), the mass median size (L_M) was estimated by Eq. (3-22) assuming a log normal particle size distribution with a geometric standard deviation (σ_g) of 1.47 obtained by averaging over all the measured CSD data:

$$L_M = \bar{L} e^{-0.5(\ln 1.47)^2} = 0.93\bar{L} \quad (3\text{-}22)$$

In this regard, the mass fraction of each size fraction could be known. Moreover, the solid concentration of the suspension (M_T) was determined according to

$$M_T = \frac{F_1 \times \tau}{V} = \frac{F_1 \times \rho}{F} \quad (3\text{-}23)$$

where V is the total volume of all the crystallizers (m^3), F_1 is the discharge rate of $KHCO_3$ solids in the outflow slurry (kg s^{-1}), ρ is the density of the suspension (kg m^{-3}) and F is the flow rate of the feed solution (kg s^{-1}).

The presence of PZ in the PCB solution affected both the relative supersaturation level and the solid concentration of the slurry. A regression equation was applied to account for this effect (R^2 = 0.88):

$$\frac{\sigma_1}{\sigma_0} = 1.22[PZ]^{0.04} \quad (3\text{-}24)$$

where [PZ] is the molar concentration of PZ (molecular PZ equivalent).

For practical purposes, a hydrocyclone is considered a low cost option for separating crystal solids from the slurry. The grade efficiency of solid-liquid separation is a quadratic function of the particle size (Licht, 1988). A mean overall crystal size of 80 μm was adopted as a design criterion for all the crystallizers, assuming the newly formed nuclei grew to a certain size (29.5 μm) and the remaining content of new solids were grown on the surfaces of existing seed

particles. The efficiency of separating crystal particles with a mean diameter of 80 μm by a hydrocyclone was assumed to be 100% (Hsieh and Rajamani, 1991; Monredon et al., 1992). When necessary, a portion of the separated solids was recycled to the crystallizer to maintain a desired seed concentration (i.e., 10 wt%). Crystal growth could be accelerated with increasing solid concentrations in the suspension. At a low seed concentration, newly formed nuclei contributed to the crystallization; whereas, crystal growth on existing seed particles became dominant at a high seed concentration (Chivate et al., 1979; Kubota et al., 2001). In the Hot CAP, the solid concentration was high enough that the latter mechanism prevailed. The criterion size of 80 μm was used to obtain a preliminary estimate of the required mean residence time and volume of each crystallizer based on Eqs. (3-13), (3-22) and (3-23).

Table 3-4. Design parameters for crystallization in five tanks operated in sequence.

Unit No.	Feed solution				Crystallization				
	Composition (with seeds)	Flow rate (+seeds, t h^{-1})	Temperature (°C)	Density (kg m^{-3})	Temperature (°C)	Relative super saturation	Solid flow rate[a] (t h^{-1})	Solid conc. (kg m^{-3})	Agitation speed (rpm)
PZ (622t hr^{-1}) present in the CO_2 rich PCB solution									
1	PCB 45-36.6/PZ	22,885+1,689	70 to 80	1,330	60	0.169	1,321	126.3	350
2	PCB 43.8-33.1/PZ	22,117+1,774	60	1,320	55	0.156	615	125.4	350
3	PCB 42.9-30.0/PZ	21,502+1,721	55	1,310	50	0.180	601	124.4	350
4	PCB 41.9-26.7/PZ	20,901+1,689	50	1,300	45	0.206	570	123.5	350
5	PCB 40.9-23.2/PZ	20,331+1,734	45	1,290	40	0.206	472	122.5	350
PZ absent in the CO_2 rich PCB solution									
1	PCB 45-36.6	22,263+1,733	70 to 80	1,330	60	0.143	1,219	126.3	350
2	PCB 44-33.6	21,597+1,693	60	1,320	55	0.158	634	125.3	350
3	PCB 43-30.4	20,963+1,658	55	1,310	50	0.177	604	124.4	350
4	PCB 42-27.1	20,359+1,622	50	1,300	45	0.203	576	123.5	350
5	PCB 41-23.6	19,784+1,587	45	1,290	38	0.240	550	122.5	350

[a] 95 wt% $KHCO_3$, 1 wt% K_2CO_3 and 4 wt% H_2O were assumed.

Table 3-5. Predicted crystallization performance in each crystallizer without/with PZ present.

Unit no.	Effective growth rate $G_m \times 10^8$ (m s^{-1})	Average growth rate $G_{av} \times 10^8$ (m s^{-1})[a]	Total nucleation rate $B_{TOT} \times 10^{-8}$ (s^{-1} m^{-3})	Residence time τ (s)	Crystallizer volume V (m^3)
1	8.57/7.97	7.45/6.89	3.09/1.33	100/108	501/555
2	7.27/6.84	6.32/5.92	2.24/1.25	118/126	578/633
3	6.18/6.59	5.37/5.70	1.62/1.10	139/131	666/644
4	5.28/6.31	4.59/5.46	1.15/0.97	162/137	763/660
5	4.09/5.58	3.56/4.83	0.69/0.89	210/154	965/734

[a] L_m was assumed to be 1,000 μm as a conservative estimate.

A preliminary design analysis was performed to size the crystallizers for the Hot CAP integrated to a 550 MWe (net output) coal fired power plant with a CO_2 removal rate of 598 ton hr^{-1} (3 and

10 wt% working capacity for CO_2 absorption and desorption, respectively). The process conditions are summarized in Table 3-4, and results of the design analyses are presented in Table 3-5 and Fig. 3-12. When PZ was present in the PCB solution, the total slurry flow was estimated at 3,579 ton hr^{-1} (95% $KHCO_3$, 1% K_2CO_3 and 4% H_2O), and the total volume and mean residence time of all the crystallizers were predicted to be 3,226 m^3 and 10.9 min, respectively, compared with 3,473 m^3 and 12.1 min when PZ was absent. The volume of each crystallizer (or mean residence time) was similar when PZ was added, which was beneficial for the crystallization process. The above estimation was conservative, because the solid concentration in the suspension could be increased above 10 wt% to enhance the seeding effect and thus the crystal growth could be accelerated further. As a result, the required mean residence time or the volume of each crystallizer would be reduced.

While the Hot CAP was developed to overcome the energy use disadvantages associated with the conventional PCC technologies, the crystallization step would result in an increase of liquid residence time and thus incur additional space and land use requirements for CO_2 capture.

3.5 Conclusions

Crystallization of $KHCO_3$ from a CO_2 rich PCB solution (40 wt%) enables the $KHCO_3$ rich slurry to be used for CO_2 desorption at an elevated stripping pressure to reduce the energy use for CO_2 capture. In this chapter, parametric experiments were conducted using an MSMPR reactor to investigate the CSD and kinetic performance of $KHCO_3$ crystallization under the simulated process conditions. The crystal growth rate was size dependent, increasing with increasing particle size and leveling off when a critical size was reached (600 μm). The crystallization of $KHCO_3$ was fast and could be completed within a mean residence time of 15 min. A longer mean residence time decreased the overall rates of both nucleation and crystal growth but resulted in the formation of larger crystal particles. An increase in agitation speed enhanced the nucleation process but slowed the crystal growth, which resulted in an overall reduction in crystal size. A higher supersaturation level favored the crystal growth and formation of larger particles. The effect of the presence of PZ in the PCB solution on the crystallization kinetics also was evaluated. A three parameter, size dependent crystal growth model was

developed to describe the rates of crystal growth and nucleation and to predict the mean crystal size. The model was applied to perform a preliminary analysis of the crystallizer design for the CO_2 capture process, and a total crystallizer volume of 3,226 m^3 in the presence of PZ was identified in a conservative process case.

CHAPTER 4: SCREENING AND EVALUATION OF NOVEL BIPHASIC SOLVENTS FOR ENERGY EFFICIENT POSTCOMBUSTION CO_2 CAPTURE

4.1 Introduction

The hot carbonate absorption process coupled with a liquid-solid phase transition (crystallization of bicarbonate) reported in the previous chapter is a promising technical option to replace the conventional MEA process. However, operational issues associated with slurry handling exist as the major drawback of this process. As another variant of the phase transitional processes, the liquid-liquid phase change process, or the BiCAP, has been gaining interest. The BiCAP features a LLPS of the solvent upon CO_2 loading. Only the CO_2 rich phase is used for CO_2 stripping, thus reducing the amount of solvent required for regeneration and facilitating the attainment of a high stripping pressure. As a result, both the heat use for CO_2 stripping and the CO_2 compression work required to deliver CO_2 to a storage site can be reduced.

Several studies on biphasic solvents and the enabled processes have been reported in the literature. Researchers from the IFPEN (Rueil-Malmaison, France) investigated a class of undisclosed DMX^{TM} solvents that can form two liquid phases during CO_2 absorption (Aleixo et al., 2011; Raynal et al., 2011a; Raynal et al., 2011b). Researchers from a German team (Zhang et al., 2011a; Zhang et al., 2011b; Zhang et al., 2011c; Zhang et al., 2012a, b; Zhang et al., 2013) tested a series of solvents that blended lipophilic DMCA with DPA or CHxMA. When heated to 60 to 80°C, the CO_2 laden solvents exhibited a thermally induced biphasic transition. The researchers proposed a multistage extraction process configuration that applied an inert alkyl solvent to extract the unreacted amines in the aqueous phase; thus, the regeneration reactions of the carbamate and bicarbonate species were facilitated. A group of Norwegian researchers (Arshad et al., 2013a; Ciftja et al., 2013b; Hartono et al., 2013) conducted quantitative speciation analyses, and VLE and absorption heat measurements for a solvent blend of 2 M MAPA and 5 M DEEA that could form dual phases after CO_2 was loaded. Studies on CO_2 absorption and speciation analyses were conducted for a similar biphasic solvent, a blend of 2 M BDA and 4 M DEEA (Xu et al., 2013a, b). A “self concentrating” phase transitional process was investigated

by Hu (2009) using a partially miscible solvent consisting of alamines as typical activators of absorption rate and isooctanol as an extractive agent.

Although most of these studies have been focused on the absorption performance of biphasic solvents, their desorption performance and related phase equilibrium behavior have seldom been reported. In addition, the relationships between the characteristic structures of solvents and their performance for PCC have not been identified systematically. Therefore, research efforts to screen biphasic solvents and elaborate on the relationships between solvent structure and performance are necessary to identify desirable biphasic solvents and develop an energy efficient BiCAP for PCC.

The biphasic solvents investigated in this study are a class of ternary solvent systems (A-B-H_2O), which can be either homogenous or heterogeneous. Component A possesses at least one primary (–NH_2) or secondary (–NH) amino group, which functions as an absorption accelerator. Component B has a tertiary (–N) amino group, which provides extra CO_2 loading capacity as an absorption sink and serves as a regeneration promoter. Such solvent blends can exhibit both rapid absorption rates and large CO_2 uptake based on a "shuttle mechanism" (Astarita et al., 1981; Rangwala et al., 1992; Zhang et al., 2013). The schematic diagram of the proposed BiCAP is illustrated in Fig. 2-2. In this process, CO_2 in the flue gas is absorbed into a solvent at 40 to 50°C, during which the solvent undergoes a phase transition to form dual liquid phases. The two liquid phases are separated in a downstream phase separation unit. The resultant CO_2 rich phase is preheated in a cross heat exchanger by the hot regenerated solution from the stripper, and fed to the stripper operated at 80 to 120°C. The regenerated solution from the stripper, as well as the CO_2 lean phase obtained from the phase separation unit, are mixed and recycled to the absorber.

In this study, 24 amine (or amine analog) based A compounds with various structural configurations and 2 B compounds, i.e., DMCA and DEEA, which have been identified in the literature as attractive CO_2 absorption sinks, were selected to formulate various blended solvents for screening purposes. Laboratory experiments were conducted to investigate the absorption and desorption performance of the formulated solvents. The results were examined to elucidate the relationships between solvent performance and important structural factors, such as the carbon

chain length, the numeric ratio of N to C atoms, and molecular conformation (e.g., linear, branched, cyclic or heterocyclic) of the solvent components. A couple of solvents were identified as favorable for use in the BiCAP based on the overall performance of their phase transition behavior, absorption kinetics, CO_2 loading capacity and attainable CO_2 desorption pressure under the selected test conditions.

4.2 Material and methods

4.2.1 Selection of solvent components

Twenty four amines or amine analogs representing different types of molecular structures were selected as component A based on their boiling points (BP, >100°C), saturated vapor pressures (VP, <10 mm Hg at 20°C unless specified otherwise) and commercial availability (including cost). Two amines, i.e., hydrophobic DMCA (BP = 160°C, VP = 3.6 mm Hg) and hydrophilic DEEA (BP = 161°C, VP = 1 mm Hg), were selected as component B. Alkanolamines were excluded from the list of component A because no firm evidence exists that a hydroxyl group (–OH) as a potential electron acceptor to a neighboring amino group in alkanolamines can enhance their absorption performance (Singh et al., 2007, 2009). However, alkanolamines (e.g., DEEA) can be used as component B because they are soluble in water and have high boiling points owing to the H bonds, which can improve solvent regenerability. Additionally, aromatic amines (unsaturated cyclic amines) were excluded as candidates of either A or B because of their poor capacities for CO_2 absorption (Singh et al., 2009).

The selected A compounds were categorized into seven groups according to their structural configurations (Table 4-1). An individual A compound was blended with a B compound (either DMCA or DEEA) to form a candidate aqueous solvent. The blend of components A and B is referred to hereafter as A-B. For example, the blend of pentylamine (PtA) and DMCA is abbreviated as PtA-DMCA. For comparison purposes, a 30 wt% MEA solution was tested as a baseline, and aqueous solutions of neat DMCA and neat DEEA were tested as controls.

Table 4-1. Structures and basic properties of the selected A compounds.

Structural configuration	Compound	Abbreviation	Structural formula	Boiling point (°C)	Vapor pressure (mmHg)
Linear aliphatic primary monoamine	Pentylamine	PtA	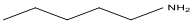	104	34.9 (26°C)
	Hexylamine	HxA	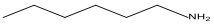	132	8
	Heptylamine	HtA	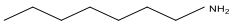	155	2.7 (25°C)
	2-heptylamine	2-HtA	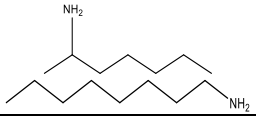	143	4.9 (25°C)
	Octylamine	OtA		176	1
Linear aliphatic secondary monoamine	Dipropylamine	DPA	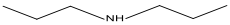	110	20.1 (25°C)
	Dibutylamine	DBA	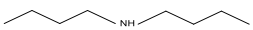	159	1.9
	Dihexylamine	DHA	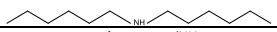	236	0.038
Saturated cyclic primary monoamine	Cyclohexyl-amine	CHxA	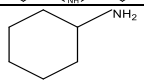	134	10 (22°C)
	Cycloheptyl-amine	CHtA	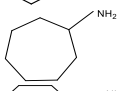	148 (estimated[a])	3 to 10 (estimated)
	Cyclooctyl-amine	COtA	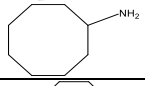	190	0.27
Saturated cyclic/ heterocyclic secondary monoamine	Hexamethylene-imine	HxMI		138[b] (749 mmHg)	7.4 (21.1°C)
	Methylcyclo-hexylamine	CHxMA	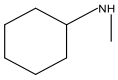	149	11 (40°C)
	Dicyclohexyl-amine	DCHxA	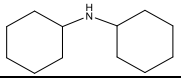	256	12 (37.7°C)
Linear diamine	1,4-butanediamine	BDA	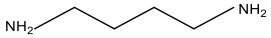	159	2.3 (25°C)
	Hexamethylene-diamine	HxDA	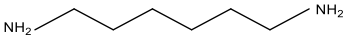	205	0.12 (25°C)
	1,8-diaminooctane	OtDA	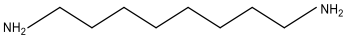	226	NA[c]
Linear polyamine	Diethylenetriamine	DETA	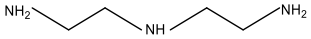	204	0.08
	Dipropylenetriamine	DPTA	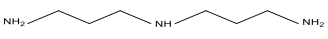	228 (estimated[a])	NA
	Triethylenetetramine	TETA	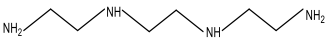	267	<0.01
	Tetraethylene-pentamine	TEPA	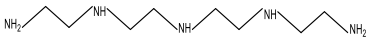	340	<0.01
	Pentaethylene-hexamine	PEHA		NA	NA
Saturated heterocyclic polyamine	1-(2-aminoethyl)-piperazine	AePZ	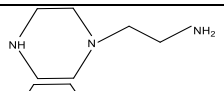	222	0.05
	4-(2-aminoethyl)-morpholine	AeML	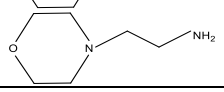	227[b] (757 mmHg)	NA

[a] Boiling point data were estimated based on a group contribution method (Stein and Brown, 1994).
[b] Boiling point data are reported at 760 mm Hg if the pressure is not otherwise specified in parentheses.
[c] NA: not available.

4.2.2 Testing of CO_2 absorption

Absorption of CO_2 into the solvents was tested by using a laboratory bubbling column (150 mL) for rapid screening purposes. A flow diagram of the experimental setup is shown in Fig. 4-1. In a typical test, 100 g of an aqueous solvent was prepared freshly in the column. Pure CO_2 at a flow rate of 105 mL min^{-1} controlled with a rotameter was bubbled through the column at atmospheric pressure for 90 min. The column was placed in an isothermal water bath at 30°C, and samples (0.5 to 1 mL) were collected at 5, 10, 20, 40, 60 and 90 min after the test began. The density of each sample was determined based on the measured volume and mass, and the CO_2 loading of the sample was determined by titration with a 2 mol L^{-1} hydrochloric acid (HCl) solution in a Chittick apparatus. If dual liquid phases were formed, the measurement of CO_2 loading was conducted for both phases, and the volumetric ratio was recorded. The overall absorption rate at each sampling time was estimated by the measured change in total CO_2 loading. To simplify the screening tests, pure CO_2 at atmospheric pressure was used rather than a simulated flue gas (i.e., containing 10 to 14% CO_2). The total solvent concentration used in the tests was kept at 5 mol kg^{-1} (including the control tests with aqueous solutions of neat DMCA and neat DEEA), a level similar to the 30 wt% MEA. The molar ratio of A to B was kept at 3:7 for all the solvents. The concentration of component A was high to increase the absorption rate and facilitate comparison of rates among the solvents. The composition of each phase for the selected biphasic solvent was determined by ^{13}C NMR spectroscopy (Varian Unity Inova spectrometer) at a spectral frequency of 100.575 MHz.

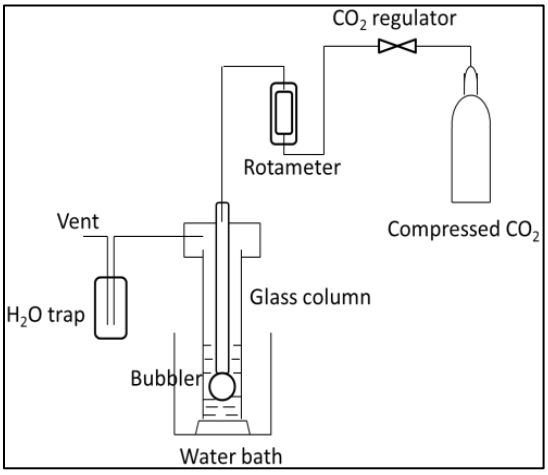

Fig. 4-1. Schematic diagram of the CO_2 bubbling absorption setup.

4.2.3 Testing of CO_2 desorption

Desorption of CO_2 from the CO_2 loaded solvents was investigated by using a 0.5 L high pressure Parr reactor (Model 4560, Parr Instrument Company) (Fig. 4-2). The reactor was placed in a thermostat controlled water bath. For screening purposes, desorption tests were conducted at 80°C. The as obtained, single phase solvents from the 90 min absorption tests described above were used directly in the desorption tests. For the as obtained solvents with two liquid phases from the 90 min absorption tests, the two phases were separated and only the CO_2 rich phase was used for the desorption test. When a polyamine DETA, triethylenetetramine (TETA), tetraethylenepentamine (TEPA) or pentaethylenehexamine (PEHA) was used as compound A, the resultant solvent with a reduced A to B blending ratio of 1:4 was used to avoid high viscosity and prevent precipitation during the desorption test. The CO_2 loaded solvents with solid precipitates present were excluded from the desorption tests.

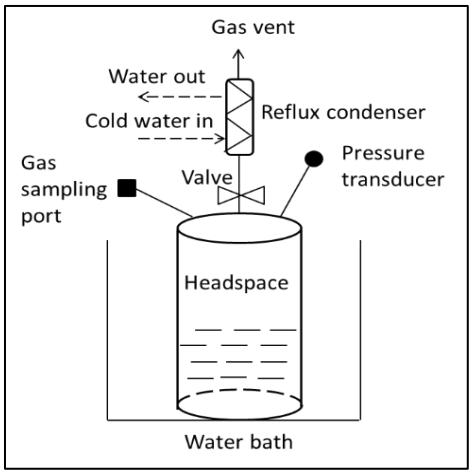

Fig. 4-2. Schematic diagram of the CO_2 desorption setup.

In a typical desorption test, the equilibrium pressures of CO_2 and water vapor were measured at three to five levels of CO_2 loading in a decreasing sequence. At the beginning of the test, the CO_2 rich solution or CO_2 rich phase was discharged to the reactor, and the headspace was filled by air. The reactor was sealed and incubated under the preset temperature until phase equilibrium was approached, as evidenced by a stable reading of the total pressure (P_{Total}) over time. The partial pressures of N_2 (P_{N2}) and O_2 (P_{O2}) at 80°C were estimated assuming ideal gas behavior. The gas sample was collected and the molar (pressure) ratio of CO_2 to N_2 was analyzed by gas chromatography (GC-2014, Shimadzu Corporation). The partial pressure of CO_2 (P_{CO2}) was

estimated based on the molar ratio of CO_2 to N_2 and the P_{N2}.The water vapor partial pressure (P_{H2O}) was calculated by subtracting the partial pressures of CO_2, N_2 and O_2 from the total pressure. The vapor pressure attributable to the amine based compounds was negligible compared with the P_{H2O} under the tested conditions. After the pressure in the reactor was released, the liquid sample was collected for analysis of CO_2 loading. The exhaust valve of the reactor was kept open to desorb the CO_2 and reduce the CO_2 loading in the solution. During the release of CO_2, a reflux condenser was connected to the reactor outlet to minimize the water vapor loss. When the CO_2 loading decreased to the next desired level, the reactor valve was closed and another measurement was conducted when the system reached equilibrium again. This procedure was repeated three to five times until the CO_2 equilibrium pressures at the required CO_2 loading levels were obtained.

4.3 Results and discussion

4.3.1 CO_2 absorption

The measured changes in total CO_2 loading (in all phases if more than one) over the reaction time were used to assess the kinetics of CO_2 absorption into different solvents. The observed difference in performance was explained qualitatively below based on the characteristic structures of different solvent components.

4.3.1.1 Monoamines as component A

Fourteen monoamines (C5 to C12) were tested as component A. PtA, hexylamine (HxA), heptylamine (HtA), 2-heptylamine (2-HtA) and octylamine (OtA) are linear aliphatic primary amines (C5 to C8). 2-heptylamine is an isomer of HtA and has an amino branch on C2. DPA (an isomer of HxA), dibutylamine (DBA, an isomer of OtA) and dihexylamine (DHA) are linear aliphatic secondary amines, with two symmetrical C3, C4 and C6 linear alkyl substituents, respectively. Cyclohexylamine (CHxA), cycloheptylamine (CHtA) and cyclooctylamine (COtA) are C6 to C8 saturated cyclic primary amines.

Hexamethyleneimine (HxMI, an isomer of CHxA) is a heterocyclic secondary amine. CHxMA (an isomer of CHtA) and dicyclohexylamine (DCHxA) are cyclic secondary amines that have a

methyl ($–CH_3$) and a hexamethylene ($–C_6H_{11}$) substituent, respectively, attached to the amino H on CHxA. The results of absorption kinetics for the monoamine + DMCA or DEEA aqueous solvents, and the aqueous solvents of neat DMCA and neat DEEA are shown in Fig. 4-3.

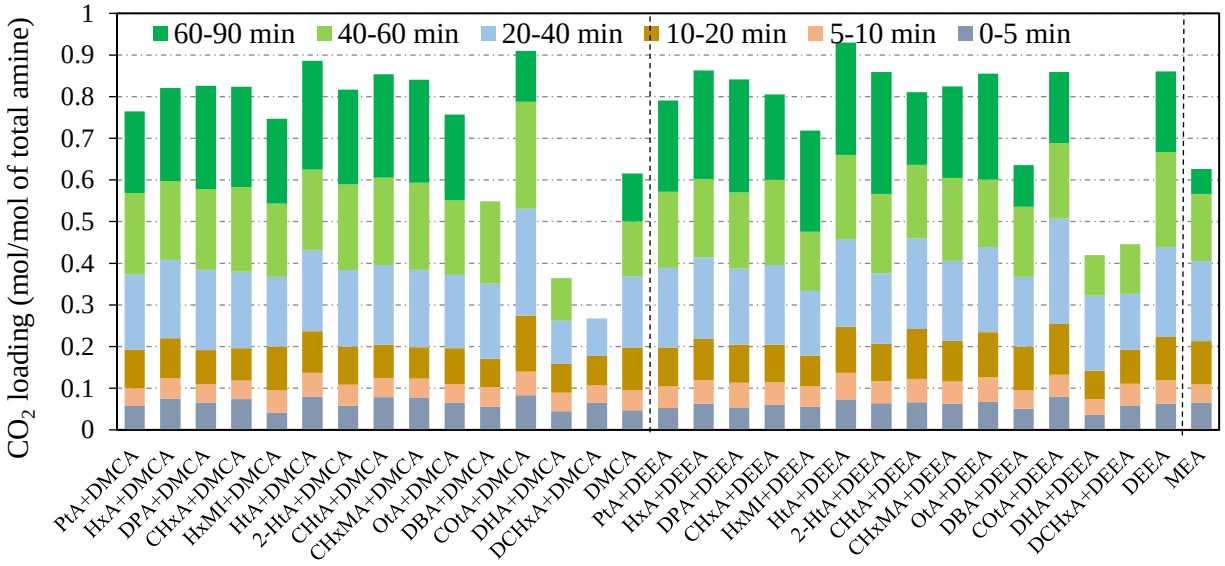

Fig. 4-3. Kinetic performance of CO_2 absorption into aqueous solvents blending the monoamines (PtA, HxA, DPA, HtA, 2-HtA, OtA, DBA and DHA with linear chain structures, and CHxA, HxMI, CHtA, CHxMA, COtA and DCHxA with cyclic structures) as component A and DMCA or DEEA as component B. Data for the aqueous solutions of neat DMCA and neat DEEA were included for comparison purposes. The CO_2 loading accumulated over the reaction time. Missing data indicate the occurrence of solid precipitates. For solvent abbreviations, see Table 4-1.

As tertiary amines, DMCA and DEEA have higher capacities of CO_2 absorption than do the primary or secondary amines. The rate of CO_2 absorption into the aqueous solution of neat DEEA (5 mol kg^{-1}) was observed to be comparable with or higher than those of most monoamine + DEEA blends with the same total concentration; whereas, the rate into the aqueous solution of neat DMCA (5 mol kg^{-1}) was lower than those of most monoamine + DMCA blends. DEEA is miscible in water and DMCA is immiscible because they have distinct hydrophobicities. Thus, the lower rate into the neat DMCA aqueous solution than that into its DEEA counterpart was because the reaction process between hydrophobic DMCA and dissolved CO_2 in the aqueous phase involved diffusion of the reactants toward the interface of the dual liquid phases and the reaction products from the interface.

Despite the aforementioned difference between the neat DMCA and neat DEEA solutions, their blends with the same A component exhibited similar absorption performance regardless of the type of A used. As the total number of C atoms in component A increased (5 to 12), the attained CO_2 loading of the solvent blend peaked for A with 7 C and declined, irrespective of whether A had a linear or cyclic structure. The solvent blends containing larger A molecules (e.g., C>8) showed lower absorption rates and formed gel like solids that were insoluble up to 60°C (e.g., DCHxA and DHA).

The solvent blends containing cyclic amines as component A did not exhibit superior absorption performance compared with those containing linear amines with the same number of C atoms. The solvent blend containing COtA as component A was an exception and showed comparable or higher CO_2 loading than did those containing DBA or OtA. The reason was that the carbamate species produced from the reaction between COtA and CO_2 was unstable and rapidly dissociated to form HCO_3^- due to the steric hindrance effect induced by the α-carbon attached to the amino group in the large (C8) ring structure, thus enhancing CO_2 absorption. In addition, CO_2 absorption into a solvent blend containing component A as a secondary amine, an amine with a side NH_2 group, or an amine with a large ring or linear alkyl substitute underperformed compared with CO_2 absorption into a solvent blend containing component A as a primary amine isomer to the secondary amine, an amine with a linear NH_2 chain, or an amine without a large substitute, respectively.

4.3.1.2 Polyamines as component A

Ten polyamines were examined as component A in the absorption tests. 1,4-diaminobutane (BDA), hexamethylenediamine (HxDA) and 1,8-diaminooctane (OtDA) are linear aliphatic diamines with one primary amino group at each end of their chain structures. DETA (C4N3), dipropylenetriamine (DPTA, C6N3), TETA (C6N4), TEPA (C8N5) and PEHA (C10N6) are polyamines, each assembled by alternating one –NH and a certain number of $–CH_2–$ groups to form a linear chain structure with $–NH_2$ attached to both ends of the chain.
1-(2-aminoethyl)piperazine (AePZ) and 4-(2-aminoethyl)morpholine (AeML) are heterocyclic polyamines with a substituent of an aminoethyl group ($–CH_2CH_2NH_2$) attached to piperazine and

morpholine, respectively. The results of CO_2 absorption into aqueous solvents consisting of a polyamine and DMCA or DEEA, as well as the aqueous solutions of neat DMCA and neat DEEA are shown in Fig. 4-4.

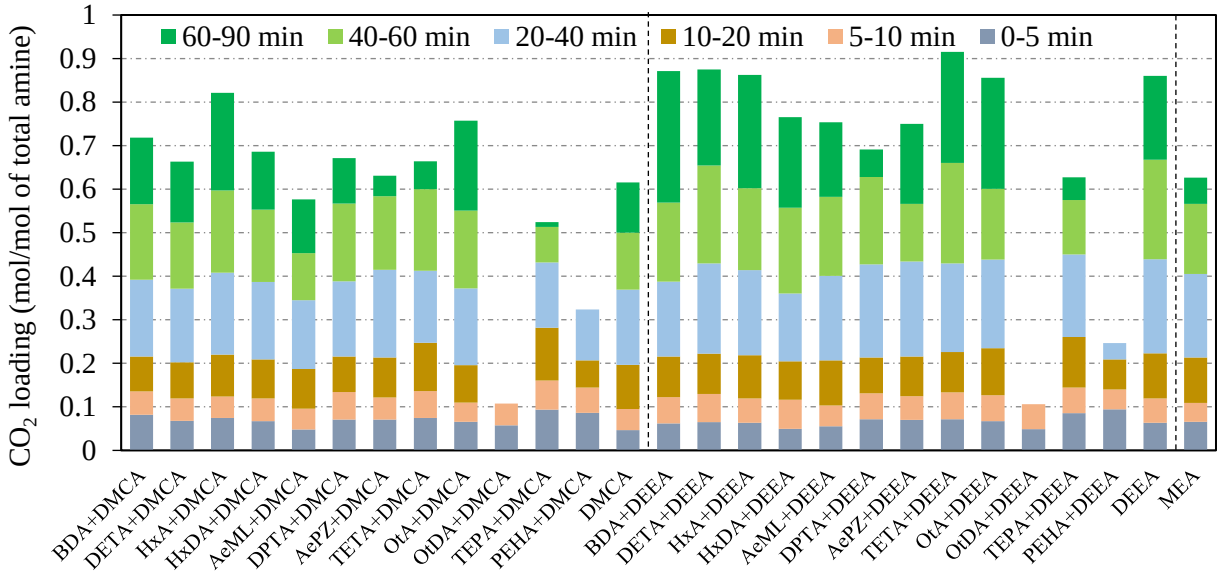

Fig. 4-4. Kinetic performance of CO_2 absorption into aqueous solvents blending a polyamine as component A and DMCA or DEEA as component B. Data for the aqueous solutions of neat DMCA and neat DEEA, and the solvent blends containing the monoamine HxA or OtA as component A were included for comparison purposes. The CO_2 loading accumulated over the reaction time. Missing data indicate the occurrence of solid precipitates. For solvent abbreviations, see Table 4-1.

The rates of absorption into most of the polyamine + DMCA aqueous solvents were faster than that into the immiscible aqueous solution of neat DMCA. In comparison, the rates of several polyamine + DEEA blends (e.g., TEPA + DEEA, AePZ + DEEA, DPTA + DEEA) that underwent phase transitions to form two phases during the absorption were lower than that into the homogeneous aqueous solution of neat DEEA. Although polyamines could enhance the absorption, the presence of a liquid-liquid interface would hinder the absorption.

The solvent blends containing either DMCA or DEEA as component B had a similar relationship between the absorption performance and the structure of component A. At the same absorption time, higher CO_2 capacities were observed for the DEEA based solvent blends than those of the

DMCA counterparts. This was due to their different phase transition behaviors (discussed in detail in Section 4.3.2). The hydrophobic DMCA molecules in the upper organic phase had to diffuse to the interface of dual liquid phases, where they could react with dissolved CO_2 molecules facilitated by component A in the lower aqueous phase. In comparison, DEEA molecules were present in a homogeneous phase and thus did not encounter transphase diffusion at the initial stage of CO_2 absorption before the dual phases were formed (Ciftja et al., 2013b).

When the molecules of component A (e.g., OtDA and PEHA) were large, the derived solvent blends were viscous and precipitation occurred upon CO_2 loading, resulting in poor CO_2 absorption performance. In addition, a polyamine A with a larger number of amino groups did not enhance the loading capacity of the derived solvent blends. For example, the solvent blends containing monoamine HxA or OtA as component A performed better than did those containing a polyamine with the same number of total C. Such a trend was different from what was observed for the aqueous solutions of neat polyamines (Singh et al., 2009). Three solvent blends consisting of DEEA as component B, and BDA (C4N2), DETA (C4N3) or TETA (C6N4) as component A demonstrated better absorption performance than did other blends of this type.

The CO_2 loading of 30 wt% MEA after absorption for 90 min under the same experimental conditions reached 0.63 mole of CO_2 per mole of MEA. In comparison, most of the tested solvent blends demonstrated higher levels of CO_2 loading. The aqueous solvents of DBA + DMCA, DHA + DMCA/DEEA, DCHxA + DMCA/DEEA, OtDA + DMCA/DEEA, AeML + DMCA, TEPA + DMCA and PEHA + DMCA/DEEA showed lower levels of CO_2 loading, and the solvents of CHxA + DMCA/DEEA and HxDA + DMCA incurred undesired solid precipitates during CO_2 absorption; thus, they were excluded from further desorption evaluation.

4.3.2 Phase transition behavior

As shown in Table 4-2, four different types of phase transition behavior were observed for the tested solvent blends. Type 1 solvents did not undergo a phase separation. Type 2 solvents underwent a transition from two immiscible phases initially to a single phase after a critical CO_2 loading was reached in 5 to 20 min. Type 3 solvents maintained two immiscible phases throughout the absorption tests. Type 4 solvents exhibited a single phase initially that was

converted to two liquid phases after CO_2 absorption for 5 to 20 min. For Types 3 and 4 solvents, most of the loaded CO_2 was accumulated in the lower aqueous phase. Representative photographs of Types 3 and 4 solvents before and after CO_2 loading are shown in Fig. 4-5.

Table 4-2. Different phase transition phenomena observed for the tested solvent blends.

Type	Description[b]	Solvent composition[a] Component A	Component B
1	1 phase at t_0 → 1 phase at t_{90}	PtA, HxA, HtA, 2-HtA, OtA, DPA, DBA, CHtA, COtA, CHxMA, BDA, HxDA, HxMI, AeML	DEEA
2	2 phases at t_0 → 1 phase at $t_{5\text{-}20}$ → 1 phase at t_{90}	PtA, HxA, HtA, 2-HtA, OtA, DPA, CHtA, COtA, HxMI, CHxMA	DMCA
3	2 phases at t_0 → 2 phases at t_{90}	BDA, DETA, DPTA, TETA, AePZ	DMCA
4	1 phase at t_0 → 2 phases at $t_{5\text{-}20}$ → 2 phases at t_{90}	DETA, DPTA, TETA, TEPA, AePZ	DEEA

[a] See Table 4-1 for solvent abbreviations.
[b] t_0 represents the beginning of an absorption test, $t_{5\text{-}20}$ represents 5 to 20 min after the absorption began and t_{90} represents the end of the absorption test (90 min).

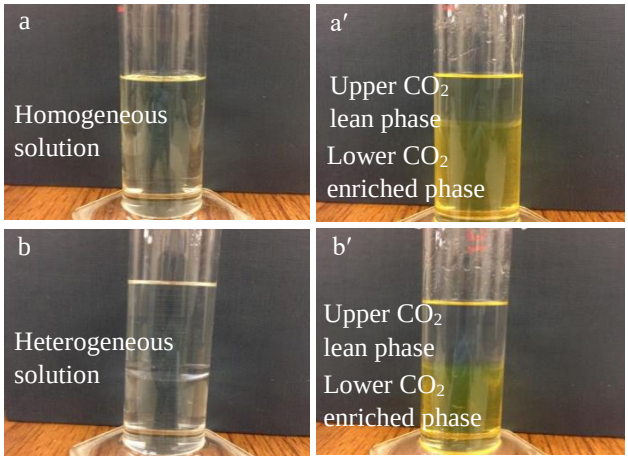

Fig. 4-5. Photographs of a Type 4 solvent blend of PEHA + DEEA (5 mol kg^{-1}, 1:4) (a) before and (a') after 90 min of CO_2 loading (2.83 mol L^{-1}) with the dominant presence of the absorbed CO_2 in the lower phase (3.93 mol L^{-1}, 67.8 vol%), and a Type 3 solvent blend of TEPA + DMCA (5 mol kg^{-1}, 1:4) (b) before and (b′) after 90 min of CO_2 loading (2.68 mol L^{-1}) with the dominant presence of the absorbed CO_2 in the lower phase (4.73 mol L^{-1}, 55.5 vol%). The absorption tests were conducted at 30°C and ambient pressure with pure CO_2.

Distributions of CO_2 in the lean and rich phases for Types 3 and 4 solvents after CO_2 absorption for 60 and 90 min are summarized in Table 4-3. Compared with the aqueous solvent of neat

DEEA or neat DMCA, the presence of a component A improved the phase separation behavior. Volumetric portions of the lower phases for all the Types 3 and 4 solvents increased over the time of CO_2 absorption. For Type 3 solvents, the lower phases shared up to 80% of the total solvent volume after 90 min of absorption. In comparison, the lower phases of Type 4 solvents possessed larger volumetric portions. A biphasic solvent blend that can form a phase with a concentrated CO_2 loading and a proper volumetric portion is desired for the BiCAP.

Table 4-3. CO_2 loading levels (mol/L) and volumetric portions (%) of upper (u.p.) and lower (l.p.) liquid phases for Type 3 and 4 solvents after CO_2 absorption for 60 and 90 min.

Category	Component A[a]	Before absorption	After 60 min of absorption				After 90 min of absorption			
		l.p. vol. (%)	l.p. vol. (%)	l.p. loading	u.p. loading	Total loading	l.p. vol. (%)	l.p. loading	u.p. loading	Total loading
Type 3 (DMCA based)	BDA	47.7	62.3	4.10	0.22	2.64	76.3	4.33	0.18	3.35
	DETA	48.0	55.9	4.14	0.13	2.37	68.0	4.38	0.11	3.01
	DPTA	48.5	55.6	4.53	0.12	2.57	64.2	4.74	0.09	3.07
	TETA	49.2	56.2	4.56	0.39	2.73	60.0	4.87	0.36	3.07
	AePZ	48.9	65.0	3.95	0.21	2.64	70.8	4.03	0.18	2.91
	None	25.0	69.1	3.36	0.16	2.37	77.4	3.71	0.13	2.90
Type 4 (DEEA based)	DETA	0	76.3	3.91	0.45	3.09	98.1	4.18	0.42	4.11
	DPTA	0	69.8	3.98	0.66	2.98	88.0	3.72	0.49	3.33
	TETA	0	62.1	4.58	0.86	3.17	88.0	4.88	0.71	4.38
	TEPA	0	58.2	3.99	0.98	2.73	65.1	4.16	0.93	3.03
	AePZ	0	89.7	3.04	0.46	2.77	95.7	3.82	0.38	3.67

[a] See Table 4-1 for solvent definitions.

The selected A compounds contained at least one hydrophilic functional group, i.e., $–NH_2$ or –NH, and were soluble in water. Thus, it was not surprising to see an immiscible aqueous solution composed of a hydrophilic A component and lipophilic DMCA, or a miscible aqueous solution composed of a hydrophilic A component and hydrophilic DEEA. Upon CO_2 loading, new ionic species (carbamates, bicarbonates and protonated amines) with different levels of aqueous solubility were formed and a phase change occurred.

A qualitative one dimensional (1D) ^{13}C NMR analysis was performed to identify the species in both phases for two selected aqueous biphasic solvents, i.e., DPTA + DEEA and DPTA + DMCA, and the aqueous solutions of their neat components. The nonequivalent C atoms of DPTA, DEEA and DMCA are labeled as 1 to 12 in Fig. 4-6. The NMR spectra for the neat DPTA, DEEA and DMCA solutions are shown in Fig. 4-6a. The reaction products between

DEEA and CO_2 were HCO_3^-/CO_3^{2-} species as indicated by the chemical shift from 161 to 162 ppm shown on the horizontal axis. The DMCA solution formed two phases upon CO_2 loading, with the lower phase possessing a pattern similar to that of DEEA and the upper phase containing pure DMCA. The reaction products between DPTA and CO_2 were complicated because DPTA has multiple amino groups. The peaks at chemical shifts of 42 to 46 ppm, 36 to 39 ppm and 25 to 29 ppm correspond to C12, C10 and C11, respectively. The peaks at chemical shifts of 162 to 165 ppm are C signals for carbamate and HCO_3^-/CO_3^{2-} species. Based on the NMR spectra, for the aqueous solvent of either DPTA + DMCA or DPTA + DEEA, the lower phase was CO_2 rich because the carbamate species of DPTA and HCO_3^-/CO_3^{2-} were partitioned into this phase. The upper CO_2 lean phase was dominated by DEEA or DMCA molecules. The chemical shifts of C atoms for the reacted solvents drifted from those for the unreacted species due to a different electron shield for each C. Because the NMR analysis was for qualitative purposes, no further exploration (e.g., 2D NMR) of individual peaks was attempted.

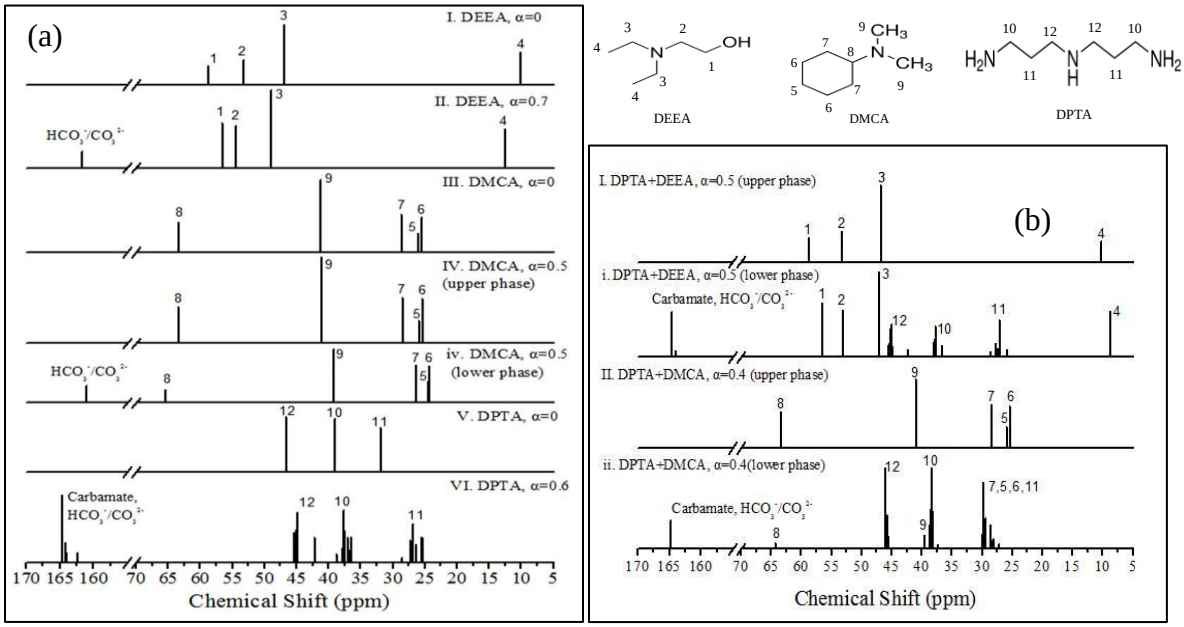

Fig. 4-6. ^{13}C NMR spectra of (a) aqueous solutions of 5 mol kg^{-1} neat DEEA, neat DMCA and neat DPTA before and after CO_2 loading and (b) solvent blends of 5 mol kg^{-1} (3:7) DPTA + DEEA and DPTA + DMCA after CO_2 loading. α denotes CO_2 loading (mole of CO_2 per mole of total amines). The peak heights were scaled from the NMR analysis results.

The molar ratio of A to B and the total concentration of A and B imposed a fundamental effect on the phase transition behavior by affecting their relative portions partitioned into the two phases. For example, phase separation was not observed throughout the absorption of CO_2 into a 1.5 mol kg^{-1} BDA + 3.5 mol kg^{-1} DEEA solvent blend under the test conditions. However, it was reported that phase separation occurred for a 2 M BDA + 4 M DEEA solvent blend (Xu et al., 2013a, b).

4.3.3 CO_2 desorption

The approach of phase equilibrium measurement was verified by the agreement between the measured equilibrium CO_2 pressures and the reported data (Shen and Li, 1992) for 30 wt% MEA solutions. The equilibrium pressures of CO_2 as a function of the relative CO_2 loading for most of the Types 1 and 2 solvent blends as well as the reference aqueous solvents of neat DEEA and neat DMCA are displayed in Fig. 4-7a and 4-7b. The relative CO_2 loading is defined as the CO_2 loading normalized by that attained at 30°C after 90 min of CO_2 absorption with pure CO_2 (Section 4.2.2). The DMCA based solvent blends demonstrated higher equilibrium pressures of CO_2 than did their DEEA counterparts. For solvents containing the linear aliphatic primary monoamines as component A (e.g., PtA, HxA, HtA, 2-HtA and OtA) and either DMCA or DEEA as component B, the equilibrium pressures of CO_2 increased initially with increasing chain length of component A before peaking at HtA (C7). The solvent blends containing the cyclic primary amines as component A (i.e., CHtA and COtA) did not perform better than their counterparts with the linear amines as component A (i.e., HtA and OtA). In addition, the solvent blends containing the secondary amines as component A exhibited lower equilibrium pressures of CO_2 than did those containing their primary amine isomers.

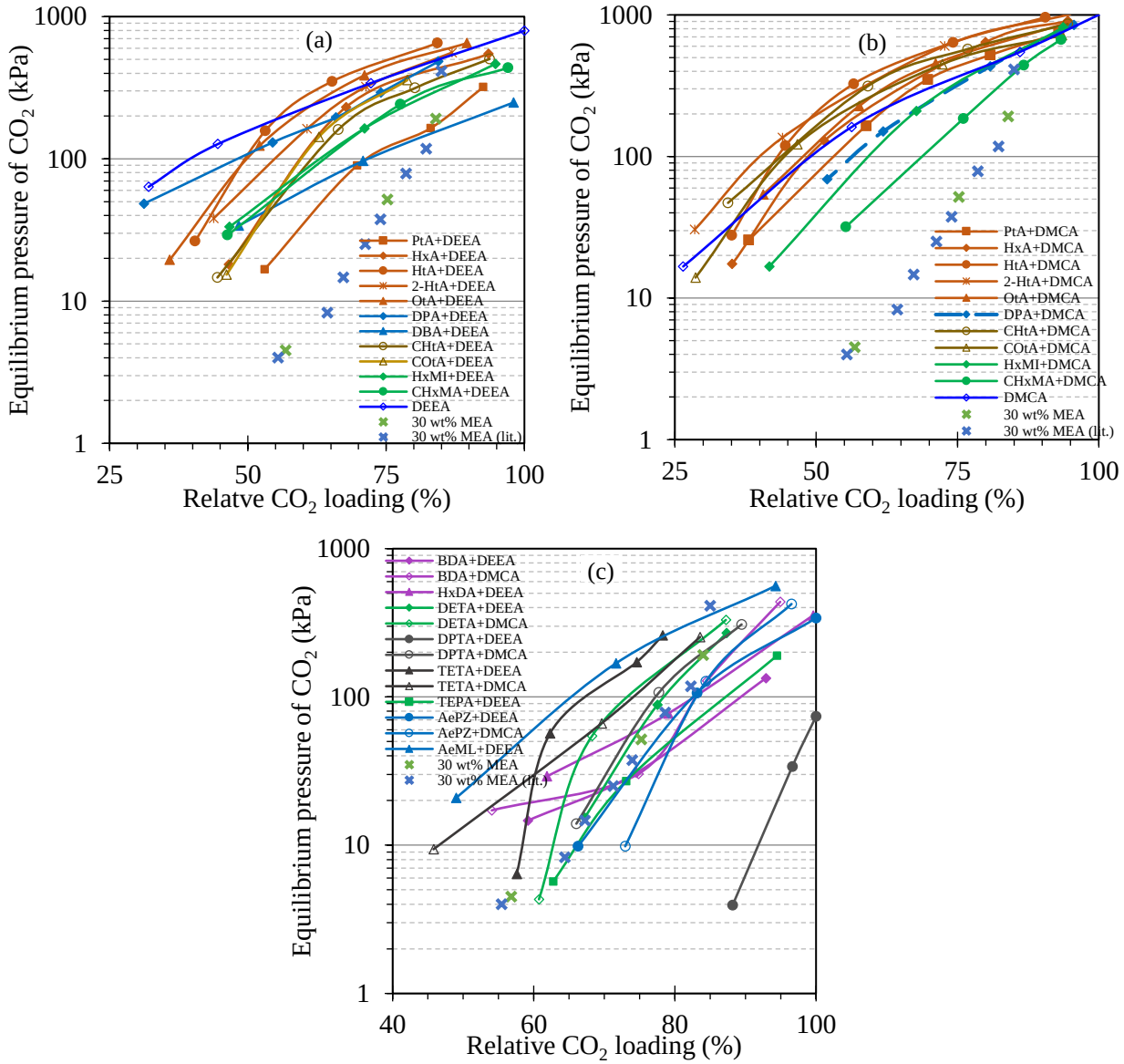

Fig. 4-7. Equilibrium pressures of CO_2 at 80°C over the selected solvents: (a) Type 1 solvents, (b) Type 2 solvents and (c) CO_2 rich phases of Types 3 and 4 solvents. Data measured for the aqueous solutions of neat DEEA and neat DMCA (5 mol kg^{-1}), and the measured and reported data for 30 wt% MEA are included for comparison purposes. For solvent abbreviations, see Table 4-1.

Types 3 and 4 solvents involved dual liquid phases. The equilibrium pressures of CO_2 over their CO_2 rich phases of interest for regeneration are displayed in Fig. 4-7c. The relative CO_2 loading in Fig. 4-7c was the amount of CO_2 loaded in the rich phase normalized by the total CO_2 uptake in this phase after 90 min of absorption under the conditions described in Section 4.2.2,

considering the upper phase was free of CO_2 as indicated from the NMR analysis. Similar to Types 1 and 2 solvents, the DMCA based Types 3 and 4 solvent blends possessed higher equilibrium CO_2 pressures than did their DEEA counterparts (except for TETA + DMCA). For the solvent blends consisting of a polyamine A, the equilibrium pressures of CO_2 were higher when the component A contained more amino groups [e.g., BDA (C4N2)<DETA (C4N3) and DPTA (C6N3)<TETA (C6N4)] or less $–CH_2–$ groups (e.g., DPTA<DETA). Compared with the 30 wt% MEA, half of the tested biphasic solvents demonstrated higher equilibrium CO_2 pressures at the similar relative CO_2 loading levels. The comparison of desorption pressures at 80°C was for preliminary solvent screening purposes; CO_2 desorption can operate at a temperature higher than 80°C in the BiCAP.

4.3.4 Discussion

According to results from the absorption and desorption tests described above, several biphasic solvents, such as DETA + DMCA, TETA + DMCA and TETA + DEEA, demonstrated both larger CO_2 absorption capacities and higher CO_2 desorption pressures compared with MEA. TETA + DEEA exhibited overall better performance than that of other solvents examined. The TETA + DEEA blend (5 mol kg^{-1}, 1:4) had a cyclic loading capacity, which was assumed equal to 40% of the highest CO_2 loading measured (0.92 mol mol^{-1}), 40% higher than that of MEA under the same absorption conditions, and demonstrated a higher reaction rate than did MEA (Fig. 4-4). This solvent blend displayed favorable phase transitional behavior, with the lower phase concentrated with the absorbed CO_2 and accounting for 60% of the total solvent volume in 60 min of absorption (Table 4-3). Moreover, the equilibrium pressures of CO_2 attained over TETA + DEEA were higher than those of MEA under the same conditions of relative CO_2 loading and desorption temperature (Fig. 4-7c), suggesting favorable VLE behavior for solvent regeneration and reduced downstream CO_2 compression work requirement. The energy use for the CO_2 stripping process consisted of three elements, i.e., heat of reaction, sensible heat and stripping heat. Compared with the conventional MEA process, the heat of absorption of the TETA + DEEA solvent was 15% lower, assuming the heat of reaction comparable to that of 2 M MAPA + 5 M DEEA reported (Arshad et al., 2013a); the sensible heat was 50% lower, due to a reduced mass flow of the rich phase used for CO_2 stripping; and the stripping heat was 30% lower, based on a product gas stream of CO_2 and water vapor at a 2:1 ratio exiting the stripper,

considering a stripping temperature of 120°C. Overall, the total energy saving compared with MEA was estimated to be greater than 30%. As indicated in Table 4-1 and from the absorption study, the solvent blend of TETA + DEEA had low viscosity and volatility, and had a low risk of precipitation and foaming.

4.4 Conclusions

More than 50 amine based aqueous solvent blends of absorption accelerator A and regeneration promoter B were investigated in this chapter. Rates of CO_2 absorption and phase transition behavior at 30°C, and phase equilibrium behavior of CO_2 desorption at 80°C were evaluated by using laboratory batch reactors.

The structural effects of various types of solvent components on the absorption and desorption performance of the solvent blends were identified. A solvent blend with a linear primary monoamine as component A showed better absorption and desorption performance than did its cyclic monoamine or secondary monoamine isomer counterpart. When component A contained more amino groups, the CO_2 loading capacity attained by the derived solvent blend was not improved, because of limitations in kinetics and solubility, but the equilibrium pressure of CO_2 desorption was enhanced.

The monoamine + DMCA solvent blends generated higher equilibrium pressures of CO_2 than did the monoamine + DEEA solvents. The polyamine + DMCA solvents displayed higher CO_2 desorption pressures but had lower CO_2 absorption capacities than did the polyamine + DEEA solvents. The relationship between absorption and desorption performance and the structure of component A was similar for the DMCA and DEEA based solvent blends, despite their differences in performance.

Phase transition during CO_2 absorption occurred only in the solvent blend containing a polyamine A as the absorption accelerator. A biphasic solvent blend with a component A containing 3 to 4 N and 4 to 6 C atoms was favorable for obtaining both high absorption capacity

and desorption pressure without the operational concerns associated with precipitation, high viscosity and high volatility.

CHAPTER 5: EXPERIMENTAL INVESTIGATION OF THE ABSORPTION, PHASE TRANSITION AND DESORPTION BEHAVIOR OF BIPHASIC SOLVENT BLENDS FOR POSTCOMBUSTION CO_2 CAPTURE

5.1 Introduction

Phase transitional processes have attracted increasing attention as technical alternatives to the benchmark MEA process. The liquid-solid phase transitional processes being investigated are precipitating systems using aqueous solvents of AAS or carbonate solutions (Darde et al., 2010; Wang et al., 2016; Ye et al., 2015a). In addition, research efforts have emerged on liquid-liquid phase transitional processes enabled by biphasic solvents. Examples of biphasic solvents reported in the literature include the DMX^{TM} solvents (Raynal et al., 2011b), solvent blend of CHxMA and DMCA (Zhang et al., 2013) and solvent blend of MAPA and DEEA (Arshad et al., 2014; Ciftja et al., 2013b; Monteiro et al., 2015b).

Biphasic solvents have advantages over conventional homogeneous solvents in several ways. First, the absorbed CO_2 in a biphasic solvent is enriched in one phase and lean in the other, and only the CO_2 rich phase with a reduced mass flow is required for thermal regeneration, thus reducing the sensible heat requirement and equipment footprint. Second, an elevated stripping pressure, enabled by the enrichment of CO_2 in the partial solvent fed to the stripper, reduces both the stripping heat use associated with water vaporization and the downstream CO_2 compression work requirement. Third, a biphasic solvent containing a tertiary amine based component blended with a rate promoter (a component with primary or secondary amino groups) has a lower heat of absorption than do primary and secondary amines (Pinto et al., 2014b). Besides, the handling of liquid streams is easier than that of solids or slurry streams involved in a liquid-solid phase transitional process.

Identification of suitable biphasic solvents is crucial to achieving the best performance of the BiCAP. In the previous chapter, various candidate biphasic solvent blends were investigated in a screening study (Ye et al., 2015b). In this chapter, further screening tests were conducted, with particular emphasis on the aqueous solvent blend of a polyamine containing primary and

secondary amino groups, i.e., DETA, and either of two hydrophobic tertiary amines, i.e., PMDETA and bis[2-(*N*,*N*-dimethylamino)ethyl]ether (BDMAEE). DETA can accelerate the absorption rate; the tertiary amine can promote the formation of dual phases and the concentration of CO_2 in one phase, and provide an extra CO_2 loading capacity. Furthermore, all these amines possess high BPs (i.e., ≥ 190°C) and low VPs (i.e., ≤ 40 Pa at 20°C) and are available commercially.

In this chapter, screening experiments of CO_2 absorption capacity, absorption rate and CO_2 desorption pressure, were carried out to identify the optimal formulations of biphasic solvent blends. Liquid species were determined by 1D and 2D NMR spectroscopic techniques to elucidate the mechanisms of phase transition and absorption reactions. Rates of CO_2 absorption and VLE data were measured using a stirred cell reactor and a high pressure reactor, respectively, to generate the data required for process development.

5.2 Material and methods

All the amines used in this chapter were purchased from TCI America (>98.0% purity) without further purification. The solvents were prepared by mixing the proper amounts of amines with deionized water. For simplicity, DETA, PMDETA and BDMAEE are abbreviated as A, B and B′, respectively. For example, the solvent blend of *x* m (mol kg^{-1}) DETA and *y* m PMDETA is abbreviated as *x*A*y*B. The concentrations and compositions of the solvent blends tested for CO_2 absorption are listed in Table 5-1. These solvents are categorized into four groups. Groups I and IV solvents (S1 to S5 and S10 to S12) represent various blending ratios of DETA to PMDETA and DETA to BDMAEE, respectively, at a total concentration of 5 m. Group II solvents (S3, S6 and S7) have the same molar ratio of DETA to PMDETA (0.54) but have sequentially decreasing total molalities (5, 4.5 and 4 m). Group III solvents (S7 to S9) have the same total molality (4 m) but vary in the molar ratio of DETA to PMDETA.

Table 5-1. Four groups of aqueous solvent blends used in CO_2 absorption experiments.

Solvent no.	Formula[a]	Total molality (mol kg^{-1})	Molar ratio of A to B	Group
S1	1A4B	5	0.25	I
S2	1.5A3.5B	5	0.43	I
S3	1.75A3.25B	5	0.54	I, II
S4	2A3B	5	0.67	I
S5	2.19A2.81B	5	0.78	I
S6	1.58A2.92B	4.5	0.54	II
S7	1.4A2.6B	4	0.54	II, III
S8	1.75A2.25B	4	0.78	III
S9	1A3B	4	0.33	III
S10	1A4B′	5	0.25	IV
S11	1.5A3.5B′	5	0.43	IV
S12	2A3B′	5	0.67	IV

[a] A: DETA; B: PMDETA; B′: BDMAEE.

5.2.1 Measurement of CO_2 absorption capacity and speciation analysis of liquid phases

The screening experiments of CO_2 absorption were conducted by using a 150 mL laboratory glass impinger. Descriptions of the experimental setup and procedures are provided elsewhere (Ye et al., 2015b). In a typical test, pure CO_2 at atmospheric pressure was bubbled into the gas impinger at a flow rate of 100 mL min^{-1} under 40°C for 120 min. The solvent was sampled at 10, 20, 40, 60, 90 and 120 min during the absorption test, and the density (g mL^{-1}) and CO_2 loading (mol L^{-1}) of both phases were measured by a gravimetric method and a Chittick titration apparatus with 2 mol L^{-1} of HCl, respectively. The volumetric ratios of the dual phases were recorded throughout the absorption.

Species present in both liquid phases were analyzed by NMR spectroscopic techniques. Samples from the typical solvents were fed to NMR tubes with the proper amounts of D_2O added as a signal lock. ^{13}C NMR spectra were obtained on a Varian Inova 600 MHz NMR spectrometer operating at a frequency of 100.62 MHz with a 5 mm Varian broadband autoX probe. The corresponding ^{1}H and 2D spectra were recorded on an Agilent VNMRS 750 MHz NMR spectrometer with a 5 mm indirect detection $^{1}H/^{13}C/^{15}N$ probe with XYZ gradient capabilities for assignment of spectroscopic peaks and quantification of species. Three 2D techniques were used, i.e., gradient correlation spectroscopy (gCOSY), gradient heteronuclear single quantum correlation spectroscopy (gHSQC) and gradient heteronuclear multiple bond correlation spectroscopy (gHMBC). All spectra were recorded at 23°C. ^{1}H and ^{13}C spectra were referenced

to the D_2O peak at 4.67 ppm and to the tetramethylsilane (TMS) peak at 0 ppm, respectively. The acquired spectra were processed with a MestReNova software (Mestrelab Research).

5.2.2 Measurement of CO_2 absorption rate

The kinetic rates of CO_2 absorption into the selected solvents and 30 wt% MEA were measured by using a stirred tank reactor. A schematic diagram of the experimental system is shown elsewhere (Zhang et al., 2011d). The reactor cell is a glass vessel (50 mL) with an inner diameter (ID) of 4 cm and a height of 4.2 cm. For optimal mixing, three internal baffles, each with a width of 0.6 cm, were positioned triangularly to the inner wall of the cell. An external magnetic stirrer provided thorough mixing of the solvent inside the cell at 500 rpm. The cell was immersed in an isothermal water bath maintained at 40°C. A stainless steel flange with a rubber O-ring gasket was placed on top of the cell for sealing, and a vacuum pump (Dekker, RVL002H-01) provided the initial vacuum level before each experiment. A gas cylinder supplied pure CO_2 to the cell through a needle valve to a preset pressure to simulate the partial pressure of CO_2 in the typical inlet or treated flue gas. The pressure of the cell was measured by a vacuum (0 to 15 psia) pressure transducer (Omegadyne, PX429-015AUSB) and was recorded online throughout the experiment.

In a typical experiment, 20 mL of a solvent blend with a total CO_2 loading of either 0.2 or 0.5 mol mol^{-1} was fed to the cell. After assembly and leakage detection, the cell was vacuumized and placed in the water bath with the stirrer powered on until the solvent inside reached gas-liquid equilibrium. Pure CO_2 was supplied to the reactor to ensure the initial partial pressure of CO_2 in the cell was 0.2 psia for the solvent at a CO_2 loading of 0.2 mol mol^{-1}, and 2 psia for the solvent at a CO_2 loading of 0.5 mol mol^{-1}. The CO_2 partial pressure was determined by subtracting the water vapor pressure from the total pressure of the cell assuming an ideal behavior of the solvent. The pressure drop over time during the test was recorded to estimate the instant rate of CO_2 absorption according to:

$$J = -\frac{dP_{CO_2,t}}{dt}\frac{V_G}{RTA} \tag{5-1}$$

where J (mol s^{-1} m^{-2}) is the CO_2 flux to the solvent, $P_{CO2,t}$ (Pa) is the instant CO_2 partial pressure at time t, V_G (m^3) is the headspace volume of the cell, R is the universal gas constant, T (K) is the

temperature and A (m^2) is the gas-liquid interfacial area. The instant rate of CO_2 absorption was estimated at a CO_2 partial pressure of 0.2 psia for the solvent with a CO_2 loading of 0.2 and 2 psia for the solvent with a loading of 0.5 to simulate the representative solution conditions at the top and bottom of an absorption column, respectively.

5.2.3 Measurement of CO_2 desorption pressure with CO_2 rich liquid phase

The CO_2 rich phase separated from the lean phase for each selected biphasic solvent was used as a feed solution for the measurement of CO_2 desorption pressure. For consistency, the rich phase sample was separated and collected from a biphasic solvent after 90 min of CO_2 absorption under the same experimental conditions as described in Section 5.2.1. The equilibrium partial pressures of CO_2 over each rich phase sample were measured at 100 and 120°C at its initial CO_2 loading, and at two lower CO_2 loadings which were achieved by regenerating the initial rich phase sample partially. The CO_2 loading was defined as moles of CO_2 per mole of total equivalent molecular amines in the rich phase. The content of total amines in the rich phase liquid (g g^{-1}) was determined by gas chromatography (Thermo Scientific, TRACE 1300 Series GC) in tandem with mass spectrometry (Thermo Scientific, ITQ 700 ion-trap MS). The gas chromatography-mass spectrometry (GC-MS) was equipped with a Restek Rtx-5 amine column (30 m length, 0.25 mm ID and 0.5 µm film thickness) and a TriPlus RSH Autosampler (Thermo Scientific) for automatic injection of 1 µL samples into the GC.

The measurement of CO_2 desorption pressure was conducted by using a 200 mL high pressure reactor (Great Wall Instruments). The reactor, rated at 250°C and 100 bar, was a stainless steel vessel equipped with a magnetic stirrer plate (60 to 2,000 rpm) and heating elements for temperature control. A wireless thermocouple and a pressure transducer (Omega, PX409-750AUSBH) were attached to the reactor for online monitoring of the system temperature and pressure. The procedure of the desorption experiment is described elsewhere (Ye et al., 2015b).

5.3 Results and discussion

5.3.1 CO_2 absorption capacity and speciation of dual liquid phases

The cumulative total CO_2 loading (combined loadings of CO_2 lean and rich phases) over the time of CO_2 absorption for all the tested solvent blends as well as the 30 wt% MEA is depicted in Fig. 5-1. Most solvents had a CO_2 loading capacity comparable with or higher than that of MEA. For solvent blends with the same molality (among the Group I, III or IV), the rate of CO_2 absorption increased with an increasing molar ratio of A to B (or B′), as indicated by the higher CO_2 loading achieved at the same absorption time. DETA played a role in promoting the CO_2 absorption rate, because a DETA molecule contains two primary amino groups and one secondary amino group, and each amino group can serve as a CO_2 bonding site and thus contribute to the CO_2 loading capacity. Based on a comparison of Group I and III solvents, a DETA-PMDETA solvent blend with a total molality of 4 m had a greater CO_2 loading capacity (>1 mol mol^{-1}) than its 5 m counterpart solvent at the same molar ratio of A to B. The observed difference was due to a higher water content in the 4 m solvent blend, which allowed more ionic species produced from the reactions between CO_2 and amines to be partitioned to the CO_2 rich phase, thus favoring more CO_2 absorption thermodynamically. Concurrently, the higher water content lowered the solvent viscosity and thus facilitated CO_2 diffusion and other mass transfer processes in the biphasic solvent. Similarly, at the same molar ratio of A to B, a solvent blend with a lower total molality (Group II) demonstrated a higher CO_2 loading capacity.

The volumetric expansion of the CO_2 rich phase with the time of CO_2 absorption for the tested solvent blends is displayed in Fig. 5-2. Dual phases were formed at a low CO_2 loading, corresponding to 10 min or less of CO_2 absorption for most of the solvent blends. After an initial accumulation of total CO_2 loading, corresponding to 20 min of CO_2 absorption, the volume of the CO_2 rich phase increased abruptly. In a late stage of the absorption experiment, the volumetric increase of the rich phase became gradual. Therefore, CO_2 absorption into a biphasic solvent underwent a two stage process after dual phases were formed. In the first stage, the absorbed CO_2 was concentrated in the aqueous CO_2 rich phase in the form of carbamate species of DETA, because DETA is hydrophilic and reacted rapidly with CO_2; whereas, most unreacted molecular B (or B′) which is hydrophobic was retained in the oily CO_2 lean phase. In the second

stage, the molecular B (or B′) initially in the oily phase diffused across the liquid-liquid interface and transferred into the aqueous phase, concomitant with a volumetric increase in the CO_2 rich phase. As a result, the CO_2 loading in the rich phase did not continuously increase over time but leveled off because of the "dilution" effect of the expanding rich phase volume.

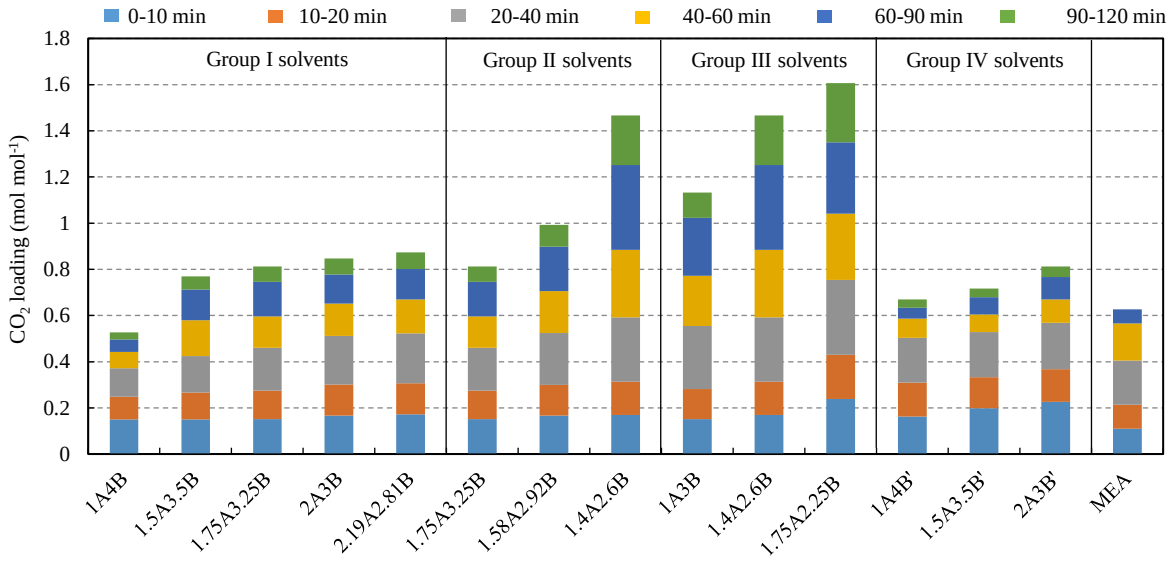

Fig. 5-1. Cumulative total CO_2 loadings in the solvent blends and 30 wt% MEA over the course of CO_2 absorption.

For Group I, III or IV solvent blends, which had the same total amine molality within each group, those with higher molar fractions of DETA had greater volumes of the CO_2 rich phase throughout the absorption. Group I solvents had volumetric fractions of the CO_2 rich phase comparable with those of Group IV solvents, indicating that BDMAEE demonstrated a hydrophobicity similar to that of PMDETA (Fig. 5-2). For Group I solvents (a total molality of 5 m), the volumetric percentages of the rich phases were not greater than 65% after 120 min of CO_2 loading. In comparison, loading CO_2 into a Group III solvent (a total molality of 4 m) resulted in an expansion of the CO_2 rich phase to >85% in the total volume; at a high molar ratio of A to B, the solvent could become homogeneous. Group II consisted of solvent blends with the same molar ratio of A to B, and a higher volume of CO_2 rich phase was formed from the solvent blend with a lower total amine concentration.

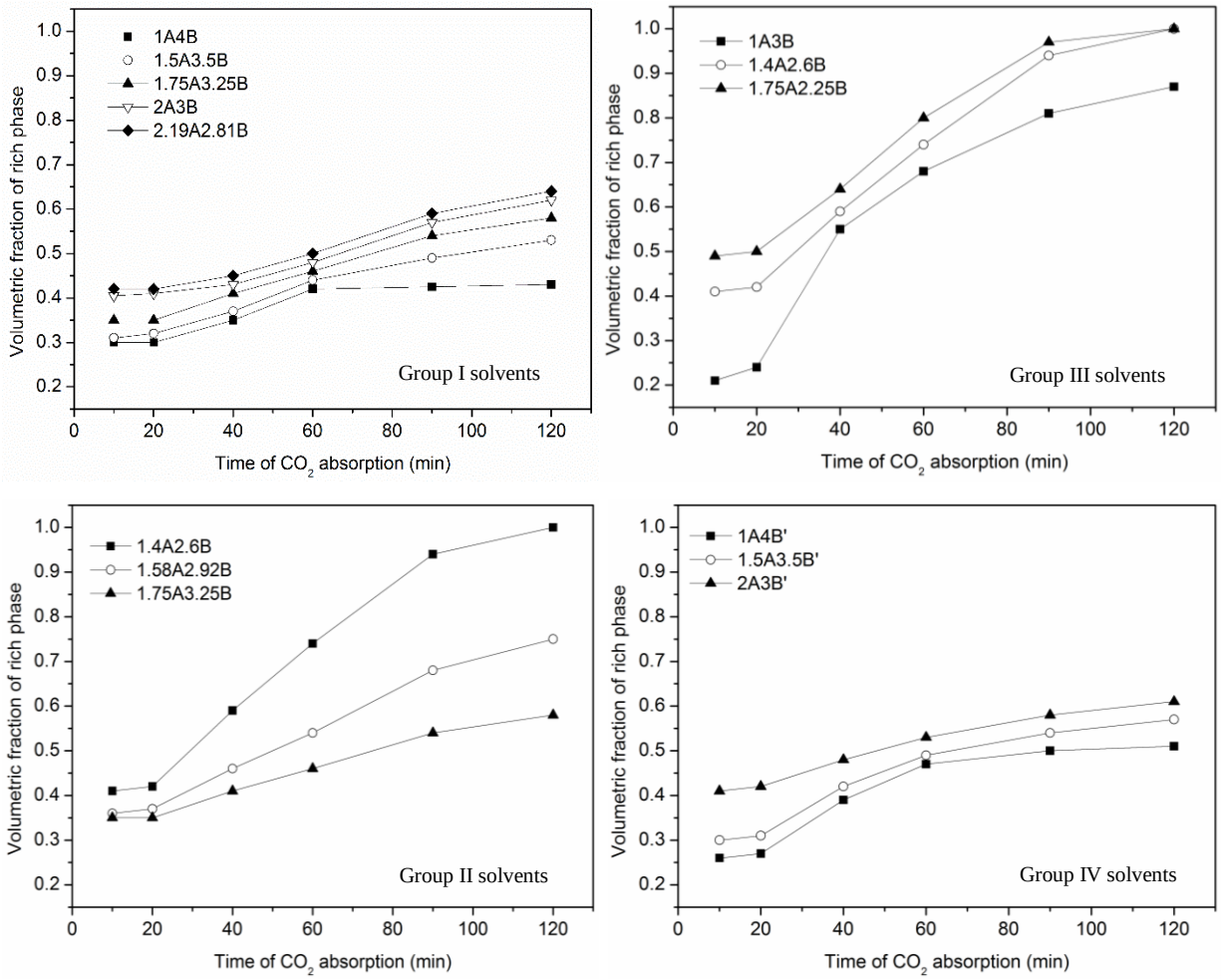

Fig. 5-2. Evolution of the volumetric fraction of the CO_2 rich phase over the course of CO_2 absorption for each of the four groups of solvent blends.

Species formed in the two liquid phases during CO_2 loading into a selected solvent (1.5A3.5B) were determined by NMR spectroscopy to corroborate the two stage process of phase transition. The ^{13}C spectra of solvent 1.5A3.5B at CO_2 loadings of 0 (fresh solvent), 0.213 (15 min of CO_2 absorption) and 0.663 (75 min of CO_2 absorption) mol mol^{-1} are presented in Fig. 5-3. At a CO_2 loading of either 0.213 or 0.663 mol mol^{-1}, the lean phase samples contained only molecular PMDETA species. For the rich phase, at a CO_2 loading of 0.213, the DETA derived species shared a dominant portion; whereas, the total PMDETA species (molecular equivalent) had a molar fraction of 20%. However, when the CO_2 loading increased to 0.663, the molar fraction of the total PMDETA species increased to 50% and the presence of HCO_3^-/CO_3^{2-} (at a chemical shift of 160 to 161 ppm on the ^{13}C spectra) was noticeable. In the early stage of CO_2 absorption,

the products of CO_2 absorption reactions were various carbamate and dicarbamate species associated with DETA. In the later stage, PMDETA molecules originally in the CO_2 lean phase, which could not be bonded directly with CO_2, were protonated and dissolved in the aqueous CO_2 rich phase of expanding volume, concomitant with the production of HCO_3^-/CO_3^{2-}.

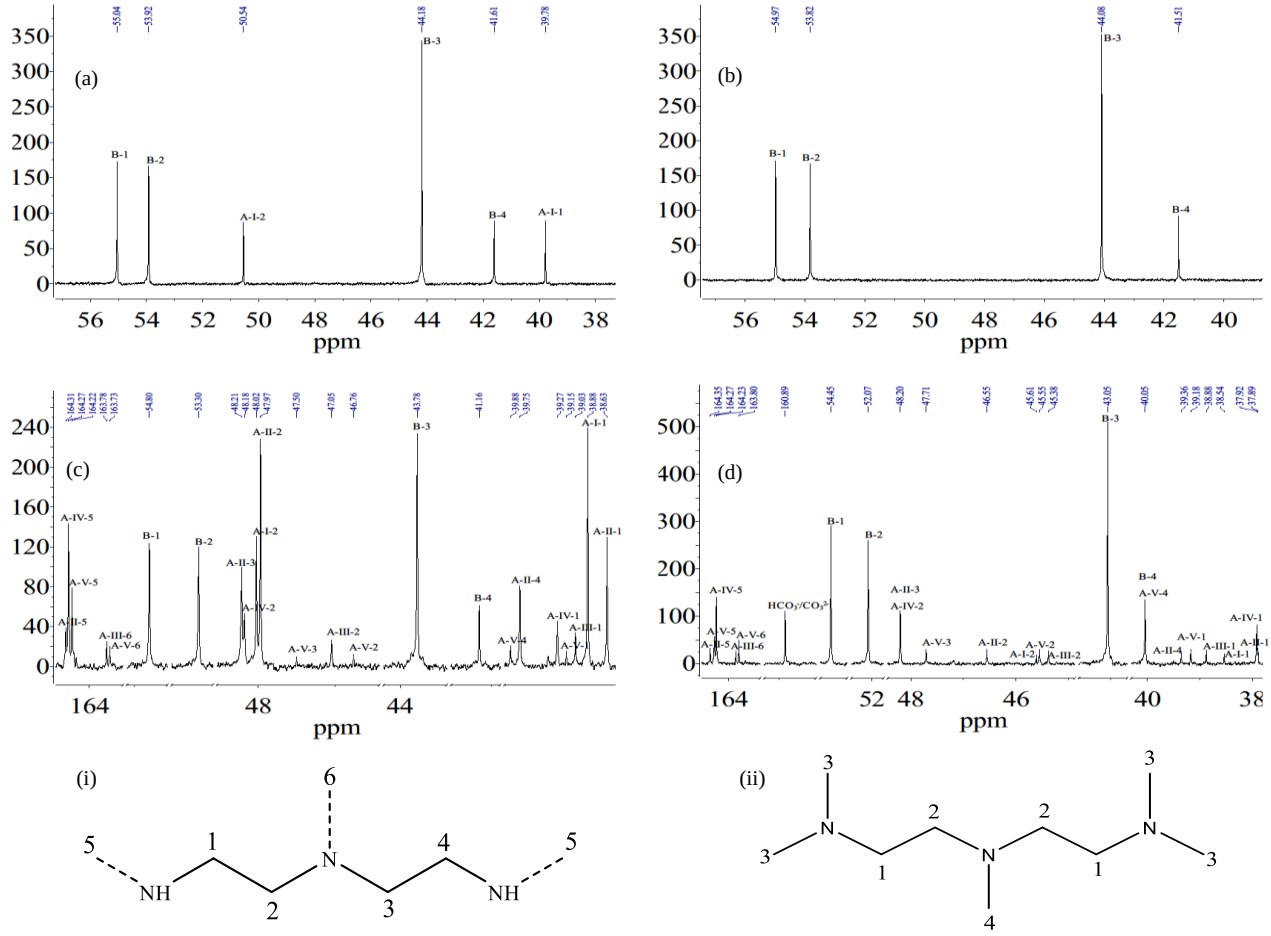

Fig. 5-3. ^{13}C NMR spectra of the samples derived from solvent 1.5A3.5B: (a) spectra of the fresh sample; (b) spectra of the lean phase samples (identical at total CO_2 loadings of 0.213 and 0.663 mol mol^{-1}); (c) spectra of the rich phase sample at a loading of 0.213 mol mol^{-1}; (d) spectra of the rich phase sample at a loading of 0.663 mol mol^{-1}. Roman numerals I (molecular DETA and its protonated species), II (primary carbamate of DETA and its protonated species), III (secondary carbamate of DETA and its protonated species), IV (primary-primary dicarbamate of DETA and its protonated species) and V (primary-secondary dicarbamate of DETA and its protonated species) represent the five groups of DETA species. Arabic numerals 1 to 6, labelled in (i) for DETA and (ii) for PMDETA, represent the various positions of carbon on each group of species. The dashed lines represent the carbamate groups.

The presence of a hydrophilic solvent component favored achieving a high total CO_2 absorption capacity but resulted in an undesired phase transition (i.e., the amount of CO_2 rich phase was dominant compared with that of the lean phase). This phase splitting behavior was undesirable because the enrichment of CO_2 in one phase was inadequate. The proper solvent formula with an optimal molality of total amines and molar ratio of A to B (or B′) was crucial to the overall solvent performance. Therefore, only four solvents, 1.5A3.5B′, 2A3B′, 1.5A3.5B and 2A3B, were selected for further studies of absorption kinetics and CO_2 desorption.

5.3.2 Rate of CO_2 absorption

As the absorption proceeded, the increase in CO_2 loading decreased, reflecting less favorable kinetics at high CO_2 loadings. The rate of CO_2 absorption into each of the four selected solvent blends at either 0.2 (typical of a lean loading) or 0.5 (typical of a rich loading) mol mol^{-1} was measured, and the results are shown in Fig. 5-4.

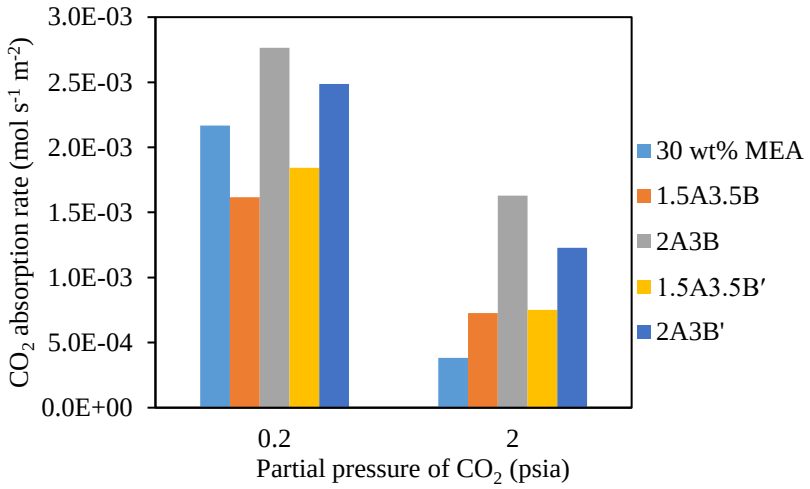

Fig. 5-4. Instant rates of CO_2 absorption into the selected biphasic solvents and 30 wt% MEA (absorption under a CO_2 partial pressure of 0.2 psia and a CO_2 loading of 0.2 mol mol^{-1}, and a CO_2 partial pressure of 2 psia and a CO_2 loading of 0.5 mol mol^{-1}).

All the solvents had lower CO_2 absorption rates when their CO_2 loadings increased from 0.2 to 0.5 mol mol^{-1}. Both solvents 2A3B and 2A3B′ revealed favorable kinetics over MEA across the range of the measured CO_2 loadings. However, for solvents 1.5A3.5B and 1.5A3.5B′, the rates were lower than those of MEA at the CO_2 loading of 0.2 mol mol^{-1} but higher at the CO_2 loading

of 0.5 mol mol^{-1}, indicating their CO_2 absorption rates were less sensitive to the CO_2 loading compared with that of MEA. The rate difference between solvents A-B and A-B′ was negligible. Solvent 2A3B maintained a high rate of CO_2 absorption even at the CO_2 loading of 0.5 mol mol^{-1}.

5.3.3 CO_2 desorption pressure

Equilibrium pressures of CO_2 desorption at 100 and 120°C under different CO_2 loadings for the four selected biphasic solvent blends, as well as the reported data for 30 wt% MEA (Aronu et al., 2011), are displayed in Fig. 5-5. The desorption pressure of CO_2 increased with increasing temperature. For either PMDETA (B) or BDMAEE (B′) as the tertiary amine component, the 1.5A3.5B (or B′) solvent blend showed higher desorption pressures of CO_2 than did the 2A3B (or B′) solvent blend, indicating the desorption pressure of CO_2 was correlated positively with the molar fraction of B (or B′) in the total amines of the original solvent blend. As shown in panels (a) and (b), a total desorption pressure of 2.6 atm (CO_2 and water vapor partial pressures of 0.6 and 2 atm, respectively) at 120°C was achieved at the lean loading conditions (e.g., at a CO_2 loading of 0.3 mol mol^{-1} for the rich phase of solvent 2A3B or 0.55 mol mol^{-1} for the rich phase of solvent 1.5A3.5B′), which was 30% higher than that for MEA (with a negligible contribution from the partial pressure of CO_2). The total CO_2 loading of a solvent blend returned to the absorber was lower than that during the desorption, because the regenerated rich phase solvent was mixed with the lean solvent not subject to desorption. The desorption pressure could be elevated further (i.e., >2.6 atm) if a higher CO_2 loading was adopted for the regenerated rich phase. Concurrently, the CO_2 desorption capacities of the solvent blends 1.5A3.5B′ and 2A3B′ were estimated at 0.56 and 0.55 mol mol^{-1} (i.e., 3.2 and 3.1 mole of CO_2 per kg of solvent), respectively. The desorption capacities of the solvent blends 1.5A3.5B and 2A3B were both 0.57 mol mol^{-1} (i.e., 3.3 mol kg^{-1}). Compared with the CO_2 desorption capacity of MEA (i.e., 1.25 mol kg^{-1}), all of these four solvent blends had larger desorption capacity. Therefore, with the CO_2 rich phase liquid, the biphasic solvent blends outperformed MEA in both the loading capacity and pressure of CO_2 desorption.

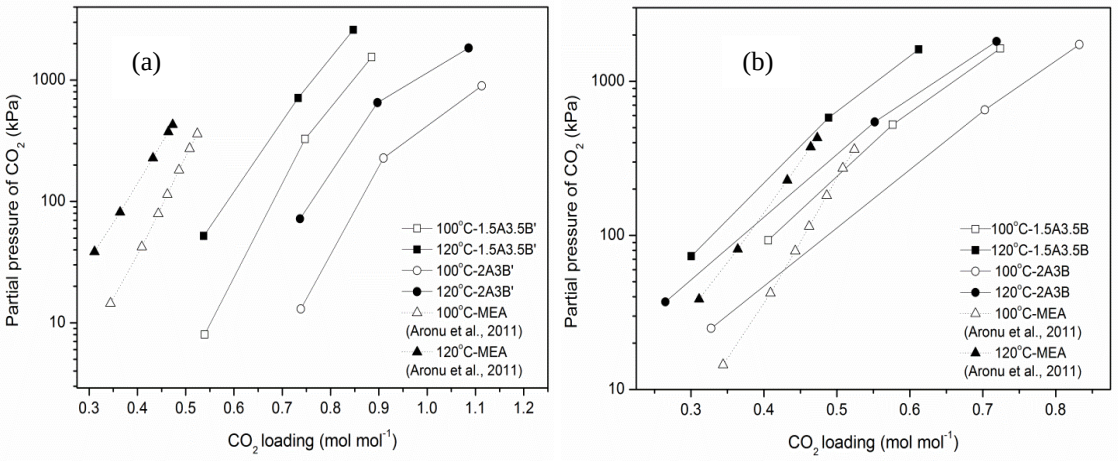

Fig. 5-5. Partial pressures of CO_2 desorbed at 100 and 120°C with CO_2 rich phase solvents derived from the selected biphasic solvent blends of (a) A-B′ and (b) A-B.

5.4 Conclusions

Biphasic solvents with various formulae were screened experimentally with respect to CO_2 absorption capacity, kinetic rate and desorption pressure. Several solvents, such as the blends of 1.5A3.5B (or B′) and 2A3B (or B′), were identified as promising because they exhibited desirable dual phase transitional behavior and had greater CO_2 loading capacities and rates for CO_2 absorption and higher CO_2 pressures and loading capacities for CO_2 desorption, in comparison with MEA. NMR speciation analyses revealed that CO_2 absorption into the biphasic solvents underwent a two stage process in which the products of reactions between CO_2 and DETA were dominant in the CO_2 rich phase liquid in the early stage, and PMDETA molecules participated in the reactions and dissolved in the CO_2 rich phase, concomitantly with the formation of HCO_3^-/CO_3^{2-} and volumetric expansion of the CO_2 rich phase, in the late stage.

The effects of formulae of biphasic solvents on their performance were examined. Blending a component with high hydrophilicity in the solvent was unfavorable for dual phase separation and CO_2 enrichment. Adding a component A with a high molar fraction was observed to promote the absorption rate and improve the CO_2 loading capacity for both the CO_2 absorption and desorption; whereas, adding a component B with a high molar fraction was observed to elevate the CO_2 desorption pressure. As a typical biphasic solvent, the blend of DETA and PMDETA

(with typical formulae of 2A3B and 1.5A3.5B) was selected in further studies (Chapters 6 to 8), which were focused on the detailed speciation during CO_2 absorption and desorption, development of VLLE based thermodynamic modeling, and kinetics of CO_2 absorption into the chosen solvent formulae.

CHAPTER 6: MECHANISMS OF CO_2 ABSORPTION AND DESORPTION WITH PHASE TRANSITIONAL SOLVENTS

6.1 Introduction

The development of biphasic solvent based CO_2 absorption processes has attracted attention to overcome the drawbacks of the conventional MEA process. In the previous two chapters, a group of aqueous biphasic solvents were formulated by blending a component that could promote the absorption rate with another component that could provide an extra capacity of CO_2 loading. A biphasic solvents with an amine accelerator containing 3 to 4 amino groups and 4 to 6 alkyl groups exhibited the best performance in CO_2 absorption and desorption. As a result, the aqueous mixture of DETA and PMDETA was selected as a feasible biphasic solvent blend.

Among the amine accelerators identified as having good performance, DETA ($C_4H_{13}N_3$) has a small molecular weight. As the tertiary counterpart of DETA, PMDETA contains 3 tertiary amino groups and thus provides multiple sites for protonation in the conversion of CO_2 to HCO_3^- /CO_3^{2-}, which allows for a high loading capacity during CO_2 absorption. Both components have high BPs (204.1°C for DETA and 198°C for PMDETA), are not volatile (VPs of 10 and 31 Pa at 20°C for DETA and PMDETA, respectively) and are available commercially in large quantities. Thus, further investigations were conducted by using the aqueous solvent blends constituting these two components.

Speciation analysis is crucial to understanding the chemistry of biphasic solvent systems. NMR spectroscopy has been the most commonly used technique to identify the species present in liquid phases during CO_2 absorption both qualitatively and quantitatively, as well as to determine the equilibrium constants of carbamate formation reactions (Bishnoi and Rochelle, 2000; Ciftja et al., 2013a, b, 2014; Cullinane and Rochelle, 2004). Ciftja et al. (2013b) revealed the major CO_2 reaction products present in a biphasic solvent system were carbamate, dicarbamate and HCO_3^-/CO_3^{2-} species, with the CO_2 lean phase being high in the tertiary amine component (e.g., DEEA) and the CO_2 rich phase being high in the primary or secondary amine species (e.g., MAPA). The mechanism governing the phase separation in the mixed solvents was the disparate

hydrophilicity (or aqueous solubility) of various species distributed in the dual phases (Xu et al., 2013a). To better understand the biphasic systems, it is valuable to extend the speciation studies to track the evolution of solvent species over the course of CO_2 absorption as well as desorption.

Two formulae of the DETA/PMDETA/H_2O solvent blend were chosen based on the screening study on the solvent composition (Chapter 5). Experiments were conducted to investigate their CO_2 absorption capacity, phase transition behavior and CO_2 desorption pressure. We emphasized ^{1}H and ^{13}C NMR spectroscopic analyses to identify and quantify the species in both CO_2 rich and lean phases under typical absorption and desorption conditions. On the basis of the NMR speciation results, mechanisms and pathways for the CO_2 absorption and desorption reactions were proposed.

6.2 Chemistry of CO_2 absorption

Reactions (6-1) to (6-3) are related to water dissociation, CO_2 dissolution and bicarbonate dissociation. DETA is a polyamine containing two primary amino groups and one secondary amino group, each of which can serve either as a proton donor for bonding with a CO_2 molecule to form a carbamate species or as a base to accept a proton. Similarly, PMDETA has multiple tertiary amino groups, and different protonated PMDETA species can be formed depending on the number of the protonated amino groups. In this regard, all the possible reactions are listed in reactions (6-4) to (6-20). Because PMDETA is a tertiary amine, no direct or stable bonding of its tertiary amino groups with CO_2 is expected to occur. It is assumed the absorption of CO_2 by PMDETA is via the reaction between CO_2 and OH^-, and the role of PMDETA is similar to that of a base catalyst by consuming H^+ produced in reaction (6-2) and becoming protonated (reactions (6-18) to (6-20)). For simplicity, DETA and PMDETA are denoted as A and B, respectively. The related reactions are expressed without distinguishing between various protonated species with regard to the amino site onto which a proton is bonded.

$H_2O = H^+ + OH^-$ (dissociation of water) (6-1)

$CO_2 + H_2O = H^+ + HCO_3^-$ (dissociation of carbonic acid) (6-2)

$HCO_3^- = H^+ + CO_3^{2-}$ (dissociation of HCO_3^-) (6-3)

$AH^+ = H^+ + A$ (dissociation of protonated DETA) (6-4)

$AH_2^{2+} = H^+ + AH^+$ (dissociation of diprotonated DETA) (6-5)

$AH_3^{3+} = H^+ + AH_2^{2+}$ (dissociation of triprotonated DETA) (6-6)

$A + CO_2 = ACOO^-(p) + H^+$ (formation of primary carbamate) (6-7)

$A + CO_2 = ACOO^-(s) + H^+$ (formation of secondary carbamate) (6-8)

$ACOO^-(p) + CO_2 = A(COO)_2^{2-}(pp) + H^+$ (formation of primary-primary dicarbamate) (6-9)

$ACOO^-(p) + ACOO^-(s) + 2CO_2 = 2A(COO)_2^{2-}(ps) + 2H^+$ (formation of primary-secondary dicarbamate) (6-10)

$A(COO)_2^{2-}(pp) + A(COO)_2^{2-}(ps) + 2CO_2 = 2A(COO)_3^{3-} + 2H^+$ (formation of tricarbamate) (6-11)

$AH^+COO^-(p) = ACOO^-(p) + H^+$ (dissociation of protonated primary carbamate) (6-12)

$AH^+COO^-(s) = ACOO^-(s) + H^+$ (dissociation of protonated secondary carbamate) (6-13)

$AH_2^{2+}COO^-(p) = AH^+COO^-(p) + H^+$ (dissociation of diprotonated primary carbamate) (6-14)

$AH_2^{2+}COO^-(s) = AH^+COO^-(s) + H^+$ (dissociation of diprotonated secondary carbamate) (6-15)

$AH^+(COO)_2^{2-}(pp) = A(COO)_2^{2-}(pp) + H^+$ (dissociation of protonated primary-primary dicarbamate) (6-16)

$AH^+(COO)_2^{2-}(ps) = A(COO)_2^{2-}(ps) + H^+$ (dissociation of protonated primary-secondary dicarbamate) (6-17)

$BH^+ = H^+ + B$ (dissociation of protonated PMDETA) (6-18)

$BH_2^{2+} = H^+ + BH^+$ (dissociation of diprotonated PMDETA) (6-19)

$BH_3^{3+} = H^+ + BH_2^{2+}$ (dissociation of triprotonated PMDETA) (6-20)

Following a protocol similar to that adopted by Hartono et al. (2007), we categorized the DETA and PMDETA associated species shown in reactions (6-4) to (6-20) into seven structural groups (A-I, A-II, A-III, A-IV, A-V, A-VI and B, as described in Fig. 6-1). Each of these groups possessed unique NMR signals from its characteristic C or H atoms for identification and quantification. Because the molecular and protonated species within a certain group (a component and its protonated species) could not be differentiated by NMR spectra because of the rapid exchange of protons, the observed signal of ^{13}C or ^{1}H specific to an individual group reflected an average signal intensity among all the species within that group. For convenience, only the nonprotonated species of each group are presented in Fig. 6-1. The functional sites (e.g., $–CH_2$, $–CH_3$ and $–COO^-$) were named with Arabic numerals. For symmetrical structures in a group, only one of them was marked out.

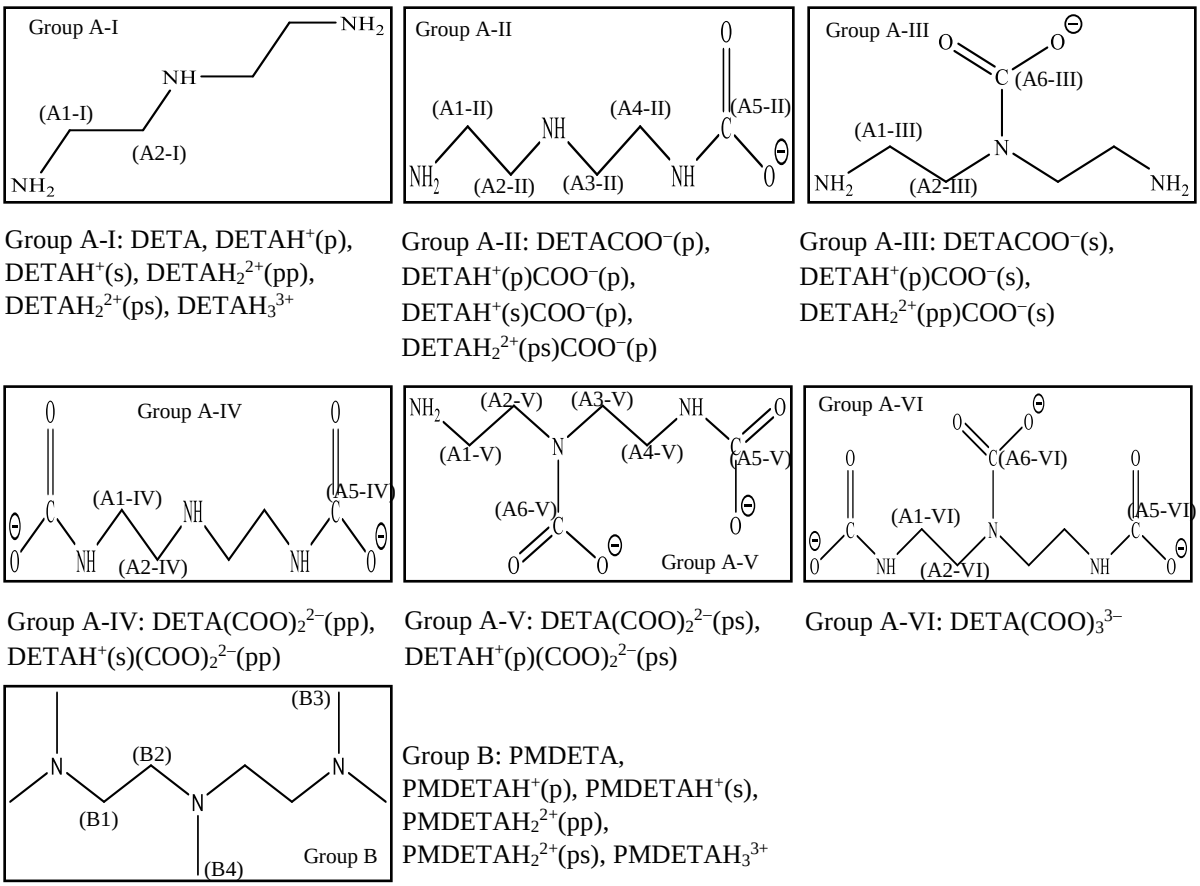

Group A-I: DETA, $DETAH^{+}$(p), $DETAH^{+}$(s), $DETAH_2^{2+}$(pp), $DETAH_2^{2+}$(ps), $DETAH_3^{3+}$

Group A-II: $DETACOO^{-}$(p), $DETAH^{+}$(p)COO^{-}(p), $DETAH^{+}$(s)COO^{-}(p), $DETAH_2^{2+}$(ps)COO^{-}(p)

Group A-III: $DETACOO^{-}$(s), $DETAH^{+}$(p)COO^{-}(s), $DETAH_2^{2+}$(pp)COO^{-}(s)

Group A-IV: $DETA(COO)_2^{2-}$(pp), $DETAH^{+}$(s)$(COO)_2^{2-}$(pp)

Group A-V: $DETA(COO)_2^{2-}$(ps), $DETAH^{+}$(p)$(COO)_2^{2-}$(ps)

Group A-VI: $DETA(COO)_3^{3-}$

Group B: PMDETA, $PMDETAH^{+}$(p), $PMDETAH^{+}$(s), $PMDETAH_2^{2+}$(pp), $PMDETAH_2^{2+}$(ps), $PMDETAH_3^{3+}$

Fig. 6-1. Groups of species present in the DETA/PMDETA/H_2O/CO_2 system. The position of carbon on $–COO^{-}$ is represented by a notation of (p) or (s) when $–COO^{-}$ is attached to a primary or secondary amino group, respectively. The symmetrical structures in each group are marked once only.

6.3 Material and methods

6.3.1 Chemicals

The DETA (purity 99%) and PMDETA (purity >99.0%) were purchased from Sigma Aldrich and TCI America, respectively, and used as received. Two formulae of DETA and PMDETA solvent blends were prepared: 1.5 and 3.5 mol kg^{-1} of DETA and PMDETA, respectively (abbreviated hereafter as 1.5A3.5B), and 2 and 3 mol kg^{-1} of DETA and PMDETA, respectively (abbreviated hereafter as 2A3B). The solutions were prepared in deionized water.

6.3.2 Absorption experiments

The experimental method for CO_2 absorption is described elsewhere (Ye et al., 2015b). The experiments were carried out in a 100 mL glass impinger. Pure CO_2, at a flow rate of 105 mL min^{-1}, was bubbled in the solution for 120 min at 40°C and atmospheric pressure. The liquid samples, including both the CO_2 rich and CO_2 lean phases if applicable, were collected at 10, 20, 40, 60, 90 and 120 min. For each sample collected, the volumetric fraction of the CO_2 rich phase was measured after the sample had settled and the two phases were separated. The density and CO_2 loading of either phase were determined by the gravimetric method and acid (2 mol L^{-1} of HCl) titration in a Chittick apparatus (a measurement error of ±7%), respectively.

6.3.3 Desorption experiments

For both solvent formulae, the CO_2 rich phase obtained from the absorption experiment was separated and used for the CO_2 desorption study at 120°C in a high pressure reactor (Great Wall Instruments). For solvent 1.5A3.5B, the CO_2 rich phase was removed from absorption at 75 min, and for solvent 2A3B, it was removed from absorption at 60 min. The reactor was 400 mL in volume with magnetic stirring and temperature control. A thermocouple and a pressure transducer were attached to monitor continuously the temperature and pressure, respectively, of the reactor.

In a typical experiment, the CO_2 loading of the solution was measured before it was fed to the reactor. The reactor vessel was sealed and vacuum was applied to remove residual air before the electric heating and stirring elements (300 rpm) were powered on. After equilibrium was reached at 120°C, the partial pressure of CO_2 was estimated by subtracting the water vapor pressure from the monitored total pressure assuming an ideal solution. The pressure inside the reactor was released without reducing the reactor temperature, during which the solution was boiled continuously. The generated vapor of water or amine was condensed in an ice bath and recycled back to the reactor, and the CO_2 gas was released to reduce the CO_2 loading to the next desired level before another desorption experiment began. This procedure was repeated until the equilibrium pressures of CO_2 desorption under three decreasing CO_2 loadings were measured. Liquid samples were collected for CO_2 loading measurements by using the Chittick apparatus. If dual phases were formed, both were subjected to the analyses.

6.3.4 NMR analysis

Quantitative speciation analyses with ^{1}H and ^{13}C NMR were conducted for the samples collected during both the CO_2 absorption and desorption experiments. For each solvent blend, the homogeneous fresh solvent and three CO_2 loaded samples were collected and measured. Each loaded sample contained the CO_2 lean and CO_2 rich phases, and the total CO_2 loadings covered the range of the absorption capacity. For CO_2 desorption samples, the rich phase feed and its derived solutions at three decreasing CO_2 loadings during the aforementioned desorption experiments were collected for NMR analysis. If dual phases were formed during a desorption experiment, samples of both phases were collected and analyzed.

For each sample in an NMR tube, D_2O was added (75% in volume) for a signal lock. ^{13}C NMR spectra were obtained on a Varian Inova 600 MHz NMR spectrometer operating at a frequency of 100.62 MHz with a 5 mm Varian broadband autoX probe. The corresponding ^{1}H and 2D NMR spectra were recorded on an Agilent VNMRS 750 MHz NMR spectrometer with a 5 mm indirect detection $^{1}H/^{13}C/^{15}N$ probe with XYZ gradient capabilities. Three 2D techniques were used to identify and assign the peaks of ^{1}H and ^{13}C spectra: gCOSY was used to identify neighboring H–H correlations, gHSQC was used to identify C and its directly attached H atoms, and gHMBC was used to identify H and C atoms connected 2 to 4 bonds apart. All NMR spectra were recorded at 23°C. For quantitative ^{1}H spectra, a 90° excitation pulse of 10 to 12 μs (depending on the sample), 8 scans, and a 14.4 s delay time ($\geq 5\ T_1$) including a 4.4 s acquisition time between scans were adopted (T_1 was the longitudinal relaxation time). For the inverse gated ^{1}H decoupled ^{13}C spectra, a 90° pulse of 6.7 μs, 32 scans, and a 100 s delay time ($\geq 5\ T_1$) including a 1.8 s acquisition time were employed. ^{1}H and ^{13}C spectra were referenced to the D_2O peak at 4.67 ppm and to the TMS peak at 0 ppm, respectively. The acquired spectra were processed and analyzed with MestReNova software (Mestrelab Research). The quantification for amine species was accomplished based on the integration values of ^{1}H peaks; whereas, that for HCO_3^-/CO_3^{2-} relied on ^{13}C spectra. The integral of overlapping peaks was assumed to be the sum of integrals of each separately assigned peak.

6.4 Results and discussion

6.4.1 CO_2 absorption and solvent speciation

6.4.1.1 CO_2 absorption and phase transition

Absorption of CO_2 into both solvents was tested on a triplicate basis, and the results of CO_2 loading and phase transition over time are presented in Table 6-1. For both solvents, dual liquid phases were formed when the overall CO_2 loading reached up to 0.2 mol mol^{-1}. The CO_2 loading in the rich (dense) phase increased over time and peaked around 6 mol L^{-1}. After dual phases were formed, the rich phase volume increased gradually until the rich phase CO_2 loading reached a certain level (e.g., 5 mol L^{-1} for solvent 1.5A3.5B and 6 mol L^{-1} for 2A3B). After that, the rich phase volume began to increase more rapidly upon CO_2 absorption while its CO_2 loading changed less. This was because the newly absorbed CO_2 was no longer concentrated in the rich phase but distributed through the volumetric expansion of the rich phase. The CO_2 loading in the lean (light) phase remained low during absorption, which was up to 0.3 mol L^{-1} at the end of the test, equivalent to up to 5% of the total amount of CO_2 absorbed, indicating a prevailing partition of CO_2 into the rich phase. Because DETA reacts with CO_2 faster than PMDETA, the later stage of CO_2 absorption in both solvents should rely more on the protonation of PMDETA and the formation of HCO_3^-/CO_3^{2-} species.

Compared with solvent 1.5A3.5B, solvent 2A3B had higher concentrations of both DETA and water, which favored the formation of a larger volume of the hydrophilic rich phase. This result was consistent with the observation that both the rich phase volume and the total CO_2 loading (lean and rich phases combined) of solvent 2A3B were greater than those of 1.5A3.5B at the same absorption time. The total CO_2 loadings (moles of CO_2 per mole of total amines) for the two biphasic solvents were compared with those of 30 wt% MEA under the same conditions (Fig. 6-2). Both solvents demonstrated greater absorption capacities than did the MEA solvent. For example, the CO_2 loading of solvent 2A3B was 35% higher than that of the MEA solvent at 90 min of absorption.

Table 6-1. Performance of CO_2 absorption into solvents 1.5A3.5B and 2A3B.

Solvent formula	Time (min)	No. of phases	Volume of rich phase (%)	CO_2 loading in lean phase (mol L^{-1})	CO_2 loading in rich phase (mol L^{-1})	Total CO_2 loading	
						(mol L^{-1})	(mol mol^{-1})
1.5A3.5B	0[a]	1	0	0	0	0	0
	10	2	31.2	0.09	1.94	0.67	0.153
	15[a]	2	31.5	0.13	2.48	0.87	0.213
	20	2	31.7	0.16	3.37	1.18	0.276
	40	2	36.0	0.18	4.75	1.82	0.433
	42.5[a]	2	37.0	0.20	5.03	1.99	0.462
	60	2	42.9	0.22	5.31	2.41	0.579
	75[a]	2	45.6	0.24	5.50 (1.102 mol mol^{-1})[b]	2.64	0.663
	90	2	48.3	0.25	5.85	2.96	0.712
	120	2	52.7	0.30	5.88	3.24	0.770
2A3B	0[a]	1	0	0	0	0	0
	10	2	40.5	0.18	1.52	0.72	0.172
	15[a]	2	40.8	0.18	2.17	0.99	0.254
	20	2	41.0	0.18	2.89	1.29	0.311
	37.5[a]	2	42.4	0.19	4.34	1.95	0.465
	40	2	42.7	0.19	4.64	2.09	0.502
	60	2	46.8	0.20	6.23	3.02	0.730
	60[a]	2	47.0	0.20	6.22 (1.163 mol mol^{-1})[b]	3.03	0.733
	90	2	57.0	0.23	5.95	3.49	0.813
	120	2	63.0	0.27	5.88	3.80	0.845

[a] Samples used for NMR analysis.
[b] Samples used as feed solutions in the desorption tests.

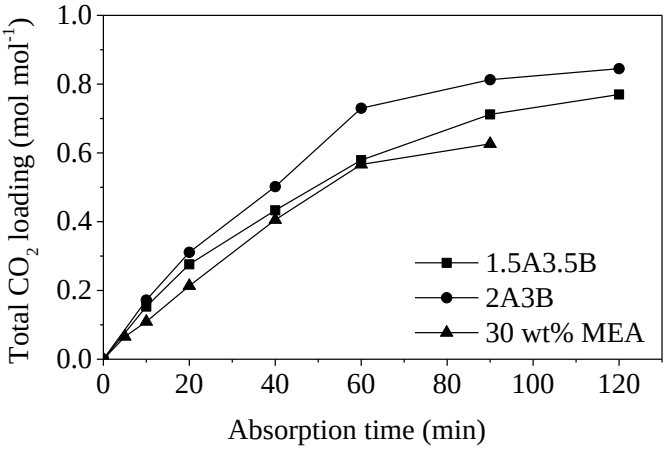

Fig. 6-2. CO_2 loading into 1.5A3.5B, 2A3B and 30 wt% MEA over time.

6.4.1.2 Identification of solvent species during CO_2 absorption

For both solvents, seven samples, i.e., a fresh sample and three pairs of CO_2 lean and rich phase samples, were collected for NMR analysis (marked with *a* in Table 6-1). These samples

represented different levels of CO_2 loading: fresh, low (29% of the capacity), medium (58% of the capacity) and high (86% of the capacity).

Comprehensive NMR results are provided in the supplementary information shown in Appendix B. The ^{1}H and ^{13}C spectra for the fresh, lean phase and rich phase samples from solvents 1.5A3.5B and 2A3B are shown in Figs. B-1 and B-2, respectively. The 2D NMR spectra of rich phase samples from solvents 1.5A3.5B and 2A3B are shown in Figs. B-3 and B-4, respectively. All the chemical shift values corresponding to individual protons and carbons assigned for each species (illustrated in Fig. 6-1) in the DETA/PMDETA/H_2O/CO_2 system are listed in Table B-1. Because proton signals could display a multiplet peak, the corresponding chemical shift was represented as the center of the multiplet (i.e., the average value). Representative ^{1}H and ^{13}C spectra are illustrated in Figs. 6-3 and 6-4, respectively, by using fresh solvent 2A3B and its CO_2 laden solvent with a total loading of 0.465 mol mol^{-1}. Correspondingly, representative 2D spectra (i.e., gCOSY, gHSQC and gHMBC) are illustrated in Fig. 6-5 by using the rich phase of solvent 2A3B at a total loading of 0.465 mol mol^{-1}.

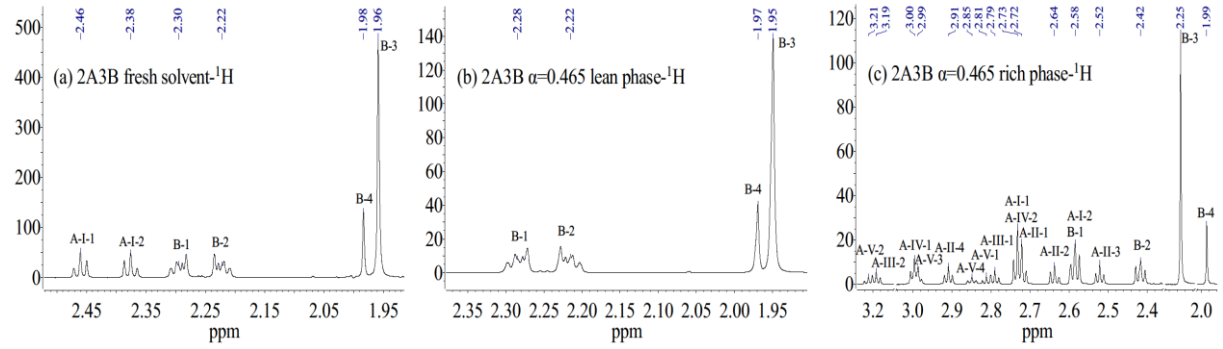

Fig. 6-3. ^{1}H spectra of solvent 2A3B at total CO_2 loadings of 0 (fresh solvent, panel a) and 0.465 mol mol^{-1} (panel b for the lean phase and panel c for the rich phase). For clarity, the assignment of each peak to an A or B group is provided in Table B-1.

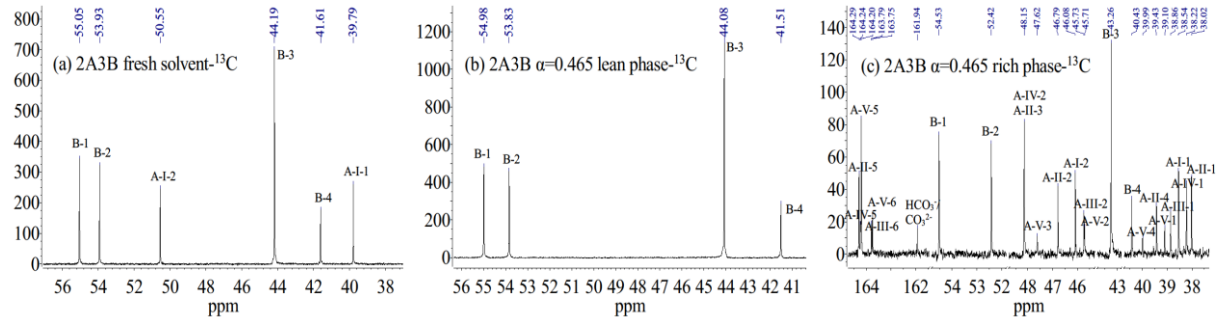

Fig. 6-4. ^{13}C spectra of solvent 2A3B at total CO_2 loadings of 0 (fresh solvent, panel a) and 0.465 mol mol^{-1} (panel b for the lean phase and panel c for the rich phase). For clarity, the assignment of each peak to an A or B group is provided in Table B-1.

According to Table B-1 and Figs. B-1 to B-4, all six lean phases obtained over the course of CO_2 absorption contained only molecular PMDETA, except for a sample from solvent 2A3B at a total CO_2 loading of 0.254 mol mol^{-1}, in which a small amount of molecular DETA was present. Such an exception was because DETA was not depleted completely at the initial period of CO_2 absorption in the lean phase of solvent 2A3B which contained more DETA than 1.5A3.5B. Neither protonated DETA nor protonated PMDETA species were present in the lean phase samples, as inferred from the fact that no oppositely charged carbamate and HCO_3^-/CO_3^{2-} species were detected. The separation of the lean phase from the rich phase was attributable to the limited solubility of PMDETA in the aqueous rich phase. The chemical shifts of the same H or C atom of PMDETA among the six lean phase samples were close to each other. The signals of the symmetrical H atoms from B1 or B2 sites (group B in Fig. 6-1) in these lean samples were a multiplet with a roof effect rather than a triplet because B1 and B2 sites were close in chemical shifts (comparing their J-coupling) to become a joint $B1_2$–$B2_2$ system.

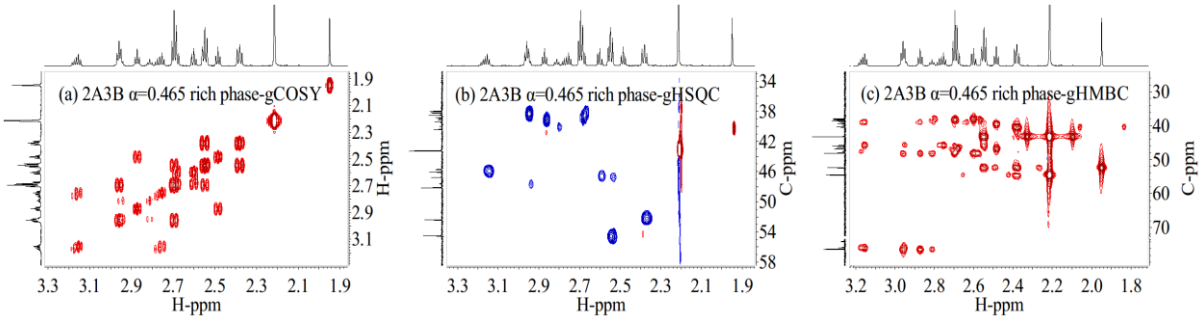

Fig. 6-5. 2D spectra of the CO_2 rich phase from solvent 2A3B at a total CO_2 loading of 0.465 mol mol^{-1}: (a) gCOSY, (b) gHSQC and (c) gHMBC spectra.

For the CO_2 rich phase samples, the patterns of ^{1}H and ^{13}C peaks were complicated compared with their lean phase counterparts because of the presence of multiple products from the reactions between amine species and CO_2. Based on the NMR results summarized in Table B-1, as the CO_2 loading increased for both solvents, the ^{1}H chemical shift of an individual functional site in each structural group of A or B shifted downfield; whereas, the ^{13}C chemical shift of it shifted upfield, with few exceptions (e.g., group A-V). The variation in chemical shift for the same site at various CO_2 loadings was due to the changing solvent pH, which caused changes in the concentrations of the protonated species and the shifts of NMR peaks, each of which represented an average signal of all related species (molecular and protonated) in a structural group of A or B. As a result, NMR peaks associated with different sites overlapped frequently. The spectral patterns for either ^{1}H or ^{13}C spectra were similar, but the intensity of an individual peak corresponding to the concentration of a structural group varied among samples. As more CO_2 was loaded, more vacant amino sites were occupied by a COO^- group, resulting in the formation of more carbamate and HCO_3^-/CO_3^{2-} species and the consumption of more molecular and protonated species. No tricarbamate species of DETA (i.e., group A-VI) were observed, which is consistent with the observation in literature (Hartono et al., 2007). For all the CO_2 rich samples, the ^{13}C chemical shifts of the C atoms in $–COO^-$ and HCO_3^-/CO_3^{2-} appeared consistently at 163 to 165 and 161 to 162 ppm, respectively, which was because their stable local electron environment was unaffected by the solvent pH.

6.4.1.3 Quantification of solvent species during CO_2 absorption

The lean phase samples contained only PMDETA molecules, except that a 2A3B sample at a total CO_2 loading of 0.254 mol mol^{-1} retained a small amount of DETA (8 mol% of total lean phase amines). By contrast, five structural groups of DETA species, A-I, A-II, A-III, A-IV and A-V, were detected in all the CO_2 rich phases. Their fractions in the rich phase at different total CO_2 loadings during CO_2 absorption are displayed in Fig. 6-6. For both solvents, the group A-I species (molecular and protonated DETA) were converted rapidly; thus, their concentrations decreased during CO_2 absorption. At the end of the absorption, the molar fraction of A-I was less than 10% among the total DETA species. The group A-II species (primary carbamate of DETA and its protonated species) was predominant during the early period of CO_2 absorption, but their

molar fractions decreased thereafter because of their conversion to the species belonging to group A-IV (primary-primary dicarbamate of DETA and its protonated species) and group A-V (primary-secondary dicarbamate of DETA and its protonated species). The final fraction of group A-II remained above 20%. Group A-III species (secondary carbamate of DETA and its protonated species) was present in small quantities during CO_2 absorption (less than 10% in the molar fraction for all the tested samples). Both the A-IV (converted solely from A-II) and A-V (converted mostly from A-II) groups showed increasing molar fractions with increasing CO_2 loadings, but the molar fraction of group A-IV was higher than that of group A-V during CO_2 absorption. Based on the observations above, a primary amino group of DETA was more reactive than the secondary amino group in forming either a monocarbamate or dicarbamate species. In addition, once a primary amino group on DETA was converted to a carbamate species, the secondary amino group became "activated". No tricarbamate of DETA (group A-VI) was detected in any sample.

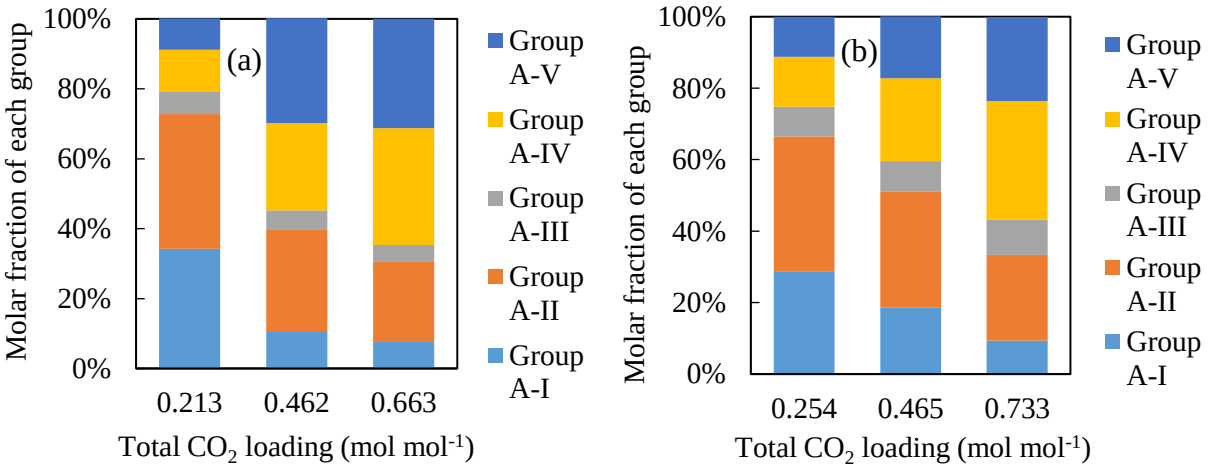

Fig. 6-6. Quantitative speciation of DETA in the CO_2 rich phases of (a) solvent 1.5A3.5B and (b) solvent 2A3B during CO_2 absorption.

The fraction of group B species (i.e., molecular PMDETA and its protonated species) distributed in the rich phase increased with the total CO_2 loading in both solvents (Fig. 6-7). An increasing amount of PMDETA was transferred to the rich phase and became "soluble" in it, likely through protonation reactions with the protonated DETA species. As the amount of HCO_3^-/CO_3^{2-} species increased in the rich phase, PMDETA played a greater role in the later period of CO_2 absorption (Fig. 6-7). Considering the formation of HCO_3^-/CO_3^{2-} caused by the dissolution of carbamate

species of DETA alone would not occur until at high CO_2 loadings (>1.3 mole of CO_2 per mole of DETA) (Hartono et al., 2007), and PMDETA (as a tertiary amine) alone absorbed CO_2 slowly, the rising NMR peaks of HCO_3^-/CO_3^{2-} over time should be attributable to a mutual effect between DETA and PMDETA. Both CO_2 hydration and production of HCO_3^-/CO_3^{2-} were promoted by an increasing consumption of protons, indicated by the formation of more protonated PMDETA which was favored by proton exchange reactions between PMDETA and the abundantly available protonated DETA species. In addition, as the amino groups of DETA protonated initially were recovered through proton exchange with PMDETA, they could be reprotonated or bonded with CO_2 to form carbamate species and provide extra CO_2 capacity. Assuming all HCO_3^-/CO_3^{2-} species were derived from PMDETA, the contributions of PMDETA to total CO_2 uptake were 0, 13.9 and 25.5% for solvent 1.5A3.5B and were 0%, 6.9 and 13.5% for solvent 2A3B at the respective three increasing CO_2 loadings. The molar fractions of both HCO_3^-/CO_3^{2-} and PMDETA species in the rich phase of solvent 1.5A3.5B were greater than those of 2A3B under similar conditions (Fig. 6-7).

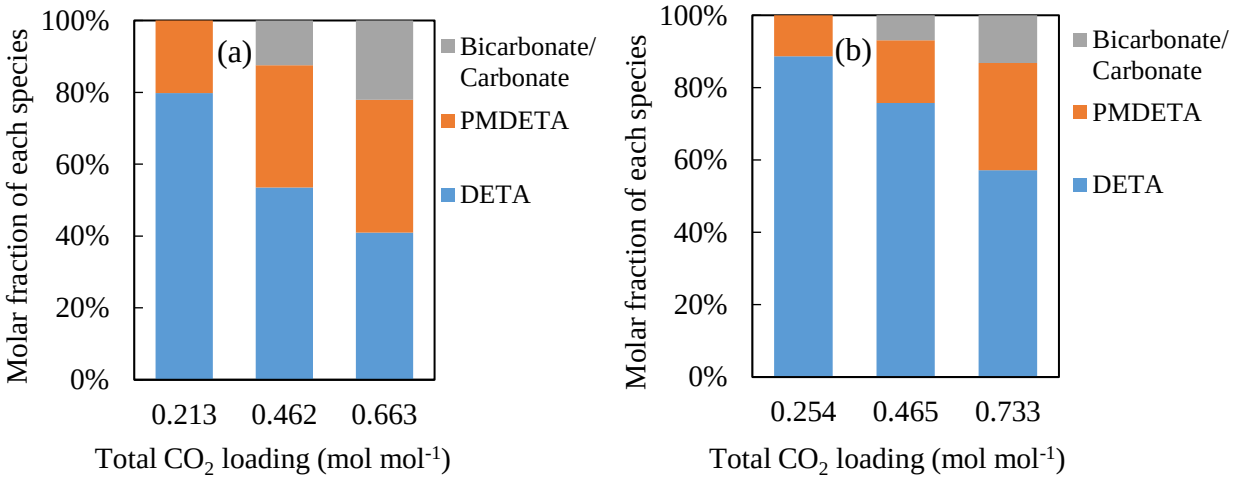

Fig. 6-7. Quantitative speciation of PMDETA and HCO_3^-/CO_3^{2-} in CO_2 rich phases of (a) solvent 1.5A3.5B and (b) solvent 2A3B during CO_2 absorption.

6.4.2 CO_2 desorption and solvent speciation

6.4.2.1 Pressure of CO_2 desorption

Tests of CO_2 desorption were carried out at 120°C with the CO_2 rich phase samples obtained from the absorption tests for the two solvent blends. The compositions of these two feed samples were described previously (Table 6-1, and Figs. 6-6 and 6-7). Desorption test results are

summarized in Table 6-2. During the desorption process, the CO_2 rich feed solution also underwent a phase separation. This could be caused by two factors. First, the reverse reactions of CO_2 absorption occurred, resulting in the regeneration of molecular PMDETA, which was less hydrophilic than the ionic species and thus formed a separate PMDETA rich phase from the bulk solution. Second, a thermally induced phase separation could occur as dual phases were observed when the feed solution was heated to 80°C. Phase transition from the CO_2 rich phase itself used for desorption can be useful in designing a stripping process with interstage phase separations. As a result, desorption tests No. 2 and 3 began with solutions containing a dense phase and a light phase.

Table 6-2. Key parameters including the equilibrium CO_2 pressure and CO_2 loading during desorption at 120°C.

Solvent	Test	Test no.		
		1	2	3
1.5A3.5B	Start solution	CO_2 rich phase from absorption tests	Solvent from test 1	Solvent from test 2
	Total CO_2 loading of the start solution (mol mol^{-1})	1.102	0.722	0.469
	Number of liquid phases of the start solution	1	2	2
	Vol% of the dense phase of the start solution	100	75.2	59.1
	Total CO_2 loading at equilibrium (mol mol^{-1})	0.837	0.631	0.449
	CO_2 partial pressure at equilibrium (kPa)	1684.8	583.0	127.8
2A3B	Total CO_2 loading of the start solution (mol mol^{-1})	1.163	0.852	0.549
	Number of liquid phases of the start solution	1	2	2
	Vol% of the dense phase of the start solution	100	77.8	63.0
	Total CO_2 loading at equilibrium (mol mol^{-1})	0.972	0.782	0.533
	CO_2 partial pressure at equilibrium (kPa)	1642.5	599.5	133.4

The measured partial pressures of CO_2 as a function of the total CO_2 loadings in the liquid are plotted in Fig. 6-8. For comparison purposes, the VLE data for 30 wt% MEA is included (Aronu et al., 2011). The CO_2 loading was given by the moles of CO_2 per mole of total amines. Assuming the CO_2 loading during desorption for MEA was reduced from 0.5 mol mol^{-1} (rich) to 0.25 mol mol^{-1} (lean), a cyclic capacity of 1.25 mole of CO_2 per kg of solvent was reached, with a total stripping pressure of 200 kPa at 120°C contributed mostly by the water vapor partial pressure (Aronu et al., 2011). In comparison, assuming the CO_2 loading of the 2A3B rich phase solvent was reduced from 0.9 to 0.5 mol mol^{-1} during desorption, a cyclic capacity of 2.5 mole of CO_2 per kg of total solvent was obtained, with a total stripping pressure of 330 kPa at 120°C

(130 and 200 kPa of CO_2 and water vapor partial pressures, respectively). Therefore, the biphasic solvent blend had both a larger cyclic loading capacity and a higher total pressure for CO_2 stripping than did MEA, which would be beneficial for reducing the energy use. The CO_2 partial pressures over the tested samples derived from solvent 1.5A3.5B were greater than those from solvent 2A3B under the same CO_2 loadings, because of the higher concentrations of PMDETA in solvent 1.5A3.5B derived samples.

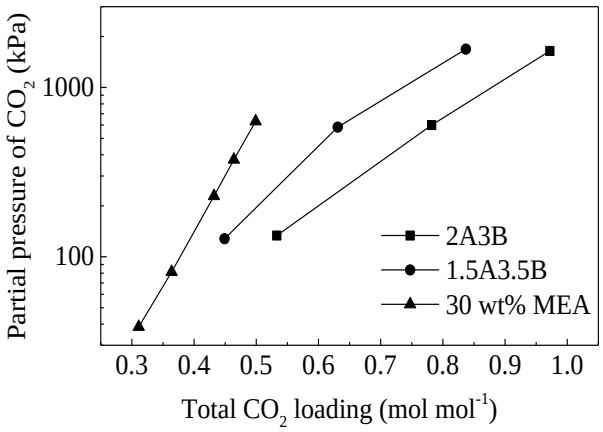

Fig. 6-8. CO_2 partial pressure as a function of total CO_2 loading (moles of CO_2 per mole of total amines) in the liquid phase.

6.4.2.2 Identification of solvent species during CO_2 desorption

All the lean and rich liquid phases that formed during the aforementioned CO_2 desorption tests at different CO_2 loadings were sampled for NMR analysis. A complete set of ^{1}H, ^{13}C and 2D spectra obtained for each sample are provided in Figs. B-5 to B-8 and the assignment of peaks is summarized in Table B-2 in Appendix B. The results of the samples used in test 1 were not provided because they were the same as the rich phase samples from solvents at the highest CO_2 loadings used for CO_2 absorption based NMR analysis (Section 6.4.1.2 and Table 6-1). The ^{1}H and ^{13}C spectra for the lean and rich phases and the 2D spectra for the rich phase of a typical desorption sample, i.e., the sample derived from 1.5A3.5B used for test No. 2, are displayed in Figs. 6-9 and 6-10, respectively.

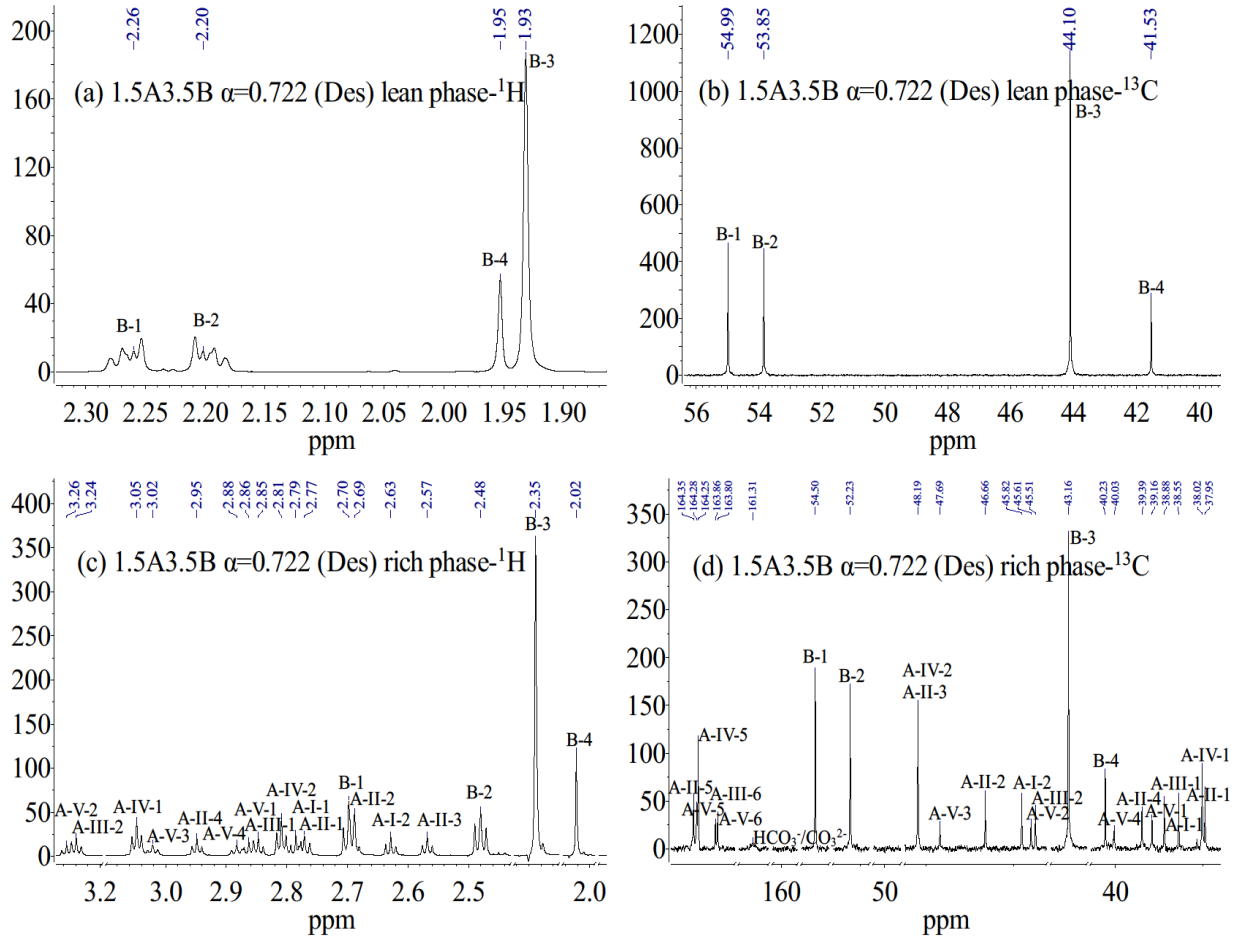

Fig. 6-9. NMR spectra of the desorption sample from solvent 1.5A3.5B at a CO_2 loading of 0.722 mol mol^{-1}: (a) and (b) ^{1}H and ^{13}C for the lean phase, and (c) and (d) ^{1}H and ^{13}C for the rich phase. For clarity, the assignment of each peak to an A or B group is provided in Table B-2.

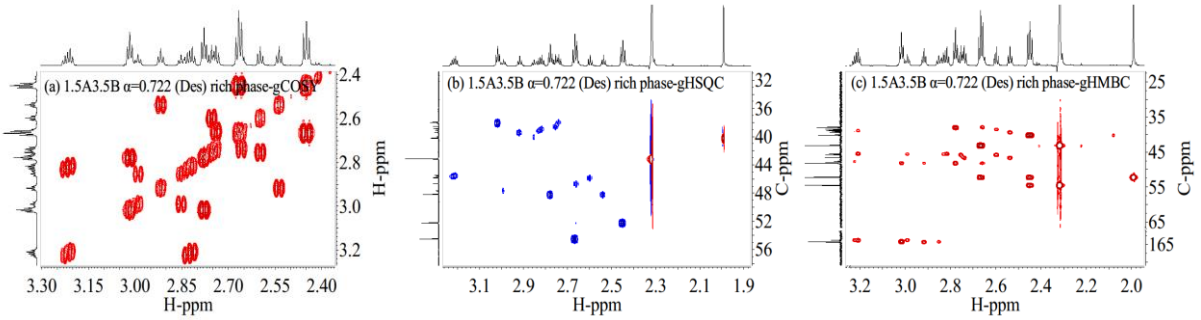

Fig. 6-10. 2D spectra of the desorption samples from solvent 1.5A3.5B at a CO_2 loading of 0.722 mol mol^{-1}: (a) gCOSY, (b) gHSQC and (c) gHMBC.

The lean phase samples formed during desorption contained molecular PMDETA only. Thus, the NMR spectra for the lean phase of desorption samples were similar to those for the lean phase of absorption samples. Molecular PMDETA was a product of CO_2 desorption when HCO_3^-/CO_3^{2-} accepted protons and the protonated PMDETA was regenerated to its molecular form. The NMR spectra for the desorption samples were similar to those from the absorption tests, indicating that desorption is a reverse process of absorption, with the desorption reactions in the dense (rich) phase and the regenerated molecular PMDETA partitioned to the newly formed light (lean) phase. As the CO_2 loading decreased in the samples, the ^1H chemical shifts of all the characteristic functional sites in both A and B groups shifted upfield or remained the same, but those of the ^{13}C spectra shifted downfield, with few exceptions. Similar to the absorption samples, variations in chemical shifts for the same site were due to pH changes during desorption. Among all the dense phase samples in the desorption tests, the corresponding peaks of an individual structural group on either ^1H or ^{13}C spectra were similar in patterns but their intensities varied, i.e., varying concentrations of a structural group among samples. As more CO_2 was desorbed, more occupied amino sites became available and greater amounts of molecular PMDETA and group A-I species were produced, with fewer carbamate and dicarbamate species remaining. Similarly, HCO_3^-/CO_3^{2-} species (with a ^{13}C chemical shift at 161 to 162 ppm) disappeared when the CO_2 loading was decreased to low levels.

6.4.2.3 Quantification of solvent species during CO_2 desorption

On the basis of the NMR analysis, the partitions of species from the feed solutions and the dense phases of the desorption samples are shown in Fig. 6-11. The results for the lean phase formed during desorption are not shown because this phase contained molecular PMDETA only. For solvent 1.5A3.5B, the molar fractions of PMDETA in the lean phase before tests No. 2 and 3 began were 51.3 and 76.6%, respectively. For solvent 2A3B, the corresponding molar fractions were 41.9 and 52.8%, respectively.

As shown in Fig. 6-11, the concentration of HCO_3^-/CO_3^{2-} decreased rapidly during desorption. At the end of desorption tests (with the CO_2 loading reduced to 0.469 mol mol^{-1} for 1.5A3.5B and 0.549 mol mol^{-1} for 2A3B), HCO_3^-/CO_3^{2-} species disappeared completely. The amount of total PMDETA in the CO_2 rich phase decreased as desorption proceeded as a result of the regenerated

molecular PMDETA being transferred to the newly formed lean phase. As expected, the concentration of group A-V species of DETA decreased throughout the CO_2 desorption, resulting in the production of species belonging to groups A-III and A-II. The A-III species accounted for 10% of the total DETA, which was smaller than that of A-II. It was difficult to quantify the fractions of A-V species to form A-III and A-II, and the fractions of A-III and A-II species to form A-I. Overall, groups A-I and A-II reached 25 and 40%, respectively, of the total DETA for either solvent by the end of the desorption tests.

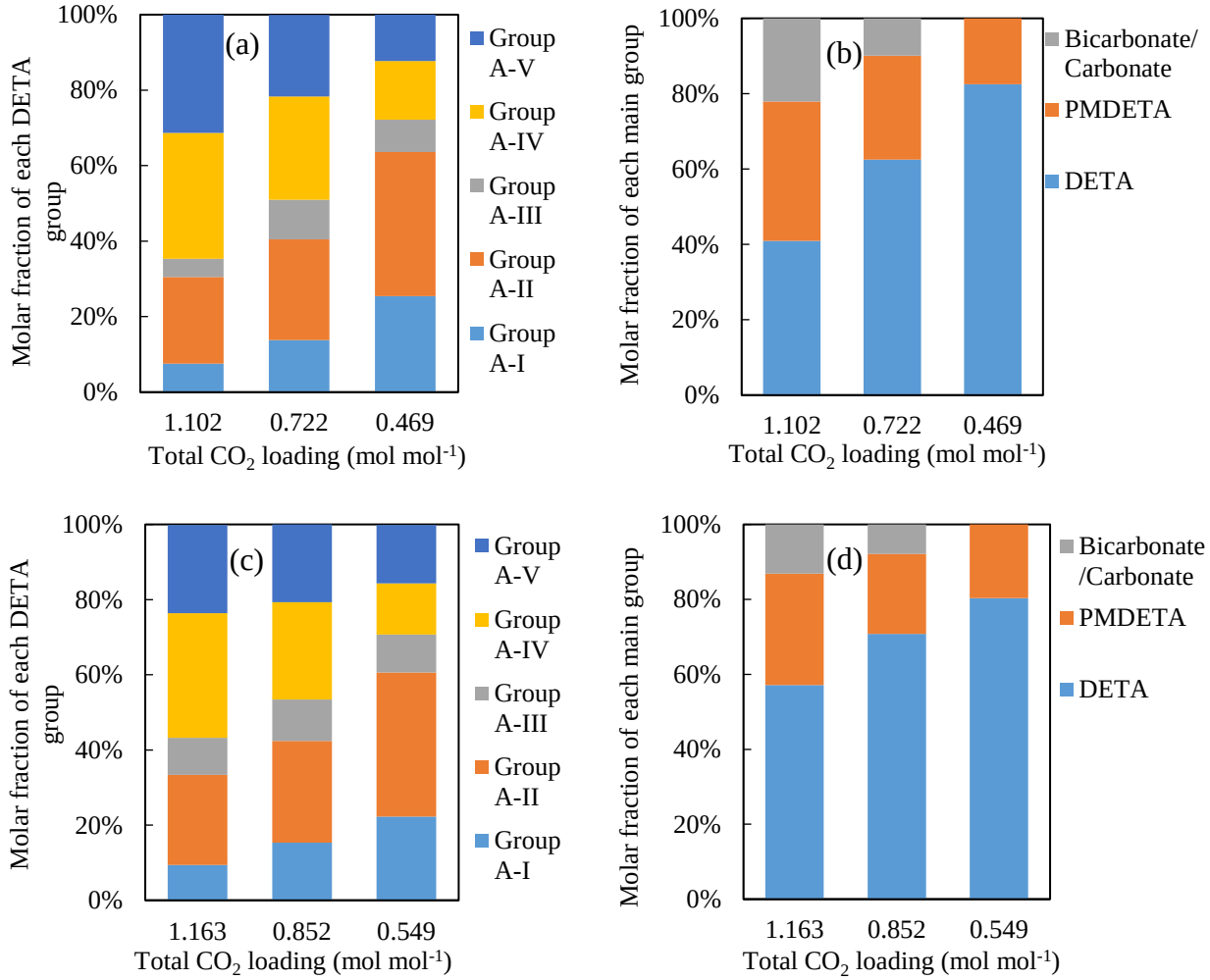

Fig. 6-11. Evolution of solvent species during CO_2 desorption: partitions of (a) structural groups of DETA and (b) DETA, PMDETA and HCO_3^-/CO_3^{2-} in the desorption samples (feed solution or dense phase) derived from solvent 1.5A3.5B; partitions of (c) structural groups of DETA and (d) DETA, PMDETA and HCO_3^-/CO_3^{2-} in the desorption samples (feed solution or dense phases) derived from solvent 2A3B. The feed solution has only one phase with a CO_2 loading of 1.102 or 1.163 mol mol^{-1}.

6.4.3 Mechanism of CO_2 absorption and desorption reactions

In a fresh solvent, DETA reacted faster than PMDETA with CO_2, and phase separation occurred after a certain CO_2 loading was reached because molecular PMDETA had limited aqueous solubility and did not transport with the DETA derived ionic species into the CO_2 rich phase formed. Therefore, molecular PMDETA species predominated in the oily phase that was lean in CO_2, and ionic DETA species predominated in the aqueous phase that was rich in CO_2. Because CO_2 did not remain in the lean phase, further mass transfer of CO_2 could occur across the interface between CO_2 and the rich phase. Reactions of CO_2 absorption occurred in the CO_2 rich phase, with DETA depleted soon in the lean phase. This result was consistent with the fact that the volume of the rich phase expanded throughout the process of CO_2 absorption, which could be divided into two stages. In the first stage, the absorbed CO_2 bonded onto DETA associated species, inducing a continuously increasing concentration of CO_2 in the rich phase with gradual volumetric expansion. In the second stage, a large amount of PMDETA was transferred across the lean-rich interface and became miscible in the rich phase because of its protonation reactions with high concentrations of the protonated species of DETA via proton exchange. As a result, the rich phase underwent a volumetric expansion, with many HCO_3^-/CO_3^{2-} species formed through reactions (6-2) and (6-3) enhanced by PMDETA as a base catalyst. The "two stage" process was similar to those mentioned in other biphasic solvent studies, in which the tertiary amine was reacted and the product species dissolved in the rich phase after the derivatives of the rate activator had appeared through reactions with CO_2 (Pinto et al., 2014b; Xu et al., 2013a).

The evolution of the lean-rich phase separation and all major reaction pathways during CO_2 absorption in the solvent mixture are illustrated in Fig. 6-12a. Arrow (1) represents the period from initial CO_2 absorption until the occurrence of phase separation, during which CO_2 was converted to the primary carbamate of DETA and the associated species of protonated DETA. Arrow (2) represents the first stage in the two stage process described above after phase separation occurred, during which CO_2 was absorbed and concentrated in the rich phase with minor volumetric expansion. In this stage, the dicarbamate (primary-primary and primary-secondary) species of DETA were produced in high quantities, and a portion of PMDETA molecules were protonated via proton exchange reactions to facilitate the hydration of CO_2 and

formation of HCO_3^-/CO_3^{2-} while recovering the amino sites on DETA simultaneously and increasing the CO_2 loading capacity. Arrow (3) represents the second stage after phase separation occurred, in which the volume of the rich phase increased rapidly because of the increasing role of PMDETA in CO_2 absorption in the rich phase.

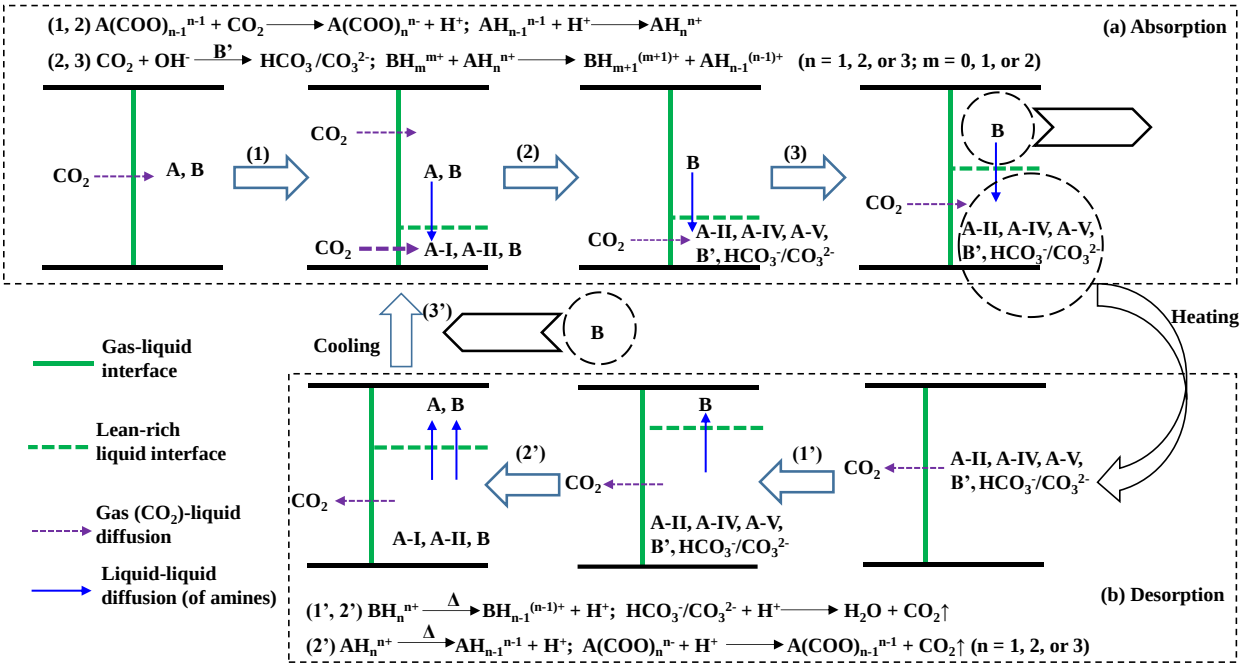

Fig. 6-12. Mechanisms of the closed loop of (a) CO_2 absorption into the biphasic blend of DETA and PMDETA and (b) CO_2 desorption from its CO_2 rich phase. The green solid and dashed lines denote the gas-liquid and lean-rich liquid interfaces, respectively. The purple dashed arrows denote the mass transfer of CO_2 from gas to liquid phase or the opposite; whereas, the blue arrows denote the diffusion of amines A and B from one liquid phase to the other. All the block arrows denote the stages between two characteristic system states. A, B, A-I, A-II, A-III, A-IV and A-V, and B′ denote molecular DETA, molecular PMDETA, species of different DETA groups and species of group B, respectively.

Understanding the mechanisms governing reactions of CO_2 absorption and phase separation is crucial in formulating solvents and optimizing the CO_2 loading capacity. For a biphasic system consisting of DETA and PMDETA, their proper ratio will result in the optimal CO_2 loading capacity and extent of phase separation. The smaller the amount of DETA in the solution, the sooner the step of arrow (2) ends. At the same time, a small portion of DETA will reduce the

overall CO_2 loading capacity because this will reduce its promotional effect on the overall CO_2 reaction with PMDETA.

At the end of an absorption experiment, the CO_2 rich phase was subjected to desorption under elevated temperature. The mechanisms of CO_2 desorption reactions were proposed based on results of the speciation analysis, as illustrated in Fig. 6-12b. Arrow (1') represents the reactions of HCO_3^-/CO_3^{2-} associated with protons (released from the protonated PMDETA species via heating) and the regeneration reactions of protonated PMDETA, which occurred during the initial stage of the desorption process. The regenerated molecular PMDETA facilitated the formation of the lean phase and was partitioned into this new phase because of its low hydrophilicity. Arrow (2') represents the depletion of HCO_3^-/CO_3^{2-} and the regeneration of carbamate species in the CO_2 rich phase, which predominated during this stage. The first route for DETA regeneration included two steps: the conversion of group A-IV and A-V species to group A-II and further to group A-I, accompanied by the release of CO_2 in each step. The second route for DETA regeneration was via the conversion of group A-V species to group A-III and further to group A-I. The protons required for both routes were released from the protonated DETA species via heating. The first route was deemed to be the primary process because group A-II had a dominant presence compared with group A-III during desorption (Fig. 6-11). Arrow (3') represents the combination of the lean phase separated from the solvent at the end of the CO_2 absorption (arrows 1 to 3) with the regenerated solvent obtained from the CO_2 desorption (arrows 1' to 3'). The resultant solvent corresponded to the one used for CO_2 absorption which was under the conditions of the stage between arrows 1 and 2. The absorption and desorption pathways shown in Fig. 6-12 constitute a closed absorption-desorption loop.

6.5 Conclusions

Two aqueous biphasic solvent blends, consisting of DETA and PMDETA, were investigated with respect to their absorption, phase transition and desorption performance. Both solvents demonstrated absorption capacities at 40°C and CO_2 desorption pressures at 120°C more favorable than MEA. The evolution of solvent species during CO_2 absorption and desorption was determined quantitatively by ^1H, ^{13}C and 2D NMR spectroscopic techniques. During absorption,

multiple structural groups of species were detected, including carbamates and dicarbamates of DETA and HCO_3^-/CO_3^{2-}. The primary carbamates prevailed at low CO_2 loadings and the primary-primary and primary-secondary dicarbamates prevailed at higher CO_2 loadings. Protonation of PMDETA played a role in CO_2 absorption by inducing the formation of HCO_3^-/CO_3^{2-} and the partial reactivation of the consumed DETA species in the CO_2 rich phase. The reverse reactions of CO_2 absorption occurred during CO_2 desorption, as implied by the rapid consumption of HCO_3^-/CO_3^{2-} species as the CO_2 loading decreased and a newly formed CO_2 lean phase enriched in molecular PMDETA. At the late stage of desorption, DETA became regenerated by the conversion of dicarbamates to carbamates and further to protonated or molecular DETA.

During CO_2 absorption, CO_2 gas was absorbed into the rich phase, where DETA was reacted and converted, followed by the protonation of PMDETA and the formation of HCO_3^-/CO_3^{2-}. As a result of the protonated PMDETA being transferred from the lean phase to the rich phase, the latter underwent a volumetric expansion. The formation of HCO_3^-/CO_3^{2-} was attributable to the proton exchange reactions, where CO_2 hydration occurred with catalytic enhancement in the presence of PMDETA. During CO_2 desorption, HCO_3^-/CO_3^{2-} species accepted protons produced by heating the protonated PMDETA, resulting in the release of CO_2 and the formation of a new, oily CO_2 lean phase due to the limited solubility of molecular PMDETA in the aqueous CO_2 rich phase. Further desorption of CO_2 incurred the association of protons (released from the protonated DETA species via heating) with carbamate or dicarbamate species to release CO_2 and recover molecular DETA.

CHAPTER 7: EXPERIMENTAL INVESTIGATION AND THERMODYNAMIC MODELING OF PHASE TRANSITION AND EQUILIBRIA IN A BIPHASIC SOLVENT SYSTEM FOR CO_2 CAPTURE

7.1 Introduction

Biphasic solvents have attracted growing attention as potential alternatives to the benchmark aqueous MEA solvent for PCC (Pinto et al., 2014b; Raynal et al., 2011b; Wang et al., 2016; Ye et al., 2015b; Zhang et al., 2013; Broutin et al., 2017). As a result of biphasic separation, the mass of solvent required for CO_2 stripping is reduced, leading to a smaller equipment footprint and less sensible heat use. The high CO_2 loading in the CO_2 rich phase is beneficial for maintaining a high CO_2 stripping pressure, which can lower the stripping heat use and CO_2 compression work requirement. Therefore, a biphasic solvent enabled process can reduce the energy use required for CO_2 capture and compression. For example, a biphasic solvent system composed of MAPA and DEEA has resulted in a reboiler heat duty as low as 2.2 GJ/ton of CO_2 (Liebenthal et al., 2013).

The VLLE behavior is important for a biphasic solvent system because it is relevant to several critical solvent properties, such as the CO_2 loading capacity, CO_2 desorption pressure and heat of reaction. However, few efforts at modeling biphasic solvent systems have been reported in the literature. A UNIQUAC model was applied to regress the measured VLE data for CO_2 unloaded neat MAPA solutions, neat DEEA solutions, and MAPA-DEEA blends (Hartono et al., 2013). More recently, a model based on the Extended UNIQUAC framework was developed to study CO_2 solubility in neat MAPA, neat DEEA and their biphasic blends (Arshad et al., 2016). The model parameters were obtained by fitting a large amount of measured CO_2 solubility data. The developed model was used to predict the mixed thermodynamic properties of the solvent blends, including the freezing point, liquid speciation, CO_2 partial pressure and heat of absorption. The liquid-liquid equilibrium (LLE) was represented by binodal curves of the total molality of MAPA against the total molality of DEEA in the dual phases. However, the modeling of LLPS was lacking, such as the volume and speciation in each of the two phases in equilibrium with varying temperatures and CO_2 loadings.

Compared with modeling a monophasic solvent, modeling a biphasic solvent system is more complex because it involves three phase (vapor-liquid-liquid) equilibria and CO_2 absorption in the two liquid phases. Research efforts are required to develop VLLE models to describe biphasic solvent systems for the CO_2 capture application.

Our group previously investigated a biphasic solvent blend of DETA and PMDETA. This solvent blend showed a fast absorption rate and high CO_2 loading capacity and could attain an elevated CO_2 desorption pressure (Ye et al., 2017b). Laboratory experiments were carried out to measure the VLLE data of two quaternary systems of DETA-PMDETA-H_2O-CO_2 under different temperatures typical of CO_2 absorption and desorption operations. A thermodynamic model that incorporated all chemical reactions and phase equilibria of such solvent systems was developed to predict the VLLE performance. The binary interaction parameters (BIPs) and unknown reaction equilibrium constants required in the thermodynamic model were retrieved from the experimentally measured VLLE and VLE data by data regression. The thermodynamic model was used to predict LLPS and species distribution in the two liquid phases under different temperatures and CO_2 loadings. The model predictions agreed with the experimentally measured VLLE data.

7.2 Material and methods

Compressed CO_2 and N_2 with a high purity (>99.9%, S.J. Smith Co.) were used in all the experiments. DETA, PMDETA and MEA (>99%, Sigma Aldrich) were used without further purification. An aqueous neat DETA solution (2 mol kg^{-1} of DETA in water, abbreviated as 2A) and two formulae of the aqueous DETA and PMDETA blend (2 mol kg^{-1} of DETA mixed with 3 mol kg^{-1} of PMDETA in water, abbreviated as 2A3B, and 1.5 mol kg^{-1} of DETA mixed with 3.5 mol kg^{-1} of PMDETA, abbreviated as 1.5A3.5B) were investigated. All the fresh solvents were prepared by mixing certain amounts of amines with deionized water at room temperature. The total liquid CO_2 loading (molality based) was analyzed by the mass difference before and after CO_2 was loaded to a fresh solvent. The equilibrium data were measured in two apparatuses, one operating at low temperatures (up to 70°C) and CO_2 partial pressures (up to 1 bar) typical for

CO_2 absorption, and the other at high temperatures (up to 130°C) and pressures (up to 50 bar) typical for CO_2 desorption.

7.2.1 Experimental setup for equilibrium measurements under absorption conditions

A gas-liquid equilibrium cell system (Fig. 7-1) was set up to measure the VLE or VLLE data at 25, 40 and 55°C for the three solvents. The equilibrium cell is a Plexiglass vessel with an ID of 4.5 inches and a height of 5 inches. The liquid inside the cell was stirred at a controllable speed up to 1,000 rpm with a magnetic stirrer (Variomag Mobil 25, Thermo Scientific) placed below the cell. The vapor phase was mixed by circulating the gas at 1 L min^{-1} using a microdiaphragm pump (Air Dimensions Inc.). The end of the tube connecting the inlet of the pump was positioned in the vapor phase to withdraw the gas, and the end of the tube connecting the outlet of the pump was immersed in the liquid to ensure thorough mixing between the circulating gas and liquid phase. Temperature control was provided by an external isothermal water bath (±0.1°C) connected with a heating coil placed inside the equilibrium cell. A N_2 cylinder was connected to flush the cell before each test began so that the initial vapor phase was considered pure N_2. The cell temperature was measured by a thermocouple, and a pressure transducer (PX409-050AUSBH, Omega) was connected to monitor the real time pressure of the gas phase. A gas sample was withdrawn with a 0.5 mL syringe (Restek Corporation) through a 1 cm septum fit into a sampling port in the gas loop. The collected sample was injected into a gas chromatograph (GC-2014, Shimadzu) equipped with a fused silica column (Restek Corporation) for composition analysis.

In a typical experiment, 350 g of a solvent with a known composition and amount of CO_2 loaded was fed to the equilibrium cell. The cell was flushed with pure N_2 for 30 s and closed with valves. Both the water bath and magnetic stirrer were turned on, and the equilibrium cell was heated by the heating coil until the thermocouple inside the cell gave a reading close to the preset temperature (25, 40 or 55°C). Meanwhile, the gas circulation pump was switched on as the system approached equilibrium. At equilibrium, the total system pressure was recorded. Water vapor pressure was estimated by Raoult's law and subtracted from the measured total pressure. The partial pressure of CO_2 was estimated from the molar ratio of N_2 to CO_2 determined by a GC measurement. At the end of a run, the system pressure was released, and the solvent inside the

cell was measured to determine the solvent mass loss (1% in each test) and was used to prepare a solvent with a higher CO_2 loading. The procedure above was repeated until a series of gaseous CO_2 partial pressures (0.02 to 14 kPa) and corresponding total liquid CO_2 loadings were obtained.

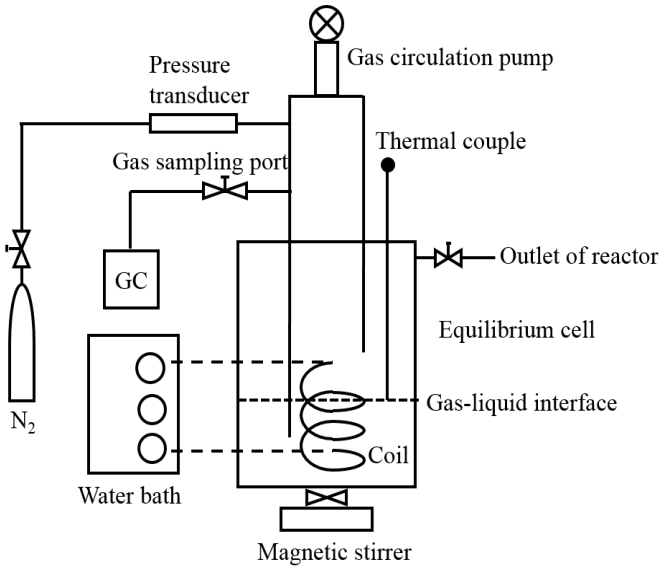

Fig. 7-1. Experimental setup for VLE and VLLE measurements under low temperature conditions.

7.2.2 Experimental setup for equilibrium measurements under desorption conditions

A high pressure reactor system (Great Wall Instrument; Fig. 7-2) was used to measure the VLE or VLLE data at 80, 100 and 120°C for the three CO_2 loaded solvents. The reactor was a 6.5 cm ID, 12 cm high cylindrical vessel rated at 350°C and 220 bar. A variable speed magnetic stirrer (Cole-Parmer, UX-04801-50) was used to mix the solution. A heating mantle with a temperature control unit was used to heat the reactor, and the real time temperature of the reactor was measured with a Type K thermocouple and logged by a temperature transmitter (MWTC-A-K-915, Omega). An external vacuum pump (DuoSeal 1402, Welch) provided the initial vacuum of the system before each test began. The real time pressure of the reactor was measured by a pressure transducer (PX409-750AUSBH, Omega). Gas samples were withdrawn from the reactor and analyzed by GC following a procedure similar to that mentioned in Section 7.2.1.

In a typical measurement, 100 mL of a CO_2 laden solvent (with a known solvent composition and CO_2 loading) was fed to the reactor. After assembly and leakage detection, the system was

vacuumed to the desired level at ambient temperature. The solvent was heated to a preset temperature with continuous stirring at 300 rpm. When the system reached equilibrium, as evidenced by negligible changes in the pressure reading over at least half an hour, the proper amount of pure N_2 gas was introduced to the reactor as an inert tracer. After stabilization, the partial pressure of N_2 in the reactor was measured as the difference between the total pressures before and after N_2 injection. A gas sample was extracted with a syringe through the sampling port for GC analysis. The partial pressure of CO_2 was calculated based on the measured molar ratio of N_2 to CO_2 in the gas sample. The equilibrium total CO_2 loading in the liquid was estimated by subtracting the portion of CO_2 in the gas phase from that in the initial CO_2 laden solvent. The foregoing procedure was repeated for multiple measurements until VLE or VLLE data were obtained at the starting CO_2 loading of each measurement across an appropriate operating range.

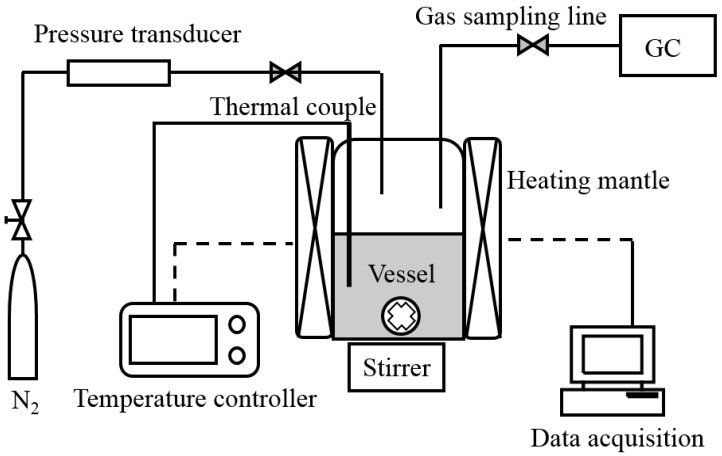

Fig. 7-2. Experimental setup for VLE and VLLE measurements under high temperature conditions.

The methodology adopted for measuring the VLE or VLLE under either the absorption or desorption conditions described above was validated by the good agreement between the data obtained for the aqueous MEA solution (30 wt%) compared with those reported in the literature.

7.3 Thermodynamic modeling

7.3.1 Main species in the equilibrium system

Because the equilibrium system involved multiple phase and chemical equilibria, determining the equilibrium composition in each phase was crucial. As reported in our previous speciation study using NMR spectroscopy, multiple amino groups in a DETA or PMDETA molecule could act as a base to receive a free proton or bond with a CO_2 molecule to form a carbamate group, resulting in the formation of various neutral and ionic species (Ye et al., 2017).

For the ternary DETA-H_2O-CO_2 system (i.e., the aqueous neat DETA solution), the monophasic liquid at equilibrium contained water, CO_2 and DETA molecules, as well as the following ionic or neutral species: H^+, OH^-, HCO_3^-, CO_3^{2-}, $DETAH(p)^+$, $DETAH(s)^+$, $DETAH_2(pp)^{2+}$, $DETAH_2(ps)^{2+}$, $DETAH_3^{3+}$, $DETACOO(p)^-$, $DETACOO(s)^-$, $DETA(COO)_2(pp)^{2-}$, $DETA(COO)_2(ps)^{2-}$, $DETAH(p)^+COO(p)^-$, $DETAH(s)^+COO(p)^-$, $DETAH(p)^+COO(s)^-$, $DETAH_2(ps)^{2+}COO(p)^-$, $DETAH_2(pp)^{2+}COO(s)^-$, $DETAH(s)^+(COO)_2(pp)^{2-}$ and $DETAH(p)^+(COO)_2(ps)^{2-}$, where "p" and "s" denote the primary and the secondary amino groups, respectively. Such a large number of species would make establishing the model and regression calculations rather difficult; thus, reasonable simplification was needed. Because the primary amino group on DETA is the preferential site to accept a proton, species of $DETAH(s)^+$, $DETAH_2(ps)^{2+}$ and $DETAH(s)^+COO(p)^-$ were disregarded in the model. For a fresh DETA molecule, the primary amino group is the dominant site where a CO_2 molecule is bonded, so $DETACOO(s)^-$, $DETAH(p)^+COO(s)^-$ and $DETAH_2(pp)^{2+}COO(s)^-$ were considered side reaction products and disregarded. However, the production of dicarbamates $DETA(COO)_{2(pp)}^{2-}$ and $DETA(COO)_{2(ps)}^{2-}$ were both important, so neither of them could be ignored (Ye et al., 2017). As a result, the following 17 species were included in modeling of the ternary system of DETA-H_2O-CO_2: H_2O, CO_2, H^+, OH^-, HCO_3^-, CO_3^{2-}, A, $AH(p)^+$, $AH_2(pp)^{2+}$, AH_3^{3+}, $ACOO(p)^-$, $A(COO)_2(pp)^{2-}$, $A(COO)_2(ps)^{2-}$, $AH(p)^+COO(p)^-$, $AH_2(ps)^{2+}COO(p)^-$, $AH(s)^+(COO)_2(pp)^{2-}$ and $AH(p)^+(COO)_2(ps)^{2-}$ (where DETA is abbreviated as "A").

For the quaternary system of DETA-PMDETA-H_2O-CO_2 (i.e., an aqueous solvent blend of DETA and PMDETA), because the tertiary amine PMDETA is not capable of bonding CO_2

molecules, only protonated PMDETA species were present. Following a similar simplification rule, besides the 17 species described above, 4 additional species were present in the CO_2 rich phase of the DETA and PMDETA blend system: B, BH^+, BH^{2+} and BH_3^{3+} (where PMDETA is abbreviated as "B"). Meanwhile, in the CO_2 lean phase of the blend system, the equilibrium composition was assumed to include only molecular A, B, H_2O and CO_2, and the equilibrium CO_2 loading in the lean phase was attributed to the presence of CO_2 molecules. Such simplification for the CO_2 lean phase was valid because this organic phase contained a dominant portion of hydrophobic PMDETA molecules, according to a prior NMR speciation study (Ye et al., 2017), and the CO_2 bearing ionic species were assumed to exist in the aqueous CO_2 rich phase only.

For either the ternary or quaternary system, the vapor phase was assumed to contain only gaseous H_2O and CO_2 because of the negligible volatility of either DETA or PMDETA molecules compared with steam vapor under experimental conditions. N_2 gas was used as a tracer in the equilibrium measurement, but it was not considered a vapor component in the modeling analysis.

7.3.2 Chemical equilibria

Numerous chemical reactions occurred in the aqueous DETA solution and the two DETA-PMDETA solvent blends. For the solvents with dual phases, chemical reactions in the CO_2 lean phase were neglected in light of the marginal presence of ionic species in this phase. On the basis of the major species identified in Section 7.3.1, 16 reactions were regarded as important. The equilibrium of each is represented by a quantitative relationship between the equilibrium constant (K, molality based) and the molality (m, mol kg^{-1}), activity coefficient (γ) and stoichiometric coefficient of each species, as listed below. Symbols for the species are shown as subscripts in the equations. The activity of water (a_W) is dimensionless and was approximated as equal to its molar fraction in the liquid phase (Weiland et al., 1993).

Dissociation of water: $H_2O = H^+ + OH^-$

$$K_1 = \frac{m_{H^+}\gamma_{H^+} m_{OH^-}\gamma_{OH^-}}{a_W} \quad (7\text{-}1)$$

Hydrolysis of CO_2: $CO_2 + H_2O = H^+ + HCO_3^-$

$$K_2 = \frac{m_{H^+}\gamma_{H^+} m_{HCO_3^-}\gamma_{HCO_3^-}}{m_{CO_2}\gamma_{CO_2} a_W} \quad (7\text{-}2)$$

Dissociation of bicarbonate ion: $HCO_3^- = H^+ + CO_3^{2-}$

$$K_3 = \frac{m_{H^+}\gamma_{H^+} m_{CO_3^{2-}}\gamma_{CO_3^{2-}}}{m_{HCO_3^-}\gamma_{HCO_3^-}} \quad (7\text{-}3)$$

Dissociation of protonated DETA: $AH(p)^+ = H^+ + A$

$$K_4 = \frac{m_{H^+}\gamma_{H^+} m_A \gamma_A}{m_{AH(p)^+}\gamma_{AH(p)^+}} \quad (7\text{-}4)$$

Dissociation of diprotonated DETA: $AH_2(pp)^{2+} = H^+ + AH(p)^+$

$$K_5 = \frac{m_{H^+}\gamma_{H^+} m_{AH(p)^+}\gamma_{AH(p)^+}}{m_{AH_2(pp)^{2+}}\gamma_{AH_2(pp)^{2+}}} \quad (7\text{-}5)$$

Dissociation of triprotonated DETA: $AH_3^{3+} = H^+ + AH_2(pp)^{2+}$

$$K_6 = \frac{m_{H^+}\gamma_{H^+} m_{AH_2(pp)^{2+}}\gamma_{AH_2(pp)^{2+}}}{m_{AH_3^{3+}}\gamma_{AH_3^{3+}}} \quad (7\text{-}6)$$

Dissociation of protonated PMDETA: $BH^+ = H^+ + B$

$$K_7 = \frac{m_{H^+}\gamma_{H^+} m_B \gamma_B}{m_{BH^+}\gamma_{BH^+}} \quad (7\text{-}7)$$

Dissociation of diprotonated PMDETA: $BH_2^{2+} = H^+ + BH^+$

$$K_8 = \frac{m_{H^+}\gamma_{H^+} m_{BH^+}\gamma_{BH^+}}{m_{BH_2^{2+}}\gamma_{BH_2^{2+}}} \quad (7\text{-}8)$$

Dissociation of triprotonated PMDETA: $BH_3^{3+} = H^+ + BH_2^{2+}$

$$K_9 = \frac{m_{H^+}\gamma_{H^+} m_{BH_2^{2+}}\gamma_{BH_2^{2+}}}{m_{BH_3^{3+}}\gamma_{BH_3^{3+}}} \quad (7\text{-}9)$$

Formation of (primary) carbamate: $CO_2 + A = H^+ + ACOO(p)^-$

$$K_{10} = \frac{m_{H^+}\gamma_{H^+} m_{ACOO(p)^-}\gamma_{ACOO(p)^-}}{m_{CO_2}\gamma_{CO_2} m_A \gamma_A} \quad (7\text{-}10)$$

Formation of dicarbamate (primary-secondary): $CO_2 + ACOO(p)^- = H^+ + A(COO)_2(ps)^{2-}$

$$K_{11} = \frac{m_{H^+}\gamma_{H^+} m_{A(COO)_2(ps)^{2-}}\gamma_{A(COO)_2(ps)^{2-}}}{m_{CO_2}\gamma_{CO_2} m_{ACOO(p)^-}\gamma_{ACOO(p)^-}} \quad (7\text{-}11)$$

Formation of dicarbamate (primary-primary): $CO_2 + ACOO(p)^- = H^+ + A(COO)_2(pp)^{2-}$

$$K_{12} = \frac{m_{H^+}\gamma_{H^+} m_{A(COO)_2(pp)^{2-}}\gamma_{A(COO)_2(pp)^{2-}}}{m_{CO_2}\gamma_{CO_2} m_{ACOO(p)^-}\gamma_{ACOO(p)^-}} \quad (7\text{-}12)$$

Dissociation of protonated (primary) carbamate: $AH(p)^+COO(p)^- = H^+ + ACOO(p)^-$

$$K_{13} = \frac{m_{H^+}\gamma_{H^+} m_{ACOO(p)^-}\gamma_{ACOO(p)^-}}{m_{AH(p)^+COO(p)^-}\gamma_{AH(p)^+COO(p)^-}} \quad (7\text{-}13)$$

Dissociation of diprotonated (primary) carbamate: $AH_2(ps)^{2+}COO(p)^- = H^+ + AH(p)^+COO(p)^-$

$$K_{14} = \frac{m_{H^+}\gamma_{H^+} m_{AH(p)^+COO(p)^-}\gamma_{AH(p)^+COO(p)^-}}{m_{AH_2(ps)^{2+}COO(p)^-}\gamma_{AH_2(ps)^{2+}COO(p)^-}} \quad (7\text{-}14)$$

Dissociation of protonated (primary-secondary) dicarbamate: $AH(p)^+(COO)_2(ps)^{2-} = H^+ + A(COO)_2(ps)^{2-}$

$$K_{15} = \frac{m_{H^+}\gamma_{H^+} m_{A(COO)_2(ps)^{2-}}\gamma_{A(COO)_2(ps)^{2-}}}{m_{AH(p)^+(COO)_2(ps)^{2-}}\gamma_{AH(p)^+(COO)_2(ps)^{2-}}} \quad (7\text{-}15)$$

Dissociation of protonated (primary-primary) dicarbamate: $AH(s)^+(COO)_2(pp)^{2-} = H^+ + A(COO)_2(pp)^{2-}$

$$K_{16} = \frac{m_{H^+}\gamma_{H^+} m_{A(COO)_2(pp)^{2-}}\gamma_{A(COO)_2(pp)^{2-}}}{m_{AH(s)^+(COO)_2(pp)^{2-}}\gamma_{AH(s)^+(COO)_2(pp)^{2-}}} \quad (7\text{-}16)$$

The values of 16 equilibrium constants for the equations above can be expressed as a function of temperature (T, K) in the following form:

$$\ln K = C_1 + \frac{C_2}{T} + C_3 \ln T + C_4 T \quad (7\text{-}17)$$

where C_1, C_2, C_3 and C_4 are empirical coefficients and their values are summarized in Table 7-1 and described as follows.

For K_1 to K_3, the values of C_1 to C_4 are available (Edwards et al., 1978). The values of K_4 to K_6 were derived from the pK_{a1}, pK_{a2} and pK_{a3} of DETA, respectively. The values of pK_{a1} and pK_{a2} of DETA were reported as 9.8 and 8.74 at 25°C, respectively (Dow Chemical Company, 2017), and the value of pK_{a3} of DETA was reported as 5 (Hartono and Svendsen, 2009). Similarly, the values of K_7 to K_9 were derived from the pK_{a1}, pK_{a2} and pK_{a3} of PMDETA, respectively. The values of pK_{a1}, pK_{a2} and pK_{a3} of PMDETA were reported as 9.1, 8 and 2.4 at 25°C, respectively (Huntsman Corporation, 2009). By the same means, the pK_a values adopted for K_{13} and K_{14} were

6.96 and 10, respectively, and the values of K_{15} and K_{16} were derived from the pK_a values of $A(COO)_2(ps)^{2-}$ (10) and $A(COO)_2(pp)^{2-}$ (10.03), respectively. All the latter four pK_a values were estimated at 25°C by using a method described elsewhere (Singh et al., 2011). The Van't Hoff equation below was used to determine the equilibrium constants from pK_a at various temperatures:

$$\ln K_{an} + \ln(10)pK_{an} = -\frac{\Delta H_{pro}{}^{n}}{R}\left(\frac{1}{T} - \frac{1}{298.15}\right) \quad (7\text{-}18)$$

where K_{an} and pK_{an} are the nth (n = 1, 2 or 3) order equilibrium constant of acid dissociation and pK_a for either DETA or PMDETA derived species, respectively; R (J mol^{-1} K^{-1}) is the ideal gas constant; $\Delta H_{pro,n}$ (J mol^{-1}) is the enthalpy of the nth order of the protonation reaction for either DETA or PMDETA derived species, which can be estimated by an empirical prediction method (Paoletti et al., 1972). As a result, the sets of values of C_1 to C_4 for K_4 to K_9, and K_{13} to K_{16} were available from Eq. (7-18). The remaining reaction equilibrium constants K_{10} to K_{12} were unknown and determined by fitting the experimental data to the model, which is described in detail in Section 7.4.1.

Table 7-1. Coefficients C_1 to C_4 used to determine the temperature dependent equilibrium constants.

Equilibrium constant	C_1	C_2	C_3	C_4	Temperature range (°C)
K_1	140.932	-13,445.9	-22.4773	0	0 to 225
K_2	235.482	-12,092.1	-36.7816	0	0 to 225
K_3	220.067	-12,431.7	-35.4819	0	0 to 225
K_4	-2.626	-5,944.86	0	0	25 to 120
K_5	-0.461	-5,862.83	0	0	25 to 120
K_6	0.917	-3,705.91	0	0	25 to 120
K_7	-8.35	-3,757.75	0	0	25 to 120
K_8	-6.092	-3,675.72	0	0	25 to 120
K_9	2.01	-2,247	0	0	25 to 120
K_{13}	3.927	-5,948.89	0	0	25 to 120
K_{14}	-8.847	-4,227.28	0	0	25 to 120
K_{15}	-2.97	-5,979.59	0	0	25 to 120
K_{16}	-7.168	-4,748.64	0	0	25 to 120
H_{CO2}	94.4914	-6,789.04	-11.4519	-0.010454	0 to 250

7.3.3 Phase equilibria

Phase equilibria were represented by the equilibrium between the vapor phase and either of the two liquid phases (VLE) and the LLE. For the vapor-liquid-liquid system, satisfying the

equilibrium between the first and second phases and between the first and third phases would indicate the equilibrium between the second and third phases.

Under a gas-liquid phase equilibrium, the isofugacity criterion applies for the common species (i.e., CO_2 and H_2O) between the two phases. A physical solubility relation (i.e., Henry's law) was adopted for noncondensable CO_2, and a vapor pressure relation was adopted for condensable water (Chen et al., 1979). Thus, the equilibrium for CO_2 and H_2O between the gas and either of the liquid phases can be expressed as

$$Py_{CO_2}\phi_{CO_2} = m_{CO_2}\gamma_{CO_2}H_{CO_2}\exp[\frac{\nu_{CO_2}{}^0(P - P_W{}^0)}{RT}] \quad (7\text{-}19)$$

$$Py_W\phi_W = a_W P_W{}^0\phi_W{}^0\exp[\frac{\nu_W{}^0(P - P_W{}^0)}{RT}] \quad (7\text{-}20)$$

where P (Pa) is the total system pressure (i.e., the summation of partial pressures of CO_2 and H_2O), and P_W^0 (Pa) is the vapor pressure of pure water, which was estimated with Buck's equation (Buck, 1981). y is the molar fraction of a vapor component ($y_{CO2} + y_w = 1$). H_{CO2} (atm kg mol^{-1}) is the Henry's law constant of CO_2 at an infinite dilution in water, which can be expressed in the form of Eq. (7-17) with the coefficients C_1 to C_4 provided in Table 7-1 (Edwards et al., 1978). v_{CO2}^0 (L mol^{-1}) is the partial molar volume of CO_2 at an infinite dilution in water and was approximated as the critical molar volume of CO_2 (0.0939 L mol^{-1}) (Austgen, 1989), and v_W^0 (L mol^{-1}) is the characteristic molar volume of water, which was reported to be a value of 0.0464 (Brelvi and Oconnell, 1972). In Eqs. (7-19) and (7-20), the exponential terms are the Poynting correction.

In Eqs. (7-19) and (7-20), ϕ_{CO2} and ϕ_W are the gaseous fugacity coefficients of CO_2 and H_2O, respectively, and ϕ_W^0 is the fugacity coefficient of saturated water vapor over pure water. To calculate these coefficients, the Redlich-Kwong-Soave (RKS) equation of state was implemented for the vapor phase as follows (Austgen, 1989):

$$P = \frac{RT}{v - b} - \frac{a\alpha}{v(v + b)} \quad (7\text{-}21)$$

where the parameters a and b reflect the strength of attraction between molecules and the effect of molecular size, respectively. They can be expressed as

$$a = 0.42748 \frac{R^2 T_c^2}{P_c} \tag{7-22}$$

$$b = 0.08664 \frac{RT_c}{P_c} \tag{7-23}$$

where T_c and P_c are the critical properties (i.e., temperature and pressure) of a vapor component (H_2O or CO_2). These values are listed in Table 7-2.

Table 7-2. Critical properties of pure compounds.

Compound	Critical property		
	Temperature (K)	Pressure (kPa)	Compressibility
DETA	692.6	4,260.2	0.253
PMDETA	640.9	2,293.7	0.255
H_2O	647.3	22,090.0	0.233
CO_2	304.2	7,376.5	0.274

The value of α is a function of temperature and an acentric factor (ω) (Austgen, 1989):

$$\alpha = [1 + f_\omega (1 - \sqrt{\frac{T}{T_c}})]^2 \tag{7-24}$$

$$f_\omega = 0.48508 + 1.55171\omega - 0.15613\omega^2 \tag{7-25}$$

The values of ω for CO_2 and H_2O are 0.225 and 0.344, respectively. ϕ_{CO2} and ϕ_W can be estimated by using the equation below (Austgen, 1989):

$$\ln \phi_i = \frac{b_i}{b_m}(\frac{Pv_m}{RT} - 1) - \ln[\frac{Pv_m}{RT}(1 - \frac{b_m}{v_m})] + \frac{(a\alpha)_m}{b_m RT} \ln(1 + \frac{b_m}{v_m})[\frac{b_i}{b_m} - \frac{2}{(a\alpha)_m} \sum_j y_j \sqrt{a_i \alpha_i a_j \alpha_j}] \tag{7-26}$$

where the subscript *i* or *j* represents the individual component CO_2 or H_2O, and the subscript *m* represents their mixture. The classical mixing rules are applied (the linear mixing rule for the parameter *b* and the quadratic mixing rule for the parameter $a\alpha$):

$$b_m = \sum_i y_i b_i \tag{7-27}$$

$$(a\alpha)_m = \sum_i \sum_j y_i y_j \sqrt{a_i \alpha_i a_j \alpha_j} \tag{7-28}$$

The term v_m ($m^3\ mol^{-1}$) in Eq. (7-26), the molar volume of gas mixture, can be obtained by solving Eq. (7-21) for *v*, with *b* replaced by b_m and $a\alpha$ replaced by $(a\alpha)_m$. ϕ_W^0 can be calculated according to Eq. (7-26) by considering water as the sole component.

When dual liquid phases are present, the LLE entails the equality of the chemical potential of each common species in both phases. The chemical potential of component *i* (μ_i) can be expressed as follows (Zerres and Prausnitz, 1994):

$$\mu_i = \mu_i^0 + RT\ln(x_i\gamma_i) \quad (7\text{-}29)$$

where μ_i^0 is the chemical potential of component *i* at the standard state, and the activity term $RT\ln(x_i\gamma_i)$ describes the nonideal behavior of component *i* in the liquid phase. Therefore, for the species present in both the CO_2 rich and CO_2 lean liquid phases, the following isoactivity expressions are valid (Wong and Sandler, 1984):

For DETA: $m_A\gamma_A = m_A'\gamma_A'$ (7-30)

For PMDETA: $m_B\gamma_B = m_B'\gamma_B'$ (7-31)

For CO_2: $m_{CO_2}\gamma_{CO_2} = m_{CO_2}'\gamma_{CO_2}'$ (7-32)

For H_2O: $a_W = a_W'$ (7-33)

where *m*' and γ' are the molality and activity coefficient of a species, respectively, in the CO_2 lean liquid phase. The symbols marked with prime superscripts are specifically for the CO_2 lean phase.

7.3.4 Material and charge balances

A charge balance (electroneutrality) was applied to either the sole liquid phase of the monophasic solvent or the CO_2 rich phase of the solvent with dual liquid phases. The charge balance was disregarded for the CO_2 lean phase of the dual phased solvent because that phase was dominant in molecular rather than ionic species, as discussed. For the aqueous DETA-PMDETA solvent blend, the total electric charge of ionic species is neutral in the CO_2 rich phase:

$$m_{H^+} + m_{AH(p)^+} + 2m_{AH_2(pp)^{2+}} + 3m_{AH_3^{3+}} + m_{BH^+} + 2m_{BH_2^{2+}} + 3m_{BH_3^{3+}} + m_{AH_2(ps)^{2+}COO(p)^-} = m_{OH^-} + m_{HCO_3^-} + 2m_{CO_3^{2-}} + m_{ACOO(p)^-} + 2m_{A(COO)_2(pp)^{2-}} + 2m_{A(COO)_2(ps)^{2-}} + m_{AH(s)^+(COO)_2(pp)^{2-}} + m_{AH(p)^+(COO)_2(ps)^{2-}} \quad (7\text{-}34)$$

In addition, the following mass balance equations were considered for either the VLE or VLLE system, i.e., the material balance was applied for each of the chemicals DETA, PMDETA, H_2O and CO_2 (Eqs. (7-35) to (7-38)) and the overall mass balance was applied for each liquid phase (Eqs. (7-39) to (7-40)):

For DETA:

$$n_A{}^0 = M'm_A'+M(m_A + m_{AH(p)^+} + m_{AH_2(pp)^{2+}} + m_{AH_3{}^{3+}} + m_{ACOO(p)^-} + m_{A(COO)_2(pp)^{2-}} + m_{A(COO)_2(ps)^{2-}} + m_{AH(p)^+COO(p)^-} + m_{AH_2(ps)^{2+}COO(p)^-} + m_{AH(s)^+(COO)_2(pp)^{2-}} + m_{AH(p)^+(COO)_2(ps)^{2-}}) \quad (7\text{-}35)$$

For PMDETA: $n_B{}^0 = M'm_B'+M(m_B + m_{BH^+} + m_{BH_2{}^{2+}} + m_{BH_3{}^{3+}})$ (7-36)

For CO_2:

$$\alpha_{CO_2}(n_A{}^0 + n_B{}^0) = M'm_{CO_2}'+M(m_{HCO_3^-} + m_{CO_2} + m_{CO_3{}^{2-}} + m_{ACOO(p)^-} + 2m_{A(COO)_2(pp)^{2-}} + 2m_{A(COO)_2(ps)^{2-}} + m_{AH(p)^+COO(p)^-} + m_{AH_2(ps)^{2+}COO(p)^-} + 2m_{AH(s)^+(COO)_2(pp)^{2-}} + 2m_{AH(p)^+(COO)_2(ps)^{2-}}) + n_{CO_2}{}^g \quad (7\text{-}37)$$

For H_2O: $n_{H_2O}{}^0 = M'm_{H_2O}'+M(m_{HCO_3^-} + m_{CO_3{}^{2-}} + m_{H_2O}) + n_{H_2O}{}^g$ (7-38)

Because of the experimental methods adopted for the equilibrium measurements, it was assumed that no initial water vapor was present in the gas phase. In addition, because the unique means of consumption of a water molecule is the formation of bicarbonate or carbonate species in a 1:1 ratio, the molalities of HCO_3^- and CO_3^{2-} were included in the balance equation of water. The proton concentration in the solvent was negligible, so the combination of a proton with a H_2O molecule to form a H_3O^+ ion was ignored.

For the CO_2 rich phase:

$$M_A(m_A + m_{AH(p)^+} + m_{AH_2(pp)^{2+}} + m_{AH_3{}^{3+}} + m_{ACOO(p)^-} + m_{A(COO)_2(pp)^{2-}} + m_{A(COO)_2(ps)^{2-}} + m_{AH(p)^+COO(p)^-} + m_{AH_2(ps)^{2+}COO(p)^-} + m_{AH(s)^+(COO)_2(pp)^{2-}} + m_{AH(p)^+(COO)_2(ps)^{2-}}) + M_B(m_B + m_{BH^+} + m_{BH_2{}^{2+}} + m_{BH_3{}^{3+}}) + M_{H_2O}(m_{HCO_3^-} + m_{CO_3{}^{2-}} + m_{H_2O}) + M_{CO_2}(m_{HCO_3^-} + m_{CO_2} + m_{CO_3{}^{2-}} + m_{ACOO(p)^-} + 2m_{A(COO)_2(pp)^{2-}} + 2m_{A(COO)_2(ps)^{2-}} + m_{AH(p)^+COO(p)^-} + m_{AH_2(ps)^{2+}COO(p)^-} + 2m_{AH(s)^+(COO)_2(pp)^{2-}} + 2m_{AH(p)^+(COO)_2(ps)^{2-}}) = 1 \quad (7\text{-}39)$$

For the CO_2 lean phase: $M_A m_A'+M_B m_B'+M_{H_2O} m_{H_2O}'+M_{CO_2} m_{CO_2}' = 1$ (7-40)

In the equations above, $n_A{}^0$, $n_B{}^0$ and $n_{H2O}{}^0$ are the total moles of DETA, PMDETA and H_2O in the initial fresh solvent. The total molar amount of DETA and its derivatives or PMTEDA and its derivatives during CO_2 absorption remains the same as the initial amount of DETA ($n_A{}^0$) or PMDETA ($n_B{}^0$) in the fresh solution. α_{CO2} is the total CO_2 loading (moles of CO_2 per mole of total amines) to the solvent before each equilibrium test. $n_{CO2}{}^g$ and $n_{H2O}{}^g$ are the moles of gaseous CO_2 and H_2O in the vapor phase at equilibrium, respectively. M' and M (kg) are the masses of the CO_2 lean and CO_2 rich liquid phases at equilibrium, respectively. M_A, M_B, M_{CO2} and M_{H2O} (kg mol^{-1}) are the molecular weights of DETA, PMDETA, CO_2 and H_2O, respectively.

7.3.5 Liquid-liquid phase separation at equilibrium

For the biphasic solvent system, a model is required to describe how the transition of the two liquid phases equilibrates at different temperatures (thermally induced LLPS) or different CO_2 loadings (chemically induced LLPS). The total liquid volume (V_s, m^3) of the system at an equilibrium state was estimated as:

$$V_S = (n_A{}^0 + n_B{}^0 + n_{H_2O}{}^0 - n_{H_2O}{}^g)\nu_S^m + [\alpha_{CO_2}(n_A{}^0 + n_B{}^0) - n_{CO_2}{}^g]\nu_{CO_2} \quad (7\text{-}41)$$

where the first term on the right hand side of Eq. (7-41) is the liquid volume of the mixture of total equivalent molecular DETA, PMDETA and H_2O at equilibrium, and v_S^m (L mol^{-1}) is the molar volume of the mixture of these three molecular species, with the superscript *m* representing the mixture. Therefore, the Rackett model can be used to estimate v_S^m (Rackett, 1970):

$$\nu_S^m = \frac{RT_c^m}{P_c^m} Z_c^{m[1+(1-\frac{T}{T_c^m})^{\frac{2}{7}}]} \quad (7\text{-}42)$$

where Z_c is the critical compressibility of a component (Table 2). The following mixing rules were adopted for Eq. (7-42):

$$\frac{T_c^m}{P_c^m} = \sum_i x_i \frac{T_{ci}}{P_{ci}} \quad (7\text{-}43)$$

$$Z_c^m = \sum_i x_i Z_{ci} \quad (7\text{-}44)$$

$$T_c^m = \frac{\sum_i \sum_j x_i x_j \nu_{ci} \nu_{cj} \sqrt{T_{ci} T_{cj}} (1 - k_{ij})}{(\sum_i x_i \nu_{ci})^2} \quad (7\text{-}45)$$

$$k_{ij} = 1 - \frac{8\sqrt{\nu_{ci}\nu_{cj}}}{(\sqrt[3]{\nu_{ci}} + \sqrt[3]{\nu_{cj}})^3} \quad (7\text{-}46)$$

where *i* or *j* represents DETA, PMDETA or H_2O. *x* is the molar fraction of a species in the mixture. v_{ci} (L mol^{-1}) is the molar volume of a pure species, which was calculated by using the same form of Eq. (7-42) and applying its critical properties shown in Table 7-2.

The second term on the right hand side of Eq. (7-41) is the volume addition by CO_2 loading, and v_{CO2} (mL mol^{-1}) is the partial molar volume of the dissolved CO_2 without considering the effects of chemical reactions between CO_2 and aqueous amines. An empirical correlation equation was used to estimate v_{CO2} (Garcia, 2001):

$$\nu_{CO_2} = 37.51 - 9.585\times10^{-2}T + 8.740\times10^{-4}T^2 - 5.044\times10^{-7}T^3 \quad (7\text{-}47)$$

Similarly, the liquid volume of the CO_2 lean phase at equilibrium was estimated as follows:

$$V_S(1-\theta) = M'(m_A' + m_B' + m_{H_2O}')\nu_{SL}^m + M' m_{CO_2}' \nu_{CO_2} \quad (7\text{-}48)$$

where v_{SL}^m (L mol^{-1}) is the molar volume of the liquid mixture of DETA, PMDETA and H_2O in the CO_2 lean phase and could be calculated based on Eqs. (7-42) to (7-46). Because the CO_2 loading in the lean phase is negligible, the second term on the right hand side of Eq. (7-48) could be omitted. θ is the volumetric fraction of the CO_2 rich phase at equilibrium (for a monophasic system, θ=1). The volume of the CO_2 rich phase ($V_s\theta$) is related to the rich phase mass (M, kg) and density ρ_R (kg L^{-1}) at equilibrium. Both θ and ρ_R are variables of the equilibrium model that were regressed based on experimental measurements.

7.3.6 Activity coefficient model

The Deshmukh-Mather model was used to calculate the activity coefficient for each species in the liquid phase (Deshmukh and Mather, 1981; Jou et al., 1995; Ma'mun et al., 2006). This model is more rigorous than a few simple approaches, such as the Kent-Eisenberg model (Kent and Eisenberg, 1976), yet it requires less computational effort than the more complex models, such as the electrolyte NRTL and UNIQUAC/UNIFAC (UNIQUAC functional group activity coefficient) models. The Deshmukh-Mather model is useful for studying the speciation of components in a complex system, such as an amine blend system, and obtaining the related dissociation constants (Weiland et al., 1993). The Deshmukh-Mather model takes the following mathematical form:

$$\ln\gamma_i = \frac{-2.303Cz_i^2\sqrt{I}}{1+Dr\sqrt{I}} + 2\sum_{j\neq W}\beta_{ij}m_j \quad (7\text{-}49)$$

The first term on the right hand side of Eq. (7-49) represents the contribution of the long range electrostatic forces based on the Debye-Huckel limiting law, C is the Debye-Huckel limiting slope, and D is a function of the density (ρ_W, g mL^{-1}) and the dielectric constant (ε_0) of pure water. The value of ε_0 can be estimated according to an empirical equation (Malmberg and Maryott, 1956). The expressions of C and D are given as follows (Anderson, 2009):

$$C = \frac{1824800\rho_W^{0.5}}{(\varepsilon_0 T)^{1.5}} \quad (7\text{-}50)$$

$$D = \frac{50.292\rho_w^{0.5}}{(\varepsilon_0 T)^{0.5}} \quad (7\text{-}51)$$

where z_i is the charge number on the ion i, r is the effective ion size in angstrom (Å) and is approximated as 4 for simplicity, and I is the ionic strength as defined by

$$I = 0.5\sum_i m_i z_i^2 \quad (7\text{-}52)$$

The second term on the right hand side of Eq. (7-49) takes into account the short range van der Waals forces. The BIPs, β_{ij}, represent the net effects of various short range, two body forces between different molecular and ionic solutes ($\beta_{ij}=\beta_{ji}$). The summation of the second term includes all the solute pairs but excludes the interactions between water and any solute. Furthermore, the interactions among like charged ions and those involving H^+, OH^- or CO_2 were negligible. β_{ij} is close to 0 when the species with low molality are involved (Weiland et al., 1993).

Because an enormous number of nonsymmetrical interaction pairs of species are present in the ternary DETA-H_2O-CO_2 VLE system or the quaternary DETA-PMDETA-H_2O-CO_2 VLLE system, there is a need to reduce the number of β_{ij} adopted in the Deshmukh-Mather model for data regression. As a result, only those BIPs with high sensitivity levels, the perturbation of which would influence the predicted CO_2 partial pressure, were kept for the model. The computational screening of sensitive BIPs was conducted in two steps. In the first step, screening was targeted at the DETA-H_2O-CO_2 system, and 8 pairs of BIPs with sensitivity to the predicted CO_2 partial pressures were identified. In the second step, screening was extended to the DETA-PMDETA-H_2O-CO_2 system, and an additional 10 pairs of BIPs were identified. Therefore, 18 pairs of BIPs were used in the current model.

7.3.7 Regression of model parameters

The model parameters were regressed based on the measured VLE and VLLE data. Lingo 17 optimization software (Lindo Systems Inc.) was used to solve the nonlinear, global optimization problem to minimize the following objective function (Weiland et al., 1993):

$$\min(F) = \sum_{i=1}^{n} \frac{(P_{CO_2}^{exp} - P_{CO_2}^{pred})^2}{P_{CO_2}^{exp} P_{CO_2}^{pred}} \quad (7\text{-}53)$$

where n=112 is the total number of equilibrium measurements at various absorption and desorption temperatures (25 to 120°C). Among the measured data, 37 sets of data were obtained from the VLE experiments for solvent 2A, and the remaining 75 sets of data were from the VLLE experiments for solvents 2A3B (35 sets of data) and 1.5A3.5B (40 sets of data). The objective function was the normalized sum of squares of deviations between the experimental (P_{CO2}^{exp}) and the predicted (P_{CO2}^{pred}) CO_2 partial pressures. The regression was considered convergent when the difference in the objective function values between two successive iterations was within a tolerance level of 10^{-6}. The Lingo codes of data regression for the VLLE systems are provided in Appendix C.

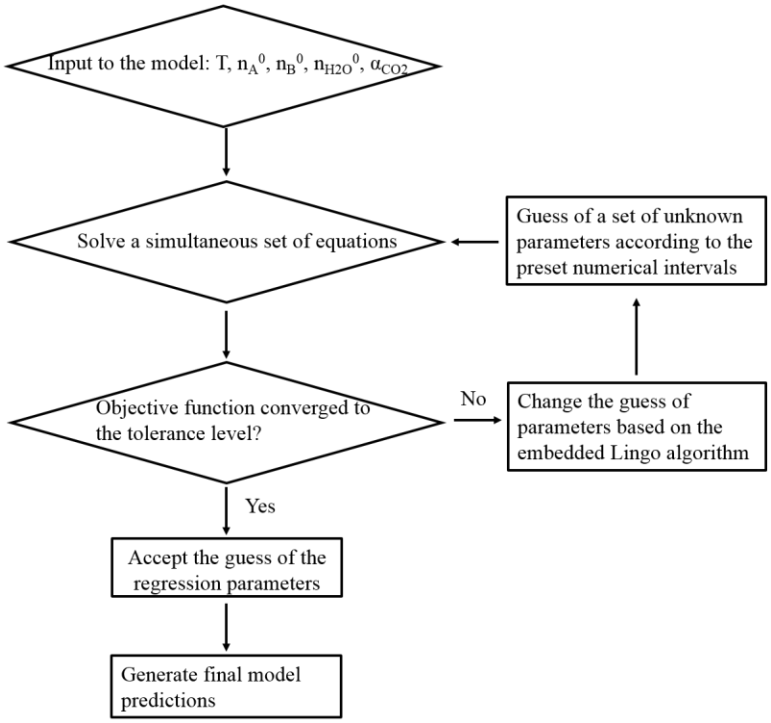

Fig. 7-3. Schematic diagram of the numerical procedure used for data regression and model prediction.

Fig. 7-3 is a diagram of the numerical procedure adopted for the data regression to determine the model parameters. The required data input included the system temperature; the molar amounts of DETA, PMDETA and H_2O in the CO_2 free solvent; and the initial total CO_2 loading in the solvent. Initial values for the regression parameters, including 6 equilibrium constant related parameters and 18 BIPs, were generated by Lingo according to the preset numerical interval for each parameter. A complete set of equations was solved, including Eqs. (7-1) to (7-16) for the

reaction equilibria, Eq. (7-34) for the charge balance in the CO_2 rich phase, Eqs. (7-19) to (7-20) for the VLE, Eqs. (7-30) to (7-33) for the LLE, Eq. (7-21) for the RKS equation of state for the vapor phase and Eqs. (7-35) to (7-40) for the mass balances of individual components among the three phases. During each iteration, the intermediate results were used to calculate the objective function. If the objective function was not minimized, a Lingo algorithm based on sequential linear programming directions would generate a new set of model parameters, and the aforementioned procedure would be repeated until the objective function converged to the required tolerance level. The regression parameters were obtained through this optimization procedure and were used to predict the thermodynamic properties of the solvent system.

7.4 Results and discussion

7.4.1 Determination of reaction equilibrium constants and binary interaction parameters

Because the equilibrium constants of CO_2 absorption reactions shown in Eqs. (7-10) to (7-12) cannot be directly measured by experiments (Hartono et al., 2011), they were determined by fitting the experimentally measured phase equilibrium data for neat solvent 2A and biphasic solvents 1.5A3.5B and 2A3B. The retrieved values of C_1 to C_4 for the equilibrium constants of DETA-CO_2 reactions are listed in Table 7-3. A retrieved complete set of 18 BIPs is shown in Table 7-4. A small value of BIP indicated a marginal effect on the objective function of data fitting. Most of the obtained BIPs shown in Table 7-4 are positive. However, a negative sign of BIP may not render particular physical significance because of the nature of data fitting.

Table 7-3. Empirical coefficients for estimating the equilibrium constants of reactions between DETA and CO_2 determined from the modeling.

Equilibrium constant	C_1	C_2	C_3	C_4	Temperature range (°C)
K_{10}	-21.148	5,220.71	0	0	25 to 120
K_{11}	-25.552	3,764.80	0	0	25 to 120
K_{12}	-28.326	4,604.76	0	0	25 to 120

Table 7-4. Binary interaction parameters determined for the thermodynamic model.

Binary interaction pair	β_{ij}
$DETAH(p)^{+}$-$DETACOO(p)^{-}$	0.067
$DETAH(p)^{+}$-$DETA(COO)_2(ps)^{2-}$	0.503
$DETAH(p)^{+}$-$DETA(COO)_2(pp)^{2-}$	0.490
$DETAH_2(pp)^{2+}$-$DETACOO(p)^{-}$	0.481
$DETAH_2(pp)^{2+}$-$DETAH(s)^{+}(COO)_2(pp)^{2-}$	0.028
$DETAH_2(ps)^{2+}COO(p)^{-}$-$HCO_3^{-}$	0.218
$DETAH_2(ps)^{2+}COO(p)^{-}$-$DETAH(p)^{+}(COO)_2(ps)^{2-}$	0.142
$DETAH_2(ps)^{2+}COO(p)^{-}$-$DETAH(s)^{+}(COO)_2(pp)^{2-}$	-0.012
PMDETA-PMDETA	-0.690
PMDETA-$PMDETAH_2^{2+}$	1.041
DETA-PMDETA	0.026
$DETACOO(p)^{-}$-$PMDETAH_2^{2+}$	0.237
$DETA(COO)_2(ps)^{2-}$-$PMDETAH_2^{2+}$	0.950
$DETA(COO)_2(pp)^{2-}$-$PMDETAH_2^{2+}$	0.950
$DETAH(p)^{+}(COO)_2(ps)^{2-}$-$PMDETAH^{+}$	0.200
$DETAH(p)^{+}(COO)_2(ps)^{2-}$-$PMDETAH_2^{2+}$	0.002
$DETAH(s)^{+}(COO)_2(pp)^{2-}$-$PMDETAH^{+}$	0.050
$DETAH(s)^{+}(COO)_2(pp)^{2-}$-$PMDETAH_2^{2+}$	0.016

7.4.2 Prediction of liquid-liquid phase separation for the biphasic solvent system

Prediction of the phase separation is crucial to solvent assessment and process design, but little research is available in the literature. This model could be used to predict the distributions of original DETA, PMDETA and water and the absorbed CO_2 in the CO_2 lean and CO_2 rich phases at different temperatures (25 to 120°C) given a certain total CO_2 loading. The distributions of DETA, PMDETA, water and CO_2 in the CO_2 lean phase are shown in Fig. 7-4. Those distributed in the CO_2 rich phase are not displayed because they can be estimated from Fig. 7-4.

The results shown in Fig. 7-4 indicate that a variation in temperature did not change the distribution of PMDETA, DETA or H_2O in the two liquid phases. However, as the CO_2 loading increased, less DETA, PMDETA or H_2O was present in the hydrophobic CO_2 lean phase and more in the hydrophilic CO_2 rich phase where the chemical reactions occurred. Specifically, the DETA species in the CO_2 lean phase became depleted when the CO_2 loading reached a certain level (e.g., 0.4 mol mol^{-1} for solvent 1.5A3.5B).

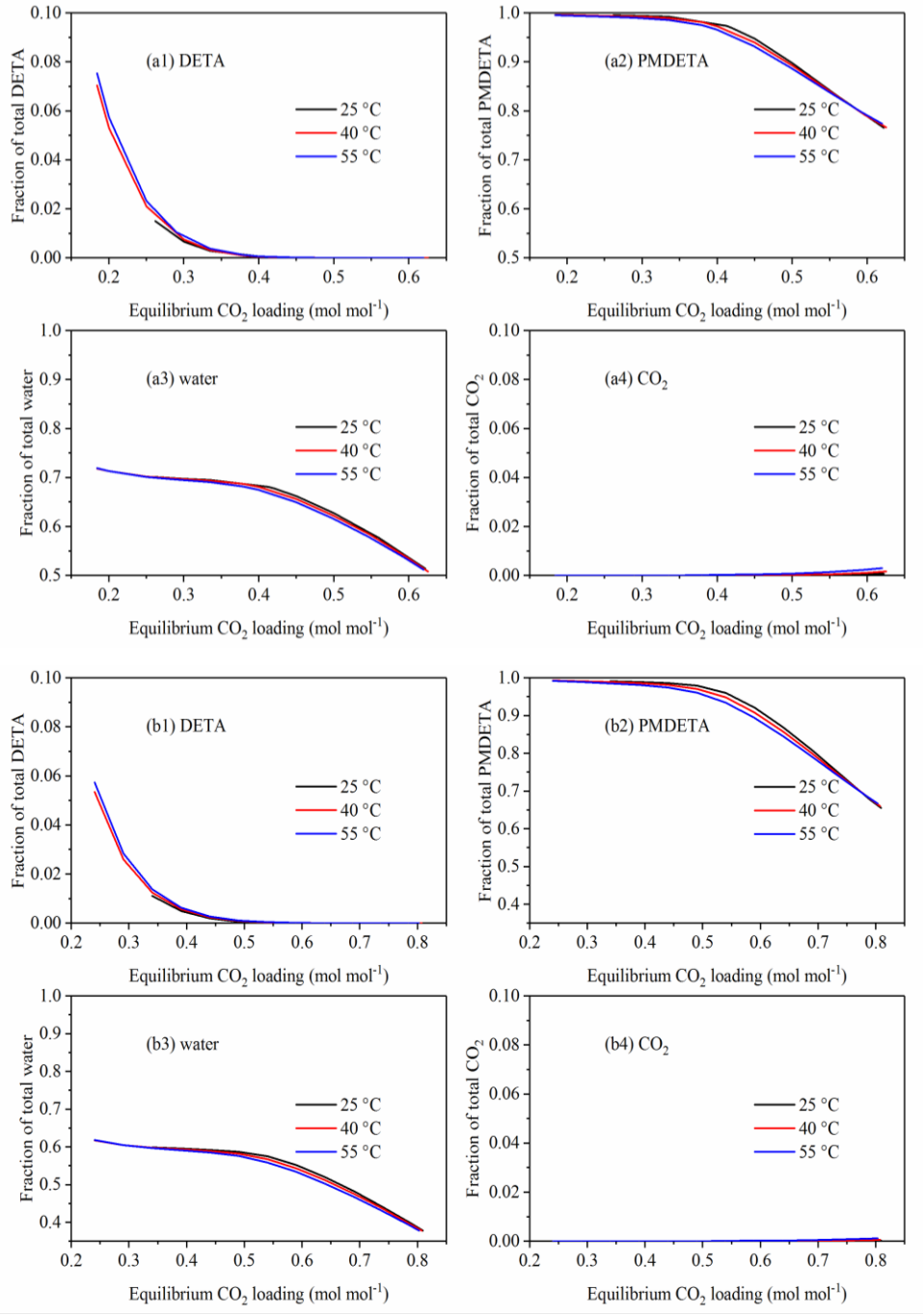

Fig. 7-4. Predicted equilibrium fraction of total liquid species of DETA, PMDETA, water and CO_2 distributed in the CO_2 lean phase of solvents (a) 1.5A3.5B and (b) 2A3B.

The results shown in Fig. 7-4 are consistent with an NMR assisted speciation study performed by our group (Ye et al., 2017). The molar ratio of total PMDETA to total DETA species in the CO_2 rich phase at 23°C was 0.90 for solvent 1.5A3.5B under a total liquid CO_2 loading of 0.663 mol

mol^{-1} and was 0.52 for solvent 2A3B under a total liquid CO_2 loading of 0.733 mol mol^{-1}. In comparison, the PMDETA to DETA ratios in the rich phase predicted by this study were 0.89 and 0.57 under the same conditions. In addition, the composition of the fresh (CO_2 free) solvent affected the partition of each species in the two liquid phases. At the same rich CO_2 loading, solvent 1.5A3.5B was closer to reaching its saturated rich CO_2 loading than was 2A3B; therefore, the fraction of total PMDETA remaining in the lean phase of solvent 1.5A3.5B was lower than that of 2A3B. In either solvent, almost all the loaded CO_2 was concentrated in the rich phase (>99.0%), leaving a negligible amount of CO_2 present in the lean phase.

Another variable characterizing LLPS is the volumetric ratio between the rich and lean phases. The total liquid volume expands with an increase in the CO_2 loading. However, the individual volumes of the CO_2 rich and CO_2 lean phases are not always easy to measure, especially under elevated temperature and pressure conditions. Thus, the current model included predictions of such liquid volumes. The predicted volumetric fraction of the rich phase in the total liquid volume as compared with a few experimental data measured under ambient conditions is shown in Fig. 7-5. The model predictions and measurements were in agreement.

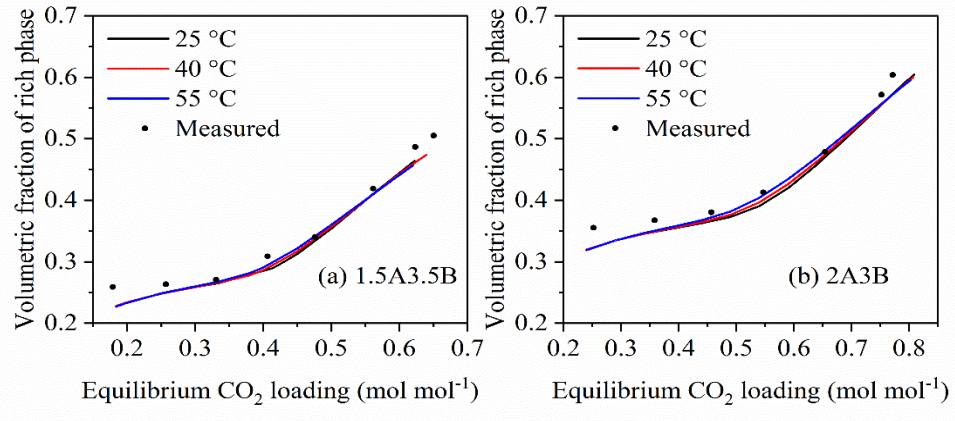

Fig. 7-5. The predicted (lines) and measured (symbols) equilibrium volumetric fractions of the CO_2 rich phase in the total liquid volume of solvents (a) 1.5A3.5B and (b) 2A3B. The scattered points are measured data at ambient temperature.

The volumetric partition of the solvent in the two liquid phases was not influenced by temperature, as indicated by the isothermal curves displayed in Fig. 7-5. The volume of the rich phase liquid increased with increasing CO_2 loading, with an inflection point occurring at a CO_2

loading of 0.4 mol mol^{-1} for solvent 1.5A3.5B and 0.5 mol mol^{-1} for solvent 2A3B. Such predictions indicated CO_2 absorption into solvent 1.5A3.5B or 2A3B was a two stage process, as observed in our previous experimental study (Ye et al., 2017a; Ye et al., 2017b). In the initial stage, the dissolved CO_2 reacted primarily with DETA associated species, and the reacted CO_2 was concentrated in the hydrophilic CO_2 rich phase, resulting in a gradual increase in the rich phase volume. In the later stage, a large number of PMDETA molecules originally in the hydrophobic CO_2 lean phase transferred to the CO_2 rich phase to provide additional CO_2 absorption capacity as proton acceptors, leading to a rapid expansion of the rich phase volume. The volume of the CO_2 rich phase depended on the fresh solvent composition. The CO_2 rich phase for a fresh solvent containing more hydrophobic species (i.e., PMDETA) should have a smaller volume.

The thermodynamic model was used to predict the density of each liquid phase for the VLLE system. The predicted density for solvent 1.5A3.5B is shown in Fig. 7-6. At 25°C, the density ranged between 1.05 and 1.1 g mL^{-1} for the CO_2 rich phase and 0.99 g mL^{-1} for the CO_2 lean phase. Increasing the temperature led to a decrease in density for either the CO_2 rich or lean phase, primarily because the liquid volume expanded under higher temperatures. The density of the CO_2 lean phase did not change with the CO_2 loading at a given temperature because the loaded CO_2 was distributed in the rich phase. For the rich phase, the density increased initially and then decreased with increasing CO_2 loadings, which was consistent with the two stage process described above. In the early stage with a CO_2 loading smaller than 0.4 mol mol^{-1}, the loaded CO_2 was concentrated in the rich phase, whose volume increased gradually, resulting in an increase in the rich phase density. In the later stage with a CO_2 loading greater than 0.4 mol mol^{-1}, however, the rapid expansion of the rich phase volume reduced the density of this phase. The densities of solvents 1.5A3.5B and 2A3B (either CO_2 rich or lean phase) were similar under the same temperatures and CO_2 loadings. The predicted density results for each solvent were validated by their agreement with the measured data at ambient conditions.

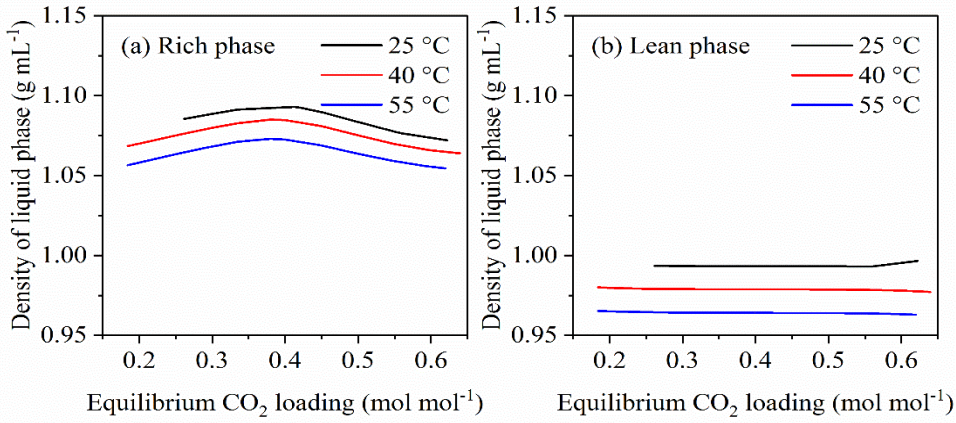

Fig. 7-6. Predicted equilibrium densities of the (a) CO_2 rich phase and (b) CO_2 lean phase for solvent 1.5A3.5B.

7.4.3 Predicted chemical speciation in the equilibrium system

The thermodynamic model was used to calculate the molality of species in each liquid phase for solvents 2A3B and 1.5A3.5B. The speciation for the CO_2 lean phase was simple because it contained the molecular species of DETA, PMDETA, H_2O and CO_2 (predominantly PMDETA and H_2O, after a certain amount of CO_2 was loaded to the solvent and DETA was transferred to the CO_2 rich phase), as shown in Fig. 7-4. However, the speciation for the rich phase was more complicated. For example, DETA in the rich phase could exist in forms of 11 ionic and neutral species, and PMDETA could exist in forms of 4 species. Therefore, we specifically address the rich phase speciation in the following discussion.

Fractional contributions by each of the 11 DETA species in the total DETA were predicted based on the model to reveal their relative importance under different CO_2 loading and temperature conditions. Examples of the predicted results at 40 and 120°C are depicted in Fig. 7-7. Fractional profiles of the 11 species were similar regardless of the temperature and fresh solvent composition. $DETAH_3^{3+}$ was a minor species, with a fraction smaller than 1.7% in the total DETA throughout the CO_2 absorption process at the modeling temperatures. This was because the third dissociation constant (pK_{a3}) of DETA was 5, indicating little tendency to form $DETAH_3^{3+}$. $DETAH(p)^+COO(p)^-$ contributed an even smaller portion, less than 0.7% of the total DETA under modeling conditions, which indicated this species was unstable and could be protonated or bonded with CO_2.

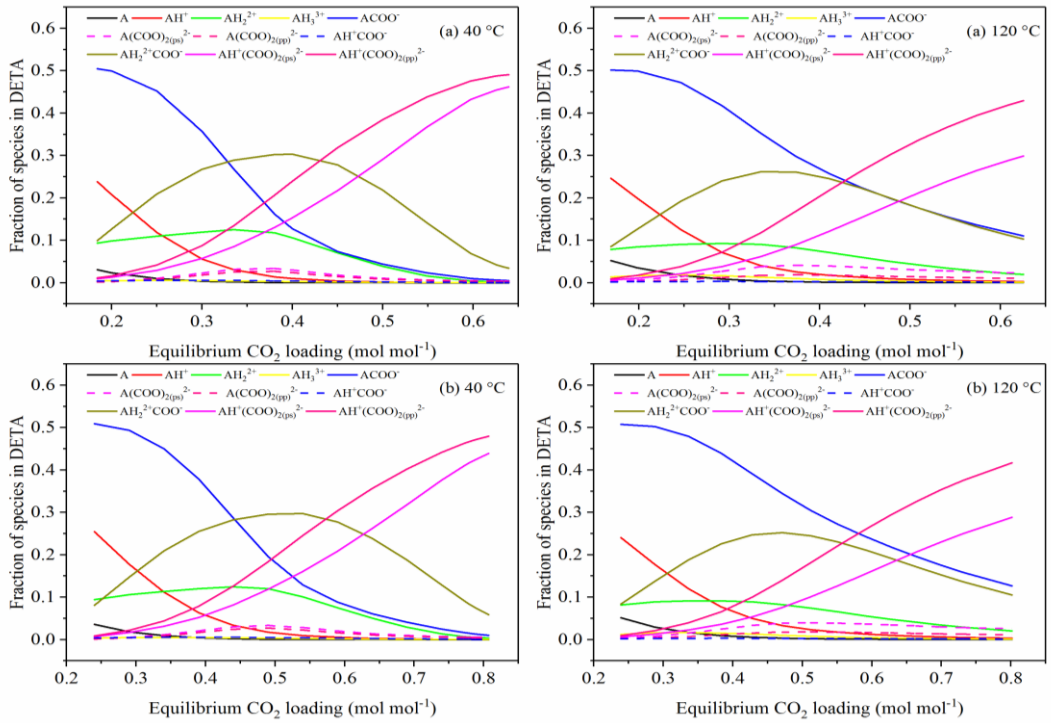

Fig. 7-7. Predicted equilibrium fraction of each of the 11 DETA species in the total DETA of the CO_2 rich phase of solvents (a) 1.5A3.5B and (b) 2A3B at 40 and 120°C. DETA is abbreviated as "A" in the figure legend.

The evolution of the other 9 DETA species was more sensitive to CO_2 loading. As the CO_2 absorption began, the more reactive species DETA, $DETAH(p)^+$ and $DETACOO(p)^-$ were consumed and converted to intermediate species, including $DETAH_2(pp)^{2+}$, $DETA(COO)_2(ps)^{2-}$, $DETA(COO)_2(pp)^{2-}$ and $DETAH_2(ps)^{2+}COO(p)^-$. As the CO_2 loading increased, the intermediate species were converted to their more stable forms through proton exchange (protonation or deprotonation) reactions. As a result, their fractions decreased following an initial increase. Upon further loading of CO_2, the $DETAH(p)^+(COO)_2(ps)^{2-}$ and $DETAH(s)^+(COO)_2(pp)^{2-}$ species, which are the two stable reaction products between DETA and CO_2, accumulated to a larger extent. Overall, at low CO_2 loadings, the dominant species were molecular DETA and $DETACOO(p)^-$, as well as their protonated species. At high CO_2 loadings, the dominant species, such as $DETAH(p)^+(COO)_2(ps)^{2-}$, $DETAH(s)^+(COO)_2(pp)^{2-}$ and $DETAH_2(ps)^{2+}COO(p)^-$, were the more stable reaction products, with more amino groups being bonded with protons or CO_2.

To validate the speciation modeling results by comparison with the NMR analysis performed in our previous study (Ye et al., 2017), we categorized the 11 DETA species into four groups according to the same protocol used in the NMR study (Table 7-5). Species were categorized by groups because with the NMR analysis, we could not differentiate between protonated or nonprotonated species. Group A-III species, including the secondary carbamate of DETA and its protonated species originally included in the NMR study, were negligible in the solvent systems investigated (Section 7.3.1) and were thus excluded from this study.

Table 7-5. Groups of species present in the CO_2 rich phase of the aqueous DETA-PMDETA solvent blend.

Group name	Species included in each group			
A-I	DETA	$DETAH(p)^+$	$DETAH_2(pp)^{2+}$	$DETAH_3^{3+}$
A-II	$DETACOO(p)^-$	$DETAH(p)^+COO(p)^-$	$DETAH_2(ps)^{2+}COO(p)^-$	
A-IV	$DETA(COO)_2(pp)^{2-}$	$DETAH(s)^+(COO)_2(pp)^{2-}$		
A-V	$DETA(COO)_2(ps)^{2-}$	$DETAH(p)^+(COO)_2(ps)^{2-}$		

Fractional contributions of each group of DETA species to the total DETA at 40 and 120°C are shown in Fig. 7-8. Group A-I species, which provided the amino sites for CO_2 bonding, were consumed during the CO_2 absorption (except for the minor $DETAH_3^{3+}$ species). For either Group A-IV or A-V, their presence increased during the CO_2 absorption, indicating they were stable reaction products. The fractional ratio of Group A-IV to Group A-V ranged between 1 and 1.5 under all the modeled conditions for either solvent, suggesting these two groups were of comparable importance. This result was consistent with the results from our NMR study (Ye et al., 2017), which revealed that the reaction routes to produce the primary-primary and primary-secondary dicarbamates of DETA (including their respective protonated species) were equally important. Group A-II species decreased upon loading of CO_2, which indicated the monocarbamate species were converted to the dicarbamate species (Groups A-IV and A-V) during CO_2 absorption. According to the NMR measurement at 23°C, Groups A-I, A-II, A-IV and A-V species accounted for respectively 8.7, 24.0, 36.8 and 30.5% of the total DETA in the CO_2 rich phase of solvent 2A3B at a total CO_2 loading of 0.733. In comparison, the predicted shares of these four groups were respectively 1.8, 18.7, 42.6 and 36.9% at 25°C. The predictions overestimated the amounts of reaction products in the A-IV and A-V species and underestimated those of the A-I and A-II species, which should be due to the simplified assumptions adopted in

the modeling equations. However, the predicted overall trend of species evolution and the relative proportions among the species groups matched those of the NMR study.

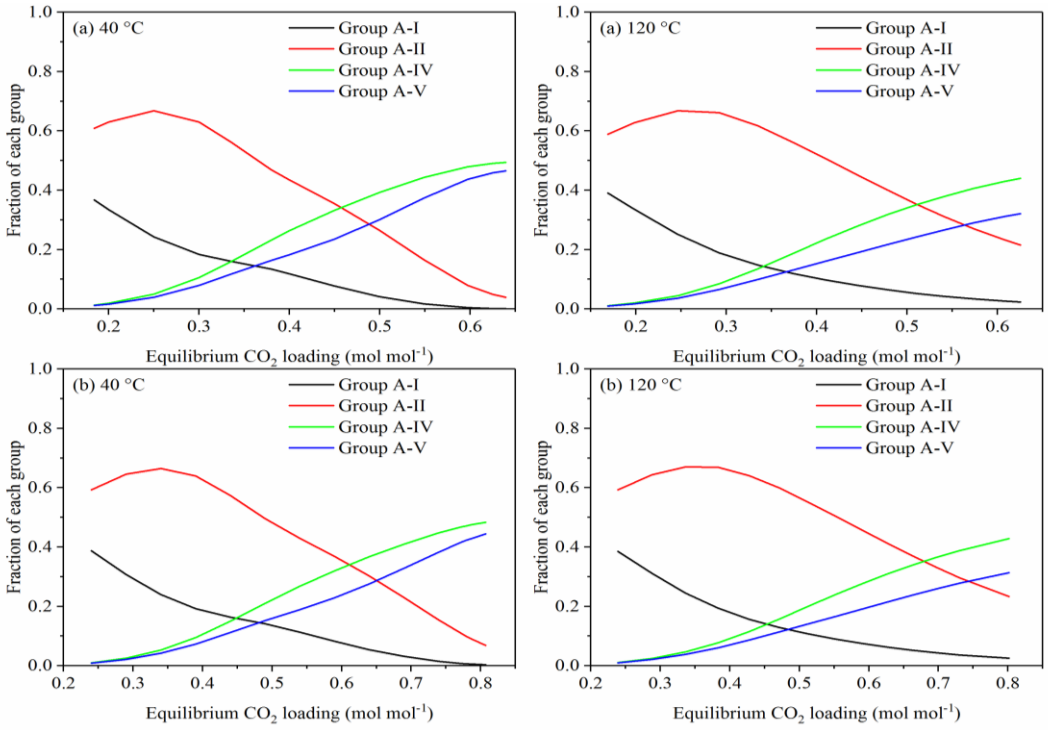

Fig. 7-8. Predicted combined equilibrium fraction of each structural group of DETA species in the CO_2 rich phase of solvents (a) 1.5A3.5B and (b) 2A3B at 40 and 120°C.

As discussed, PMDETA could be present in multiple forms, including molecular PMDETA, $PMDETAH^+$, $PMDETAH_2^{2+}$ and $PMDETAH_3^{3+}$ in the CO_2 rich phase. The shares of individual PMDETA species with respect to total PMDETA in the CO_2 rich phase at 40 and 120°C are shown in Fig. 7-9. The fraction of $PMDETAH_3^{3+}$ in the total PMDETA was negligible (<0.1%) under all the modeling conditions. This was expected because $PMDETAH_3^{3+}$ could be deprotonated, given that the value of pK_{a3} for its dissociation reaction was 2.4. With increasing CO_2 loading, molecular PMDETA and $PMDETAH^+$ decreased but $PMDETAH_2^{2+}$ increased, indicating the latter was a more stable reaction product and the former two were consumed and converted to $PMDETAH_2^{2+}$. At lean CO_2 loadings, a higher temperature resulted in lower fractions of both molecular PMDETA and $PMDETAH^+$ but a higher fraction of $PMDETAH_2^{2+}$. However, at rich CO_2 loadings, the fraction of each species was not affected by temperature changes.

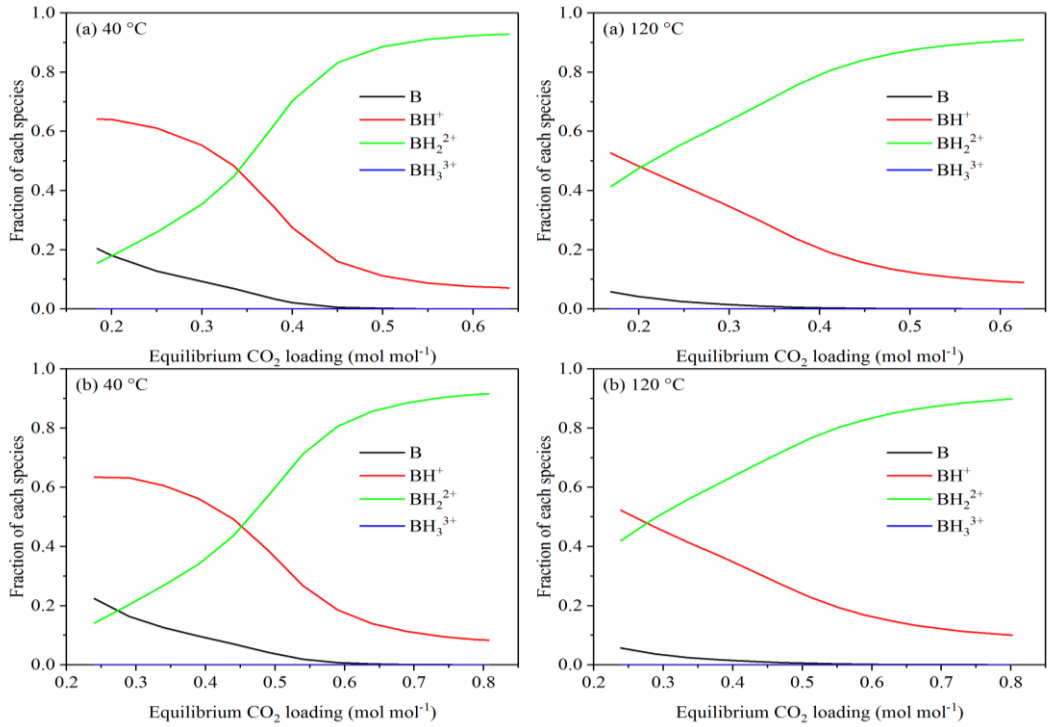

Fig. 7-9. Predicted equilibrium fractions of molecular PMDETA, $PMDETAH^+$, $PMDETAH_2^{2+}$ $PMDETAH_3^{3+}$ species in total PMDETA in the CO_2 rich phase of solvents (a) 1.5A3.5B and (b) 2A3B. PMDETA is abbreviated as "B" in the figure legend.

The predicted equilibrium molalities of protons (H^+) and total bicarbonate and carbonate ions (HCO_3^-/CO_3^{2-}) as well as the ionic strength of the rich phase solvent in relation to the total CO_2 loading at various temperatures are presented in Fig. 7-10. The molalities of both H^+ and total HCO_3^-/CO_3^{2-} increased with increasing CO_2 loading (increasing acidity). Increasing the temperature led to increases in equilibrium molalities of all these species because of enhanced water dissociation and enhanced CO_2 dissolution and hydrolysis in the liquid phase at higher temperatures (Eqs. (7-1) to (7-3)). For either solvent 1.5A3.5B or 2A3B, the ionic strengths were similar at different temperatures when the CO_2 loading was lean (up to 0.35 mol mol^{-1} for 1.5A3.5B and 0.45 mol mol^{-1} for 2A3B). However, when the CO_2 loading was high, the effect of temperature on the ionic strength became pronounced and the ionic strength increased at elevated temperatures.

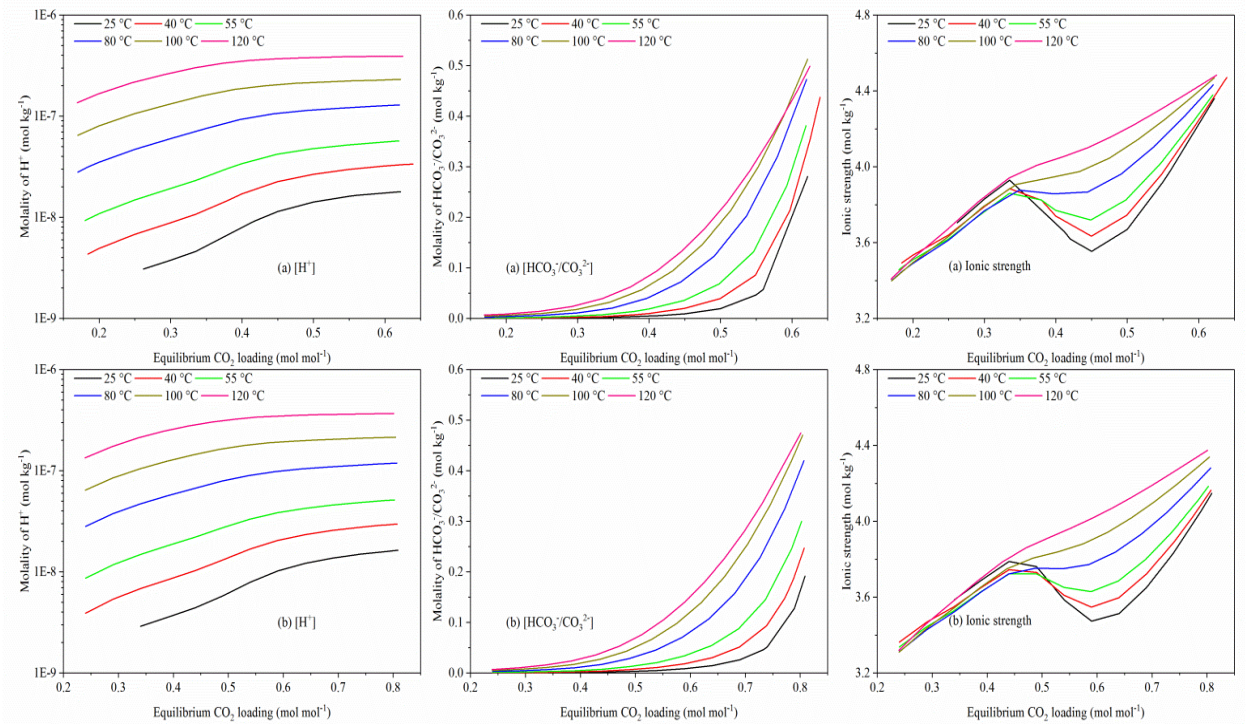

Fig. 7-10. Predicted equilibrium molality of H^+, molality of HCO_3^-/CO_3^{2-} and ionic strength in the CO_2 rich phase of solvents (a) 1.5A3.5B and (b) 2A3B at different temperatures.

7.4.4 Experimental and predicted vapor liquid equilibria

The equilibrium CO_2 partial pressures measured against CO_2 loadings at absorption and desorption temperatures, together with those from the model predictions, are plotted in Fig. 7-11. Model predictions agreed with the experimental data for the two VLLE solvent systems shown in panels (a) and (b), with an average deviation of 25.2% between the modeled and measured data. Only a few measured data exhibited noticeable deviations from the predicted results under low temperatures and at high CO_2 loadings. As expected, the CO_2 partial pressure increased logarithmically with increases in both CO_2 loading and temperature for both solvents. Solvent 1.5A3.5B retained higher CO_2 equilibrium pressures than did 2A3B under the same conditions. According to the model predictions, the equilibrium CO_2 loadings corresponding to an operating CO_2 partial pressure of 5,000 Pa (assumed to be half that of typical flue gas influent, considering a mass transfer driving force requirement for CO_2 absorption), which simulates the solvent exiting a CO_2 absorber, were 0.508 and 0.689 mole CO_2 per mole of total amines at 40°C for solvents 1.5A3.5B and 2A3B, respectively. Likewise, the predicted equilibrium CO_2 loadings corresponding to an operating CO_2 partial pressure of 20 Pa (assumed to be 2% of that of typical

flue gas effluent when considering the same mass transfer driving force requirement), which simulates the solvent entering a CO_2 absorber, were 0.214 and 0.291 mol mol^{-1} at 40°C for the two solvents, respectively. Solvent 2A3B had a higher working capacity (0.398 mol mol^{-1}) for CO_2 absorption than did 1.5A3.5B (0.294 mol mol^{-1}). Under similar conditions, the working capacity of 30 wt% MEA amounted to 0.26 mol mol^{-1} (Aronu et al., 2011). Therefore, the working capacity of solvent 2A3B was 53% larger than that of 30 wt% MEA.

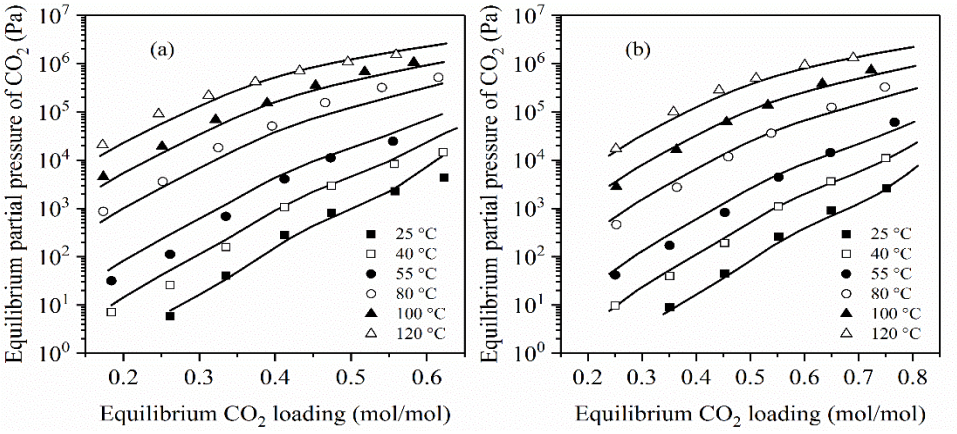

Fig. 7-11. Measured (symbols) and predicted (solid lines) equilibrium partial pressures of CO_2 for solvents (a) 1.5A3.5B and (b) 2A3B.

The predicted partial pressures of water vapor and the fugacity coefficients of CO_2 and water vapor are shown in Figs. 7-12 and 7-13, respectively. The predicted water vapor pressures over each solvent remained similar across the examined range of CO_2 loadings at a given temperature because increasing the CO_2 loading did not decrease the molar fraction of water in the liquid. The fugacity coefficients of both CO_2 and water vapor decreased with increasing temperature or CO_2 loading, suggesting the nonideal behavior of the vapor phase was dominant under high gaseous pressures.

In a biphasic solvent enabled CO_2 capture process, only the CO_2 rich phase solvent (after being separated from the CO_2 lean phase) was required for CO_2 stripping regeneration. A higher CO_2 partial pressure could be attained in the CO_2 stripper because the absorbed CO_2 was concentrated in the rich phase liquid used for CO_2 stripping. The developed model was used to predict the equilibrium CO_2 partial pressure generated from the CO_2 rich phase alone when its composition was known.

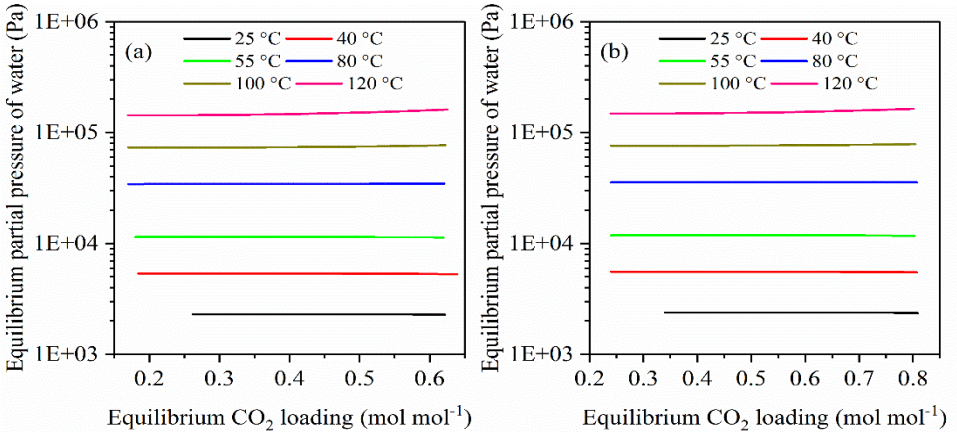

Fig. 7-12. Predicted equilibrium partial pressures of water vapor for solvents (a) 1.5A3.5B and (b) 2A3B.

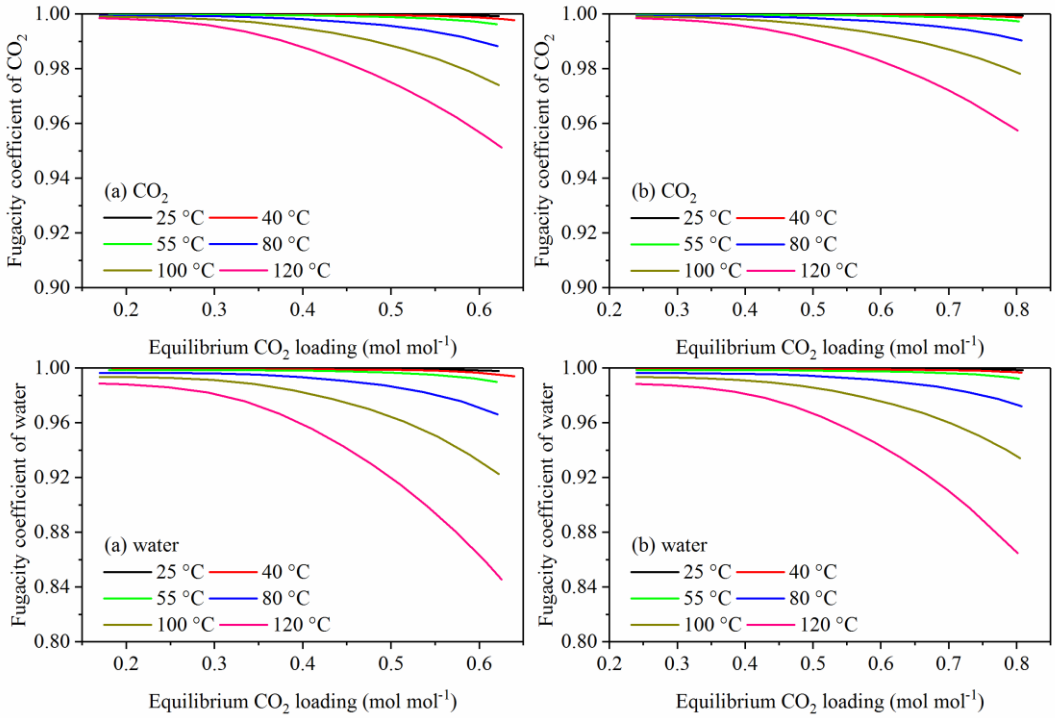

Fig 7-13. Predicted equilibrium fugacity coefficients of CO_2 and water vapor in the gas phase for solvents (a) 1.5A3.5B and (b) 2A3B.

The predicted partial pressures of CO_2 for the rich phase solvents alone when they were heated to the regeneration temperatures (i.e., 80, 100 and 120°C) are shown in Fig. 7-14. The CO_2 rich phase samples used for the desorption equilibrium study were the CO_2 rich phase solvents

obtained by separation from the biphasic solvent after it had reached equilibrium under a CO_2 partial pressure of 2 psia (the typical partial pressure of CO_2 in the flue gas) at 40°C. For solvents 1.5A3.5B and 2A3B, the compositions of their rich phases could be represented as 3.12A2.20B and 3.33A2.22B, respectively. These two rich phase solvents had similar compositions; thus, their predicted CO_2 pressures under the same temperature were indistinguishable (Fig. 7-14). To validate the model predictions, only a rich phase sample with an "averaged" composition, 3.2A2.2B, was prepared for the experimental measurement; the measured partial pressures of CO_2 are displayed in Fig. 7-14. The experimental data matched the predictions, suggesting the thermodynamic methods developed were valid to describe the biphasic solvent system.

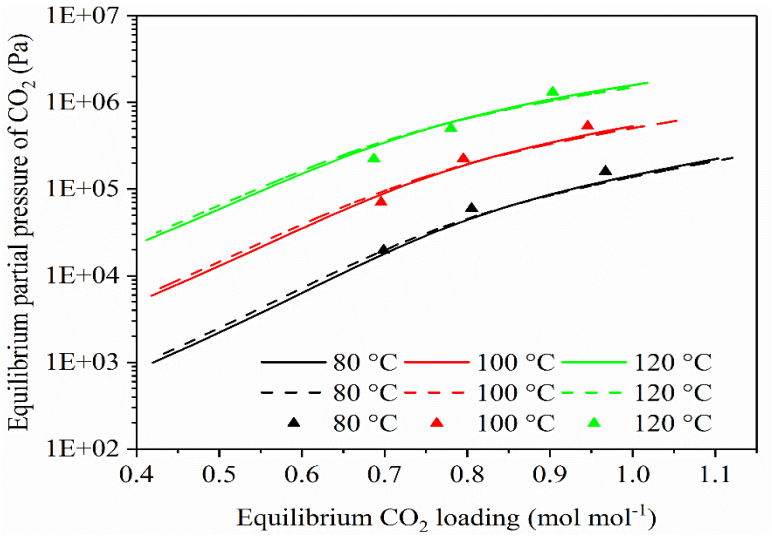

Fig. 7-14. Predicted (lines) and measured (symbols) equilibrium partial pressures of CO_2 over the CO_2 rich phase solvents at 80, 100 and 120°C. The CO_2 rich phase solvents were obtained after being separated from the biphasic solvents 1.5A3.5B (solid lines) and 2A3B (dashed lines) equilibrated with 2 psia of CO_2 gas at 40°C. The measured data are for the "averaged" solvent composition of 3.2A2.2B.

7.4.5 Prediction of reaction heat

The predicted equilibrium partial pressures of CO_2 were used to estimate the heat of CO_2 absorption and desorption for the studied solvents. The heat of the absorption reaction was similar to that of the desorption reaction for a conventional monophasic solvent but was different for a biphasic solvent because the composition of the CO_2 rich phase used for CO_2 desorption was not the same as that of the mother solvent used for CO_2 absorption. Therefore, these two

reaction heat values were determined separately. The Gibbs-Helmholtz equation was implemented to calculate the heat of the absorption or desorption reaction (ΔH_{rea}, kJ/mol CO_2):

$$\ln \frac{P_{CO_2}'}{P_{CO_2}} = \frac{-\Delta H_{rea}}{R}\left(\frac{1}{T} - \frac{1}{T'}\right) \quad (7\text{-}54)$$

where T is the reference temperature, adopted as 313.15 K and 393.15 K, for determining the heat of absorption and desorption, respectively. P_{CO2} and P_{CO2}' are the predicted CO_2 partial pressures at temperatures T and T', respectively.

The predicted heat of absorption as a function of CO_2 loading at 40°C for solvents 1.5A3.5B, 2A3B and 2A are shown in Fig. 7-15a. The modeled trend for the DETA and PMDETA solvent blend (2A3B or 1.5A3.5B) was similar to the measured data for the MAPA and DEEA solvent blend (Arshad et al., 2013a). The heat of absorption decreased during CO_2 absorption because the prevailing products of CO_2 absorption (and their partitions in the two liquid phases) varied during CO_2 absorption. According to the speciation analysis described in Section 7.4.3, at low CO_2 loadings, the dominant products were Group A-II species, which were converted to Group A-IV or A-V species when the CO_2 loading increased. The strength of CO_2 bonding to a secondary amino group of DETA is weaker than that to a primary group; thus, the heat of CO_2 absorption associated with the formation of dicarbamate species becomes lower (Kim and Svendsen, 2007). In the VLLE system, the reaction between CO_2 and PMDETA resulted in the protonation of PMDETA and the formation of HCO_3^-/CO_3^{2-} species. This reaction became dominant when DETA was consumed, resulting in a lower CO_2 bonding strength and heat of absorption at high CO_2 loadings.

The heat of absorption was sensitive to the composition of the fresh solvent. PMDETA, as a tertiary amine, had a lower heat of absorption compared with DETA, which contained multiple primary and secondary amino groups. The heat of absorption of an amine blend ranges between those of its sole constituent amine solutions under comparable conditions (Arshad et al., 2013a; Pinto et al., 2014b). Therefore, compared with solvent 1.5A3.5B, solvent 2A3B had a higher heat of absorption under the similar conditions. The heat of absorption for solvent 2A3B at 40°C was predicted to be greater than 90 kJ mol^{-1} at a CO_2 loading of 0.291 mol mol^{-1} and less than 70 kJ mol^{-1} at a CO_2 loading of 0.689 mol mol^{-1}, corresponding to CO_2 partial pressures of 20 and

5,000 Pa, respectively. The heat of absorption for 2A3B was comparable to that for the 30 wt% MEA (80 kJ mol^{-1}).

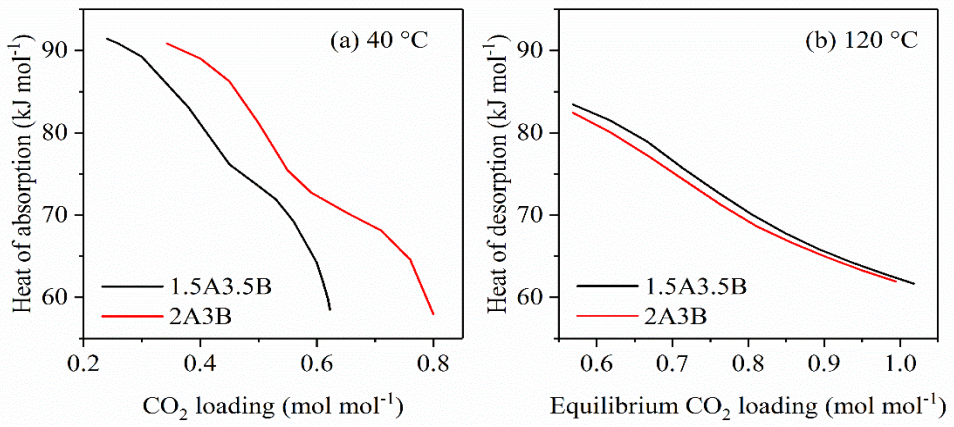

Fig. 7-15. Predicted heat of absorption under 40°C for solvents 1.5A3.5B and 2A3B (panel a), and predicted heat of desorption under 120°C for the CO_2 rich phase solvents separated from biphasic solvents 1.5A3.5B and 2A3B in equilibrium with 13.8 kPa (or 2 psia) of CO_2 at 40°C (panel b).

The predicted heat of desorption at 120°C for the rich phase solvents separated from the two biphasic solvents (1.5A3.5B and 2A3B) equilibrated with 13.8 kPa of CO_2 at 40°C are shown in Fig. 7-15b. As described in Section 7.4.4, the two rich phase liquids had similar compositions (3.12A2.20B and 3.33A2.22B), and the predicted heat of desorption profiles as a function of CO_2 loading were similar to each other. The heat of desorption, which is a reverse process of CO_2 absorption, increased during CO_2 desorption. Following a similar principle as discussed for the heat of absorption, the species with a lower bonding strength with CO_2 underwent CO_2 desorption preferentially, which resulted in an increase in the heat of desorption. In addition, because the CO_2 rich phase solvent required for CO_2 desorption contained a higher molar fraction of DETA species in the total amines than did the mother solvent used for CO_2 absorption, its heat of desorption was higher than the heat of absorption of the mother solvent under equivalent conditions. This high heat of desorption would help the solvent attain a high pressure of CO_2 stripping.

7.5 Conclusions

A comprehensive thermodynamic model was established to predict the liquid-liquid phase transition, equilibrium reactions and VLLE behavior of two aqueous DETA-PMDETA biphasic solvents for CO_2 absorption. Unknown reaction equilibrium constants and BIPs were determined by fitting the measured equilibrium data to the model. The predicted CO_2 partial pressures against CO_2 loading agreed with the experimental data. The model was used to predict the desorption pressures of CO_2 over the CO_2 rich phase solvent after being separated from the biphasic solvent. The model provided detailed speciation information for either liquid phase of the biphasic solvent as a function of the CO_2 loading or temperature. The predicted evolution of various species under different CO_2 loadings was consistent with the experimental results from our prior NMR study. Specifically, the LLPS behavior with respect to volumetric fractions of the CO_2 lean and CO_2 rich phases and the partition of amine species between the two phases was predicted with accuracy. The heat of either the absorption or desorption reaction could be predicted by the model. The heat of desorption for the CO_2 rich phase solvent was higher than the heat of absorption for its mother biphasic solvent. Although this thermodynamic model was developed for the DETA-PMDETA biphasic solvent, this generic approach can be applied to other biphasic solvent systems.

CHAPTER 8: KINETICS OF CO_2 ABSORPTION INTO AQUEOUS SOLUTIONS OF DIETHYLENETRIAMINE, *N,N,N′,N″,N″*-PENTAMETHYLDIETHYLENETRIAMINE, AND THEIR BLEND

8.1 Introduction

The biphasic solvent based CO_2 absorption process has become an alternative technology option to the benchmark monophasic aqueous MEA process by reducing the energy penalty associated with it (Pinto et al., 2014b; Raynal et al., 2011b; Ye et al., 2015b). The majority of the absorbed CO_2 is distributed in one (dense) liquid phase, and the other (light) liquid phase is lean in CO_2 and rich in unreacted solvent molecules (Ciftja et al., 2013b; Xu et al., 2013a; Ye et al., 2017). After the phase split, a high desorption pressure of CO_2 can be attained from the partial liquid with an enriched CO_2 concentration. As a result, the sensible heat, stripping heat and CO_2 compression work requirement can be lowered.

Blends comprised of polyamines (including diamines) with primary or secondary amino groups (rate activators) and tertiary or sterically hindered amines (regeneration promoters) have been used as biphasic solvents; these include the family of aqueous blends of 2-(diethylamino)ethanol (DEEA) and 3-(methylamino)propylamine (MAPA) that was studied by Svendsen's group (Arshad et al., 2013a; Ciftja et al., 2013b; Monteiro et al., 2015b; Pinto et al., 2014b). Besides the aqueous solvent blends, quasiaqueous biphasic solvent blends were reported, such as the mixtures of MEA/H_2O/1-propanol (Zhang et al., 2017a), amine/H_2O/ether (Machida et al., 2017) and diethylenetriamine (DETA)/H_2O/sulfolane (Luo et al., 2016a). A typical quasiaqueous biphasic solvent has two diluent components for the amine, i.e., water and a water miscible organic compound, the latter of which is chemically inert to CO_2 but physically CO_2 philic. The presence of a water miscible organic compound can enhance the CO_2 solubility in the solvent, and induce compulsive liquid-liquid phase separation upon CO_2 loading due to its limited solubility in the aqueous CO_2 rich phase dominant with the ionic amine species produced by CO_2 absorption.

Although the discovery and characterization of new biphasic solvents have been emerging, it is difficult for a solvent to satisfy all the criteria simultaneously, including the favorable performance of CO_2 absorption and desorption, desired phase separation behavior, negligible operational concerns (e.g., foaming, precipitation, vaporization and degradation), good commercial availability and environmental benignity. Among these criteria, a favorable kinetic rate of CO_2 absorption is indispensable for a biphasic solvent and could not be compromised when seeking the optimal trade off with the other criteria. Fundamental understanding of the mass transfer and kinetic characteristics of CO_2 absorption is crucial to the biphasic solvent development. This topic has been investigated in a few biphasic solvent systems with the established mass transfer theory and kinetic rate modeling, such as the blend of 1,4-butanediamine (BDA) and DEEA (Xu et al., 2013b), the blend of 2-(2-aminoethylamino)ethanol (AEEA) and DEEA (Kierzkowska-Pawlak, 2015), and the blend of MAPA and DEEA (Monteiro et al., 2015b) as well as its individual components of MAPA (Monteiro et al., 2014) and DEEA (Monteiro et al., 2015a). In these studies, the "initial" kinetics of CO_2 absorption were measured, i.e., at an approximate zero CO_2 loading in the biphasic solvent (a monophasic mixture actually). However, in this regard, the obtained kinetics could not provide insight to the kinetic performance of a biphasic solvent with high CO_2 loadings, and the effect of the presence of dual liquid phases in the solvent on the kinetics remains unknown.

The kinetics of CO_2 absorption into a biphasic solvent blend of a polyamine DETA and a tertiary amine *N*,*N*,*N*′,*N*′′,*N*′′-pentamethyldiethylenetriamine (PMDETA) was investigated in this study. CO_2 absorption into aqueous monophasic solutions of neat DEEA and neat PMDETA was evaluated first with a laboratory wetted wall column (WWC) reactor and a stirred cell reactor (SCR), respectively. The retrieved kinetic rate constants related to each individual monophasic system were used to predict the CO_2 absorption into the solvent blend of DETA and PMDETA; the results were compared with the experimental data of the solvent blend measured by the WWC reactor. The conventional two film theory based on a single gas-liquid interface was modified to accommodate the presence of two distinct liquid phases, and the roles of the liquid-liquid interface in the absorption kinetics were discussed.

8.2 Material and methods

8.2.1 Chemicals

Compressed CO_2 (>99.9%) and N_2 (>99.9%) were supplied by S. J. Smith Company. DETA (>99.0%) and PMDETA (>99.0%) were purchased from Sigma Aldrich and TCI America, respectively, without further purification. All solutions were prepared by dissolving a certain amount of amine compounds in deionized water. For DETA, three aqueous solutions were studied, i.e., 1, 1.75 and 2.5 m (mol kg^{-1}), under various CO_2 loadings. For PMDETA, three CO_2 free aqueous solutions were tested, i.e., 3, 3.8 and 4.6 m. For the aqueous blend of DETA and PMDETA, two solvent formulae were studied, i.e., 2 m DETA mixed with 3 m PMDETA (abbreviated as 2A3B), and 2 m DETA mixed with 1.5 m PMDETA (abbreviated as 2A1.5B), to simulate the presence and absence of two liquid phases upon CO_2 loading, respectively. The total CO_2 loading in a solvent was determined gravimetrically and reported as moles of CO_2 per mole of total amines in the solvent.

8.2.2 Physical properties

The following physical properties of a solvent-CO_2 system are necessary to interpret the results obtained in the experiments, i.e., solvent density and viscosity, Henry's law solubility constant of CO_2 in the solvent, diffusion coefficients of CO_2 in the solvent and in the gas phase, and diffusion coefficients of solute species in the solvent.

8.2.2.1 Density and viscosity

These two properties were measured directly under a certain temperature. For density, a gravimetric-volumetric method was adopted, and for viscosity, a falling ball viscometer (Gilmont Instruments) was used. When two liquid phases were present, the measurements were conducted for both phases. The overall viscosity of the mixed two liquid phases can be estimated by the following equation (Gambill, 1959):

$$\left(\frac{\mu}{\rho}\right)^{1/3} = x_L\left(\frac{\mu_L}{\rho_L}\right)^{1/3} + x_R\left(\frac{\mu_R}{\rho_R}\right)^{1/3} \quad (8\text{-}1)$$

where μ, μ_L and μ_R (cp) are the dynamic viscosities of the mixture, the CO_2 lean phase and the CO_2 rich phase, respectively. ρ, ρ_L and ρ_R (g mL^{-1}) are the measured densities of the mixture, the

CO_2 lean phase and the CO_2 rich phase, respectively. x_L and x_R are the mass fractions of the CO_2 lean and rich phases, respectively.

8.2.2.2 Henry's constant

The Henry's law solubility constant of CO_2 in the solvent (H_{CO2}, m^3 Pa mol^{-1}) was calculated under a certain temperature (T, K) based on a N_2O analogy method (Versteeg et al., 1996; Versteeg and Van Swaaij, 1988b):

$$\frac{H_{CO_2}}{H_{N_2O}} = \frac{H_{CO_2,w}}{H_{N_2O,w}} \tag{8-2}$$

$$H_{CO_2,w} = 2.825\times10^{6} e^{\frac{-2044}{T}} \tag{8-3}$$

$$H_{N_2O,w} = 8.547\times10^{6} e^{\frac{-2284}{T}} \tag{8-4}$$

where $H_{CO2,w}$ and $H_{N2O,w}$ (m^3 Pa mol^{-1}) are the Henry's constants of CO_2 and N_2O in pure water, respectively. H_{N2O} (m^3 Pa mol^{-1}) is the Henry's constant of N_2O in the solvent. The experimental data of H_{N2O} in fresh DETA solutions (Hartono et al., 2008) were used to estimate the values of H_{N2O} for the DETA solutions in the current study. The values of H_{N2O} for aqueous PMDETA solutions (binary systems) and for solvent mixtures of DETA-PMDETA-H_2O (ternary systems) were estimated according to a semiempirical, "excess Henry's quantity" based method (Wang et al., 1992). The excess thermodynamic quantities for PMDETA were assumed to be equal to those for *N*-methyldiethanolamine (MDEA) in the estimation. When the two liquid phases were present, the reciprocal value of H_{CO2} for the solvent blend were estimated to be the volumetric averaged reciprocal value of H_{CO2} for each individual phase.

8.2.2.3 Diffusion coefficient of CO_2

The diffusion coefficient of CO_2 in the solvent ($D_{CO2,l}$, m^2 s^{-1}) was calculated based on the N_2O analogy method (Versteeg and Van Swaaij, 1988b):

$$\frac{D_{CO_2,l}}{D_{N_2O,l}} = \frac{D_{CO_2,w}}{D_{N_2O,w}} \tag{8-5}$$

$$D_{CO_2,w} = 2.35\times10^{-6} e^{\frac{-2119}{T}} \tag{8-6}$$

$$D_{N_2O,w} = 5.07\times10^{-6} e^{\frac{-2371}{T}} \tag{8-7}$$

where $D_{CO2,w}$ and $D_{N2O,w}$ ($m^2\ s^{-1}$) are the diffusion coefficients of CO_2 and N_2O in pure water, respectively. $D_{N2O,l}$ ($m^2\ s^{-1}$) is the diffusion coefficient of N_2O in the solvent, which was estimated as follows (Cullinane and Rochelle, 2006):

$$D_{N_2O,l} = \frac{5.533 \times 10^{-12} T}{\mu_l^{0.545}} \tag{8-8}$$

where μ_l (cp) is the measured dynamic viscosity of the solvent. The diffusion coefficient of CO_2 in the gas phase ($D_{CO2,g}$, $m^2\ s^{-1}$) was estimated as the binary diffusion coefficient of CO_2 in N_2 (Bird et al., 2002).

8.2.2.4 Diffusion coefficients of solute species

For a fast reaction in a solvent, diffusion of solute species in the gas-liquid interface may limit the overall reaction rate. The diffusion coefficient of a solute species (D_{Am}, $cm^2\ s^{-1}$) is related to its diffusion coefficient at an infinite dilution in water (D_{Am}^{∞}, $cm^2\ s^{-1}$) by a modified Stokes-Einstein equation (Snijder et al., 1993):

$$\mu_l^{0.6} D_{Am} = \mu_w^{0.6} D_{Am}^{\infty} \tag{8-9}$$

where μ_w (cp) is the dynamic viscosity of water. D_{Am}^{∞} was estimated by the Wilke-Chang correlation equation (Wilke and Chang, 1955):

$$D_{Am}^{\infty} = 7.4 \times 10^{-8} \frac{\sqrt{xM}\,T}{\mu_w V_{Am}^{0.6}} \tag{8-10}$$

where x is an association parameter introduced to define the effective molecular weight of the solvent with respect to the diffusion process. For water, the value of x is 2.6. M (g mol^{-1}) is the molecular weight of water. V_{Am} (mL mol^{-1}) is the molar volume of a solute species at the normal boiling point, which was estimated by a group contribution method (Schotte, 1992). The estimated molar volumes of the solute species concerned in this study are listed in Table 8-1.

Table 8-1. Estimated molar volumes of the concerned solute species.

Species	Molar volume
DETA, $DETAH^+$(p), $DETAH_2^{2+}$(pp), $DETAH_3^{3+}$	130.58
$DETACOO^-$(p), $DETAH^+COO^-$(p), $DETAH_2^{2+}COO^-$(p)	158.37
$DETA(COO)_2^{2-}$(pp), $DETAH^+(COO)_2^{2-}$(pp)	186.80
$DETA(COO)_2^{2-}$(ps), $DETAH^+(COO)_2^{2-}$(ps)	183.62
PMDETA, $PMDETAH^+$, $PMDETAH_2^{2+}$, $PMDETAH_3^{3+}$	253.00
HCO_3^-, CO_3^2-	40.40

8.2.3 Speciation in liquids

The molalities of liquid species in the neat DETA solutions under various CO_2 loadings were measured directly via quantitative nuclear magnetic resonance (NMR) spectroscopy (detailed methodology described in Chapter 6), which would enable an accurate kinetic modeling analysis. For the solvent blends of DETA and PMDETA, the prediction of kinetic performance was based on the molalities of liquid species in each phase (if more than one) which were estimated according to the thermodynamic model established and validated in Chapter 7.

8.2.4 The WWC reactor

WWC reactors are commonly used for measuring fast absorption reactions (Danckwerts, 1970). The fluxes of CO_2 absorption into aqueous solutions of neat DETA and aqueous blends of DETA and PMDETA were measured with a laboratory WWC reactor.

8.2.4.1 WWC setup and experimental procedures

The schematic diagram of the WWC reactor is shown in Fig. 8-1. The WWC tube was made of stainless steel with the dimension of 0.5 in outer diameter (OD) and 3.75 in height, and the base of the tube was connected to the feed liquid. The tube was enclosed by a glass chamber of 1.05 in inner diameter (ID). The space within the chamber was where the up flowing gas contacted countercurrently the liquid stream flowing downward on the outer surface of the tube after overflowing through the inner space of the tube. Two gas entry ports were positioned symmetrically at the base of the glass chamber to secure a homogenous gas distribution inside the chamber. After gas analysis, the gas outlet was vented to the air to make the whole setup operating at atmospheric conditions. Two liquid exit ports were positioned at the bottom of the chamber for the liquid falling evenly along the outer surface of the tube to return to the liquid reservoir flask via gravity after contacting the gas. The glass chamber for gas-liquid contact was water jacketed with an outer Plexiglass chamber of 3.3 in ID, and the water within was circulating from and to an external thermostat water bath operating at the desired temperature.

In a typical experiment, 800 g of a solvent was prepared by loading a certain amount of CO_2 into a fresh solvent with a designated composition. The prepared solvent was stored in a 2 L, three neck round bottom glass flask, which was placed in an external water bath maintained at a preset

temperature. The solvent, especially with two liquid phases present, was mixed thoroughly by a magnetic stirrer (Variomag Mobil 25, Thermo Scientific) before it was fed to the WWC reactor with a gear pump (EW-75211-10, Cole Parmer). The tubing connecting the pump to the WWC tube was covered by heating tapes, which were heated to make sure the liquid temperature at the inlet of the WWC tube stabilized at the preset temperature. The liquid flow rate was controlled by a rotameter and measured with a gravimetric-volumetric method, and was maintained at 85 mL min^{-1}. Two mass flow controllers (FC-280S, Tylan), metered by a soap film flowmeter (Sensidyne 800272), were used to control the flow rates of pure N_2 and CO_2, respectively, before they were mixed according to a desired volumetric ratio. The total flow rate of gas mixture fed to the WWC reactor was maintained at 1,700 mL min^{-1} in this study to obtain a constant ratio of gas to liquid flow (G/L=20). The gas mixture was heated in a coil and saturated with water vapor in a gas bubbler, both placed in a water bath, before being fed to the gas-liquid contact chamber. The same water bath was used to provide isothermal water circulating within the Plexiglass chamber of the WWC reactor.

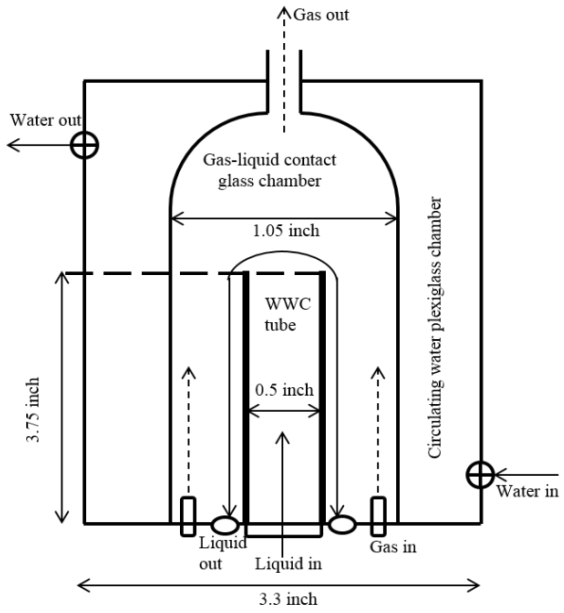

Fig. 8-1. Schematic diagram of the WWC reactor.

When the gas-liquid contact reached the steady state, the gas composition at the outlet of the WWC reactor became stable. The effluent gas passed through an iced acid (2 mol L^{-1} HCl) bath to condense water or amine vapor. The fraction of CO_2 in the dried gas mixture was measured by

an online infrared CO_2 analyzer (Model 906, Quantek Instruments). After one test was completed, the volumetric ratio of N_2 to CO_2 in the feed gas stream was adjusted to the next desired level by the mass flow controllers, while maintaining the same total flow rate. When the new steady state was reached, the fraction of CO_2 was measured again. This procedure was repeated until at least four pairs of CO_2 concentrations at the inlet and outlet of the WWC reactor were obtained. The WWC reactor used in this study was validated by the agreement between the reported and measured data of 30 wt% MEA.

8.2.4.2 Mass transfer in the WWC

At the steady state of a WWC experiment, the fractions of CO_2 measured in the dry gases (moisture removed) at the inlet (c_{in}) and outlet (c_{out}) of the WWC reactor are used to determine their respective CO_2 partial pressures $P_{CO2,\,in}$ (Pa) and $P_{CO2,\,out}$ (Pa). The logarithmic mean of $P_{CO2,\,in}$ and $P_{CO2,\,out}$ is defined as the operational partial pressure of CO_2 (P_{CO2}, Pa) in the bulk gas phase (Cullinane and Rochelle, 2006):

$$P_{CO_2} = \frac{P_{CO_2,in} - P_{CO_2,out}}{\ln\left(\frac{P_{CO_2,in}}{P_{CO_2,out}}\right)} \tag{8-11}$$

The difference between P_{CO2} and the CO_2 partial pressure equilibrated with the solvent at a certain CO_2 loading (P_{CO2}^*, Pa) is the driving force of CO_2 absorption. P_{CO2}^* is related to the CO_2 absorption flux (J_{CO2}, mol m^{-2} s^{-1}) by (Cullinane and Rochelle, 2006):

$$J_{CO_2} = K_{ov}(P_{CO_2} - P_{CO_2}^*) \tag{8-12}$$

where K_{ov} (mol s^{-1} m^{-2} Pa^{-1}) is the overall mass transfer coefficient. J_{CO2} can be obtained by the following equation:

$$J_{CO_2} = \frac{Q_g(c_{in} - c_{out})}{A_a(1 - c_{out})V_m} \tag{8-13}$$

where Q_g (m^3 s^{-1}) is the dry gas flow rate at the inlet of the reactor, A_a (m^2) is the gas-liquid contact area in the WWC reactor and V_m (m^3 mol^{-1}) is the molar volume of CO_2 under atmospheric pressure and the experimental temperature. K_{ov} and P_{CO2}^* can be retrieved by fitting a linear curve of J_{CO2} against P_{CO2}, where K_{ov} is the slope and P_{CO2}^* is the negative ratio of the intercept to the slope of the curve.

Based on the conventional two film theory, J_{CO2} can be expressed as:

$$J_{CO_2} = k_G(P_{CO_2} - P_{CO_2,i}^*) = k_L(m_{CO_2,i}^* - m_{CO_2}) \quad (8\text{-}14)$$

$$P_{CO_2,i}^* = H_{CO_2} m_{CO_2,i}^* \quad (8\text{-}15)$$

$$P_{CO_2}^* = H_{CO_2} m_{CO_2} \quad (8\text{-}16)$$

where k_G (mol s^{-1} m^{-2} Pa^{-1}) and k_L (m s^{-1}) are the mass transfer coefficients in the gas film and liquid film, respectively. $P_{CO2,i}^*$ (Pa) is the CO_2 partial pressure at the gas-liquid interface equilibrated with the CO_2 concentration ($m_{CO2,i}^*$, mol L^{-1}) at the interface, and m_{CO2} (mol L^{-1}) is the concentration of CO_2 in the bulk liquid phase. Eqs. (8-15) and (8-16) indicate the Henry's law relationship between the CO_2 partial pressure and CO_2 concentration. After rearranging Eqs. (8-12) and (8-14) to (8-16), the following equation was obtained:

$$\frac{H_{CO_2}}{k_L} + \frac{1}{k_G} = \frac{1}{K_{ov}} \quad (8\text{-}17)$$

Eq. (8-17) reveals that the total mass transfer resistance ($1/K_{ov}$) is the sum of the mass transfer resistances on the gas side ($1/k_G$) and liquid side (H_{CO2}/k_L). The gas film mass transfer coefficient in a WWC reactor can be expressed as (Li, 2015):

$$k_G = \frac{D_{CO_2,g} Sh}{RTd_h} \quad (8\text{-}18)$$

where R (8.314 J mol^{-1} K^{-1}) is the ideal gas constant. d_h (m) is the hydraulic diameter of the annulus for gas flow, i.e., the difference between the ID of the gas-liquid contact chamber and the OD of the WWC tube. *Sh* is the Sherwood number that is correlated to the Reynolds number (*Re*) and Schmidt number (*Sc*) by the same equation used in Li (2015) due to the similar dimensions of the WWC reactor:

$$Sh = 1.075(Re\, Sc \frac{d_h}{h})^{0.85} \quad (8\text{-}19)$$

where h (m) is the height of the WWC tube, and the expressions for *Re* and *Sc* are:

$$Re = \frac{d_h \nu_g \rho_g}{\mu_g} \quad (8\text{-}20)$$

$$Sc = \frac{\mu_g}{\rho_g D_{CO_2,g}} \quad (8\text{-}21)$$

where ρ_g (kg m^{-3}) and μ_g (Pa·s) are the density and dynamic viscosity of the gas phase, respectively, both of which are cancelled out in Eq. (8-19). ν_g (m s^{-1}) is the velocity of gas flow, which is calculated as the quotient of the gas flow rate and the transverse section area of the annulus for gas flow (A_T, m^2).

The liquid film mass transfer coefficient (k_L) is calculated from Eq. (8-17) with the prior determined K_{ov} and k_G. Because chemical reactions between CO_2 and amines in the solvent enhance the mass transfer across the liquid film, an enhancement factor (E) is defined as the ratio of k_L to the physical liquid film mass transfer coefficient without chemical reactions incorporated (k_L^0, m s^{-1}):

$$E = \frac{k_L}{k_L^0} \tag{8-22}$$

k_L^0 can be expressed as (Li, 2015):

$$k_L^0 = \frac{Q_L}{A_a}(1-\theta) \tag{8-23}$$

where Q_L (m^3 s^{-1}) is the liquid flow rate. θ is the dimensionless driving force that is expressed as:

$$\theta = 1 - 3\sqrt{\frac{\eta}{\pi}} \ (\eta<0.01) \tag{8-24}$$

or, $\theta = 0.7857\exp(-5.121\eta) + 0.1001\exp(39.21\eta) + 0.036\exp(-105.6\eta) + 0.0181\exp(-204.7\eta)$

(η>0.01) (8-25)

where η is the dimensionless penetration distance, and can be estimated by:

$$\eta = \frac{D_{CO_2,l}\tau}{\delta^2} \tag{8-26}$$

where τ (s) is the gas-liquid contact time and δ (m) is the liquid film thickness on the wetted column, which are calculated with the following equations:

$$\tau = \frac{h}{v_l} \tag{8-27}$$

$$v_l = \frac{\rho_l g \delta^2}{2\mu_l} \tag{8-28}$$

$$\delta = \sqrt[3]{\frac{3\mu_l Q_L}{\rho_l g W}} \tag{8-29}$$

where v_l (m s^{-1}) is the superficial velocity of liquid flow, g (m s^{-2}) is the gravitational acceleration constant, W (m) is the circumference of the WWC tube and ρ_l (kg m^{-3}) is the liquid density.

It is essential the CO_2 absorption takes place in the pseudo first order (PFO) regime for the convenience of retrieving the kinetic rate constants. The PFO regime applies to a fast but not instantaneous reaction, in which amine species are present in excess compared with CO_2, the

amine concentrations across the liquid boundary layer are not depleted (remain equal to those in the bulk liquid), and there is no accumulation of reaction products near the gas-liquid interface. In this regime, a linear relationship between J_{CO2} and P_{CO2} is expected. Mathematically, the PFO regime is satisfied when the following condition is met (Hartono et al., 2009; Xu et al., 2013b):

$$3 < \mathrm{Ha} << \mathrm{E}_{\infty} \tag{8-30}$$

where *Ha* is the Hatta number and E_∞ is the infinite enhancement factor. E_∞ is the enhancement factor for an irreversible and instantaneous reaction (with respect to mass transfer) in which the absorption rate is limited completely by the gas diffusion. E_∞ can be represented according to a penetration model as (Higbie, 1935; Kierzkowska-Pawlak, 2015; Xu et al., 2013b):

$$\mathrm{E}_{\infty} = 1 + \frac{\mathrm{D}_{\mathrm{Am}}}{\mathrm{D}_{\mathrm{CO}_2,\mathrm{l}}} \frac{[\mathrm{Am}]\mathrm{H}_{\mathrm{CO}_2}}{\psi_{\mathrm{Am}} \mathrm{P}^{*}_{\mathrm{CO}_2,\mathrm{i}}} \tag{8-31}$$

where ψ_{Am} is the stoichiometric coefficient of the reactant species (ψ_{Am}=1 in this study), and [Am] is the concentration (mol L^{-1}) of the reactant species in the bulk liquid. The Hatta number is defined in Eq. (8-32):

$$\mathrm{Ha} = \frac{\sqrt{\mathrm{k}_{\mathrm{obs}} \mathrm{D}_{\mathrm{CO}_2,\mathrm{l}}}}{\mathrm{k}_{\mathrm{L}}{}^{0}} \tag{8-32}$$

where k_{obs} (s^{-1}) is the observed PFO absorption rate constant. In the PFO regime, the Hatta number and the enhancement factor follow the relationship below (Monteiro et al., 2015a):

$$\mathrm{E} = \frac{\mathrm{Ha}}{\tanh(\mathrm{Ha})} \tag{8-33}$$

The enhancement factor (Eq. (8-33)) is similar to the Hatta number in the PFO regime because tanh(*Ha*) approaches 1 when *Ha*>3 (Van Swaaij and Versteeg, 1992).

However, when the CO_2 partial pressure increases, E_∞ decreases and is not sufficiently larger than *Ha*, and depletion of amines at the interface may occur. This is called an intermediate regime and the following equation adapted from the DeCoursey's model (Decoursey, 1974) is used to estimate the Hatta number:

$$\mathrm{Ha} = \sqrt{\frac{(\mathrm{E}^2 - 1)(\mathrm{E}_{\infty} - 1)}{\mathrm{E}_{\infty} - \mathrm{E}}} \tag{8-34}$$

When the CO_2 partial pressure increases further, and the Hatta number is sufficiently larger than the infinite enhancement factor ($3<E_\infty<<Ha$), the absorption is in an instantaneous regime, in which the reaction rate is limited entirely by the diffusion of CO_2.

When *Ha* is smaller than 0.3, the reaction is in a slow regime and there is little enhancement due to chemical reactions. The absorption flux depends on the liquid flow rate only.

8.2.5 Stirred cell reactor

For slow absorption reactions, the difference of CO_2 partial pressures at the gas inlet and outlet may not be measurable in a WWC reactor. Thus, a batch SCR is regarded as a more accurate tool for studying slow absorption reactions such as CO_2 absorption into tertiary amines (Laddha and Danckwerts, 1981). CO_2 absorption into the aqueous solutions of neat PMDETA was measured with a laboratory SCR based on a fall in pressure technique. The experimental setup is described in detail elsewhere (Zhang et al., 2011d; Ye et al., 2017b).

8.2.5.1 Experimental procedures

In a typical experiment, 20 g of an aqueous, CO_2 free PMDETA solution at a certain concentration (3, 3.8 or 4.6 m) was fed to the reactor cell. The cell was closed, vacuumed and placed in a circulating water bath maintained at a preset temperature. The stirrer was powered on until the solvent inside reached equilibrium with the gas phase, as evidenced by negligible changes of gaseous pressure read from the pressure transducer (PX409-015AUSB, Omega). Pure CO_2 was fed to the cell to ensure the initial partial pressure of CO_2 in the cell arrived instantly at a preset value, which was determined beforehand for a certain concentration of PMDETA solution to satisfy the criterion of a fast PFO regime (Eq. (8-30)). In this study, it was in the range of 20 to 35 kPa. The pressure decrease within 60 s was recorded online from the time when the initial CO_2 partial pressure was reached (t=0 s). The real time partial pressure of CO_2 inside the cell was estimated by subtracting the reference pressure observed before CO_2 was fed from the recorded total gaseous pressure during the experiment.

8.2.5.2 Mass transfer in SCR

According to Eqs. (8-14) and (8-15), assuming the concentration of CO_2 in the bulk liquid is negligible, the CO_2 absorption flux (J_{CO2}, mol m^{-2} s^{-1}) in the SCR can be expressed as (m_{CO2}=0 for zero CO_2 loading in the liquid):

$$J_{CO_2} = k_L \frac{P_{CO_2,i}^*}{H_{CO_2}} \quad (8\text{-}35)$$

In the PFO regime, the Hatta number is assumed to be the same as the enhancement factor. Thus, according to Eqs. (8-22) and (8-32), the following expression is applied:

$$J_{CO_2} = \sqrt{k_{obs} D_{CO_2,l}} \frac{P_{CO_2,i}^*}{H_{CO_2}} \quad (8\text{-}36)$$

Because the gas phase mass transfer resistance is negligible with pure CO_2 gas, the $P_{CO2,i}^*$ in the equation above is the same as the real time partial pressure of CO_2 in the bulk gas phase of the SCR ($P_{CO2,t}$). In addition, the CO_2 absorption flux in the SCR based on the fall in pressure technique can be estimated as:

$$J_{CO_2} = -\frac{dP_{CO_2,t}}{dt} \frac{V_G}{RTA_a} \quad (8\text{-}37)$$

where A_a (m^2) is the gas-liquid contact area in the SCR, which is a plane surface maintained by the triangularly arranged baffles under all test conditions. V_G (m^3) is the headspace of the reactor. By rearranging Eqs. (8-36) and (8-37), the following expression is obtained:

$$\frac{d\ln P_{CO_2,t}}{dt} = -\frac{RTA_a}{V_G H_{CO_2}} \sqrt{k_{obs} D_{CO_2,l}} \quad (8\text{-}38)$$

It is implied from Eq. (8-38) that the logarithmic partial pressure of CO_2 decreased linearly with time in the PFO regime, and the slope is determined from experimental data and used to calculate the observed PFO CO_2 absorption rate constant (k_{obs}).

8.3 Kinetic model

In the biphasic solvent system of DETA-PMDETA-H_2O-CO_2, CO_2 is reacted and converted to carbamate, dicarbamate and bicarbonate species. Based on our previous study, the following reactions should occur (Ye et al., 2017a):

$OH^- + CO_2 = HCO_3^-$ (8-39)

$H_2O + CO_2 = H_2CO_3$ (8-40)

$H_2O + CO_2 + Base = HCO_3^- + BaseH^+$ (8-41)

$DETA + CO_2 + Base = DETACOO^-(p) + BaseH^+$ (8-42)

$DETACOO^-(p) + CO_2 + Base = DETA(COO)_2^{2-}(pp) + BaseH^+$ (8-43)

$DETACOO^-(p) + CO_2 + Base = DETA(COO)_2^{2-}(ps) + BaseH^+$ (8-44)

The formation of HCO_3^- in Eq. (8-39) is a fast reaction which can enhance mass transfer, even though the concentration of hydroxyl ion is low usually. The reaction rate (r_{CO2}, mol L^{-1} s^{-1}) of Eq. (8-39) can be expressed as:

$$r_{CO_2} = -k_{OH^-}[CO_2][OH^-] \quad (8\text{-}45)$$

where k_{OH-} (L mol^{-1} s^{-1}) is the second order rate constant and expressed as:

$$\ln k_{OH^-} = \ln k_{OH^-}^{*} + b[IS] \quad (8\text{-}46)$$

where k_{OH-}^{*} (L mol^{-1} s^{-1}) is the second order rate constant at an infinite dilution and takes the following expression (Pohorecki and Moniuk, 1988):

$$\log(k_{OH^-}^{*}) = 11.916 - \frac{2382}{T} \quad (8\text{-}47)$$

The second term on the right hand side of Eq. (8-46) represents a correction of ionic strength ([IS], mol L^{-1}), especially for CO_2 loaded solutions, and b (L mol^{-1}) is a fitting constant to be determined by experimental data.

Eq. (8-40) refers to an uncatalyzed reaction of CO_2 hydration to form carbonic acid; it is slow and the contribution to the overall reaction rate is negligible (Hartono et al., 2009). Eq. (8-41) is the base catalyzed hydration of CO_2 and formation of bicarbonate (Littel et al., 1990). Eqs. (8-42) to (8-44) are the intrinsic reactions between DETA and CO_2 revealed in our prior study (Ye et al., 2017a). The "Base" in Eqs. (8-41) to (8-44) represents an acceptor of the protons released from the reactions. In the DETA-PMDETA-H_2O-CO_2 system, the base species can be H_2O, OH^-, CO_3^{2-}, DETA, $DETAH^+$(p), $DETAH_2^{2+}$(pp), $DETACOO^-$(p), $DETAH^+COO^-$(p), $DETA(COO)_2^{2-}$(pp), and $DETA(COO)_2^{2-}$(ps), PMDETA, $PMDETAH^+$ and $PMDETAH_2^{2+}$.

When the aqueous solutions of neat PMDETA (CO_2 free) are studied, only Eqs. (8-39) and (8-41) are considered, because PMDETA, as a tertiary amine, cannot react directly with CO_2 (Versteeg and Van Swaaij, 1988a). As a result, the base species for Eq. (8-41) are H_2O, OH^-, PMDETA and $PMDETAH^+$.

In the aqueous solutions of neat DETA, Eq. (8-41) is slower than the reactions between DETA and CO_2 in Eqs. (8-42) to (8-44); its contribution to the overall reaction rate is considered, especially at high CO_2 loadings of the solutions in which amine species are consumed. Moreover,

as $DETA(COO)_2^{2-}$(pp) and $DETA(COO)_2^{2-}$(ps) are both prevailing reaction products from $DETACOO^-$(p) (Ye et al., 2017a) shown in Eqs. (8-43) and (8-44), it is difficult to differentiate their respective kinetics. Therefore, an overall reaction is presented in replacement of Eqs. (8-43) and (8-44):

$$DETACOO^-(p) + CO_2 + Base = DETA(COO)_2^{2-} + BaseH^+ \quad (8\text{-}48)$$

where $DETA(COO)_2^{2-}$ represents the total dicarbamate species in the solutions. However, $DETA(COO)_2^{2-}$(pp) and $DETA(COO)_2^{2-}$(ps) are considered as individual base species.

The rate expression for each of the reactions in Eqs. (8-41), (8-42) and (8-48) takes a general form of:

$$r_{CO_2} = \sum(-k_{Rea-Ba}[Rea][CO_2][Ba] + \frac{k_{Rea-Ba}}{K_{eq,Rea-Ba}}[BaH^+][ReaCO_2]) \quad (8\text{-}49)$$

in which a simple single step, termolecular mechanism (Crooks and Donnellan, 1989; da Silva and Svendsen, 2004) is adopted and the reversible reaction is considered (Chen and Rochelle, 2013). The single step, termolecular mechanism assumes the bonding of CO_2 to an amine molecule and the proton transfer take place simultaneously. In Eq. (8-49), [Rea], [CO_2], [Ba], [BaH^+] and [$ReaCO_2$] are the concentrations (mol L^{-1}) of the reactant species, CO_2, base species, protonated base species and product species, respectively. The sum symbol in the equation indicates the contributions to the overall reaction rate from multiple base species. The 3rd order forward reaction rate constant, k_{Rea-Ba} (L^2 mol^{-2} s^{-1}), is a combined constant with the reactant species "Rea" in the presence of the base species "Ba". The 2nd order reverse rate constant can be expressed as $k_{Rea-Ba}/K_{eq,Rea-Ba}$ (L mol^{-1} s^{-1}), where $K_{eq,Rea-Ba}$ (L mol^{-1}) is the combined equilibrium constant of the intrinsic reaction between CO_2 and the reactant species "Rea" and the protonation reaction of the base species "Ba". All the protonation reactions are considered to be at instant equilibrium. A two step, zwitterion mechanism is used frequently to explain the reactions of carbamate formation, by which CO_2 reacts with an amine molecule to form a net neutral but locally charged intermediate, followed by the proton extraction by a base (Caplow, 1968). According to a previous kinetic study on the CO_2 absorption by DETA solutions (Hartono et al., 2009), the data fitting to the termolecular mechanism was more robust than the zwitterion mechanism; therefore in this study, the termolecular mechanism was used to represent the kinetic reactions.

The value of $k_{\text{Rea-Ba}}$ in Eq. (8-49) can be estimated by the following Arrhenius equation which includes the ionic strength related salt effects (Cullinane and Rochelle, 2006):

$$\ln k_{\text{Rea-Ba}} = a - \frac{E_a}{RT} + b[\text{IS}] \tag{8-50}$$

where a is an empirical fitting constant and E_a (kJ mol^{-1}) is the activation energy of the reaction. Because of the many combinations of a reactant species "Rea" and a base species "Ba" in the DETA-PMDETA-H_2O-CO_2 system, it is difficult to obtain the value of each individual $k_{\text{Rea-Ba}}$. A simplified method using Bronsted theory was adopted to correlate the rate constants to the pK_a values of the participating base species (Bronsted, 1928; Bronsted and Guggenheim, 1927). The correlation takes the following form:

$$\ln k_{\text{Rea-Ba}_2} - \ln k_{\text{Rea-Ba}_1} = \chi(\text{p}K_{\text{a,Ba}_2} - \text{p}K_{\text{a,Ba}_1}) \tag{8-51}$$

The equation above indicates the catalytic effect of a base species on the reaction rate is a linear function of the base strength (i.e., dissociation constant) with a constant Bronsted slope factor (χ) which can be regressed from experimental data. Therefore, for a certain reaction involving multiple bases, the other unknown rate constants can be obtained by retrieving only one rate constant. The correlation in Eq. (8-51) does not depend on the type of molecule (but only on pK_a), thus, the nonamine base species such as water and hydroxide ion can be represented by the same correlation used for amine base species.

The overall CO_2 absorption rate (r_{CO2}, mol L^{-1} s^{-1}) is the sum of the reaction rates expressed in Eqs. (8-45) and (8-49) considering all the combinations of reactant species "Rea" and base species "Ba". r_{CO2} is expressed in Eq. (8-52) as

$$\text{r}_{\text{CO}_2} = -\text{k}_{\text{obs}}[\text{CO}_2] \tag{8-52}$$

k_{obs} (s^{-1}) is the observed PFO absorption rate constant, and can be derived as

$$k_{\text{obs}} = k_{\text{OH}^-}[\text{OH}^-] + \sum k_{\text{Rea-Ba}}([\text{Rea}][\text{Ba}] - \frac{[\text{BaH}^+][\text{ReaCO}_2]}{K_{\text{eq,Rea-Ba}}[\text{CO}_2]}) \tag{8-53}$$

The values of a, b, E_a and χ can be obtained by fitting the experimentally measured k_{obs} to Eq. (8-53) to minimize the following objective function:

$$\text{F} = (\frac{\text{k}_{\text{obs}}^{\text{calc}} - \text{k}_{\text{obs}}^{\text{exp}}}{\text{k}_{\text{obs}}^{\text{exp}}})^2 \tag{8-54}$$

8.4 Results and discussion

8.4.1 Absorption of CO_2 into aqueous DETA solutions

The CO_2 absorption by aqueous solutions of neat DETA (1, 1.75 and 2.5 m) at various CO_2 loadings was conducted in the WWC reactor at 298, 308 and 318 K. Determination of the kinetic rate constants required the prior knowledge of the concentration of each species present in the solution. Quantitative NMR spectroscopic measurements for the neat DETA solutions were conducted to determine the molar fraction of each structural group of species derived from DETA in the solution at 23°C (with detailed descriptions provided in Chapters 6 and 7) (Table 8-2). The measured molar fraction of each group was approximated to be constant across the range of experimental temperatures, which was validated by the results shown in Fig. 7-8. To determine the concentrations of species within the same structural group under a certain experimental temperature, the equilibrium equations of proton dissociation reactions (with detailed descriptions provided in Chapter 7) were required for the molarity calculations. Because the formation of the secondary carbamate of DETA (and its protonated species) was not a preferred reaction route (Ye et al., 2017a), the presence of these species was neglected. The molar concentrations of the concerned species in each kinetic test were thus obtained (results omitted).

Table 8-2. The molar fraction of each structural group among the total DETA in the CO_2 loaded solutions measured by quantitative NMR spectroscopy at 23°C.

Total DETA, mol kg^{-1}	CO_2 loading, mol mol^{-1}	Group A-I	Group A-II	Group A-IV	Group A-V	Presence of HCO_3^-/CO_3^{2-}
1	0.295	71.1%	28.9%	0	0	No
1	0.574	51.2%	40.2%	5.1%	3.5%	No
1	0.815	35.4%	47.9%	9.4%	7.3%	No
1	1.079	28.1%	36.3%	21.2%	14.4%	Yes
1	1.234	23.7%	30.0%	27.8%	18.5%	Yes
1.75	0.333	69.1%	30.9%	0	0	No
1.75	0.521	57.0%	34.0%	5.7%	3.3%	No
1.75	0.843	35.1%	46.1%	10.7%	8.1%	No
1.75	1.065	29.3%	35.0%	21.3%	14.4%	Yes
1.75	1.150	27.2%	30.8%	25.2%	16.8%	Yes
2.5	0.140	86.1%	13.9%	0	0	No
2.5	0.263	73.9%	26.1%	0	0	No
2.5	0.351	65.2%	34.8%	0	0	No
2.5	0.584	52.9%	35.8%	8.2%	3.1%	No
2.5	0.845	36.6%	42.4%	12.6%	8.4%	No
2.5	1.014	28.1%	36.7%	20.6%	14.6%	Yes

Table 8-3. Mass transfer and kinetics related parameters for CO_2 absorption into aqueous solutions of neat DETA.

T, K	DETA, m	CO_2 ldg, mol mol^{-1}	P_{CO2}^*, Pa	H_{CO2}, m^3 Pa mol^{-1}	$D_{CO2,l}$ $\times 10^9$, m^2 s^{-1}	$K_{ov}\times 10^6$, mol s^{-1} m^{-2} Pa^{-1}	$k_G\times 10^6$, mol s^{-1} m^{-2} Pa^{-1}	$k_L^0\times 10^5$, m s^{-1}	$k_L\times 10^3$, m s^{-1}	K_{ov}/k_G, %	*Ha*	$k_{obs}\times 10^{-4}$, s^{-1}
298.55	1	0	0.3	2882.0	1.523	1.287	3.181	6.470	6.231	40.47	96.3	2.549
308.45	1	0	0.6	3699.6	1.650	1.232	3.017	6.788	7.699	40.82	113.4	3.591
318.45	1	0	2.8	4488.7	1.812	1.311	3.207	7.457	9.957	40.89	133.5	5.470
298.25	1	0.295	0.7	2958.5	1.373	1.102	3.130	5.955	5.033	35.21	84.5	1.845
308.15	1	0.295	1.2	3774.7	1.464	1.135	3.192	6.323	6.648	35.56	105.1	3.019
318.25	1	0.295	3.8	4570.1	1.574	1.142	3.091	6.587	8.280	36.95	125.7	4.357
298.35	1	0.574	6.1	3060.9	1.320	0.931	3.063	5.694	4.092	30.38	71.9	1.268
308.15	1	0.574	18.2	3866.4	1.409	0.938	3.040	6.007	5.246	30.86	87.3	1.952
318.15	1	0.574	40.4	4651.8	1.518	0.970	3.084	6.332	6.584	31.46	104.0	2.857
298.15	1	0.815	15.6	3123.5	1.305	0.747	3.064	5.660	3.087	24.39	54.5	0.730
307.95	1	0.815	38.2	3927.7	1.375	0.752	3.043	5.900	3.926	24.73	66.5	1.121
318.45	1	0.815	84.6	4750.3	1.461	0.772	3.078	6.165	4.894	25.08	79.4	1.639
298.15	1	1.079	102.6	3208.7	1.290	0.444	3.093	5.607	1.663	14.35	29.7	0.214
308.25	1	1.079	245.7	4034.7	1.347	0.449	3.068	5.775	2.121	14.63	36.7	0.334
318.25	1	1.079	481.1	4815.9	1.408	0.481	3.089	5.954	2.741	15.56	46.0	0.534
298.35	1	1.234	3335.2	3274.6	1.277	0.202	3.046	5.586	0.709	6.63	12.7	0.039
308.05	1	1.234	6720.7	4066.6	1.321	0.214	3.046	5.714	0.938	7.04	17.5	0.076
318.05	1	1.234	9995.7	4847.4	1.370	0.231	3.060	5.854	1.209	7.53	22.5	0.127
297.95	1.75	0	1.4	3517.9	1.192	1.242	2.962	5.197	7.526	41.93	144.8	4.752
308.05	1.75	0	2.8	4336.2	1.333	1.258	2.942	5.664	9.524	42.74	168.2	6.806
318.45	1.75	0	3.1	5140.8	1.538	1.361	3.103	6.420	12.466	43.87	194.2	10.107
297.75	1.75	0.333	2.6	3683.3	1.174	1.153	3.084	5.182	6.781	37.38	130.9	3.918
308.75	1.75	0.333	8.9	4568.3	1.280	1.180	3.093	5.577	8.715	38.15	156.3	5.933
318.25	1.75	0.333	16.5	5298.3	1.396	1.229	3.131	5.951	10.712	39.23	180.0	8.217
298.25	1.75	0.521	10.9	3823.1	1.132	1.004	3.002	5.024	5.771	33.46	114.9	2.941
308.25	1.75	0.521	22.1	4625.1	1.232	1.075	3.032	5.400	7.701	35.45	142.6	4.813
317.95	1.75	0.521	44.2	5369.5	1.355	1.149	3.143	5.848	9.728	36.56	166.3	6.982
298.35	1.75	0.843	30.4	3994.0	1.074	0.729	3.135	4.856	3.797	23.26	78.2	1.342
308.05	1.75	0.843	97.5	4768.0	1.178	0.777	3.150	5.222	4.917	24.66	94.2	2.052
317.95	1.75	0.843	200.5	5524.3	1.318	0.847	3.193	5.688	6.369	26.53	112.0	3.077
298.55	1.75	1.065	445.8	4118.0	1.017	0.451	3.073	4.593	2.177	14.68	47.4	0.466
308.25	1.75	1.065	900.7	4888.6	1.107	0.475	3.045	4.918	2.750	15.60	55.9	0.683
318.25	1.75	1.065	1699.3	5649.2	1.228	0.506	3.087	5.321	3.420	16.39	64.3	0.952
298.25	1.75	1.150	2692.6	4134.0	0.998	0.307	3.025	4.553	1.413	10.15	31.0	0.200
308.15	1.75	1.150	4990.1	4920.2	1.060	0.325	3.038	4.758	1.792	10.70	39.5	0.333
318.05	1.75	1.150	8503.2	5672.8	1.134	0.350	3.130	5.068	2.237	11.19	47.6	0.514
298.75	2.5	0	0.9	4269.5	0.960	1.242	2.944	4.372	9.174	42.19	209.8	8.765
308.45	2.5	0	1.4	5036.1	1.068	1.273	2.929	4.742	11.334	43.45	239.0	12.025
318.45	2.5	0	1.8	5792.8	1.223	1.361	3.124	5.345	13.963	43.55	261.2	15.947
299.05	2.5	0.140	1.4	4393.3	0.939	1.231	3.058	4.324	9.046	40.24	209.2	8.713
307.85	2.5	0.140	6.4	5086.9	1.031	1.266	3.054	4.640	11.003	41.46	237.1	11.744
318.05	2.5	0.140	7.8	5858.1	1.174	1.298	3.092	5.126	13.109	41.98	255.7	14.635
298.25	2.5	0.263	6.9	4414.1	0.884	1.197	3.112	4.142	8.586	38.47	207.3	8.342
308.65	2.5	0.263	9.4	5231.6	1.000	1.198	3.087	4.552	10.245	38.81	225.0	10.496
318.15	2.5	0.263	18.5	5946.5	1.152	1.241	3.105	5.077	12.285	39.95	242.0	13.101
298.05	2.5	0.351	23.9	4457.6	0.850	1.109	3.014	3.958	7.826	36.81	197.7	7.206
308.35	2.5	0.351	27.8	5266.6	0.961	1.103	2.944	4.348	9.291	37.47	213.7	8.982
318.45	2.5	0.351	41.9	6025.3	1.119	1.167	2.995	4.891	11.513	38.95	235.4	11.843
298.05	2.5	0.584	50.6	4610.3	0.841	0.959	2.971	3.904	6.529	32.28	167.3	5.072
308.45	2.5	0.584	78.4	5422.9	0.927	0.960	2.938	4.202	7.730	32.67	183.9	6.448
318.15	2.5	0.584	120.1	6148.3	1.032	1.021	2.988	4.562	9.540	34.18	209.1	8.814
297.75	2.5	0.845	99.5	4756.9	0.779	0.716	2.957	3.666	4.496	24.22	122.7	2.596
308.25	2.5	0.845	169.4	5565.9	0.843	0.749	2.957	3.900	5.580	25.32	143.1	3.695
318.35	2.5	0.845	297.6	6310.1	0.920	0.794	3.001	4.164	6.810	26.45	163.5	5.043
298.25	2.5	1.014	254.6	4889.4	0.738	0.509	2.945	3.538	3.012	17.30	85.1	1.230
308.15	2.5	1.014	542.5	5656.4	0.809	0.544	2.943	3.793	3.774	18.48	99.5	1.761
318.45	2.5	1.014	1195.8	6420.4	0.906	0.577	2.960	4.135	4.599	19.48	111.2	2.335

All the kinetic measurements were conducted in the WWC reactor with a low (CO_2 partial pressure of 0 to 2.5 kPa) driving force to secure the fulfilment of the PFO criterion. In the PFO

regime, the linear relationship between the absorption flux (J_{CO2}) and the driving force crossed the origin, and a typical graph of this relationship is presented in Fig. 8-2 under the selected experimental conditions.

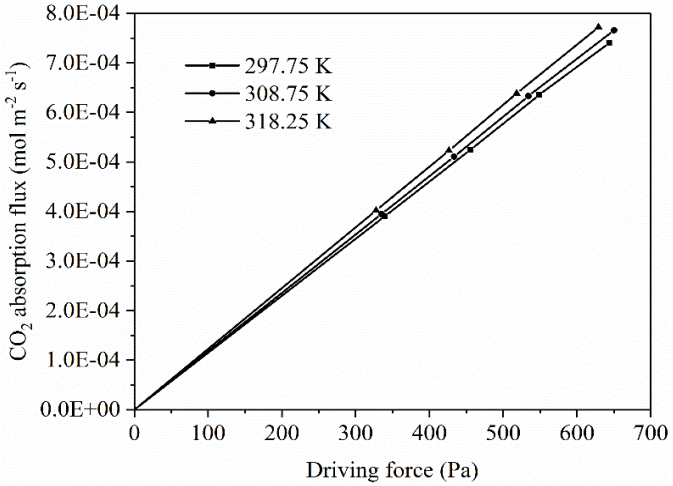

Fig. 8-2. Relationship between the CO_2 absorption flux and the driving force for the 1.75 m DETA solution at the CO_2 loading of 0.333.

The kinetic data from 57 tests are presented in Table 8-3. The gas to liquid flow ratio (G/L) in all these tests was fixed at 20.1. Because all the tests were conducted at a constant gas flow rate of 1,700 mL min^{-1}, the gas film mass transfer coefficients (k_G) were circa 3E-06 mol s^{-1} m^{-2} Pa^{-1}. A high temperature, a high amine concentration or a low CO_2 loading favored the increase of the liquid film mass transfer coefficient (k_L) and the observed PFO kinetic rate constant (k_{obs}), and resulted in a high ratio of K_{ov}/k_G (fraction of gas phase mass transfer resistance in the total resistance).

Because the reactions between CO_2 and DETA in the aqueous solutions were complex, with multiple products of carbamate, dicarbamate and HCO_3^-/CO_3^{2-} species that were dominant sequentially at increasing CO_2 loadings, the kinetic rate constants of all reactions were determined simultaneously by fitting the measured k_{obs} to Eq. (8-53), such that a single set of parameters were retrieved by minimizing the objective function in Eq. (8-54). For the aqueous solvents of neat DETA, the intrinsic reactant species "Rea" in Eq. (8-53) included DETA, $DETACOO^-$(p) and H_2O. Correspondingly, the reaction products between "Rea" and CO_2, i.e., "$ReaCO_2$", were $DETACOO^-$(p) when "Rea" was DETA, $DETA(COO)^{2-}$(pp) and $DETA(COO)^{2-}$

(ps) when "Rea" was $DETACOO^-$(p), and HCO_3^- when "Rea" was H_2O. The base species "Ba" included H_2O, OH^-, CO_3^{2-}, DETA, $DETAH^+$(p), $DETAH_2^{2+}$(pp), $DETACOO^-$(p), $DETAH^+COO^-$(p), $DETA(COO)_2^{2-}$(pp) and $DETA(COO)_2^{2-}$(ps), without considering the relative importance of each reaction they were involved in. The Bronsted relationship among the third order absorption rate constants $k_{Rea\text{-}Ba}$ (L^2 mol^{-2} s^{-1}) is presented in Table 8-4 for the DETA-H_2O-CO_2 system. All these rate constants were corrected by the effect of ionic strength, which was determined simultaneously when calculating the concentrations of species.

Table 8-4. Bronsted relationship among various third order absorption rate constants.

logarithm of $k_{Rea\text{-}Ba}$	pK_a of the base	Formula*
$k_{DETA\text{-}DETA}$	9.8	a_1-E_1/T+b[IS]
$k_{DETA\text{-}H2O}$	-1.74	ln $k_{DETA\text{-}DETA}$-11.54χ
$k_{DETA\text{-}OH\text{-}}$	15.74	ln $k_{DETA\text{-}DETA}$+5.94χ
$k_{DETA\text{-}CO32\text{-}}$	10.33	ln $k_{DETA\text{-}DETA}$+0.53χ
$k_{DETA\text{-}DETAH+(p)}$	8.74	ln $k_{DETA\text{-}DETA}$-1.06χ
$k_{DETA\text{-}DETAH22+(pp)}$	5	ln $k_{DETA\text{-}DETA}$-4.8χ
$k_{DETA\text{-}DETACOO\text{-}(p)}$	10	ln $k_{DETA\text{-}DETA}$+0.2χ
$k_{DETA\text{-}DETAH+COO\text{-}(p)}$	6.96	ln $k_{DETA\text{-}DETA}$-2.84χ
$k_{DETA\text{-}DETA(COO)22\text{-}(pp)}$	10.03	ln $k_{DETA\text{-}DETA}$+0.23χ
$k_{DETA\text{-}DETA(COO)22\text{-}(ps)}$	10	ln $k_{DETA\text{-}DETA}$+0.2χ
$k_{DETACOO\text{-}(p)\text{-}DETACOO\text{-}(p)}$	10	a_2-E_2/T+b[IS]
$k_{DETACOO\text{-}(p)\text{-}H2O}$	-1.74	ln $k_{DETACOO\text{-}(p)\text{-}DETACOO\text{-}(p)}$-11.74χ
$k_{DETACOO\text{-}(p)\text{-}OH\text{-}}$	15.74	ln $k_{DETACOO\text{-}(p)\text{-}DETACOO\text{-}(p)}$+5.74χ
$k_{DETACOO\text{-}(p)\text{-}CO32\text{-}}$	10.33	ln $k_{DETACOO\text{-}(p)\text{-}DETACOO\text{-}(p)}$+0.33χ
$k_{DETACOO\text{-}(p)\text{-}DETA}$	9.8	ln $k_{DETACOO\text{-}(p)\text{-}DETACOO\text{-}(p)}$-0.2χ
$k_{DETACOO\text{-}(p)\text{-}DETAH+(p)}$	8.74	ln $k_{DETACOO\text{-}(p)\text{-}DETACOO\text{-}(p)}$-1.26χ
$k_{DETACOO\text{-}(p)\text{-}DETAH22+(pp)}$	5	ln $k_{DETACOO\text{-}(p)\text{-}DETACOO\text{-}(p)}$-5χ
$k_{DETACOO\text{-}(p)\text{-}DETAH+COO\text{-}(p)}$	6.96	ln $k_{DETACOO\text{-}(p)\text{-}DETACOO\text{-}(p)}$-3.04χ
$k_{DETACOO\text{-}(p)\text{-}DETA(COO)22\text{-}(pp)}$	10.03	ln $k_{DETACOO\text{-}(p)\text{-}DETACOO\text{-}(p)}$+0.03χ
$k_{DETACOO\text{-}(p)\text{-}DETA(COO)22\text{-}(ps)}$	10	ln $k_{DETACOO\text{-}(p)\text{-}DETACOO\text{-}(p)}$
$k_{H2O\text{-}OH\text{-}}$	15.74	a_3-E_3/T+b[IS]
$k_{H2O\text{-}H2O}$	-1.74	$k_{H2O\text{-}OH\text{-}}$-17.48χ
$k_{H2O\text{-}CO32\text{-}}$	10.33	$k_{H2O\text{-}OH\text{-}}$-5.41χ
$k_{H2O\text{-}DETA}$	9.8	$k_{H2O\text{-}OH\text{-}}$-5.94χ
$k_{H2O\text{-}DETAH+(p)}$	8.74	$k_{H2O\text{-}OH\text{-}}$-7χ
$k_{H2O\text{-}DETAH22+(pp)}$	5	$k_{H2O\text{-}OH\text{-}}$-10.74χ
$k_{H2O\text{-}DETACOO\text{-}(p)}$	10	$k_{H2O\text{-}OH\text{-}}$-5.74χ
$k_{H2O\text{-}DETAH+COO\text{-}(p)}$	6.96	$k_{H2O\text{-}OH\text{-}}$-8.78χ
$k_{H2O\text{-}DETA(COO)22\text{-}(pp)}$	10.03	$k_{H2O\text{-}OH\text{-}}$-5.71χ
$k_{H2O\text{-}DETA(COO)22\text{-}(ps)}$	10	$k_{H2O\text{-}OH\text{-}}$-5.74χ

* $E = E_a/R$

The predicted and experimental data of k_{obs} as a function of CO_2 loading in the DETA solutions under various temperatures were compared in Fig. 8-3. The predicted results matched the experimental data. The correction factor for ionic strength (b) was 0.567 and the Bronsted slope

factor (χ) was 0.220 from the regression results. Eqs. (8-55) to (8-57) are the formulae of the regressed kinetic rate constants at an infinite dilution related to the three reactant species in the aqueous DETA solutions, i.e., DETA, DETACOO$^-$(p) and H_2O, respectively (with an average error of 9.7%):

$$k_{\text{DETA-DETA}} = 3.481\times10^{8}\exp(-\frac{3315.9}{T}) \quad (8\text{-}55)$$

$$k_{\text{DETACOO}^-\text{(p)}-\text{DETACOO}^-\text{(p)}} = 2.917\times10^{9}\exp(-\frac{3910.2}{T}) \quad (8\text{-}56)$$

$$k_{\text{H}_2\text{O}-\text{OH}^-} = 3.187\times10^{11}\exp(-\frac{7429.6}{T}) \quad (8\text{-}57)$$

In Eqs. (8-55) and (8-56), the base species were chosen to be the same as the respective reactant species to approach the intrinsic rate constants. The ionic strength effect could be corrected by the regressed parameter *b*. The other rate constants could be derived based on the Bronsted relationship mentioned earlier.

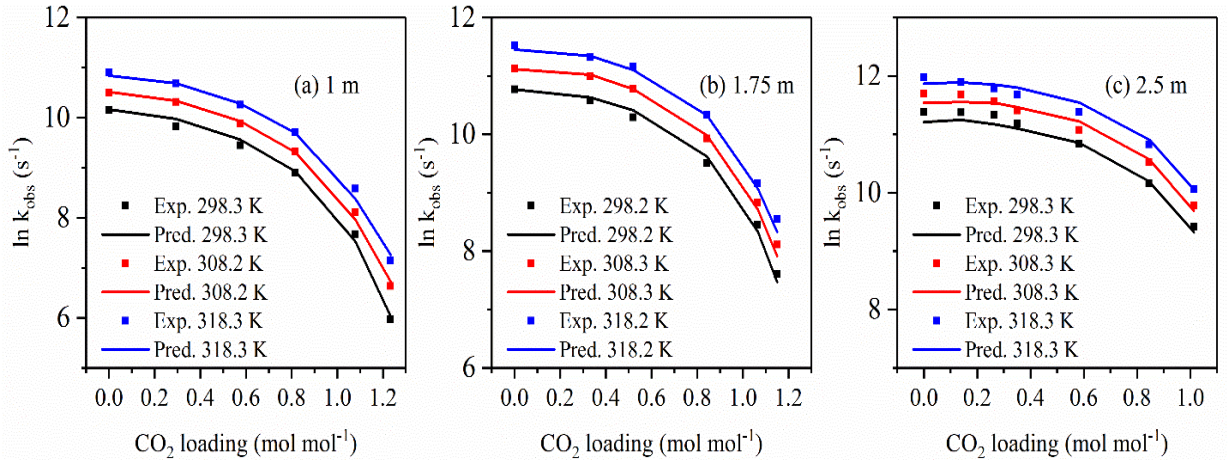

Fig. 8-3. The predicted (lines) and experimental (symbols) data of k_{obs} as a function of CO_2 loading for DETA solutions of (a) 1 m, (b) 1.75 m and (c) 2.5 m.

The activation energies indicated from the above three rate constant expressions are 27.6, 32.5 and 61.8 kJ mol^{-1}, respectively. At 298.15 K, the third order rate constant of the reaction between CO_2 and DETA (with DETA as the base) was predicted to be 5,149.1 L^2 mol^{-2} s^{-1}, and that for the reaction between CO_2 and DETACOO$^-$(p) (with DETACOO$^-$(p) as the base) was predicted to be 5,879.3 L^2 mol^{-2} s^{-1}, indicating that DETACOO$^-$(p) is as reactive as molecular DETA intrinsically. Compared with MEA, which had a reported rate constant of 1,730 L^2 mol^{-2} s^{-1} at 298.15 K and an activation energy of 36.7 kJ mol^{-1} (Aboudheir et al., 2003), the intrinsic reaction

between CO_2 and DETA or $DETACOO^-$(p) was three times as fast as MEA. However, compared to another kinetic study of aqueous DETA solutions at a negligible CO_2 loading by using a string of discs contactor, in which a rate constant of 17,300 L^2 mol^{-2} s^{-1} and an activation energy of 32.2 kJ mol^{-1} were reported (Hartono et al., 2009), the activation energy values between both studies were close, but the rate constant obtained from our study was lower. The deviation was due to the lower k_{obs} values measured in the WWC reactor under comparable conditions in our study. The deviation was not as noticeable for 1 m DETA as for 2.5 m DETA (Fig. 8-4).

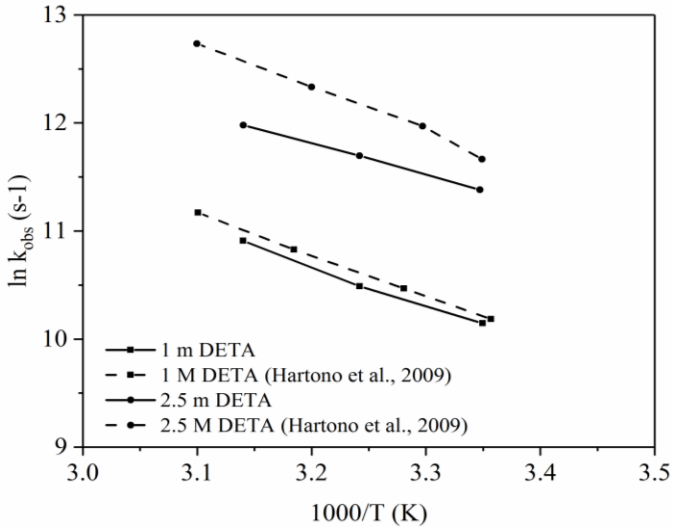

Fig. 8-4. The measured pseudo first order rate constants in this study (solid lines) compared with those reported by Hartono et al. (2009) (dashed lines) for 1 m and 2.5 m DETA solutions. The CO_2 loadings in these tests were all negligible.

8.4.2 Absorption of CO_2 into aqueous PMDETA solutions

CO_2 absorption into the CO_2 free, neat PMDETA solutions (3, 3.8 and 4.6 m) was conducted in the SCR at 296, 308 and 318 K. The driving force, equal to the initial CO_2 partial pressure in the SCR, was in the range of 20 to 35 kPa to satisfy the criterion of a fast PFO regime (Eq. (8-30)). The driving force used in this study was not too low to make sure the Hatta number was greater than 3, and not too high to ensure a sufficiently larger infinite enhancement factor than the Hatta number. The Hatta number in the SCR was estimated by Eq. (8-32) by assuming the value of the physical liquid film mass transfer coefficient (k_L^0, m s^{-1}) to be 4E-05 (Vaidya and Kenig, 2009). The infinite enhancement factor in the SCR was estimated by Eq. (8-31). The experimental results for the PMDETA solutions are summarized in Table 8-5.

Table 8-5. Kinetic parameters of CO_2 absorption into aqueous PMDETA solutions.

T (K)	Molality (m)	H_{CO2} (m^3 Pa mol^{-1})	$D_{CO2,l}$ (m^2 s^{-1})	Ha	E_∞	k_{obs} (s^{-1})
296.65	3	3923.5	6.568E-10	9.6	88.0	226.2
295.65	3.8	3724.4	4.148E-10	7.8	88.7	236.7
295.40	4.6	3748.8	2.798E-10	6.7	79.9	253.2
308.15	3	5162.2	7.482E-10	14.7	115.1	462.0
307.65	3.8	5100.4	5.182E-10	12.4	120.4	477.8
307.15	4.6	5039.1	3.420E-10	10.2	105.8	489.9
318.15	3	6227.1	8.413E-10	20.7	136.6	814.2
318.15	3.8	6516.5	6.941E-10	19.9	151.3	913.4
319.15	4.6	6968.5	5.093E-10	18.7	142.8	1094.8

The observed absorption rate constant k_{obs} (s^{-1}) for the neat PMDETA solutions was expressed as:

$$k_{obs} = k_{OH^-}[OH^-] + \left(k_{H_2O-H_2O}[H_2O] + k_{H_2O-OH^-}[OH^-]\right)[H_2O] + k_{2,B}[PMDETA] + k_{2,BH^+}[PMDETAH^+] \quad (8\text{-}58)$$

where [PMDETA], [$PMDETAH^+$], [OH^-] and [H_2O] were the concentrations (mol L^{-1}) of the respective species in the aqueous PMDETA solutions. k_{OH^-} was the aforementioned second order rate constant. $k_{H2O-H2O}$ and k_{H2O-OH^-} were the third order rate constants determined in Section 8.4.1. $k_{2,B}$ and k_{2,BH^+} (L mol^{-1} s^{-1}) were the second order rate constants of PMDETA and $PMDETAH^+$ catalyzed hydration reaction of CO_2, respectively. $k_{2,B}$ and k_{2,BH^+} followed the Bronsted relationship (with the pK_a difference of 1.1), and the slope (χ) was assumed to be the same as that determined for the aqueous DETA solutions. Because the contribution from molecular PMDETA to the k_{obs} was dominant compared with that from $PMDETAH^+$ in a fresh PMDETA solution, and $k_{2,B}$ and k_{2,BH^+} followed the Bronsted relationship, only the regressed formula of $k_{2,B}$ was presented as follows (an average error of 9.0%):

$$k_{2,B} = 1.903 \times 10^9 \exp\left(-\frac{5186.5}{T}\right) \quad (8\text{-}59)$$

$k_{2,B}$ relied solely on the temperature and was independent of the concentration of PMDETA in the solution. The activation energy of the reaction between aqueous PMDETA and CO_2 revealed from Eq. (8-59) was 43.1 kJ mol^{-1}, a value comparable with that of 44.9 kJ mol^{-1} for an aqueous MDEA solution (Ko and Li, 2000).

8.4.3 Absorption of CO_2 into aqueous blends of DETA and PMDETA

The CO_2 absorption kinetics into the aqueous blends of DETA and PMDETA were measured in the WWC reactor and the results are shown in Table 8-6. Compared with the neat DETA

solutions, the presence of PMDETA did not favor the kinetics because of the smaller PFO rate constant of 2A3B or 2A1.5B observed under similar conditions than those predicted for solvent 2A (aqueous solution of neat DETA, 2 mol kg^{-1}) based on the results in Section 8.4.1. This was expected because a tertiary amine such as PMDETA can enhance CO_2 absorption capacity rather than kinetics.

To determine the effect of two liquid phases on the absorption kinetics, a modified two film mass transfer model was developed to account for the presence of the liquid-liquid interface and predict the rate constant of CO_2 absorption into the biphasic solvents. A schematic diagram comparing the classic and the modified two film models is shown in Fig. 8-5.

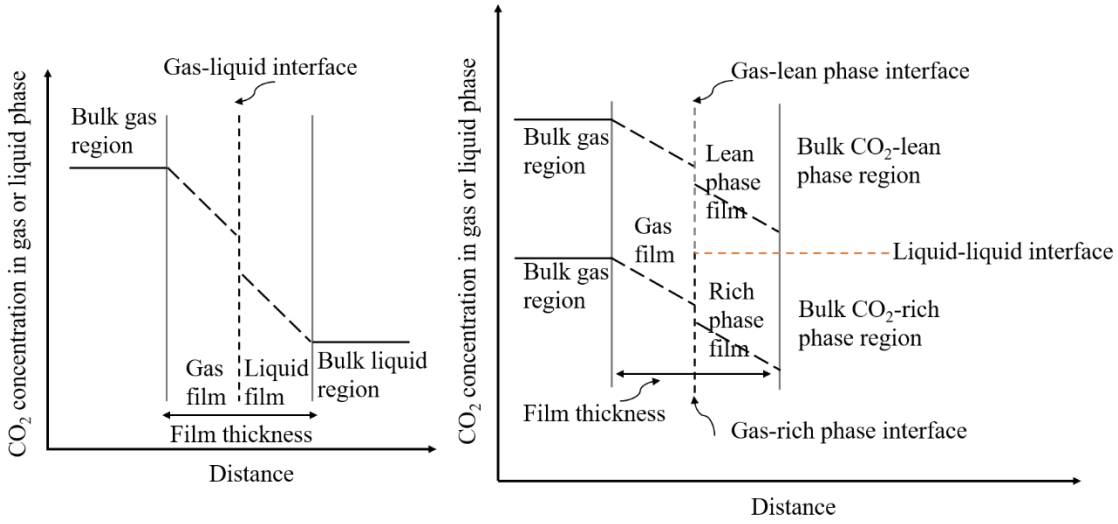

Fig. 8-5. The classic two film theory (left panel) and the modified two film model accounting for the presence of two liquid phases in a biphasic solvent (right panel).

The modified two film model simulated the absorption of CO_2 into the biphasic solvents as the simultaneous absorption of CO_2 into two monophasic solvents (Fig. 8-5), i.e., one CO_2 rich phase, an aqueous solution of the blend of DETA and PMDETA, and one CO_2 lean phase, an aqueous solution of PMDETA (presence of DETA in this phase is negligible, based on the NMR analysis described in Chapter 6). The gas film for both phases was regarded as the same, but the CO_2 rich phase liquid film and CO_2 lean phase liquid film had distinct properties and possessed different mass transfer characteristics. The fractional contact area between gas and the CO_2 rich phase (σ_R) was assumed to be equal to the volumetric fraction of the CO_2 rich phase in the total

solvent. The thermodynamic model established and validated in Chapter 7 served the purpose of estimating the volumetric fraction of each liquid phase with accuracy relative to the measured results. The two liquid phases were regarded to be in equilibrium with each other, and the mass transfer of CO_2 or amines across the liquid-liquid interface was assumed to be negligible within a short time of reaction (<1 s) in the WWC reactor.

Mathematically, the overall absorption flux can be expressed as the sum of the fluxes of CO_2 absorption into each monophasic solution:

$$J_{CO_2} = \frac{J_{CO_2,R} A_R + J_{CO_2,L} A_L}{A_R + A_L} = J_{CO_2,R} \sigma_R + J_{CO_2,L} (1 - \sigma_R) \tag{8-60}$$

where $J_{CO2,R}$ and $J_{CO2,L}$ (mol m^{-2} s^{-1}) are the absorption fluxes of CO_2 into the CO_2 rich phase and CO_2 lean phase, respectively. A_R (m^2) is the contract area between the gas and the CO_2 rich phases, and similarly, A_L (m^2) is that between the gas and the lean phases. Because the equilibrated two liquid phases have the same P_{CO2}^*, the following equation applies according to Eq. (8-12):

$$\frac{J_{CO_2}}{K_{ov}} = \frac{J_{CO_2,R}}{K_{ov,R}} = \frac{J_{CO_2,L}}{K_{ov,L}} = P - P_{CO_2}^* \tag{8-61}$$

where $K_{ov,R}$ and $K_{ov,L}$ (Pa^{-1} mol m^{-2} s^{-1}) are the overall mass transfer coefficients in the CO_2 rich and lean phases, respectively. By rearranging the two equations above, the following expression applies:

$$K_{ov} = K_{ov,R} \sigma_R + K_{ov,L} (1 - \sigma_R) \tag{8-62}$$

Eq. (8-62) can be expanded in the following form according to the definitions of the overall mass transfer coefficients for the CO_2 rich phase, the CO_2 lean phase and the mixture solvent presented in Eq. (8-17):

$$\frac{1}{\frac{1}{k_G} + \frac{H_{CO_2}}{k_L}} = \frac{1}{\frac{1}{k_G} + \frac{H_{CO_2}}{k_{L,R}}} \sigma_R + \frac{1}{\frac{1}{k_G} + \frac{H_{CO_2}}{k_{L,L}}} (1 - \sigma_R) \tag{8-63}$$

where k_G is the mass transfer coefficient in the common gas film, and $k_{L,R}$ and $k_{L,L}$ (m s^{-1}) are the liquid film mass transfer coefficients for the CO_2 rich and lean phases, respectively. In the PFO regime, the Hatta number is the same as the enhancement factor, so the following expression applies according to Eq. (8-32):

$$\frac{1}{\frac{1}{k_G}+\frac{H_{CO_2}}{\sqrt{k_{obs}D_{CO_2,l}}}}=\frac{1}{\frac{1}{k_G}+\frac{H_{CO_2}}{\sqrt{k_{obs,R}D_{CO_2,lR}}}}\sigma_R+\frac{1}{\frac{1}{k_G}+\frac{H_{CO_2}}{\sqrt{k_{obs,L}D_{CO_2,lL}}}}(1-\sigma_R) \quad (8\text{-}64)$$

where $D_{CO2,lR}$ and $D_{CO2,lL}$ ($m^2\ s^{-1}$) are the diffusion coefficients of CO_2 in the CO_2 rich and lean phase solvents, respectively. $k_{obs,R}$ and $k_{obs,L}$ (s^{-1}) are the measured PFO rate constants of CO_2 absorption into the CO_2 rich and lean phase solvents, respectively.

The values of $k_{obs,R}$ and $k_{obs,L}$ also were predicted directly based on the intrinsic kinetic rate constants of CO_2 absorption reactions retrieved from Sections 8.4.1 and 8.4.2. Eq. (8-53) was used for such predictions with DETA, $DETACOO^-$(p) and H_2O as the reactant species "Rea" and all the proton acceptors as the base species "Ba" in either liquid phase. The concentration of each relevant species in either phase was predicted according to the methodology revealed in Chapter 7, and the obtained speciation results are deemed to be reasonable.

The predicted results of the PFO rate constants (k_{obsp}, s^{-1}) are shown in Table 8-6. The error of the predicted rate constants relative to the measured results lied within ±30%, indicating that the predicted rate constants agreed with the measured results. The observed difference between the predicted and measured results could reflect the heterogeneities of mixing in the liquid phase and the gas-liquid contact. When this difference is large enough, a correction factor can be applied to the nominal fractional contact area between gas and the CO_2 rich phase (σ_R). Because the CO_2 rich phase contributed to a majority of the overall kinetics, a large portion of the CO_2 rich phase should favor the kinetics. However, a large portion of the rich phase solvent indicates a high CO_2 loading in a certain solvent, which results in less favorable kinetics. Based on the results above, the modified mass transfer model proposed in this study was valid in predicting the kinetics of CO_2 absorption into the dual liquid phase system, with known physicochemical properties (e.g., density and viscosity) of each phase.

Table 8-6. Mass transfer and kinetics related parameters for CO_2 absorption into aqueous blends of DETA and PMDETA.

T, K	Solvent	CO_2 ldg, mol mol^{-1}	Overall density, g mL^{-1}	Overall viscosity, cp	P_{CO2}^*, Pa	Rich phase vol%	H_{CO2}, m^3 Pa mol^{-1}	$D_{CO2,l}$ $\times 10^{10}$, m^2 s^{-1}	*K*ov×10^6, mol s^{-1} m^{-2} Pa^{-1}	k_G×10^6, mol s^{-1} m^{-2} Pa^{-1}	k_L^0×10^5, m s^{-1}	k_L×10^3, m s^{-1}	*K*ov/k_G, %	*Ha*	k_{obs}×10^{-4}, s^{-1}	k_{obsp}×10^{-4}, s^{-1}
296.75	2A3B	0	0.967	35.9	0.4	0	2493.3	2.527	1.003	2.978	1.477	3.768	33.7	255.1	5.618	5.561
306.85	2A3B	0	0.958	24.4	2.3	0	2846.6	3.135	1.062	2.928	1.744	4.746	36.3	272.1	7.185	7.586
315.65	2A3B	0	0.949	14.4	3.5	0	3172.5	4.202	1.205	3.122	2.209	6.224	38.6	281.7	9.218	10.108
297.55	2A3B	0.269	1.026	40.8	4.3	39.7%	2719.1	2.357	0.743	2.994	1.414	2.688	24.8	190.1	3.065	3.216
306.15	2A3B	0.269	1.019	30.9	17.9	39.7%	3033.5	2.759	0.845	2.970	1.599	3.582	28.4	224.0	4.650	4.162
316.45	2A3B	0.269	1.009	19.0	72.0	39.7%	3430.3	3.621	0.958	2.909	1.961	4.899	32.9	249.8	6.629	5.452
297.65	2A3B	0.476	1.033	43.4	76.2	42.5%	2871.4	2.279	0.558	3.069	1.391	1.960	18.2	140.9	1.686	1.583
308.45	2A3B	0.476	1.024	32.1	272.9	42.5%	3280.8	2.705	0.637	3.001	1.581	2.651	21.2	167.7	2.597	2.211
315.85	2A3B	0.476	1.018	24.4	631.4	42.5%	3575.0	3.155	0.758	2.963	1.829	3.643	25.6	199.2	4.207	3.311
297.35	2A3B	0.670	1.040	57.8	779.6	54.6%	2995.9	1.950	0.275	3.070	1.228	0.904	9.0	73.6	0.419	0.413
307.15	2A3B	0.670	1.032	45.4	2208.3	54.6%	3375.4	2.237	0.352	2.948	1.349	1.348	11.9	99.9	0.812	0.757
316.15	2A3B	0.670	1.025	33.9	5208.1	54.6%	3740.6	2.638	0.444	2.970	1.536	1.952	14.9	127.1	1.444	1.252
297.35	2A1.5B	0	1.008	16.7	0.7	0	3105.0	3.836	1.017	2.931	2.070	4.838	34.7	233.7	6.102	5.798
307.15	2A1.5B	0	0.998	13.3	1.2	0	3622.6	4.370	1.105	3.012	2.321	6.321	36.7	272.3	9.144	8.147
316.05	2A1.5B	0	0.990	10.2	1.8	0	4131.9	5.081	1.144	2.914	2.612	7.779	39.3	297.8	11.911	10.892
297.15	2A1.5B	0.487	1.046	31.8	7.2	0	3480.2	2.701	0.667	2.976	1.579	2.991	22.4	189.4	3.312	3.954
306.65	2A1.5B	0.487	1.037	22.7	24.4	0	4005.8	3.261	0.742	2.961	1.833	3.968	25.1	216.4	4.827	5.540
316.15	2A1.5B	0.487	1.029	13.6	74.8	0	4570.8	4.330	0.854	2.984	2.296	5.472	28.6	238.3	6.915	8.682
297.35	2A1.5B	0.795	1.057	35.0	105.5	0	3719.1	2.563	0.504	3.055	1.532	2.243	16.5	146.4	1.963	2.513
307.25	2A1.5B	0.795	1.049	28.4	333.3	0	4282.4	2.888	0.594	3.000	1.674	3.174	19.8	189.6	3.488	3.909
316.15	2A1.5B	0.795	1.040	22.5	964.2	0	4823.4	3.297	0.662	2.984	1.847	4.104	22.2	222.2	5.109	6.212

8.5 Conclusions

The kinetics of CO_2 absorption by neat DETA and neat PMDETA solutions were studied by a laboratory WWC reactor and a SCR, respectively. Intrinsic rate constants of reactions between CO_2 and DETA were determined by fitting the experimental data of the observed PFO absorption rate constants to a kinetic model. The formation of dicarbamate species from monocarbamate of DETA was as fast as the reactions of producing the monocarbamate from molecular DETA. At 298.15 K, CO_2 absorption into DETA was three times as fast as that into the MEA solution. The reaction rate constants of CO_2 hydration catalyzed by PMDETA species also were determined. The kinetics of CO_2 absorption into the solvent blends of DETA and PMDETA were measured under various temperatures and CO_2 loadings with and without the presence of two liquid phases by using the WWC reactor. The kinetics of the biphasic solvent system also were predicted according to a modified mass transfer model. It was indicated from the modeling results that the absorption of CO_2 into two liquid phases could be described as the simultaneous absorption of CO_2 into each of the two liquid phase solvents.

CHAPTER 9: CONCLUSIONS AND RECOMMENDATIONS

9.1 Conclusions

9.1.1 Energy consumption of phase transitional solvents based processes

The energy use of an absorption process for PCC includes the heat usage for solvent regeneration, CO_2 compression work and auxiliary power use by fans and pumps. The former two are the main contributors to the energy consumption. The total heat usage (Q_{total}, kJ per kg CO_2) for solvent regeneration in the stripping column comes from the steam use in the reboiler and includes three elements, i.e., sensible heat ($Q_{sensible}$, kJ per kg CO_2) required to heat the CO_2 rich solvent from the temperature of the solvent at the inlet of the stripper (T_{inlet}) to the reboiler temperature ($T_{reboiler}$), stripping heat ($Q_{stripping}$, kJ per kg CO_2) associated with water evaporation during CO_2 stripping and reaction heat ($Q_{reaction}$, kJ per kg CO_2) required to desorb CO_2 from the CO_2 rich solvent. The CO_2 compression work (W_{comp}, kJ per kg CO_2) is required to compress the CO_2 from the pressure of the CO_2 product stream exiting the stripping column to the pressure ready for CO_2 storage (153 bar or 2,215 psia). The general expressions for $Q_{sensible}$, $Q_{stripping}$, $Q_{reaction}$ and W_{comp} are shown in Eqs. (9-1) to (9-4):

$$\mathrm{Q_{sensible}} = \frac{\mathrm{C_p(T_{reboiler} - T_{inlet})}}{\mathrm{M_{CO_2} C_{des}}} \tag{9-1}$$

$$\mathrm{Q_{stripping}} = \Delta \mathrm{H_{vap,H_2O}} \frac{\mathrm{M_{H_2O}}}{\mathrm{M_{CO_2}}} \frac{\mathrm{P_{H_2O}}}{\mathrm{P_{CO_2}}} \tag{9-2}$$

$$\mathrm{Q_{reaction}} = -\mathrm{R} \frac{\partial \ln(\mathrm{P^*_{CO_2}})}{\partial(1/\mathrm{T})} \tag{9-3}$$

$$\mathrm{W_{comp}} = 98.86 \ln(\frac{153}{\mathrm{P_{in}}}) - 79.77 \tag{9-4}$$

where C_p (kJ kg^{-1} K^{-1}) is the specific heat capacity of the solvent fed to the stripper; C_{des} (mol CO_2 per kg solvent) is the desorption working capacity of the solvent in the stripping step; M_{CO2} and M_{H2O} (g mol^{-1}) are the molecular weights of CO_2 and H_2O, respectively; P_{H2O} and P_{CO2} (kPa) are the partial pressures of water vapor and CO_2 at the top of the stripping column, respectively; $\Delta H_{vap,H2O}$ is the heat of vaporization of water (40 kJ per mole of water). Eq. (9-3) is the Gibbs-Helmholtz equation used to estimate the reaction heat of the solvent based on the measured equilibrium partial pressures of CO_2 (P^*_{CO2}, kPa) at different temperatures (T, K). Eq.

(9-4) is an approximate correlation equation used to calculate the compression work (Rochelle et al., 2011), in which P_{in} (bar) is the gas pressure at the inlet of the compressor.

In this work, two phase transitional processes, the Hot CAP (a liquid-solid process) and BiCAP (a liquid-liquid process), were investigated to reduce the energy use for CO_2 capture. The major assumptions used to estimate the energy use for the two processes are summarized in Table 9-1. Based on the assumptions, preliminary energy use analyses were conducted for both the Hot CAP and BiCAP. The results and the comparisons with the benchmark MEA process (DOE Case 12, USDOE/NETL, 2013) also are presented in Table 9-1. The total reboiler heat duty (Q_{total}) for solvent regeneration and CO_2 stripping can be converted to electricity power consumption (W_{elec}, kJ per kg CO_2) by the following correlation equation (Lin, 2016):

$$W_{elec} = 90\%\left(\frac{T_{steam} - 313.15K}{T_{steam}}\right)Q_{total} \quad (9\text{-}5)$$

where 90% represents the turbine efficiency and T_{steam} (K) is the condensing temperature of the heating steam. The auxiliary power use for the Hot CAP or BiCAP is assumed to be the same as that of the MEA process. The estimated total parasitic power loss is a sum of the equivalent work of steam use (loss of electricity output), the CO_2 compression work and the auxiliary power use.

The phase transitional solvents based processes have lower steam use and CO_2 compression work requirement than the benchmark MEA process (Table 9-1). For the Hot CAP, the total parasitic power loss was 27.6% lower than the MEA process, and for the BiCAP, this value was 28.1%. The BiCAP employing solvent 2A3B has similar steam usage compared with other biphasic solvents based CO_2 capture technologies reported in the literature, such as the DMX™ process (2,100 kJ kg^{-1}) (Raynal et al., 2011a) and the blend of 2 M MAPA and 5 M DEEA based process (2,200 to 2,400 kJ kg^{-1}) (Pinto et al., 2014a). The energy requirements are estimated based on the assumed conditions that are not optimized for both processes.

Costs of Hot CAP and BiCAP are compared with that of the MEA process referenced from DOE Case 12 (USDOE/NETL, 2013), in which CO_2 is captured and compressed from a supercritical PC fired power plant generating a net 550 MWe of electricity after accounting for the energy demand of the benchmark MEA process. In DOE Case 12, 61% of the total COE increase (47.6

mills kWh^{-1}) was attributable to the parasitic electric power loss caused by CO_2 capture (Lu et al., 2014). The total energy savings for the Hot CAP and BiCAP are each 28%, compared with the MEA process. Assuming other nonenergy related costs of the Hot CAP and BiCAP are comparable to those of the MEA process as a preliminary analysis, the COE increases due to CO_2 capture with the Hot CAP and BiCAP were estimated to be 16.9 and 17.2% lower than that of the MEA process.

Table 9-1. Assumptions used and estimated results for the energy use of the two phase transitional processes in comparison with the benchmark MEA process.

Items	MEA process (DOE Case 12)	Hot CAP	BiCAP
Major assumptions			
Composition of CO_2 rich solvent for stripping	30 wt% MEA, α=0.50	PCB60-79	2A3B (rich), α=1.30[#]
Composition of regenerated CO_2 lean solvent	30 wt% MEA, α=0.25	PCB60-29	Desorbed 2A3B (rich), α=0.56[##]
T_{inlet} (°C)	110	150	110
$T_{reboiler}$ (°C)	120	160	120
C_p (kJ kg^{-1} K^{-1})	3.44	2.33[*]	2.35
P_{CO2} (kPa)	70	260[**]	175
P_{H2O} (kPa)	90	70[**]	75
Energy usage			
(1) Solvent regeneration/CO_2 Stripping	3,556	1,845	2,149
Reaction heat (kJ/kg CO_2)	1,717	1,331[**]	1,610
Sensible heat (kJ/kg CO_2)	670	269	149
Stripping heat (kJ/kg CO_2)	1,169	245	390
T_{steam} (°C)	152	192	152
Electricity equivalent (kWh/kg CO_2)	0.233	0.150	0.141
(2) Compression work (kWh/kg CO_2)	0.103	0.083	0.091
(3) Auxiliary power use (kWh/kg CO_2)	0.035	0.035	0.035
Total parasitic power loss (kWh/kg CO_2)	0.371	0.268	0.266

[*] Data source: Kohl and Nielson (1997); [**] Data source: Zhang et al. (2014). The estimated reaction heat of Hot CAP solvent includes the heat of dissolution of the slurry; [#] CO_2 rich phase of solvent 2A3B (vol% = 50), with an equivalent CO_2 loading of 1.30 mol mol^{-1}; [##] Lean solvent derived from the CO_2 rich phase[#] with a CO_2 loading of 0.56 mol mol^{-1}. α denotes the CO_2 loading (mol CO_2 per mole of total amine).

9.1.2 Kinetics of bicarbonate crystallization in a carbonate based (liquid-solid) process

In Chapter 3, the parameters affecting the crystallization kinetics of $KHCO_3$ were studied. A size dependent crystal growth model was developed based on the experimental data. The model was used to conduct a preliminary analysis of the Hot CAP crystallizers. The major findings are summarized as follows:

(1) The crystallization kinetics were affected by parameters such as the mean residence time of the crystallizer, agitation speed and supersaturation level of $KHCO_3$. The crystal growth rate was inhibited and the average crystal size decreased when the agitation speed was elevated. However, when the supersaturation level was increased (e.g., by lowering the crystallization temperature), both growth rate and crystal size increased. The crystallization of $KHCO_3$ was rapid and could be completed within a mean residence time of 15 min.

(2) A three parameter, size dependent crystal growth model was developed to simulate the crystal growth rate as a function of crystal size under a certain crystallization temperature and relative supersaturation level. Data from the model were in agreement with the experimental data.

(3) A preliminary analysis of the Hot CAP crystallizer validated the feasibility of a unique design of five cascading MSMPR crystallizers with a 5 to 10°C temperature difference between two consecutive ones. This configuration facilitated the heat recovery required in the process compared with the scenario in which a single crystallizer was used with a greater temperature difference between the inlet solvent stream from the absorber (70 to 80°C) and the outlet stream after cooling crystallization (30 to 35°C).

9.1.3 Development of novel liquid-liquid phase transitional solvents

- Solvent screening

In Chapters 4 and 5, relationships between the solvent structure or formula and the performance of CO_2 capture and LLPS were studied. The main findings are summarized as follows:

(1) The performance of CO_2 capture (in terms of the rate and capacity of CO_2 absorption as well as the desorption partial pressure of CO_2) and the behavior of LLPS (in terms of the volumetric fraction of the CO_2 rich phase) were favored by using an aqueous blend of “A” (rate activator) and “B” (regeneration promoter) components with the following characteristics: (i) A linear structured “A” containing 2 to 4 N and 4 to 6 C atoms resulted in the good performance of CO_2 capture, and a polyamine “A” was desired to incur a phase separation; (ii) A hydrophobic “B” facilitated the phase separation and elevated the CO_2 desorption pressure, while a hydrophilic “B” favored a high CO_2 absorption capacity; (iii) A high molar fraction of “A” increased both the rate

and capacity of CO_2 absorption, while a high molar fraction of "B" benefited a high CO_2 desorption pressure.

(2) An aqueous blend of DETA and PMDETA was identified among the candidate solvents with the best overall performance (a trade off among the defined criteria). This solvent had a desired volumetric fraction of the CO_2 rich phase (40 to 60%) at rich loadings, a cyclic capacity up to 50% higher than that of the 30 wt% MEA, a comparable CO_2 absorption rate with that of the MEA across the range of operating CO_2 loadings (5E-04 to 2.5E-03 mol s^{-1} m^{-2}) and a desorption pressure of CO_2 (>1 bar) higher than that of the MEA at 120°C.

- Mechanisms of phase separation during CO_2 absorption and desorption

In Chapter 6, speciation of the biphasic solvent blend of DETA and PMDETA loaded with CO_2 was studied by quantitative NMR spectroscopic analyses. The key findings are listed below:

(1) The CO_2 lean phase was rich in PMDETA, and the CO_2 rich phase contained various molecular and protonated species derived from PMDETA and DETA, including carbamates and dicarbamates of DETA. As CO_2 loading increased, DETA and carbamates of DETA species decreased, and dicarbamates of DETA and PMDETA species increased. The secondary carbamate of DETA remained negligible compared with its primary counterpart, indicating the formation of the latter was preferential. Emerging of HCO_3^-/CO_3^{2-} in the CO_2 rich phase was concomitant with increasing PMDETA species observed in this phase.

(2) The CO_2 absorption into the biphasic solvent blend of DETA and PMDETA underwent the following two stage process. At the early stage, the reaction products between DETA and CO_2 were accumulated in the CO_2 rich phase with a gradual volumetric increase. The molecular PMDETA was partitioned mainly to the CO_2 lean phase. At the later stage, molecular PMDETA transferred to the CO_2 rich phase and was dissolved as protonated species, accompanied by the formation of HCO_3^-/CO_3^{2-} species and a rapid volumetric expansion of the CO_2 rich phase.

(3) The CO_2 desorption from the CO_2 rich phase (separated from the mixture solvent) at an elevated temperature was a reverse process of CO_2 absorption. HCO_3^-/CO_3^{2-} species were

consumed by protons dissociated from the protonated PMDETA, and the dicarbamates were consumed to regenerate the carbamate and the molecular DETA species.

- Development of a VLLE based thermodynamic model

In Chapter 7, a thermodynamic model applicable for VLLE systems was developed based on the principles of VLE, LLE and liquid-liquid phase partition. This model represented the first effort to describe a VLLE system for CO_2 capture. The liquid-liquid phase transition and the thermodynamic properties of the three phases were predicted with the developed model. The key modeling results are listed below:

(1) The predicted partitions of each nominal species (DETA, PMDETA, H_2O and CO_2) in the two liquid phases, and the predicted evolution of each individual species present in the CO_2 rich phase, under various temperatures and CO_2 loadings, were consistent with those from the NMR analyses. The partitioning of species between the two liquid phases and the evolving trends of individual species in the CO_2 rich phase were dependent on the CO_2 loading but not dependent on temperature.

(2) The predicted volumetric fraction and density of each liquid phase were consistent with those from the experimental measurements. The volumetric expansion of the CO_2 rich phase followed the two stage process and was not affected by a temperature change. The density of the CO_2 lean phase did not change with CO_2 loadings; whereas, that of the CO_2 rich phase initially increased and then decreased upon the increasing CO_2 loading.

(3) The equilibrium partial pressures of CO_2 over either the biphasic solvents or their CO_2 rich phases were predicted, and the predictions matched with the experimental results (error<30%). Heats of CO_2 absorption for the biphasic solvent blend of DETA and PMDETA were predicted at 70 to 80 kJ mol^{-1} depending on solvent compositions.

- Kinetics of CO_2 absorption

In Chapter 8, a kinetic study was conducted for neat PMDETA solutions, neat DETA solutions, and aqueous blends of DETA and PMDETA. The key findings are presented below:

(1) Rate constants were determined for aqueous solutions of DETA. At 25°C, the intrinsic (3rd order) rate constant of the reaction between CO_2 and DETA was 5,149 L^2 mol^{-2} s^{-1}, and the rate constant of the reaction between CO_2 and the primary carbamate of DETA was 5,879 L^2 mol^{-2} s^{-1}, indicating the DETA and primary carbamate of DETA species had similar reactivity, which was a level three times higher than that of MEA.

(2) At 25°C, the intrinsic (2nd order) reaction rate constant of the PMDETA catalyzed CO_2 hydration reaction was determined to be 53.0 L mol^{-1} s^{-1}.

(3) CO_2 absorption into the biphasic solvent blend of DETA and PMDETA was simulated with a modified two film mass transfer model by assuming the absorption of CO_2 simultaneously into two monophasic solvents (CO_2 lean and rich phase solvents). The model was validated by the agreement between the predicted CO_2 reaction rate constants and the experimental data.

9.2 Recommendations for future research

Recommendations for future research include two aspects: (1) further characterization of present biphasic solvents and (2) development of biphasic solvents with novel formulations.

The first aspect will lead to the following research activities: (i) measure and predict the additional thermodynamic properties of a biphasic solvent. These properties are crucial to the BiCAP development, which include viscosity, heat capacity and Henry's law solubility constant of CO_2; (ii) measure extra VLLE data which cover a wider range of solvent formulations, i.e., total molality of solvent and molar ratio of components. This will improve the accuracy of prediction by the developed thermodynamic model; (iii) measure the kinetics of CO_2 absorption into a biphasic solvent consisting of two partially mixed liquid phases. The determined "effective" kinetics will facilitate more accurate sizing of the BiCAP absorber.

The second aspect will lead to the following research activities: (i) develop the "A + B + X" type biphasic solvents. Besides the conventional components "A" and "B", an extra functional

component “X” can be added to favor particular aspects of solvent performance or satisfy certain process requirements. For example, an additive applied to a biphasic solvent will reduce its CO_2 rich phase viscosity at rich loadings. As another example, an additive applied to a biphasic solvent will regulate its LLPS behavior; (ii) develop the “AB + X” type biphasic solvents. Instead of the formulation with two components “A” and “B”, a single component “AB” containing a primary or secondary amino group and a tertiary amino group in the same molecule can be the base of novel formulations of biphasic solvents. For this type of “AB” molecule, the intramolecular tertiary amino group will promote the CO_2 absorption rate of the intramolecular primary or secondary amino group and enhance the CO_2 absorption capacity compared with the solvent blend of equal molar MEA (containing only one primary group) and MDEA (containing only one tertiary group) (Cao et al., 2015; Zhang et al., 2016b). An extra component “X” can serve the need for the formulated solvent blend to function as a conventional biphasic solvent.

References

Aboudheir, A., P. Tontiwachwuthikul, A. Chakma, and R. Idem, 2003, Kinetics of the reactive absorption of carbon dioxide in high CO_2-loaded, concentrated aqueous monoethanolamine solutions: *Chemical Engineering Science*, v. 58, p. 5195-5210.

Aleixo, M., M. Prigent, A. Gibert, F. Porcheron, I. Mokbel, J. Jose, and M. Jacquin, 2011, Physical and chemical properties of DMX™ solvents: *10th International Conference on Greenhouse Gas Control Technologies*, GHGT-10, v. 4, p. 148-155.

Anderson, G., 2009, Thermodynamics of Natural Systems, 2nd edition. Cambridge, United Kingdom, Cambridge University Press.

Aronu, U. E., S. Gondal, E. T. Hessen, T. Haug-Warberg, A. Hartono, K. A. Hoff, and H. F. Svendsen, 2011, Solubility of CO_2 in 15, 30, 45 and 60 mass% MEA from 40 to 120 degrees C and model representation using the extended UNIQUAC framework: *Chemical Engineering Science*, v. 66, p. 6393-6406.

Aronu, U. E., I. Kim, and G. Haugen, 2014, Evaluation of energetic benefit for solid-liquid phase change CO_2 absorbents: *12th International Conference on Greenhouse Gas Control Technologies*, GHGT-12, v. 63, p. 532-541.

Aronu, U. E., H. F. Svendsen, K. A. Hoff, and O. Juliussen, 2009, Solvent selection for carbon dioxide absorption: *9th International Conference on Greenhouse Gas Control Technologies*, GHGT-9, v. 1, p. 1051-1057.

Arshad, M. W., P. L. Fosbol, N. von Solms, H. F. Svendsen, and K. Thomsen, 2013a, Heat of absorption of CO_2 in phase change solvents: 2-(diethylamino)ethanol and 3-(methylamino)propylamine: *Journal of Chemical and Engineering Data*, v. 58, p. 1974-1988.

Arshad, M. W., H. F. Svendsen, P. L. Fosbol, N. von Solms, and K. Thomsen, 2014, Equilibrium total pressure and CO_2 solubility in binary and ternary aqueous solutions of 2-(diethylamino)ethanol (DEEA) and 3-(methylamino)propylamine (MAPA): *Journal of Chemical and Engineering Data*, v. 59, p. 764-774.

Arshad, M. W., N. von Solms, and K. Thomsen, 2016, Thermodynamic modeling of liquid-liquid phase change solvents for CO_2 capture: *International Journal of Greenhouse Gas Control*, v. 53, p. 401-424.

Arshad, M. W., N. von Solms, K. Thomsen, and H. F. Svendsen, 2013b, Heat of absorption of CO_2 in aqueous solutions of DEEA, MAPA and their mixture: *11th International Conference on Greenhouse Gas Control Technologies*, GHGT-11, v. 37, p. 1532-1542.

Astarita, G., D. W. Savage, and J. M. Longo, 1981, Promotion of CO_2 mass-transfer in carbonate solutions: *Chemical Engineering Science*, v. 36, p. 581-588.

Austgen, D. M., 1989, A model of vapor-liquid equilibria for acid gas-alkanolamine-water systems: Ph.D. dissertation, The University of Texas at Austin, Austin, Texas.

Barzagli, F., S. Lai, and F. Mani, 2013a, CO_2 capture by liquid solvents and their regeneration by thermal decomposition of the solid carbonated derivatives: *Chemical Engineering & Technology*, v. 36, p. 1847-1852.

Barzagli, F., F. Mani, and M. Peruzzini, 2013b, Efficient CO_2 absorption and low temperature desorption with non-aqueous solvents based on 2-amino-2-methyl-1-propanol (AMP): *International Journal of Greenhouse Gas Control*, v. 16, p. 217-223.

Barzagli, F., F. Mani, and M. Peruzzini, 2016, Carbon dioxide uptake as ammonia and amine carbamates and their efficient conversion into urea and 1,3-disubstituted ureas: *Journal of CO_2 Utilization*, v. 13, p. 81-89.

Barzagli, F., F. Mani, and M. Peruzzini, 2017, Novel water-free biphasic absorbents for efficient CO_2 capture: *International Journal of Greenhouse Gas Control*, v. 60, p. 100-109.

Benson, H. E., J. H. Field, and R. M. Jimeson, 1954, CO_2 absorption employing hot potassium carbonate solutions: *Chemical Engineering Progress*, v. 50, p. 356-364.

Benson, H. E., and R. W. Parrish, 1974, Hipure process removes CO_2-H_2S: *Hydrocarbon Processing*, v. 53, p. 81-82.

Benson, S. M., and T. Surles, 2006, Carbon dioxide capture and storage: an overview with emphasis on capture and storage in deep geological formations: *Proceedings of the IEEE*, v. 94, p. 1795-1805.

Bird, B., W. Stewart, E. Lightfoot, 2002, Transport phenomena, 2nd edition. Hoboken, John Wiley & Sons.

Bishnoi, S., and G. T. Rochelle, 2000, Absorption of carbon dioxide into aqueous piperazine: reaction kinetics, mass transfer and solubility: *Chemical Engineering Science*, v. 55, p. 5531-5543.

Brelvi, S. W., and J. P. Oconnell, 1972, Corresponding states correlations for liquid compressibility and partial molal volumes of gases at infinite dilution in liquids: *AIChE Journal*, v. 18, p. 1239-1243.

Bretherton, T., and A. Rodgers, 1998, Crystallization of calcium oxalate in minimally diluted urine: *Journal of Crystal Growth*, v. 192, p. 448-455.

Bronsted, J. N., 1928, Acid and basic catalysis: *Chemical Reviews*, v. 5, p. 231-338.
Bronsted, J. N., and E. A. Guggenheim, 1927, Contribution to the theory of acid and basic catalysis. The mutarotation of glucose: *Journal of the American Chemical Society*, v. 49, p. 2554-2584.
Broutin, P., P. Briot, S. Ehlers, and A. Kather, 2017, Benchmarking of the DMX™ CO_2 capture process: *Energy Procedia*, v. 114, p. 2561-2572.
Buck, A. L., 1981, New equations for computing vapor-pressure and enhancement factor: *Journal of Applied Meteorology*, v. 20, p. 1527-1532.
Camblor, M. A., A. Mifsud, and J. Perezpariente, 1991, Influence of the synthesis conditions on the crystallization of zeolite beta: *Zeolites*, v. 11, p. 792-797.
Cao, L. D., H. F. Dong, X. P. Zhang, S. J. Zhang, Z. J. Zhao, S. J. Zeng, and J. B. Gao, 2015, Highly efficient carbon dioxide capture by a novel amine solvent containing multiple amino groups: *Journal of Chemical Technology and Biotechnology*, v. 90, p. 1918-1926.
Caplow, M., 1968, Kinetics of carbamate formation and breakdown: *Journal of the American Chemical Society*, v. 90, p. 6795-6803.
Chen, C. C., H. I. Britt, J. F. Boston, and L. B. Evans, 1979, Extension and application of the pitzer equation for vapor-liquid-equilibrium of aqueous-electrolyte systems with molecular solutes: *AIChE Journal*, v. 25, p. 820-831.
Chen, X., and G. T. Rochelle, 2013, Modeling of CO_2 absorption kinetics in aqueous 2-methylpiperazine: *Industrial & Engineering Chemistry Research*, v. 52, p. 4239-4248.
Chen, Y., and H. Hu, 2017, Carbon Dioxide capture by diethylenetriamine hydrobromide in nonaqueous systems and phase-change formation: *Energy & Fuels*, v. 31, p. 5363-5375.
Chivate, M. R., B. G. Palwe, and N. S. Tavare, 1979, Effect of seed concentration in a batch dilution crystallizer: *Chemical Engineering Communications*, v. 3, p. 127-133.
Ciferno, J. P., T. E. Fout, A. P. Jones, and J. T. Murphy, 2009, Capturing carbon from existing coal-fired power plants: *Chemical Engineering Progress*, v. 105, p. 33-41.
Ciferno, J.P., 2007, Pulverized coal oxycombustion power plants: final report of USDOE/NETL, report No. 2007/1291.
Ciftja, A. F., A. Hartono, and H. F. Svendsen, 2013a, C^{13} NMR as a method of species determination in CO_2 absorbent systems: *International Journal of Greenhouse Gas Control*, v. 16, p. 224-232.
Ciftja, A. F., A. Hartono, and H. F. Svendsen, 2013b, Experimental study on phase change solvents in CO_2 capture by NMR spectroscopy: *Chemical Engineering Science*, v. 102, p. 378-386.
Ciftja, A. F., A. Hartono, and H. F. Svendsen, 2014, Amine neutralized amino acid as CO_2 absorbents: A quantitative C^{13} NMR study: *International Journal of Greenhouse Gas Control*, v. 27, p. 169-177.
Coulier, Y., A. R. Lowe, A. Moreau, K. Ballerat-Busserolles, and J. Y. Coxam, 2017, Liquid-liquid phase separation of amine-H_2O-CO_2 systems: new methods for key data: *Fluid Phase Equilibria*, v. 431, p. 1-7.
Crooks, J. E., and J. P. Donnellan, 1989, Kinetics and mechanism of the reaction between carbon-dioxide and amines in aqueous-solution: *Journal of the Chemical Society-Perkin Transactions*, v. 2, p. 331-333.
Cullinane, J. T., and G. T. Rochelle, 2004, Carbon dioxide absorption with aqueous potassium carbonate promoted by piperazine: *Chemical Engineering Science*, v. 59, p. 3619-3630.
Cullinane, J. T., and G. T. Rochelle, 2006, Kinetics of carbon dioxide absorption into aqueous potassium carbonate and piperazine: *Industrial & Engineering Chemistry Research*, v. 45, p. 2531-2545.
da Silva, E. F., and H. F. Svendsen, 2004, Ab initio study of the reaction of carbamate formation from CO_2 and alkanolamines: *Industrial & Engineering Chemistry Research*, v. 43, p. 3413-3418.
Danckwerts, P. V., 1970, Gas-liquid reactions, McGraw-Hill, New York, USA.
Darde, V., K. Thomsen, W. J. M. Van Well, and E. H. Stenby, 2009, Chilled ammonia process for CO_2 capture: *9th International Conference on Greenhouse Gas Control Technologies*, GHGT-9, v. 1, p. 1035-1042.
Darde, V., K. Thomsen, W. J. M. Van Well, and E. H. Stenby, 2010, Chilled ammonia process for CO_2 capture: *International Journal of Greenhouse Gas Control*, v. 4, p. 131-136.
David, R., J. Villermaux, P. Marchal, and J. P. Klein, 1991, Crystallization and precipitation engineering: 4. kinetic model of adipic acid crystallization: *Chemical Engineering Science*, v. 46, p. 1129-1136.
Davis, J., and G. Rochelle, 2009, Thermal degradation of monoethanolamine at stripper conditions: *9th International Conference on Greenhouse Gas Control Technologies*, GHGT-9, v. 1, p. 327-333.
Decoursey, W. J., 1974, Absorption with chemical-reaction: development of a new relation for Danckwerts model: *Chemical Engineering Science*, v. 29, p. 1867-1872.
Deshmukh, R. D., and A. E. Mather, 1981, A mathematical model for equilibrium solubility of hydrogen-sulfide and carbon-dioxide in aqueous alkanolamine solutions: *Chemical Engineering Science*, v. 36, p. 355-362.

Dow Chemical Company, 2017. Amines pK_a and pH. https://dowac.custhelp.com/app/answers/detail/a_id/12881/~/amines-pka-and-ph.

Edwards, T. J., G. Maurer, J. Newman, and J. M. Prausnitz, 1978, Vapor-liquid-equilibria in multicomponent aqueous-solutions of volatile weak electrolytes: *AIChE Journal*, v. 24, p. 966-976.

EIA, 2016, US energy-related carbon dioxide emissions, US Energy Information Administration.

Evans, T. W., G. Margolis, and A. F. Sarofim, 1974, Mechanisms of secondary nucleation in agitated crystallizers: *AIChE Journal*, v. 20, p. 950-958.

Fernandez, E. S., and E. L. V. Goetheer, 2011, DECAB: process development of a phase change absorption process: *10th International Conference on Greenhouse Gas Control Technologies*, GHGT-10, v. 4, p. 868-875.

Fernandez, E. S., K. Heffernan, L. V. van der Ham, M. J. G. Linders, E. Eggink, F. N. H. Schrama, D. W. F. Brilman, E. L. V. Goetheer, and T. J. H. Vlugt, 2013, Conceptual design of a novel CO_2 capture process based on precipitating amino acid solvents: *Industrial & Engineering Chemistry Research*, v. 52, p. 12223-12235.

Freeman, S. A., J. Davis, and G. T. Rochelle, 2010a, Degradation of aqueous piperazine in carbon dioxide capture: *International Journal of Greenhouse Gas Control*, v. 4, p. 756-761.

Freeman, S. A., R. Dugas, D. H. Van Wagener, T. Nguyen, and G. T. Rochelle, 2010b, Carbon dioxide capture with concentrated, aqueous piperazine: *International Journal of Greenhouse Gas Control*, v. 4, p. 119-124.

Freguia, S., and G. T. Rochelle, 2003, Modeling of CO_2 capture by aqueous monoethanolamine: *AIChE Journal*, v. 49, p. 1676-1686.

Gambill, W.R., 1959, How to estimate mixtures viscosities: *Chemical Engineering*, v. 66, p. 151-152.

Garcia, J., 2001, Density of aqueous solutions of CO_2, Lawrence Berkeley National Laboratory, Berkeley, CA.

Garside, J., L. Brecevic, and J. W. Mullin, 1982, The effect of temperature on the precipitation of calcium-oxalate: *Journal of Crystal Growth*, v. 57, p. 233-240.

Garside, J., and R. J. Davey, 1980, Secondary contact nucleation: kinetics, growth and scale-up: *Chemical Engineering Communications*, v. 4, p. 393-424.

Garside, J., V. R. Phillips, and M. B. Shah, 1976, Size-dependent crystal-growth: *Industrial & Engineering Chemistry Fundamentals*, v. 15, p. 230-233.

Garside, J., and M. B. Shah, 1980, Crystallization kinetics from msmpr crystallizers: *Industrial & Engineering Chemistry Process Design and Development*, v. 19, p. 509-514.

Global CCS Institute, 2010, Good plant design and operation for onshore carbon capture installations and onshore pipelines: a recommended practice guidance document.

Global CCS Institute, 2011, Accelerating the uptake of CCS: industrial use of captured carbon dioxide.

Goff, G. S., and G. T. Rochelle, 2004, Monoethanolamine degradation: O_2 mass transfer effects under CO_2 capture conditions: *Industrial & Engineering Chemistry Research*, v. 43, p. 6400-6408.

Gomez, A., P. Briot, L. Raynal, P. Broutin, M. Gimenez, M. Soazic, P. Cessat, and S. Saysset, 2014, ACACIA project: development of a post-combustion CO_2 capture process. case of the DMX^{TM} process: *Oil & Gas Science and Technology-Rev. IFP Energies Nouvelles*, v. 69, p. 1121-1129.

Gomez-Diaz, D., D. Lopez-Rivas, J. M. Navaza, and A. Couvert, 2016, Carbon dioxide and n-Hexane absorption using a gas-liquid-liquid reactor: *Chemical Engineering & Technology*, v. 39, p. 751-757.

Hanak, D. P., C. Biliyok, and V. Manovic, 2015, Rate-based model development, validation and analysis of chilled ammonia process as an alternative CO_2 capture technology for coal-fired power plants: *International Journal of Greenhouse Gas Control*, v. 34, p. 52-62.

Hartono, A., E. F. da Silva, H. Grasdalen, and H. F. Svendsen, 2007, Qualitative determination of species in DETA-H_2O-CO_2 system using C^{13} NMR spectra: *Industrial & Engineering Chemistry Research*, v. 46, p. 249-254.

Hartono, A., E. F. da Silva, and H. F. Svendsen, 2009, Kinetics of carbon dioxide absorption in aqueous solution of diethylenetriamine (DETA): *Chemical Engineering Science*, v. 64, p. 3205-3213.

Hartono, A., K. A. Hoff, T. Mejdell, and H. F. Svendsen, 2011, Solubility of carbon dioxide in aqueous 2.5 M of diethylenetriamine (DETA) solution: *10th International Conference on Greenhouse Gas Control Technologies*, GHGT-10, v. 4, p. 179-186.

Hartono, A., O. Juliussen, and H. F. Svendsen, 2008, Solubility of N_2O in aqueous solution of diethylenetriamine: *Journal of Chemical and Engineering Data*, v. 53, p. 2696-2700.

Hartono, A., F. Saleem, M. W. Arshad, M. Usman, and H. F. Svendsen, 2013, Binary and ternary VLE of the 2-(diethylamino)-ethanol (DEEA)/3-(methylamino)-propylamine (MAPA)/water system: *Chemical Engineering Science*, v. 101, p. 401-411.

Hartono, A., and H. F. Svendsen, 2009, Kinetics reaction of primary and secondary amine group in aqueous solution of diethylenetriamine (DETA) with carbon dioxide: *9th International Conference on Greenhouse Gas Control Technologies*, GHGT-9, v. 1, p. 853-859.

Herrera, M. L., and R. W. Hartel, 2000, Effect of processing conditions on crystallization kinetics of a milk fat model system: *Journal of the American Oil Chemists Society*, v. 77, p. 1177-1187.

Higbie, R., 1935, The rate of absorption of a pure gas into a still liquid during short periods of exposure: *Transactions of the American Institute of Chemical Engineers*, v. 31, p. 365-389.

Hsieh, K. T., and R. K. Rajamani, 1991, Mathematical-model of the hydrocyclone based on physics of fluid-flow: *AIChE Journal*, v. 37, p. 735-746.

Hu, L., 2009. CO_2 capture from flue gas by phase transitional absorption: final report of USDOE/NETL, report No. DE-FG26-05NT42488.

Huntsman Corporation, 2009. Amine applications and properties data. http://www.huntsman.com/performance_products/Media%20Library/a_MC348531CFA3EA9A2E040EBCD2B6B7B06/Products_MC348531D0B9FA9A2E040EBCD2B6B7B06/Amines_MC348531D0BECA9A2E040EBCD2B6B7B06/files/amine_applications_and_properties_data_2009.pdf

Idem, R., M. Wilson, P. Tontiwachwuthikul, A. Chakma, A. Veawab, A. Aroonwilas, and D. Gelowitz, 2006, Pilot plant studies of the CO_2 capture performance of aqueous MEA and mixed MEA/MDEA solvents at the University of Regina CO_2 capture technology development plant and the Boundary Dam CO_2 capture demonstration: *Industrial & Engineering Chemistry Research*, v. 45, p. 2414-2420.

IEA, 2013, Technology roadmap: carbon capture and storage, 2013 edition.

IPCC, 2007, Fourth Assessment Report, climate change 2007: synthesis report.

IPCC, 2013, Fifth Assessment Report, climate change 2013: the physical science basis.

IPCC, 2014, Fifth Assessment Report, climate change 2014: synthesis report.

Jeon, S. B., S. W. Cho, S. S. Lee, S. Y. Jang, and K. J. Oh, 2014, Absorption characteristics of carbon dioxide into an O/W emulsion absorbent containing *N*-methylcyclohexylamine/2,6-dimethylpiperidine: *Journal of the Taiwan Institute of Chemical Engineers*, v. 45, p. 2673-2680.

Jeon, S. B., J. H. Jung, H. D. Lee, B. J. Kim, and K. J. Oh, 2016, Absorption of carbon dioxide in O/W emulsion absorbent: kinetics of absorption in *N*-methylcyclohexylamine and 2,6-dimethylpiperidine emulsion: *International Journal of Greenhouse Gas Control*, v. 44, p. 1-10.

Jones, A. G., J. Budz, and J. W. Mullin, 1986, Crystallization kinetics of potassium-sulfate in an MSMPR agitated vessel: *AIChE Journal*, v. 32, p. 2002-2009.

Jou, F. Y., A. E. Mather, and F. D. Otto, 1995, The solubility of CO_2 in a 30-mass-percent monoethanolamine solution: *Canadian Journal of Chemical Engineering*, v. 73, p. 140-147.

Kang, M., S. Jeon, J. Cho, J. Kim, K. Oh, 2017, Characterization and comparison of the CO_2 absorption performance into aqueous, quasi-aqueous and non-aqueous MEA solutions: *International Journal of Greenhouse Gas Control*, v. 63, p. 281-288.

Karpinski, P. H., 1985, Importance of the 2-step crystal-growth model: *Chemical Engineering Science*, v. 40, p. 641-646.

Kassim, M. A., N. A. Sairi, R. Yusoff, Y. Alias, and M. K. Aroua, 2016, Evaluation of 1-butyl-3-methylimidazolium bis(trifluoromethylsulfonyl)imide-alkanolamine sulfolane-based system as solvent for absorption of carbon dioxide: *Industrial & Engineering Chemistry Research*, v. 55, p. 7992-8001.

Kent, R. L., and B. Eisenberg, 1976, Better data for amine treating: *Hydrocarbon Processing*, v. 55, p. 87-90.

Kierzkowska-Pawlak, H., 2015, Kinetics of CO_2 absorption in aqueous *N*,*N*-diethylethanolamine and its blend with *N*-(2-aminoethyl)ethanolamine using a stirred cell reactor: *International Journal of Greenhouse Gas Control*, v. 37, p. 76-84.

Kierzkowska-Pawlak, H., and E. Kruszczak, 2017, Revised kinetics of CO_2 absorption in aqueous *N*,*N*-diethylethanolamine (DEEA) and its blend with *N*-methyl-1,3-propane-diamine (MAPA): *International Journal of Greenhouse Gas Control*, v. 57, p. 134-142.

Kim, I., and H. F. Svendsen, 2007, Heat of absorption of carbon dioxide (CO_2) in monoethanolamine (MEA) and 2-(aminoethyl)ethanolamine (AEEA) solutions: *Industrial & Engineering Chemistry Research*, v. 46, p. 5803-5809.

Kim, S. S., and D. R. Lloyd, 1992, Thermodynamics of polymer diluent systems for thermally induced phase separation: 1. determination of equation of state parameters: *Polymer*, v. 33, p. 1026-1035.

Kim, Y. E., J. H. Park, S. H. Yun, S. C. Nam, S. K. Jeong, and Y. I. Yoon, 2014, Carbon dioxide absorption using a phase transitional alkanolamine-alcohol mixture: *Journal of Industrial and Engineering Chemistry*, v. 20, p. 1486-1492.

Knuutila, H. K., and A. Nannestad, 2017, Effect of the concentration of MAPA on the heat of absorption of CO_2 and on the cyclic capacity in DEEA-MAPA blends: *International Journal of Greenhouse Gas Control*, v. 61, p. 94-103.

Ko, J. J., and M. H. Li, 2000, Kinetics of absorption of carbon dioxide into solutions of *N*-methyldiethanolamine plus water: *Chemical Engineering Science*, v. 55, p. 4139-4147.

Kohl, A.L., and R.B. Nielson, 1997, Gas Purification, 5th edition, Houston, Texas, Gulf Publishing.

Kougoulos, E., A. G. Jones, and M. W. Wood-Kaczmar, 2005, Estimation of crystallization kinetics for an organic fine chemical using a modified continuous cooling mixed suspension mixed product removal (MSMPR) crystallizer: *Journal of Crystal Growth*, v. 273, p. 520-528.

Kozak, F., A. Petig, E. Morris, R. Rhudy, and D. Thimsen, 2009, Chilled ammonia process for CO_2 capture: *9th International Conference on Greenhouse Gas Control Technologies*, GHGT-9, v. 1, p. 1419-1426.

Kubota, N., N. Doki, M. Yokota, and A. Sato, 2001, Seeding policy in batch cooling crystallization: *Powder Technology*, v. 121, p. 31-38.

Laddha, S. S., and P. V. Danckwerts, 1981, Reaction of CO_2 with ethanolamines: kinetics from gas-absorption: *Chemical Engineering Science*, v. 36, p 479-482.

Li, L., 2015. Carbon dioxide solubility and mass transfer in aqueous amines for carbon capture: Ph.D. dissertation, The University of Texas at Austin, Austin, Texas.

Licht, W., 1988, Air pollution control engineering: basic calculations for particulate collection, 2nd edition, New York, Marcel Dekker.

Liebenthal, U., D. D. Pinto, J. Monteiro, H. F. Svendsen, and A. Kather, 2013, Overall process analysis and optimisation for CO_2 capture from coal fired power plants based on phase change solvents forming two liquid phases: *11th International Conference on Greenhouse Gas Control Technologies*, GHGT-11, v. 37, p. 1844-1854.

Lin, Y., 2016. Modeling advanced flash stripper for carbon dioxide capture using aqueous amines: Ph.D. dissertation, The University of Texas at Austin, Austin, Texas.

Littel, R. J., W. P. M. Van Swaaij, and G. F. Versteeg, 1990, Kinetics of carbon dioxide with tertiary amines in aqueous solution: *AIChE Journal*, v. 36, p. 1633-1640.

Lu, Y., N. DeVries, D. Ruhter, M. Sahu, Q. Ye, X. Ye, S. Zhang, S. Chen, Z. Li, K. O'Brien, 2014. Bench-scale development of a hot carbonate absorption process with crystallization-enabled high-pressure stripping for post-combustion CO_2 capture, final report of USDOE/NETL, report No. DE-FE0004360.

Luo, W. L., D. F. Guo, J. H. Zheng, S. W. Gao, and J. Chen, 2016a, CO_2 absorption using biphasic solvent: blends of diethylenetriamine, sulfolane, and water: *International Journal of Greenhouse Gas Control*, v. 53, p. 141-148.

Luo, X., N. Chen, S. Liu, W. Rongwong, R. O. Idem, P. Tontiwachwuthikul, and Z. W. Liang, 2016b, Experiments and modeling of vapor-liquid equilibrium data in DEEA-CO_2-H_2O system: *International Journal of Greenhouse Gas Control*, v. 53, p. 160-168.

Ma'mun, S., J. P. Jakobsen, H. F. Svendsen, and O. Juliussen, 2006, Experimental and modeling study of the solubility of carbon dioxide in aqueous 30 mass % 2-((2-aminoethyl)amino)ethanol solution: *Industrial & Engineering Chemistry Research*, v. 45, p. 2505-2512.

Ma'mun, S., and I. Kim, 2013, Selection and characterization of phase-change solvent for carbon dioxide capture: precipitating system: *11th International Conference on Greenhouse Gas Control Technologies*, GHGT-11, v. 37, p. 331-339.

Ma'mun, S., H. F. Svendsen, K. A. Hoff, and O. Juliussen, 2007, Selection of new absorbents for carbon dioxide capture: *Energy Conversion and Management*, v. 48, p. 251-258.

Machida, H., K. Oba, T. Tomikawa, T. Esaki, T. Yamaguchi, and H. Horizoe, 2017, Development of phase separation solvent for CO_2 capture by aqueous (amine plus ether) solution: *Journal of Chemical Thermodynamics*, v. 113, p. 64-70.

Maheswari, A. U., and K. Palanivelu, 2015, Carbon dioxide capture and utilization by alkanolamines in deep eutectic solvent medium: *Industrial & Engineering Chemistry Research*, v. 54, p. 11383-11392.

Maheswari, A. U., and K. Palanivelu, 2017, Alkyl amine and vegetable oil mixture-a viable candidate for CO_2 capture and utilization: *Environmental Science and Pollution Research*, v. 24, p. 5733-5745.

Malmberg, C. G., and A. A. Maryott, 1956, Dielectric constant of water from 0-degrees-C to 100-degrees-C: *Journal of Research of the National Bureau of Standards*, v. 56, p. 1-8.

Mathias, P. M., S. Reddy, and J. P. O'Connell, 2010, Quantitative evaluation of the chilled-ammonia process for CO_2 capture using thermodynamic analysis and process simulation: *International Journal of Greenhouse Gas Control*, v. 4, p. 174-179.

McClements, D. J., 2012, Crystals and crystallization in oil-in-water emulsions: implications for emulsion-based delivery systems: *Advances in Colloid and Interface Science*, v. 174, p. 1-30.
Meldon, J. H., 2011, Amine screening for flue gas CO_2 capture at coal-fired power plants: should the heat of desorption be high, low or in between?: *Current Opinion in Chemical Engineering*, v. 1, p. 55-63.
Monredon, T. C., K. T. Hsieh, and R. K. Rajamani, 1992, Fluid-flow model of the hydrocyclone: an investigation of device dimensions: *International Journal of Mineral Processing*, v. 35, p. 65-83.
Monteiro, J., S. Hussain, H. Majeed, E. O. Mba, A. Hartono, H. Knuutila, and H. F. Svendsen, 2014, Kinetics of CO_2 absorption by aqueous 3-(methylamino)propylamine solutions: experimental results and modeling: *AIChE Journal*, v. 60, p. 3792-3803.
Monteiro, J., H. Knuutila, N. Penders-van Elk, G. Versteeg, and H. F. Svendsen, 2015a, Kinetics of CO_2 absorption by aqueous *N*,*N*-diethylethanolamine solutions: literature review, experimental results and modeling: *Chemical Engineering Science*, v. 127, p. 1-12.
Monteiro, J., H. Majeed, H. Knuutila, and H. F. Svendsen, 2015b, Kinetics of CO_2 absorption in aqueous blends of *N*,*N*-diethylethanolamine (DEEA) and *N*-methyl-1,3-propane-diamine (MAPA): *Chemical Engineering Science*, v. 129, p. 145-155.
Monteiro, J., D. D. D. Pinto, S. A. H. Zaidy, A. Hartono, and H. F. Svendsen, 2013, VLE data and modelling of aqueous *N*,*N*-diethylethanolamine (DEEA) solutions: *International Journal of Greenhouse Gas Control*, v. 19, p. 432-440.
Mortaheb, H. R., A. A. Nozaeim, M. Mafi, and B. Mokhtarani, 2012, Absorption of carbon dioxide in emulsions of aqueous monoethanolamine/diethanolamine solutions in kerosene/n-heptane: *Chemical Engineering Science*, v. 82, p. 44-51.
Muchan, P., J. Narku-Tetteh, C. Saiwan, R. Idem, and T. Supap, 2017, Effect of number of amine groups in aqueous polyamine solution on carbon dioxide (CO_2) capture activities: *Separation and Purification Technology*, v. 184, p. 128-134.
Mullin, J.W., 2001. Crystallization, 4th edition, Oxford, Butterworth Heinemann, p. 447.
Mumford, K. A., K. H. Smith, C. J. Anderson, S. F. Shen, W. D. Tao, Y. A. Suryaputradinata, A. Qader, B. Hooper, R. A. Innocenzi, S. E. Kentish, and G. W. Stevens, 2012, Post-combustion capture of CO_2: results from the solvent absorption capture plant at Hazelwood Power Station using potassium carbonate solvent: *Energy & Fuels*, v. 26, p. 138-146.
Mydlarz, J., and A. G. Jones, 1993, On the estimation of size-dependent crystal-growth rate-functions in MSMPR crystallizers: *Chemical Engineering Journal and the Biochemical Engineering Journal*, v. 53, p. 125-135.
Myerson A.S., 2002, Handbook of Industrial Crystallization, 2nd edition, Amsterdam, Elsevier.
NASA/GISS, 2017, https://climate.nasa.gov/vital-signs/global-temperature/
NOAA/ESRL, 2017, Annual greenhouse gas index, https://www.esrl.noaa.gov/gmd/aggi/
Nysing, R., and H. Kramers, 1958, Absorption of CO_2 in carbonate bicarbonate buffer solutions in a wetted wall column: *Chemical Engineering Science*, v. 8, p. 81-89.
Ooshima, H., K. Igarashi, H. Iwasa, and R. Yamamoto, 2013, Structure of supersaturated solution and crystal nucleation induced by diffusion: *Journal of Crystal Growth*, v. 373, p. 2-6.
Ottens, E. P. K., and E. J. D. Jong, 1973, Model for secondary nucleation in a stirred vessel cooling crystallizer: *Industrial & Engineering Chemistry Fundamentals*, v. 12, p. 179-184.
Oyenekan, B. A., and G. T. Rochelle, 2006, Energy performance of stripper configurations for CO_2 capture by aqueous amines: *Industrial & Engineering Chemistry Research*, v. 45, p. 2457-2464.
Oyenekan, B. A., and G. T. Rochelle, 2009, Rate modeling of CO_2 stripping from potassium carbonate promoted by piperazine: *International Journal of Greenhouse Gas Control*, v. 3, p. 121-132.
Paoletti, P., R. Barbucci, and A. Vacca, 1972, Evaluation of substituent effects on the enthalpies of protonation of amines: an empirical formula of prediction: *Journal of the Chemical Society, Dalton Transactions*, v. 0, p. 2010-2013.
Perry, R. J., B. R. Wood, S. Genovese, M. J. O'Brien, T. Westendorf, M. L. Meketa, R. Farnum, J. McDermott, I. Sultanova, T. M. Perry, R. K. Vipperla, L. A. Wichmann, R. M. Enick, L. Hong, and D. Tapriyal, 2012, CO_2 capture using phase-changing sorbents: *Energy & Fuels*, v. 26, p. 2528-2538.
Pinto, D. D. D., H. Knuutila, G. Fytianos, G. Haugen, T. Mejdell, and H. F. Svendsen, 2014a, CO_2 post-combustion capture with a phase change solvent: pilot plant campaign: *International Journal of Greenhouse Gas Control*, v. 31, p. 153-164.
Pinto, D. D. D., S. A. H. Zaidy, A. Hartono, and H. F. Svendsen, 2014b, Evaluation of a phase change solvent for CO_2 capture: absorption and desorption tests: *International Journal of Greenhouse Gas Control*, v. 28, p. 318-327.

Plaza, J. M., E. Chen, and G. T. Rochelle, 2010, Absorber intercooling in CO_2 absorption by piperazine-promoted potassium carbonate: *AIChE Journal*, v. 56, p. 905-914.
Pohorecki, R., and W. Moniuk, 1988, Kinetics of reaction between carbon-dioxide and hydroxyl ions in aqueous electrolyte solutions: *Chemical Engineering Science*, v. 43, p. 1677-1684.
Qin, F., S. J. Wang, I. Kim, H. F. Svendsen, and C. H. Chen, 2011, Heat of absorption of CO_2 in aqueous ammonia and ammonium carbonate/carbamate solutions: *International Journal of Greenhouse Gas Control*, v. 5, p. 405-412.
Rackett, H. G., 1970, Equation of state for saturated liquids: *Journal of Chemical and Engineering Data*, v. 15, p. 514-517.
Raksajati, A., M. T. Ho, and D. E. Wiley, 2014, Reducing the cost of CO_2 capture from flue gases using phasechange solvent absorption: *12th International Conference on Greenhouse Gas Control Technologies, GHGT-12*, v. 63, p. 2280-2288.
Raksajati, A., M. T. Ho, and D. E. Wiley, 2016, Understanding the impact of process design on the cost of CO_2 capture for precipitating solvent absorption: *Industrial & Engineering Chemistry Research*, v. 55, p. 1980-1994.
Randolph, A. D., and E. T. White, 1977, Modeling size dispersion in prediction of crystal-size distribution: *Chemical Engineering Science*, v. 32, p. 1067-1076.
Rangwala, H. A., B. R. Morrell, A. E. Mather, and F. D. Otto, 1992, Absorption of CO_2 into aqueous tertiary amine mea solutions: *Canadian Journal of Chemical Engineering*, v. 70, p. 482-490.
Raynal, L., P. Alix, P. A. Bouillon, A. Gomez, M. L. de Nailly, M. Jacquin, J. Kittel, A. di Lella, P. Mougin, and J. Trapy, 2011a, The DMX™ process : an original solution for lowering the cost of post-combustion carbon capture: *10th International Conference on Greenhouse Gas Control Technologies*, GHGT-10, v. 4, p. 779-786.
Raynal, L., P. A. Bouillon, A. Gomez, and P. Broutin, 2011b, From MEA to demixing solvents and future steps, a roadmap for lowering the cost of post-combustion carbon capture: *Chemical Engineering Journal*, v. 171, p. 742-752.
Raynal, L., P. Briot, M. Dreillard, P. Broutin, A. Mangiaracina, B. S. Drioli, M. Politi, C. La Marca, J. Mertens, M. L. Thielens, G. Laborie, and L. Normand, 2014, Evaluation of the DMX process for industrial pilot demonstration: methodology and results: *12th International Conference on Greenhouse Gas Control Technologies*, GHGT-12, v. 63, p. 6298-6309.
Rochelle, G. T., 2009, Amine scrubbing for CO_2 capture: *Science*, v. 325, p. 1652-1654.
Rochelle, G., E. Chen, S. Freeman, D. Van Wagener, Q. Xu, and A. Voice, 2011, Aqueous piperazine as the new standard for CO_2 capture technology: *Chemical Engineering Journal*, v. 171, p. 725-733.
Sanchez-Fernandez, E., K. Heffernan, L. van der Ham, M. J. G. Linders, D. W. F. Brilman, E. L. V. Goetheer, and T. J. H. Vlugt, 2014a, Analysis of process configurations for CO_2 capture by precipitating amino acid solvents: *Industrial & Engineering Chemistry Research*, v. 53, p. 2348-2361.
Sanchez-Fernandez, E., K. Heffernan, L. van der Ham, M. J. G. Linders, E. L. V. Goetheer, and C. J. H. Vlugt, 2014b, Precipitating amino acid solvents for CO_2 capture: opportunities to reduce costs in post combustion capture: *12th International Conference on Greenhouse Gas Control Technologies*, GHGT-12, v. 63, p. 727-738.
Sanchez-Fernandez, E., F. D. Mercader, K. Misiak, L. van der Ham, M. Linders, and E. Goetheer, 2013, New process concepts for CO_2 capture based on precipitating amino acids: *11th International Conference on Greenhouse Gas Control Technologies*, GHGT-11, v. 37, p. 1160-1171.
Schotte, W., 1992, Prediction of the molar volume at the normal boiling-point: *Chemical Engineering Journal and the Biochemical Engineering Journal*, v. 48, p. 167-172.
Sha, Z. L., H. Hatakka, M. LouhiKultanen, and S. Palosaari, 1996, Crystallization kinetics of potassium sulfate in an MSMPR stirred crystallizer: *Journal of Crystal Growth*, v. 166, p. 1105-1110.
Shen, K. P., and M. H. Li, 1992, Solubility of carbon-dioxide in aqueous mixtures of monoethanolamine with methyldiethanolamine: *Journal of Chemical and Engineering Data*, v. 37, p. 96-100.
Shen, S. F., Y. Y. Bian, and Y. Zhao, 2017, Energy-efficient CO_2 capture using potassium prolinate/ethanol solution as a phase-changing absorbent: *International Journal of Greenhouse Gas Control*, v. 56, p. 1-11.
Singh, P., J. P. M. Niederer, and G. F. Versteeg, 2007, Structure and activity relationships for amine based CO_2 absorbents-I: *International Journal of Greenhouse Gas Control*, v. 1, p. 5-10.
Singh, P., J. P. M. Niederer, and G. F. Versteeg, 2009, Structure and activity relationships for amine-based CO_2 absorbents-II: *Chemical Engineering Research & Design*, v. 87, p. 135-144.

Singh, P., W. P. M. Van Swaaij, and D. W. F. Brilman, 2011, Kinetics study of carbon dioxide absorption in aqueous solutions of 1,6-hexamethyldiamine (HMDA) and 1,6-hexamethyldiamine, *N,N'*-dimethyl (HMDA, *N,N'*): *Chemical Engineering Science*, v. 66, p. 4521-4532.

Smith, K. H., C. J. Anderson, W. Tao, K. Endo, K. A. Mumford, S. E. Kentish, A. Qader, B. Hooper, and G. W. Stevens, 2012, Pre-combustion capture of CO_2: results from solvent absorption pilot plant trials using 30 wt% potassium carbonate and boric acid promoted potassium carbonate solvent: *International Journal of Greenhouse Gas Control*, v. 10, p. 64-73.

Snijder, E. D., M. J. M. Teriele, G. F. Versteeg, and W. P. M. Van Swaaij, 1993, Diffusion-coefficients of several aqueous alkanolamine solutions: *Journal of Chemical and Engineering Data*, v. 38, p. 475-480.

Steeneveldt, R., B. Berger, and T. A. Torp, 2006, CO_2 capture and storage: closing the knowing-doing gap: *Chemical Engineering Research & Design*, v. 84, p. 739-763.

Stein, S. E., and R. L. Brown, 1994, Estimation of normal boiling points from group contributions: *Journal of Chemical Information and Computer Sciences*, v. 34, p. 581-587.

Stern, N., 2007. The Economics of Climate Change: The Stern Review. Cambridge, United Kingdom, Cambridge University Press.

Sutter, D., M. Gazzani, and M. Mazzotti, 2016, A low-energy chilled ammonia process exploiting controlled solid formation for post-combustion CO_2 capture: *Faraday Discussions*, v. 192, p. 59-83.

Svendsen, H. F., E. T. Hessen, and T. Mejdell, 2011, Carbon dioxide capture by absorption, challenges and possibilities: *Chemical Engineering Journal*, v. 171, p. 718-724.

Svensson, H., J. Edfeldt, V. Z. Velasco, C. Hulteberg, and H. T. Karlsson, 2014a, Solubility of carbon dioxide in mixtures of 2-amino-2-methyl-1-propanol and organic solvents: *International Journal of Greenhouse Gas Control*, v. 27, p. 247-254.

Svensson, H., C. Hulteberg, and H. T. Karlsson, 2014b, Precipitation of AMP carbamate in CO_2 absorption process: *12th International Conference on Greenhouse Gas Control Technologies*, GHGT-12, v. 63, p. 750-757.

Svensson, H., V. Z. Velasco, C. Hulteberg, and H. T. Karlsson, 2014c, Heat of absorption of carbon dioxide in mixtures of 2-amino-2-methyl-1-propanol and organic solvents: *International Journal of Greenhouse Gas Control*, v. 30, p. 1-8.

Tanrikulu, S. U., I. Eroglu, A. N. Bulutcu, and S. Ozkar, 2000, Crystallization kinetics of ammonium perchlorate in MSMPR crystallizer: *Journal of Crystal Growth*, v. 208, p. 533-540.

Tanthapanichakoon, W., A. Veawab, and B. McGarvey, 2006, Electrochemical investigation on the effect of heat-stable salts on corrosion in CO_2 capture plants using aqueous solution of MEA: *Industrial & Engineering Chemistry Research*, v. 45, p. 2586-2593.

Tosh, J.S., J.H. Field, H.E. Benson, W.P. Haynes, 1959, Equilibrium study of the system potassium carbonate, potassium bicarbonate, carbon dioxide, and water, report No. BM-RI-5484.

USDOE/NETL, 2013, Cost and performance baseline for fossil energy plants, volume 1: bituminous coal and natural gas to electricity, report No. 2010/1397, Revision 2a.

USDOE/NETL, Office of Fossil Energy, 2015. Cost and performance baseline for fossil energy plants, volume 1a: bituminous coal and natural gas to electricity, revision 3.

USDOE/NETL, Office of Fossil Energy, Clean Coal Research Program, 2012. Technology readiness assessment: analysis of active research portfolio.

Vaidya, P. D., and E. Y. Kenig, 2009, A study on CO_2 absorption kinetics by aqueous solutions of *N,N*-diethylethanolamine and *N*-ethylethanolamine: *Chemical Engineering & Technology*, v. 32, p. 556-563.

Vaidya, P. D., and E. Y. Kenig, 2010, Termolecular kinetic model for CO_2-alkanolamine reactions: an overview: *Chemical Engineering & Technology*, v. 33, p. 1577-1581.

Van Swaaij, W. P. M., and G. F. Versteeg, 1992, Mass transfer accompanied with complex reversible chemical-reactions in gas-liquid systems: an overview: *Chemical Engineering Science*, v. 47, p. 3181-3195.

Versteeg, G. F., L. A. J. Van Dijck, and W. P. M. Van Swaaij, 1996, On the kinetics between CO_2 and alkanolamines both in aqueous and non-aqueous solutions: an overview: *Chemical Engineering Communications*, v. 144, p. 113-158.

Versteeg, G. F., and W. P. M. Van Swaaij, 1988a, On the kinetics between CO_2 and alkanolamines both in aqueous and non-aqueous solutions: 2. tertiary-amines: *Chemical Engineering Science*, v. 43, p. 587-591.

Versteeg, G. F., and W. P. M. Van Swaaij, 1988b, Solubility and diffusivity of acid gases (CO_2, N_2O) in aqueous alkanolamine solutions: *Journal of Chemical and Engineering Data*, v. 33, p. 29-34.

Versteeg, P., and E. S. Rubin, 2011, A technical and economic assessment of ammonia-based post-combustion CO_2 capture at coal-fired power plants: *International Journal of Greenhouse Gas Control*, v. 5, p. 1596-1605.

Wang, L. D., S. L. An, Q. W. Li, S. H. Yu, and S. Y. Wu, 2017, Phase change behavior and kinetics of CO_2 absorption into DMBA/DEEA solution in a wetted-wall column: *Chemical Engineering Journal*, v. 314, p. 681-687.

Wang, X. F., N. G. Akhmedov, Y. H. Duan, and B. Y. Li, 2015, Nuclear magnetic resonance studies of CO_2 absorption and desorption in aqueous sodium salt of alanine: *Energy & Fuels*, v. 29, p. 3780-3784.

Wang, X. F., N. G. Akhmedov, D. Hopkinson, J. Hoffman, Y. H. Duan, A. Egbebi, K. Resnik, and B. Y. Li, 2016, Phase change amino acid salt separates into CO_2-rich and CO_2-lean phases upon interacting with CO_2: *Applied Energy*, v. 161, p. 41-47.

Wang, Y. W., S. Xu, F. D. Otto, and A. E. Mather, 1992, Solubility of N_2O in alkanolamines and in mixed-solvents: *Chemical Engineering Journal and the Biochemical Engineering Journal*, v. 48, p. 31-40.

Weiland, R. H., T. Chakravarty, and A. E. Mather, 1993, Solubility of carbon-dioxide and hydrogen-sulfide in aqueous alkanolamines: *Industrial & Engineering Chemistry Research*, v. 32, p. 1419-1430.

Weiland, R. H., J. C. Dingman, and D. B. Cronin, 1997, Heat capacity of aqueous monoethanolamine, diethanolamine, *N*-methyldiethanolamine, and *N*-methyldiethanolamine-based blends with carbon dioxide: *Journal of Chemical and Engineering Data*, v. 42, p. 1004-1006.

Wey, J. S., and J. P. Terwilliger, 1980, Effect of temperature on suspension crystallization processes: *Chemical Engineering Communications*, v. 4, p. 297-305.

Wilke, C. R., and P. Chang, 1955, Correlation of diffusion coefficients in dilute solutions: *AIChE Journal*, v. 1, p. 264-270.

Williamson, R. V., and J. H. Mathews, 1924, Rate of absorption and equilibrium of carbon dioxide in alkaline solutions: *Industrial and Engineering Chemistry*, v. 16, p. 1157-1161.

Wong, D. S. H., and S. I. Sandler, 1984, Calculation of vapor liquid liquid equilibrium with cubic equations of state and a corresponding states principle: *Industrial & Engineering Chemistry Fundamentals*, v. 23, p. 348-354.

Xu, Z. C., S. J. Wang, and C. H. Chen, 2013a, CO_2 absorption by biphasic solvents: mixtures of 1,4-butanediamine and 2-(diethylamino)ethanol: *International Journal of Greenhouse Gas Control*, v. 16, p. 107-115.

Xu, Z. C., S. J. Wang, and C. H. Chen, 2013b, Kinetics study on CO_2 absorption with aqueous solutions of 1,4-butanediamine, 2-(diethylamino)ethanol, and their mixtures: *Industrial & Engineering Chemistry Research*, v. 52, p. 9790-9802.

Xu, Z. C., S. J. Wang, J. Z. Liu, and C. H. Chen, 2012, Solvents with low critical solution temperature for CO_2 capture: *6th Trondheim Conference on CO_2 Capture, Transport and Storage*, v. 23, p. 64-71.

Xu, Z. C., S. J. Wang, G. J. Qi, J. Z. Liu, B. Zhao, and C. H. Chen, 2014a, CO_2 absorption by biphasic solvents: comparison with lower phase alone: *Oil & Gas Science and Technology-Rev. IFP Energies Nouvelles*, v. 69, p. 851-864.

Xu, Z. C., S. J. Wang, G. J. Qi, A. A. Trollebo, H. F. Svendsen, and C. H. Chen, 2014b, Vapor liquid equilibria and heat of absorption of CO_2 in aqueous 2-(diethylamino)ethanol solutions: *International Journal of Greenhouse Gas Control*, v. 29, p. 92-103.

Yang, H. Q., Z. H. Xu, M. H. Fan, R. Gupta, R. B. Slimane, A. E. Bland, and I. Wright, 2008, Progress in carbon dioxide separation and capture: a review: *Journal of Environmental Sciences*, v. 20, p. 14-27.

Yang, N., D. Y. Xu, C. C. Wei, G. Puxty, H. Yu, M. Maeder, S. Norman, and P. Feron, 2014, Protonation constants and thermodynamic properties of amino acid salts for CO_2 capture at high temperatures: *Industrial & Engineering Chemistry Research*, v. 53, p. 12848-12855.

Ye, Q., X. L. Wang, and Y. Q. Lu, 2015a, Kinetic behavior of potassium bicarbonate crystallization in a carbonate-based CO_2 absorption process: *Chemical Engineering Research & Design*, v. 93, p. 136-147.

Ye, Q., X. L. Wang, and Y. Q. Lu, 2015b, Screening and evaluation of novel biphasic solvents for energy-efficient post-combustion CO_2 capture: *International Journal of Greenhouse Gas Control*, v. 39, p. 205-214.

Ye, Q., L. Y. Zhu, X. L. Wang, and Y. Q. Lu, 2017a, On the mechanisms of CO_2 absorption and desorption with phase transitional solvents: *International Journal of Greenhouse Gas Control*, v. 56, p. 278-288.

Ye, Q., H. Lu, Y. Du, S. H. Zhang, X. L. Wang, and Y. Q. Lu, 2017b. Experimental investigation of the absorption, phase transition, and desorption behavior of biphasic solvent blends for postcombustion CO_2 capture: *Energy Procedia*, v. 114, p. 813-822.

Zauner, R., and A. G. Jones, 2000, Determination of nucleation, growth, agglomeration and disruption kinetics from experimental precipitation data: the calcium oxalate system: *Chemical Engineering Science*, v. 55, p. 4219-4232.

Zerres, H., and J. M. Prausnitz, 1994, Thermodynamics of phase-equilibria in aqueous-organic systems with salt: *AIChE Journal*, v. 40, p. 676-691.

Zhang, F., K. X. Gao, Y. N. Meng, M. Qi, J. Geng, Y. T. Wu, and Z. B. Zhang, 2016a, Intensification of dimethyaminoethoxyethanol on CO_2 absorption in ionic liquid of amino acid: *International Journal of Greenhouse Gas Control*, v. 51, p. 415-422.

Zhang, J. F., D. W. Agar, X. H. Zhang, and F. Geuzebroek, 2011a, CO_2 absorption in biphasic solvents with enhanced low temperature solvent regeneration: *10th International Conference on Greenhouse Gas Control Technologies*, GHGT-10, v. 4, p. 67-74.

Zhang, J. F., J. Chen, R. Misch, and D. W. Agar, 2010, Carbon dioxide absorption in biphasic amine solvents with enhanced low temperature solvent regeneration: *13th International Conference on Process Integration, Modelling and Optimisation for Energy Saving and Pollution Reduction*, v. 21, p. 169-174.

Zhang, J. F., R. Misch, Y. D. Tan, and D. W. Agar, 2011b, Novel thermomorphic biphasic amine solvents for CO_2 absorption and low-temperature extractive regeneration: *Chemical Engineering & Technology*, v. 34, p. 1481-1489.

Zhang, J. F., O. Nwani, Y. Tan, and D. W. Agar, 2011c, Carbon dioxide absorption into biphasic amine solvent with solvent loss reduction: *Chemical Engineering Research & Design*, v. 89, p. 1190-1196.

Zhang, J. F., Y. Qiao, and D. W. Agar, 2012a, Improvement of lipophilic-amine-based thermomorphic biphasic solvent for energy-efficient carbon capture: *6th Trondheim Conference on CO_2 Capture, Transport and Storage*, v. 23, p. 92-101.

Zhang, J. F., Y. Qiao, and D. W. Agar, 2012b, Intensification of low temperature thermomorphic biphasic amine solvent regeneration for CO_2 capture: *Chemical Engineering Research & Design*, v. 90, p. 743-749.

Zhang, J. F., Y. Qiao, W. Z. Wang, R. Misch, K. Hussain, and D. W. Agar, 2013, Development of an energy-efficient CO_2 capture process using thermomorphic biphasic solvents: *11th International Conference on Greenhouse Gas Control Technologies*, GHGT-11, v. 37, p. 1254-1261.

Zhang, R., X. Luo, Q. Yang, F. Cao, S. P. X. Chen, and Z. W. Liang, 2016b, Impact of the inter- and intramolecular tertiary amino group on the primary amino group in the CO_2 absorption process: *Industrial & Engineering Chemistry Research*, v. 55, p. 7210-7217.

Zhang, S. H., X. H. Ye, and Y. Q. Lu, 2014, Development of a potassium carbonate-based absorption process with crystallization-enabled high-pressure stripping for CO_2 capture: vapor-liquid equilibrium behavior and CO_2 stripping performance of carbonate/bicarbonate aqueous systems: *12th International Conference on Greenhouse Gas Control Technologies*, GHGT-12, v. 63, p. 665-675.

Zhang, S. H., Z. H. Zhang, Y. Q. Lu, M. Rostam-Abadi, and A. Jones, 2011d, Activity and stability of immobilized carbonic anhydrase for promoting CO_2 absorption into a carbonate solution for post-combustion CO_2 capture: *Bioresource Technology*, v. 102, p. 10194-10201.

Zhang, W. D., X. H. Jin, W. W. Tu, Q. Ma, M. L. Mao, and C. H. Cui, 2017a, A novel CO_2 phase change absorbent: MEA/1-Propanol/H_2O: *Energy & Fuels*, v. 31, p. 4273-4279.

Zhang, W. D., X. H. Jin, W. W. Tu, Q. Ma, M. L. Mao, and C. H. Cui, 2017b, Development of MEA-based CO_2 phase change absorbent: *Applied Energy*, v. 195, p. 316-323.

Zhang, Z., W. B. Zhao, J. J. Nong, D. Feng, Y. H. Li, Y. Chen, and J. Chen, 2017c, Liquid-solid phase-change behavior of diethylenetriamine in nonaqueous systems for carbon dioxide absorption: *Energy Technology*, v. 5, p. 461-468.

Zhao, M., A. I. Minett, and A. T. Harris, 2013, A review of techno-economic models for the retrofitting of conventional pulverised-coal power plants for post-combustion capture (PCC) of CO_2: *Energy & Environmental Science*, v. 6, p. 25-40.

Zheng, S. D., M. N. Tao, Q. Liu, L. Q. Ning, Y. He, and Y. Shi, 2014, Capturing CO_2 into the precipitate of a phase-changing solvent after absorption: *Environmental Science & Technology*, v. 48, p. 8905-8910.

APPENDIX A: PYTHON (V2.7) CODES USED FOR THE SDG MODEL

```
import pylab
import collections
import numpy
from scipy import optimize
Hold=True
def f(p,x):
     b,a,c,g=p
     y=b+a*x-(1+1/a/937/g)*numpy.log((numpy.e**(a*x)-numpy.e**(-
a*c))/(1-numpy.e**(-a*c)))
     return y
def resid(p,x,y):
     return y-f(p,x)
x,y=numpy.loadtxt("/home/qing/Downloads/Python-2.7.5/0.05PZ.txt",
unpack=True)
param=collections.namedtuple('param','b a c g')
p_guess=param(b=45,a=15000,c=1e-09,g=1e-07)
p_guess=param(b=45,a=15000,c=1e-09,g=1e-07)
p=param(*p)
xp=numpy.linspace(x[0],x[-1],5000)
print('''\
     b={p.b}
     a={p.a}
     c={p.c}
     g={p.g}
     '''.format(p=p))
b=41.4924010632
a=7440.85247449
c=2.16068821886e-06
g=1.07463427212e-07
pxp=f(p,xp)
resid=resid(p,x,y)
print(resid)
[-0.31431693 -0.01725805  0.12407994  0.48565472  0.36771168
0.24069392
  0.08760339 -0.08818884 -0.26357549 -0.4084526  -0.49461894 -
0.49580429
 -0.3984671  -0.25185695 -0.08235752  0.08017183  0.23237822
0.34464578
  0.37027719  0.33648379  0.33612455  0.33732689  0.31350244
0.25303667
  0.17955708  0.03830054 -0.08149239 -0.18219893 -0.2423669  -
0.28640035
 -0.29120014 -0.27176236 -0.2222007  -0.09898028  0.0386926
0.22239639
  0.24130801]
```

```
print(infodict['fvec'])
[-0.31431693 -0.01725805  0.12407994  0.48565472  0.36771168
0.24069392
  0.08760339 -0.08818884 -0.26357549 -0.4084526  -0.49461894 -
0.49580429
 -0.3984671  -0.25185695 -0.08235752  0.08017183  0.23237822
0.34464578
  0.37027719  0.33648379  0.33612455  0.33732689  0.31350244
0.25303667
  0.17955708  0.03830054 -0.08149239 -0.18219893 -0.2423669  -
0.28640035
 -0.29120014 -0.27176236 -0.2222007  -0.09898028  0.0386926
0.22239639
  0.24130801]
ss_err=(infodict['fvec']**2).sum()
ss_tot=((y-y.mean())**2).sum()
rsquared=1-(ss_err/ss_tot)
print(rsquared)
0.996374469788
pylab.plot(x*1e06,y,'.',color="red",label="experimental data")
[<matplotlib.lines.Line2D object at 0x2806350>]
pylab.plot(xp*1e06,pxp,'-
',color="blue",linewidth=0.5,label="size-dependent growth model")
[<matplotlib.lines.Line2D object at 0x2806990>]
pylab.legend(loc='upper right')
<matplotlib.legend.Legend object at 0x2806590>
pylab.xlabel('crystal size (micron)')
<matplotlib.text.Text object at 0x24fbf90>
pylab.ylabel('log-population density',rotation='vertical')
<matplotlib.text.Text object at 0x25046d0>
pylab.grid(True)
pylab.show()
```

APPENDIX B: SUPPLEMENTARY MATERIAL OF NMR SPECTROSCOPIC STUDIES

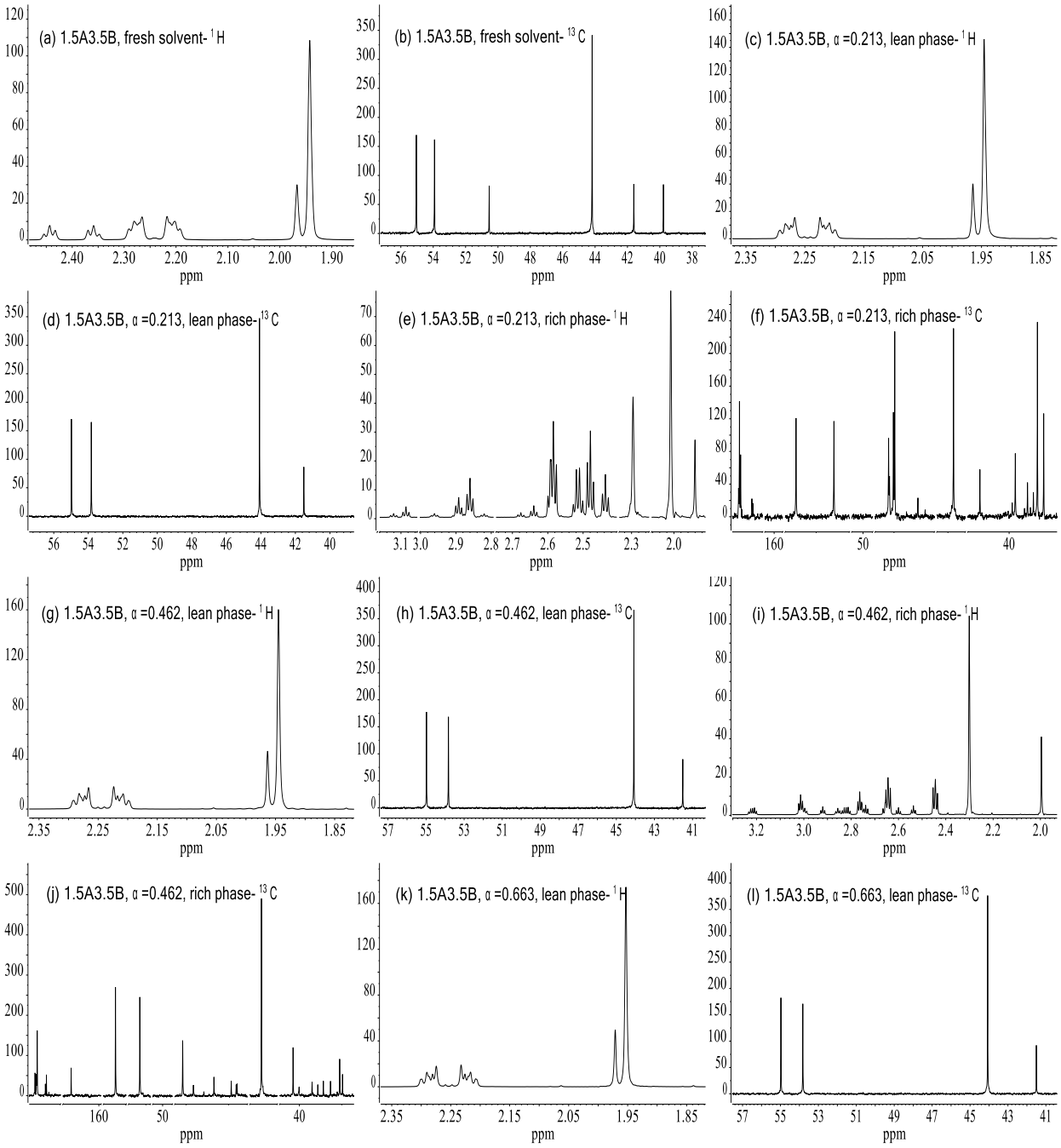

Fig. B-1 (cont.)

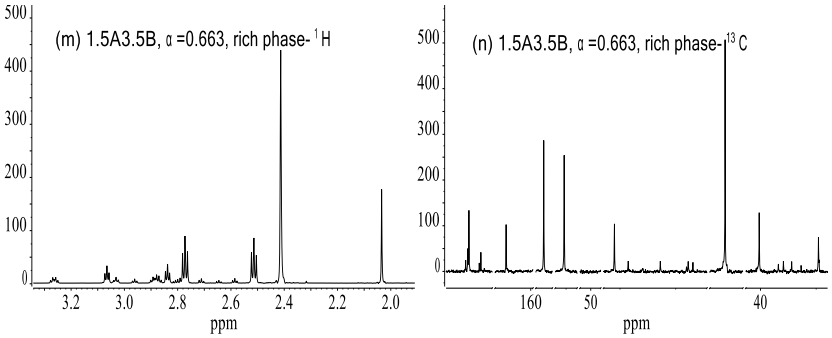

Fig. B-1. NMR spectra of samples from 1.5A3.5B. (a) ^{1}H and (b) ^{13}C spectra of fresh samples; (c) ^{1}H and (d) ^{13}C spectra of lean samples and (e) ^{1}H and (f) ^{13}C spectra of rich samples at a total CO_2 loading of 0.213 mol mol^{-1}; (g) ^{1}H and (h) ^{13}C spectra of lean samples and (i) ^{1}H and (j) ^{13}C spectra of rich samples at a total CO_2 loading of 0.462 mol mol^{-1}; (k) ^{1}H and (l) ^{13}C spectra of lean samples and (m) ^{1}H and (n) ^{13}C spectra of rich samples at a total CO_2 loading of 0.663 mol mol^{-1}. α stands for the total CO_2 loading in the unit of mol mol^{-1}.

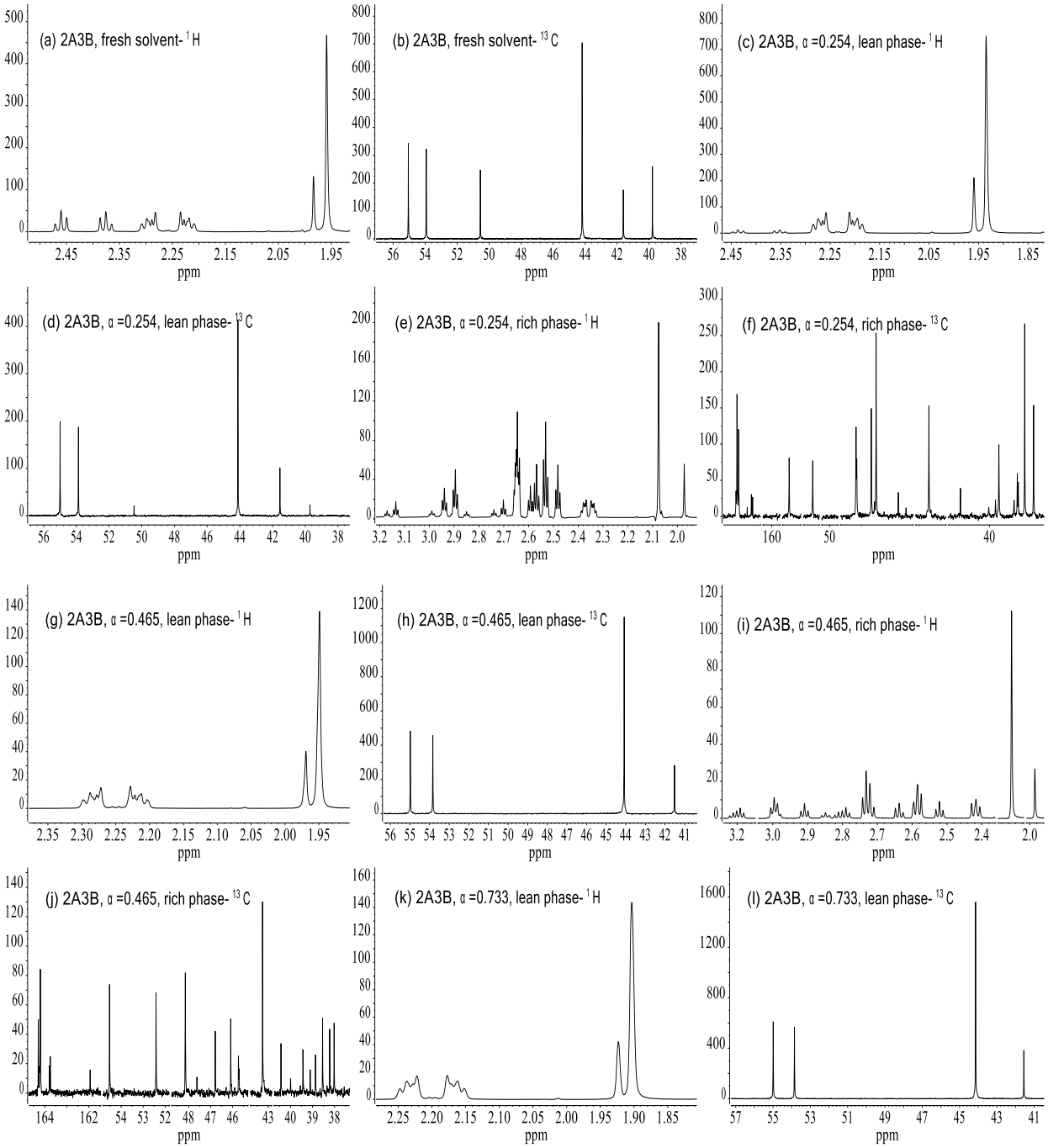
(a) 2A3B, fresh solvent- 1 H
(b) 2A3B, fresh solvent- 13 C
(c) 2A3B, α =0.254, lean phase- 1 H
(d) 2A3B, α =0.254, lean phase- 13 C
(e) 2A3B, α =0.254, rich phase- 1 H
(f) 2A3B, α =0.254, rich phase- 13 C
(g) 2A3B, α =0.465, lean phase- 1 H
(h) 2A3B, α =0.465, lean phase- 13 C
(i) 2A3B, α =0.465, rich phase- 1 H
(j) 2A3B, α =0.465, rich phase- 13 C
(k) 2A3B, α =0.733, lean phase- 1 H
(l) 2A3B, α =0.733, lean phase- 13 C
ppm

Fig. B-2 (cont.)

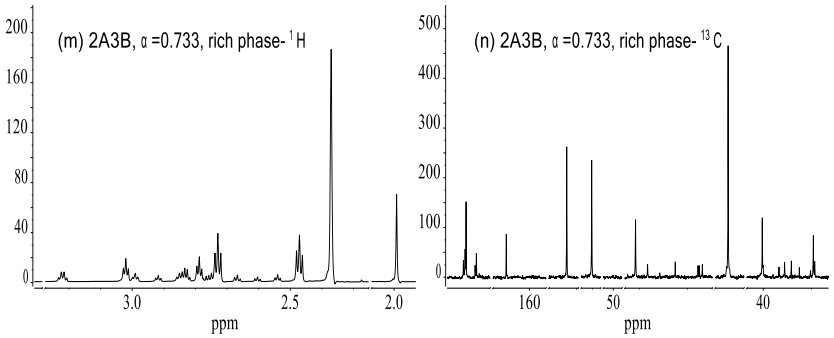

Fig. B-2. NMR spectra of samples from 2A3B. (a) ^{1}H and (b) ^{13}C spectra of fresh samples; (c) ^{1}H and (d) ^{13}C spectra of lean samples and (e) ^{1}H and (f) ^{13}C spectra of rich samples at a total CO_2 loading of 0.254 mol mol^{-1}; (g) ^{1}H and (h) ^{13}C spectra of lean samples and (i) ^{1}H and (j) ^{13}C spectra of rich samples at a total CO_2 loading of 0.465 mol mol^{-1}; (k) ^{1}H and (l) ^{13}C spectra of lean samples and (m) ^{1}H and (n) ^{13}C spectra of rich samples at a total CO_2 loading of 0.733 mol mol^{-1}. α stands for the total CO_2 loading in the unit of mol mol^{-1}.

Table B-1. (H, C) Chemical shifts (ppm) of the characteristic sites for each structural group during CO_2 absorption (N/A: not applicable; N/D: not detected).

Solvent formula	CO_2 ldg (mol mol^{-1})	Phase	Group A-I		Group A-II					Group A-III			Group A-IV			Group A-V						Group B				HCO_3^- /CO_3^{2-}
			2	1	1	2	3	4	5	2	1	6	2	1	5	1	2	3	4	6	5	4	2	1	3	
1.5A3.5B	0	N/A	2.36, 50.54	2.44, 39.78			N/D				N/D			N/D				N/D				1.97, 41.61	2.21, 53.92	2.28, 55.04	1.94, 44.18	N/D
	0.213	Lean	N/D				N/D				N/D			N/D				N/D				1.96, 41.51	2.21, 53.82	2.28, 54.97	1.95, 44.08	N/D
		Rich	2.49, 48.02	2.59, 38.87	2.52, 38.62	2.60, 47.96	2.45, 48.22	2.87, 39.75	164.27	3.10, 47.04	2.65, 39.03	163.78	2.53, 48.18	2.90, 39.27	164.23	2.69, 39.15	3.13, 46.76	2.97, 47.5	2.83, 39.87	163.74	164.17	1.95, 41.2	2.30, 53.29	2.31, 54.79	2.02, 43.77	
	0.462	Lean	N/D				N/D				N/D			N/D				N/D				1.96, 41.51	2.21, 53.82	2.28, 54.98	1.94, 44.08	N/D
		Rich	2.60, 45.87	2.75, 38.53	2.74, 37.96	2.66, 46.69	2.54, 48.16	2.92, 39.4	164.29	3.21, 45.60	2.81, 38.87	163.80	2.76, 48.16	3.01, 38.1	164.19	2.83, 39.13	3.23, 45.64	3.00, 47.66	2.86, 40.02	163.75	164.22	2.00, 40.29	2.44, 52.28	2.64, 54.49	2.3, 43.16	161.31
	0.663	Lean	N/D				N/D				N/D			N/D				N/D				1.97, 41.50	2.22, 53.82	2.29, 54.98	1.95, 44.07	N/D
		Rich	2.64, 45.61	2.80, 38.54	2.79, 37.89	2.71, 46.55	2.58, 48.2	2.96, 39.36	164.34	3.26, 45.38	2.87, 38.87	163.86	2.84, 48.2	3.06, 37.91	164.23	2.88, 39.18	3.27, 45.54	3.03, 47.7	2.89, 40.05	163.80	164.26	2.03, 40.05	2.51, 52.06	2.77, 54.45	2.41, 43.04	160.88
2A3B	0	N/A	2.38, 50.55	2.46, 39.79			N/D				N/D			N/D				N/D				1.98, 41.61	2.22, 53.93	2.30, 55.05	1.96, 44.18	N/D
	0.254	Lean	2.35, 50.47	2.44, 39.71			N/D				N/D			N/D				N/D				1.96, 41.55	2.20, 53.87	2.28, 55.00	1.93, 44.12	N/D
		Rich	2.53, 47.48	2.65, 38.76	2.66, 38.45	2.57, 47.65	2.48, 48.19	2.90, 39.67	164.31	3.14, 46.7	2.70, 38.98	163.81	2.59, 48.16	2.94, 39.02	164.25	2.74, 39.13	3.17, 46.43	2.99, 47.54	2.85, 40.02	163.76	164.24	1.97, 41.01	2.34, 53.11	2.37, 54.74	2.08, 43.65	
	0.465	Lean	N/D				N/D				N/D			N/D				N/D				1.97, 41.51	2.22, 53.83	2.29, 54.98	1.95, 44.08	N/D
		Rich	2.59, 46.08	2.74, 38.54	2.72, 38.01	2.64, 46.78	2.52, 48.14	2.91, 39.43	164.29	3.19, 45.73	2.79, 38.86	163.79	2.74, 48.14	3.00, 38.22	164.24	2.81, 39.10	3.21, 45.70	2.99, 47.61	2.85, 39.99	163.75	164.20	1.99, 40.42	2.42, 52.35	2.59, 54.5	2.25, 43.24	161.94
	0.733	Lean	N/D				N/D				N/D			N/D				N/D				1.92, 41.55	2.17, 53.85	2.24, 54.99	1.90, 44.14	N/D
		Rich	2.60, 45.51	2.76, 38.50	2.75, 37.86	2.66, 46.51	2.54, 48.15	2.91, 39.35	164.28	3.21, 45.38	2.82, 38.83	163.79	2.79, 48.15	3.02, 37.92	164.17	2.83, 39.11	3.22, 45.56	2.99, 47.65	2.85, 40.01	163.74	164.20	1.99, 40.04	2.47, 52.02	2.72, 54.39	2.37, 43.00	160.96

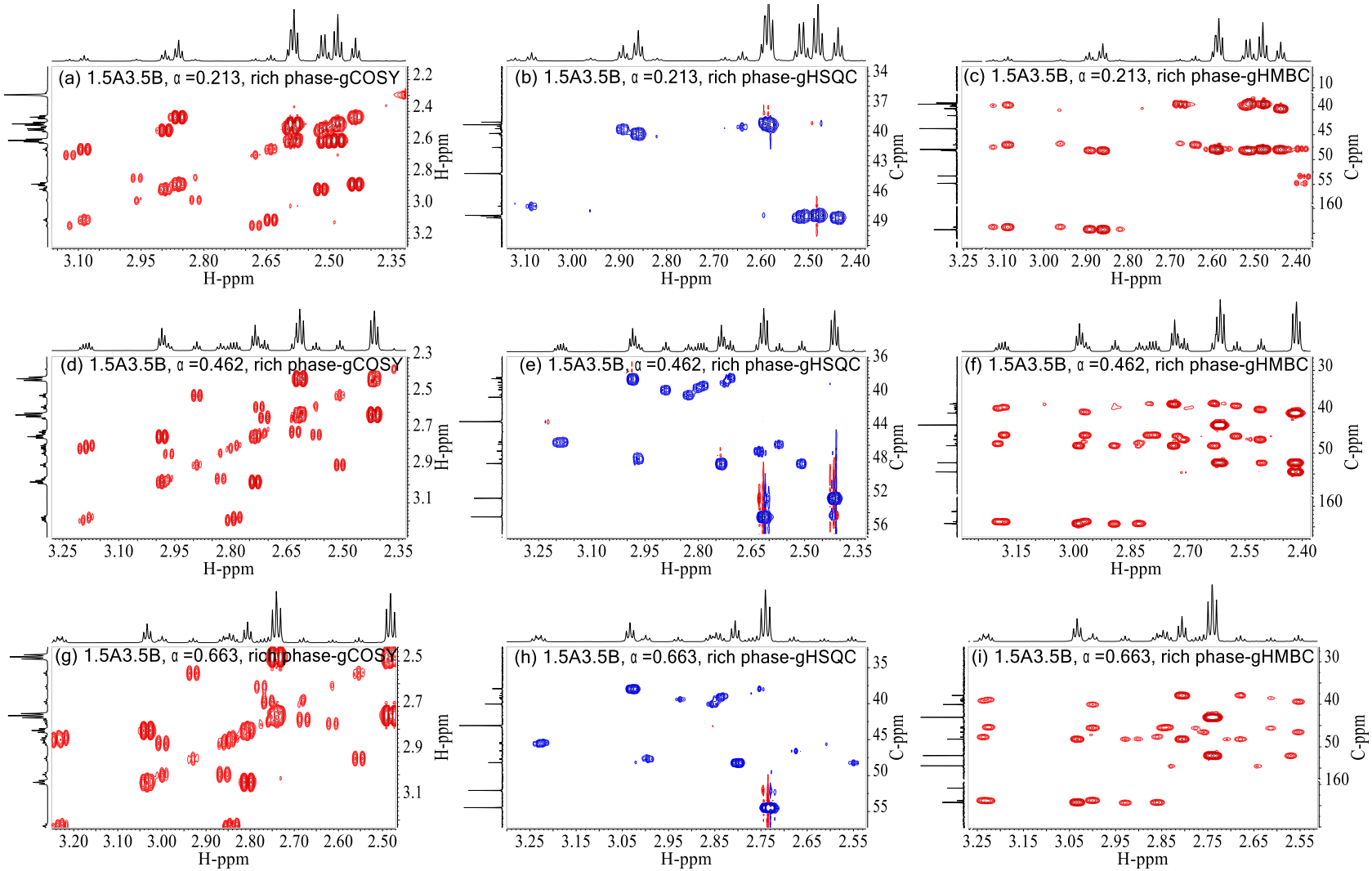

Fig. B-3. 2D NMR spectra (gCOSY, gHSQC and gHMBC) of the CO_2 rich phase samples from 1.5A3.5B. (a to c) spectra of samples at a total CO_2 loading of 0.213 mol mol^{-1}; (d to f) spectra of samples at a total CO_2 loading of 0.462 mol mol^{-1}; (g to i) spectra of samples at a total CO_2 loading of 0.663 mol mol^{-1}. α is the total CO_2 loading in the unit of mol mol^{-1}.

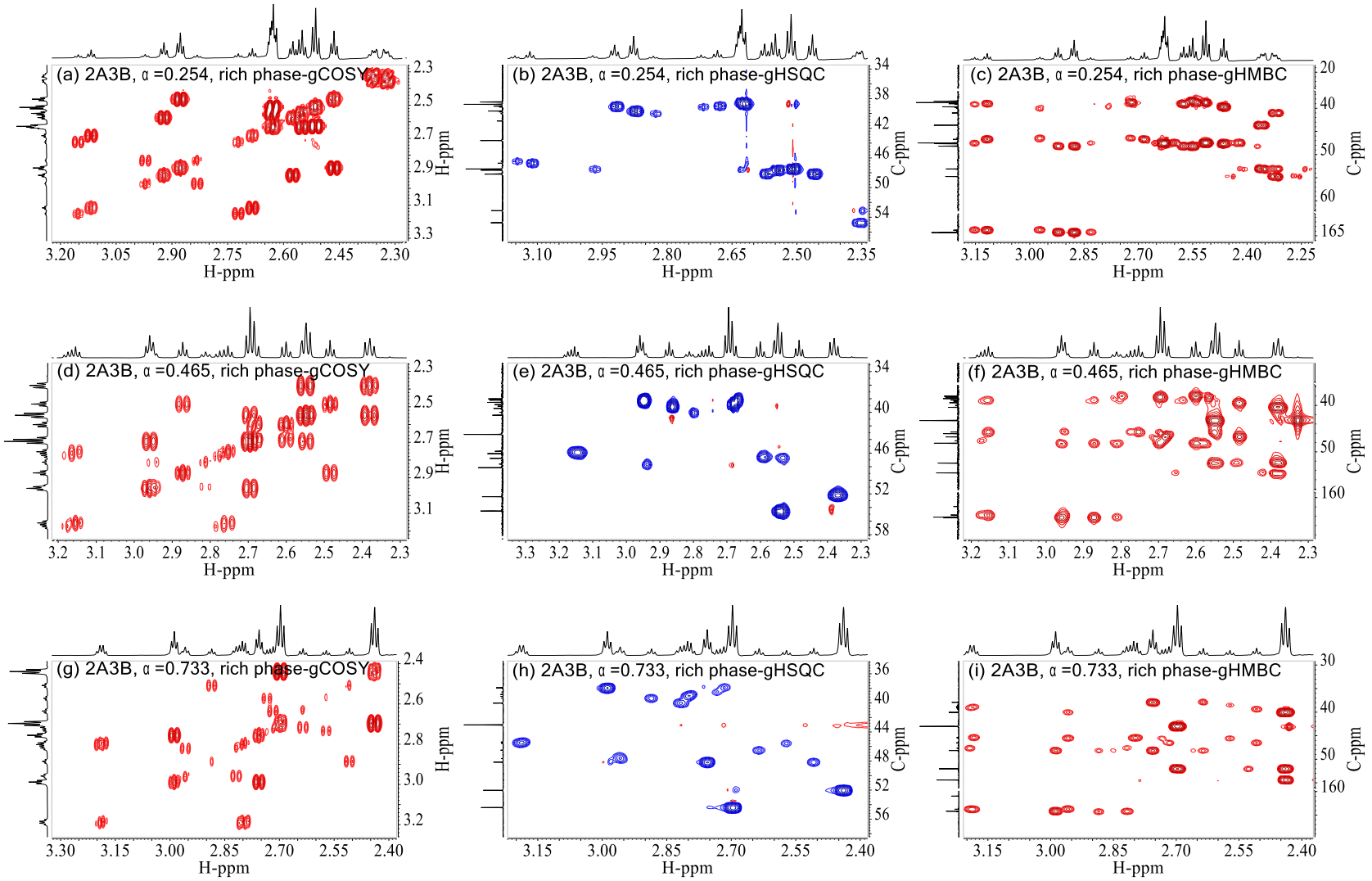

Fig. B-4. 2D NMR spectra (gCOSY, gHSQC and gHMBC) of the CO_2 rich phase samples from 2A3B. (a to c) spectra of samples at a total CO_2 loading of 0.254 mol mol^{-1}; (d to f) spectra of samples at a total CO_2 loading of 0.465 mol mol^{-1}; (g to i) spectra of samples at a total CO_2 loading of 0.733 mol mol^{-1}. α is the total CO_2 loading in the unit of mol mol^{-1}.

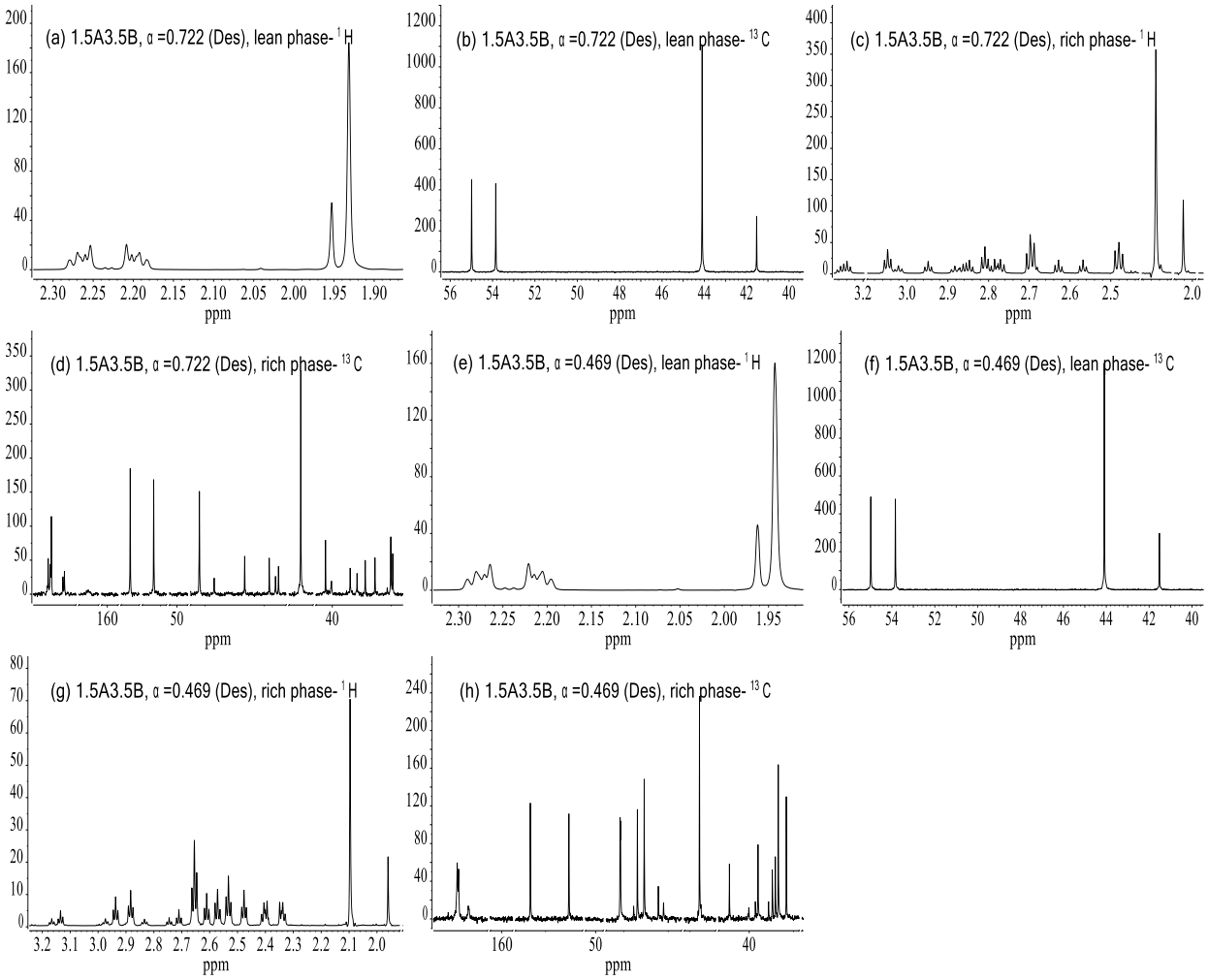

Fig. B-5. NMR spectra of desorption samples derived from 1.5A3.5B. (a) ^{1}H and (b) ^{13}C spectra of lean samples and (c) ^{1}H and (d) ^{13}C spectra of rich samples at a total CO_2 loading of 0.722 mol mol^{-1}; (e) ^{1}H and (f) ^{13}C spectra of lean samples and (g) ^{1}H and (h) ^{13}C spectra of rich samples at a total CO_2 loading of 0.469 mol mol^{-1}. α stands for the total CO_2 loading in the unit of mol mol^{-1}.

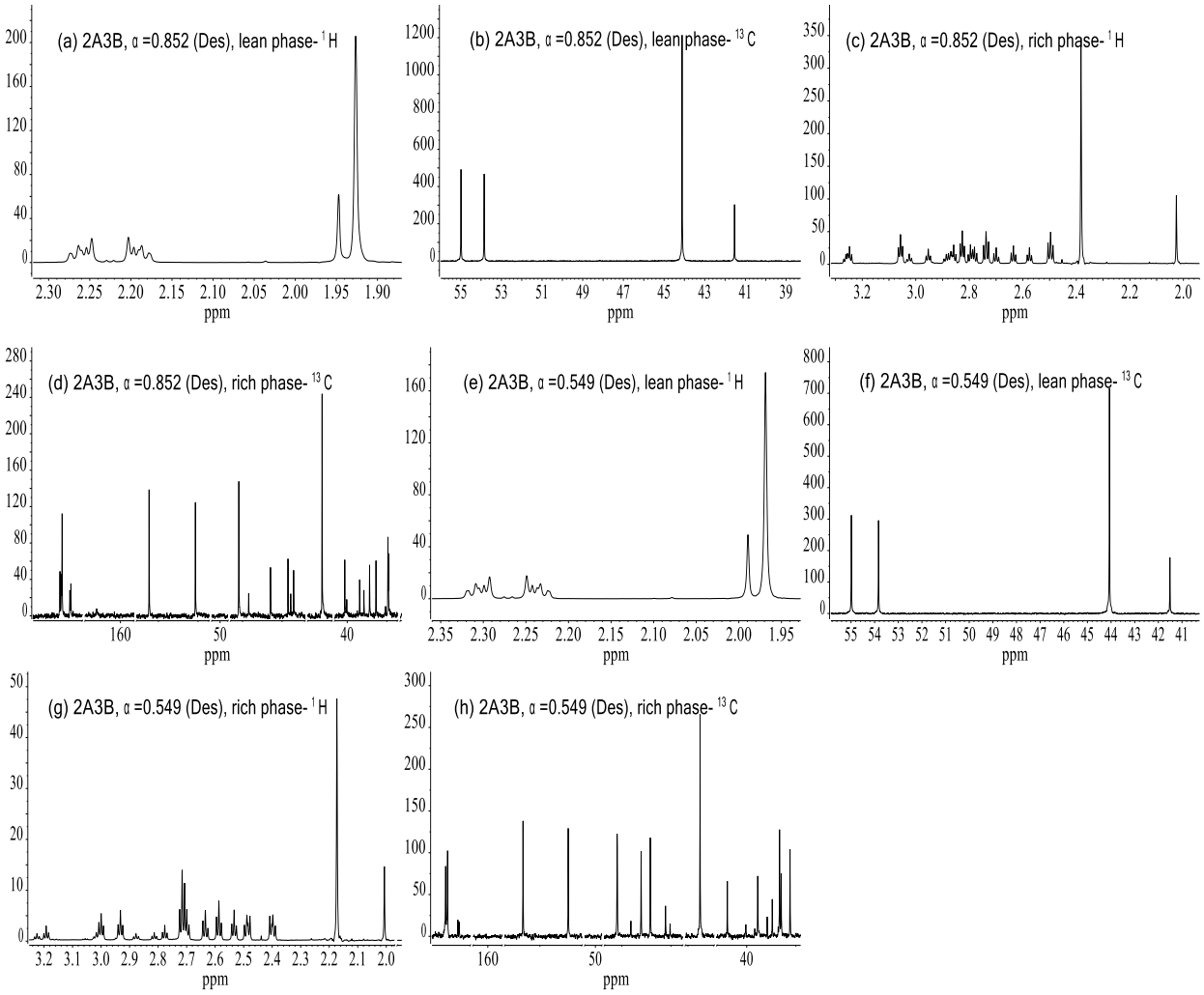

Fig. B-6. NMR spectra of desorption samples derived from 2A3B. (a) ^{1}H and (b) ^{13}C spectra of lean samples and (c) ^{1}H and (d) ^{13}C spectra of rich samples at a total CO_2 loading of 0.852 mol mol^{-1}; (e) ^{1}H and (f) ^{13}C spectra of lean samples and (g) ^{1}H and (h) ^{13}C spectra of rich samples at a total CO_2 loading of 0.549 mol mol^{-1}. α (mol mol^{-1}) is the total CO_2 loading.

Table B-2. Summary of the chemical shifts (H, C) for the characteristic sites of each structural group during CO_2 desorption (N/A: not applicable; N/D: not detected).

Solvent formula	CO_2 ldg. (mol mol^{-1})	Phase	Group A-I		Group A-II					Group A-III			Group A-IV			Group A-V						Group B				HCO_3^- /CO_3^{2-}
			2	1	1	2	3	4	5	2	1	6	2	1	5	1	2	3	4	6	5	4	2	1	3	
1.5A3.5B	1.102	N/A	2.64, 45.61	2.80, 38.54	2.79, 37.89	2.71, 46.55	2.58, 48.2	2.96, 39.36	164.34	3.26, 45.38	2.87, 38.87	163.80	2.84, 48.2	3.06, 37.91	164.23	2.88, 39.36	3.27, 45.54	3.03, 47.7	2.89, 40.05	163.80	164.26	2.03, 40.05	2.51, 52.06	2.77, 54.45	2.41, 43.04	160.88
		Lean	N/D				N/D				N/D			N/D				N/D				1.95, 41.53	2.20, 53.85	2.27, 54.99	1.93, 44.10	N/D
	0.722	Rich	2.63, 45.82	2.78, 38.55	2.77, 37.95	2.69, 46.66	2.57, 48.19	2.95, 39.39	164.35	3.24, 45.51	2.85, 38.88	163.85	2.81, 48.19	3.05, 38.02	164.24	2.86, 39.16	3.25, 45.61	3.02, 47.68	2.88, 40.02	163.79	164.27	2.02, 40.23	2.48, 52.22	2.70, 54.49	2.35, 43.14	161.3
		Lean	N/D				N/D				N/D			N/D				N/D				1.96, 41.52	2.21, 53.84	2.28, 54.98	1.94, 44.09	N/D
	0.469	Rich	2.53, 47.08	2.65, 38.68	2.65, 38.32	2.57, 47.39	2.47, 48.16	2.88, 39.6	164.3	3.13, 46.45	2.71, 38.95	163.8	2.61, 48.17	2.93, 38.82	164.23	2.74, 39.12	3.16, 46.21	2.97, 47.56	2.83, 40.01	163.76	164.23	1.96, 40.89	2.34, 52.94	2.40, 54.67	2.09, 43.56	N/D
2A3B	1.163	N/A	2.60, 45.51	2.76, 38.50	2.75, 37.86	2.66, 46.51	2.54, 48.15	2.91, 39.35	164.28	3.21, 45.38	2.82, 38.83	163.79	2.79, 48.15	3.02, 37.92	164.17	2.83, 39.11	3.22, 45.56	2.99, 47.65	2.85, 40.01	163.74	164.20	1.99, 40.04	2.47, 52.02	2.72, 54.39	2.37, 43.00	160.96
		Lean	N/D				N/D				N/D			N/D				N/D				1.95, 41.54	2.19, 53.85	2.26, 54.99	1.93, 44.11	N/D
	0.852	Rich	2.63, 45.7	2.79, 38.54	2.78, 37.91	2.70, 46.58	2.57, 48.18	2.95, 39.37	164.36	3.25, 45.41	2.86, 38.87	163.86	2.82, 48.18	3.06, 37.94	164.25	2.87, 39.15	3.26, 45.56	3.03, 47.69	2.88, 40.02	163.84	164.28	2.02, 40.11	2.49, 52.11	2.73, 54.46	2.38, 43.09	161.2
		Lean	N/D				N/D				N/D			N/D				N/D				1.99, 41.51	2.24, 53.84	2.31, 54.99	1.97, 44.07	N/D
	0.549	Rich	2.59, 46.84	2.72, 38.66	2.71, 38.23	2.64, 47.21	2.54, 48.19	2.94, 39.55	164.36	3.19, 46.22	2.78, 38.96	163.85	2.70, 48.19	3.00, 38.6	164.28	2.82, 39.16	3.22, 46.04	3.02, 47.63	2.88, 40.03	163.81	164.28	2.01, 40.78	2.40, 52.84	2.49, 54.67	2.18, 43.51	N/D

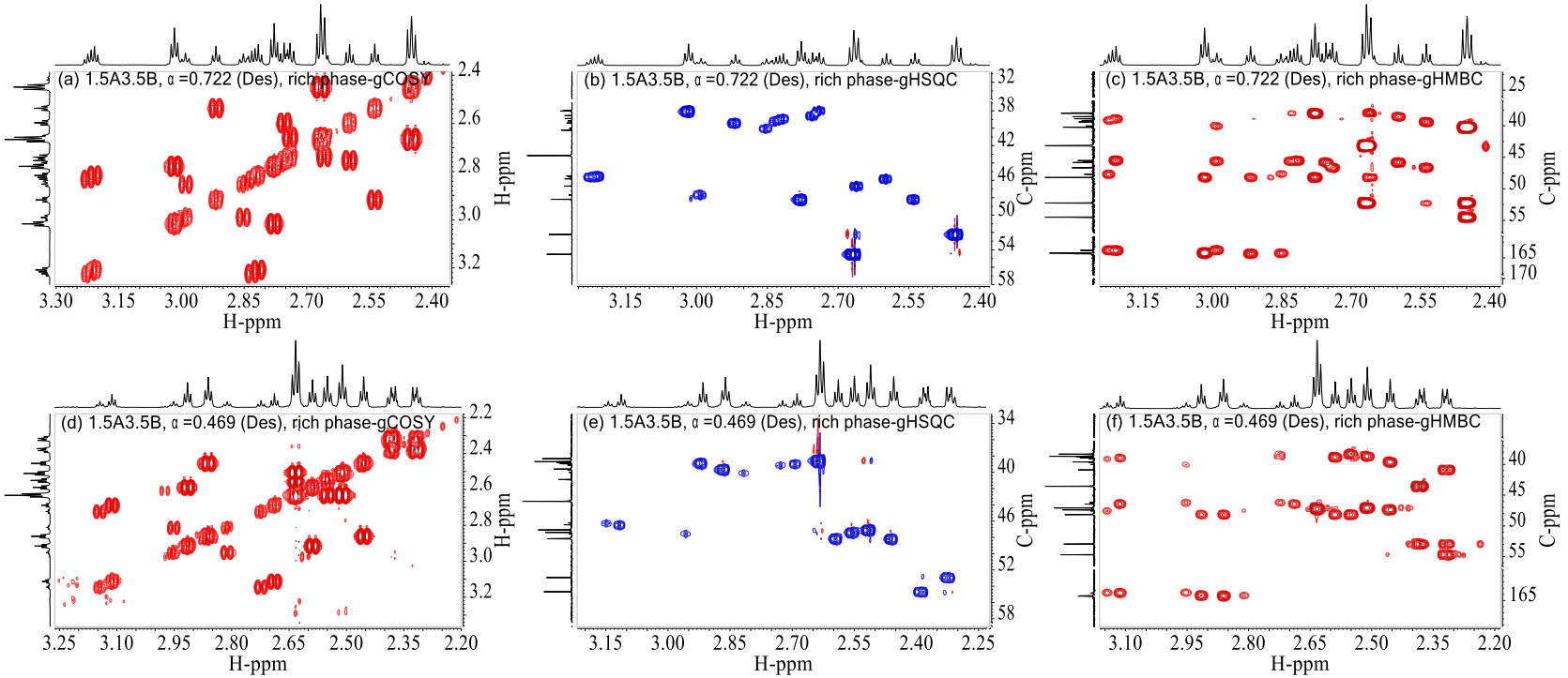

Fig. B-7. 2D NMR spectra (gCOSY, gHSQC and gHMBC) of the desorption samples (dense phase) derived from solvent 1.5A3.5B. (a to c) 2D spectra of samples at a combined CO_2 loading of 0.722 mol mol^{-1}; (d to f) 2D spectra of samples at a combined CO_2 loading of 0.469 mol mol^{-1}. α stands for the total CO_2 loading in the unit of mol mol^{-1}.

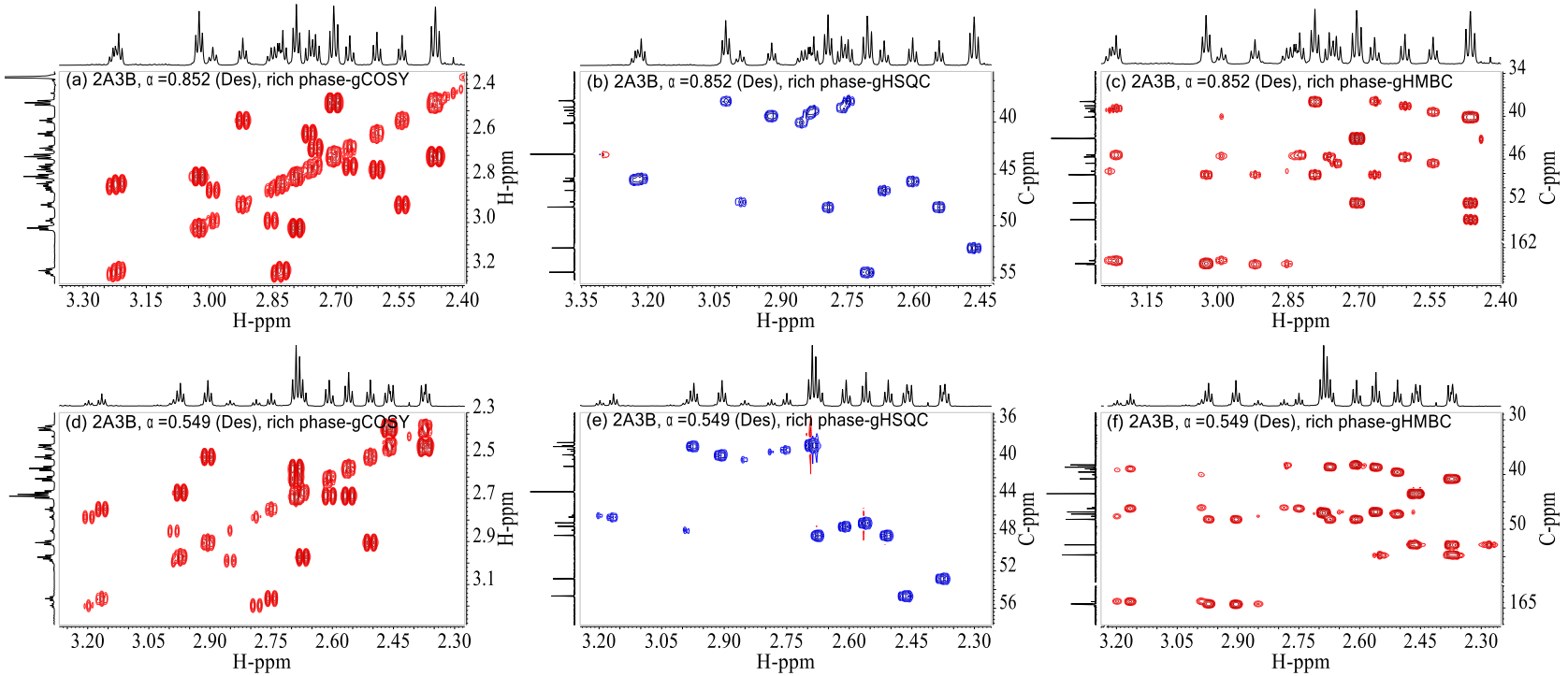

Fig. B-8. 2D NMR spectra (gCOSY, gHSQC and gHMBC) of the desorption samples (dense phase) derived from solvent 2A3B. (a to c) 2D spectra of samples at a combined CO_2 loading of 0.852 mol mol^{-1}; (d to f) 2D spectra of samples at a combined CO_2 loading of 0.549 mol mol^{-1}. α stands for the total CO_2 loading in the unit of mol mol^{-1}.

APPENDIX C: LINGO CODES FOR THE THERMODYNAMIC MODEL

```
model:
sets:
Var/1..75/:C3,C6,C7,C8,C10,C11,C12,C14,C15,C15s,C17,C18,C18s,x1,
x3,x4,x5,x6,x6L,x7,x8,x10,x10L,x11,x12,x14,x15,x15s,x16,x17,x18,
x18s,xw,xwL,r,aw,pd,IS,A,B,pW,e,MR,ML,Vg,Vm,y,Vs,vol,VA0,VB0,VW0
,P,Pw0,Am,AAC,AAW,lnH,T,nA,nB,nW,ldg,V,lnphiW0,lnphiC,lnphiW,PCE;
endsets
data:
T,nA,nB,nW,ldg,V,lnphiW0,lnphiC,lnphiW,PCE=@ole('E:\Research\Pap
er writing\VLLE paper\new data and model\A-
B','T','nA','nB','nW','ldg','V','lnphiW0','lnphiC','lnphiW','PCE
');
enddata
min=@sum(Var(i):P(i)*y(i)/PCE(i)+PCE(i)/P(i)/y(i)-2);
@for(Var(i):
@log(x1(i))+@log(x3(i))+2*@log(r(i))-@log(x4(i))-
@log(aw(i))+C3(i)=235.482-12092.1/T(i)-36.7816*@log(T(i));
@log(x1(i))+@log(x5(i))+4*@log(r(i))-@log(x3(i))-C3(i)=220.067-
12431.7/T(i)-35.4819*@log(T(i));
@log(x1(i))+@log(x6(i))-@log(x7(i))+@log(pd(i))+C6(i)-C7(i)=-
2.626-5944.86/T(i);
@log(x1(i))+@log(x7(i))-@log(x8(i))-
2*@log(r(i))+@log(pd(i))+C7(i)-C8(i)=-0.461-5862.83/T(i);
@log(x1(i))+@log(x10(i))-@log(x11(i))+@log(pd(i))+C10(i)-
C11(i)=-8.35-3757.75/T(i);
@log(x1(i))+@log(x11(i))-@log(x12(i))-
2*@log(r(i))+@log(pd(i))+C11(i)-C12(i)=-6.092-3675.72/T(i);
@log(x1(i))+@log(x14(i))-@log(x4(i))-
@log(x6(i))+2*@log(r(i))+C14(i)-C6(i)=-21.38+5399.07/T(i);
@log(x1(i))+@log(x15(i))-@log(x4(i))-
@log(x14(i))+4*@log(r(i))+C15(i)-C14(i)=-26.09+3893.42/T(i);
@log(x1(i))+@log(x15s(i))-@log(x4(i))-
@log(x14(i))+4*@log(r(i))+C15s(i)-C14(i)=-29.09+4762.08/T(i);
@log(x1(i))+@log(x14(i))-
@log(x16(i))+2*@log(r(i))+@log(pd(i))+C14(i)=3.927-5948.89/T(i);
@log(x1(i))+@log(x16(i))-@log(x17(i))+@log(pd(i))-C17(i)=-8.847-
4227.28/T(i);
@log(x1(i))+@log(x15(i))-
@log(x18(i))+4*@log(r(i))+@log(pd(i))+C15(i)-C18(i)=-2.97-
5979.59/T(i);
@log(x1(i))+@log(x15s(i))-
@log(x18s(i))+4*@log(r(i))+@log(pd(i))+C15s(i)-C18s(i)=-7.168-
4748.64/T(i);
C3(i)=b3*x7(i)+b7*x17(i)+d1*x10(i)+d2*x11(i)+d3*x12(i);
```

```
C6(i)=d13*x10(i)+d14*x11(i)+d15*x12(i);
C7(i)=b3*x3(i)+b38*x14(i)+b39*x15(i)+b40*x15s(i)+b42*x18(i)+b43*
x18s(i);
C8(i)=b44*x14(i)+b45*x15(i)+b46*x15s(i)+b48*x18(i)+b49*x18s(i);
C10(i)=d1*x3(i)+d13*x6(i)+d20*x10(i)+d21*x11(i)+d22*x12(i);
C11(i)=d2*x3(i)+d14*x6(i)+d21*x10(i)+d25*x14(i)+d29*x15(i)+d33*x
15s(i)+d42*x18(i)+d46*x18s(i);
C12(i)=d3*x3(i)+d15*x6(i)+d22*x10(i)+d26*x14(i)+d30*x15(i)+d34*x
15s(i)+d43*x18(i)+d47*x18s(i);
C14(i)=b38*x7(i)+b44*x8(i)+d25*x11(i)+d26*x12(i);
C15(i)=b39*x7(i)+b45*x8(i)+d29*x11(i)+d30*x12(i);
C15s(i)=b40*x7(i)+b46*x8(i)+d33*x11(i)+d34*x12(i);
C17(i)=b7*x3(i)+b66*x18(i)+b67*x18s(i);
C18(i)=b42*x7(i)+b48*x8(i)+b66*x17(i)+d42*x11(i)+d43*x12(i);
C18s(i)=b43*x7(i)+b49*x8(i)+b67*x17(i)+d46*x11(i)+d47*x12(i);
x1(i)+x7(i)+2*x8(i)+x11(i)+2*x12(i)+x17(i)=x3(i)+2*x5(i)+x14(i)+
2*x15(i)+2*x15s(i)+x18(i)+x18s(i);
x1(i)+x3(i)+4*x5(i)+x7(i)+4*x8(i)+x11(i)+4*x12(i)+x14(i)+4*x15(i
)+4*x15s(i)+x17(i)+x18(i)+x18s(i)=2*IS(i);
-2.303*A(i)*@sqrt(IS(i))/(1+4*B(i)*@sqrt(IS(i)))=@log(r(i));
A(i)=1824800*@sqrt(pW(i))/((e(i)*T(i))^1.5);
B(i)=50.292*@sqrt(pW(i))/@sqrt(e(i)*T(i));
pW(i)=0.00014395/(0.0112^(1+(1-T(i)/649.727)^0.05107));
e(i)=87.74-0.40008*(T(i)-273.15)+0.0009398*(T(i)-273.15)^2-
0.00000141*(T(i)-273.15)^3;
(x6(i)+x7(i)+x8(i)+x14(i)+x15(i)+x15s(i)+x16(i)+x17(i)+x18(i)+x1
8s(i))*MR(i)+x6L(i)*ML(i)=nA(i);
(x10(i)+x11(i)+x12(i))*MR(i)+x10L(i)*ML(i)=nB(i);
(x3(i)+x4(i)+x5(i)+x14(i)+2*x15(i)+2*x15s(i)+x16(i)+x17(i)+2*x18
(i)+2*x18s(i))*MR(i)+x4(i)*ML(i)+Vg(i)/Vm(i)*y(i)=ldg(i)*(nA(i)+
nB(i));
(xw(i)+x3(i)+x5(i))*MR(i)+xwL(i)*ML(i)+Vg(i)/Vm(i)*(1-
y(i))=nW(i);
Vs(i)=(nA(i)*VA0(i)+nB(i)*VB0(i)+(nW(i)-Vg(i)/Vm(i)*(1-
y(i)))*VW0(i))*0.951+(ldg(i)*(nA(i)+nB(i))-
Vg(i)/Vm(i)*y(i))*(37.51-9.585E-02*(T(i)-273.15)+8.74E-
04*((T(i)-273.15)^2)-5.044E-07*((T(i)-273.15)^3))/1E06;
Vg(i)=V(i)-Vs(i);
VA0(i)=8.31445985*692.575/4260153.9342535*(0.253025510968227^(1+
(1-T(i)/692.575)^(2/7)));
VB0(i)=8.31445985*640.862/2293712.6583579*(0.255487450140789^(1+
(1-T(i)/640.862)^(2/7)));
VW0(i)=8.31445985*647.3/22090000*(0.233^(1+(1-
T(i)/647.3)^(2/7)));
1000*pd(i)*Vs(i)*vol(i)=MR(i);
Vs(i)*(1-
vol(i))=ML(i)*(x6L(i)*VA0(i)+x10L(i)*VB0(i)+xwL(i)*VW0(i))*0.951
```

```
+ML(i)*x4(i)*(37.51-9.585E-02*(T(i)-273.15)+8.74E-04*((T(i)-
273.15)^2)-5.044E-07*((T(i)-273.15)^3))/1E06;
x6L(i)*0.10317+x10L(i)*0.1733+xwL(i)*0.018+x4(i)*0.044=1;
(x6(i)+x7(i)+x8(i)+x14(i)+x15(i)+x15s(i)+x16(i)+x17(i)+x18(i)+x1
8s(i))*0.10317+(x10(i)+x11(i)+x12(i))*0.1733+(xw(i)+x3(i)+x5(i))
*0.018+(x3(i)+x4(i)+x5(i)+x14(i)+2*x15(i)+2*x15s(i)+x16(i)+x17(i
)+2*x18(i)+2*x18s(i))*0.044=1;
(xwL(i)+x4(i)+x6L(i)+x10L(i))*aw(i)=xwL(i);
(xw(i)+x3(i)+x4(i)+x5(i)+x6(i)+x7(i)+x8(i)+x10(i)+x11(i)+x12(i)+
x14(i)+x15(i)+x15s(i)+x16(i)+x17(i)+x18(i)+x18s(i))*aw(i)=xw(i);
@log(x6(i))+C6(i)=@log(x6L(i))+d13*x10L(i);
@log(x10(i))+C10(i)=@log(x10L(i))+d13*x6L(i)+d20*x10L(i);
P(i)=8.31445985*T(i)/Vm(i)-Am(i)/(Vm(i)^2);
Am(i)=(y(i)*AAC(i)+(1-y(i))*AAW(i))^2;
AAC(i)=0.608871960476329*(1+0.82631066875*(1-@sqrt(T(i)/304.2)));
AAW(i)=0.748685957172566*(1+1.00039244032*(1-@sqrt(T(i)/647.3)));
@log(P(i))+@log(y(i))+lnphiC(i)=@log(x4(i))+lnH(i);
lnH(i)=94.4914-6789.04/T(i)-11.4519*@log(T(i))-
0.010454*T(i)+@log(101325);
@log(P(i))+@log(1-
y(i))+lnphiW(i)=@log(aw(i))+@log(Pw0(i))+lnphiW0(i);
Pw0(i)=1000*0.61121*@exp((18.678-(T(i)-273.15)/234.5)*((T(i)-
273.15)/(257.14+T(i)-273.15)));
@bnd(1E-20,x1(i),9.9);
@bnd(1E-20,x3(i),9.9);
@bnd(1E-20,x4(i),9.9);
@bnd(1E-20,x5(i),9.9);
@bnd(1E-20,x6(i),9.9);
@bnd(1E-20,x6L(i),9.9);
@bnd(1E-20,x7(i),9.9);
@bnd(1E-20,x8(i),9.9);
@bnd(1E-20,x10(i),9.9);
@bnd(1E-20,x10L(i),9.9);
@bnd(1E-20,x11(i),9.9);
@bnd(1E-20,x12(i),9.9);
@bnd(1E-20,x14(i),9.9);
@bnd(1E-20,x15(i),9.9);
@bnd(1E-20,x15s(i),9.9);
@bnd(1E-20,x16(i),9.9);
@bnd(1E-20,x17(i),9.9);
@bnd(1E-20,x18(i),9.9);
@bnd(1E-20,x18s(i),9.9);
@bnd(0.5,pd(i),1.5);
@bnd(0.00001,aw(i),0.99999);
@bnd(0.00001,r(i),0.99999);
@bnd(0.00001,y(i),0.99999);
@bnd(1000,P(i),1E+07);
```

```
@bnd(1E-5,Vm(i),9.9);
C3(i)+@log(r(i))<=0;
C7(i)+@log(r(i))<=0;
C8(i)+4*@log(r(i))<=0;
C11(i)+@log(r(i))<=0;
C12(i)+4*@log(r(i))<=0;
C14(i)+@log(r(i))<=0;
C15(i)+4*@log(r(i))<=0;
C15s(i)+4*@log(r(i))<=0;
C17(i)+@log(r(i))<=0;
C18(i)+@log(r(i))<=0;
C18s(i)+@log(r(i))<=0;
@bnd(-2,d20,1);
@bnd(-1,b67,1);
@bnd(-1,d43,1);
x15s(i)+x18s(i)<=2*(x15(i)+x18(i));
x15(i)+x18(i)<=x15s(i)+x18s(i);
);
End
```